

Robotic Assembly: Chamferless Peg-Hole Assembly Operation From X/Y/Z Directions

By

Wasim Haskiya

**Department of Mechanical and Manufacturing Engineering,
De Montfort University,
Leicester, UK**

**A thesis submitted for partial fulfilment of the degree of
Doctor of Philosophy**

July 2000

ABSTRACT

A great deal of research of the robotic peg-in hole assembly operation has evolved over the past decades. In the case of a chamfered peg-hole, it is normal to use a simple wrist such as the Remote Centre Compliance (RCC), which is fitted between the robot arm and the end effector to accommodate misalignments between the peg and the hole during the engagement stage. Otherwise jamming could occur and cause damage to the assembly robot and or the mating parts. However, in case of no chamfer on either of the mating parts, complicated and expensive devices are used to accommodate the same misalignments as the RCC.

The objective of this research is to develop a new passive assembly strategy and consequently a compliant wrist for the peg-hole insertion process. The wrist should adopt the passive technique as the RCC, but should accommodate positional errors even in case of no chamfer on either of the peg or the hole. Moreover, it should function from vertical as well as the horizontal directions.

The thesis presents a new passive assembly strategy for chamferless peg-in hole assembly operation. This strategy was inspired from a theory known as the domino effect. One principle of this theory was implemented in the design and construction of a wrist called Chamferless-Vertical-Horizontal Remote Centre Compliance (CVHRCC). After a thorough literature survey, no report was found about any passive wrist that is capable of accommodating misalignment between chamferless mating parts as the CVHRCC.

To validate the theoretical analysis, a series of peg-hole assembly experiments were carried out. The results of these experiments have coincided with the theoretical results obtained during the theoretical simulation process. It was proven that the CVHRCC could function reliably in accommodating positional misalignments between chamferless cylindrical parts with clearance over 0.3 mm for a given initial positional error of 2 mm and 3° from the vertical direction. But for mating parts with clearance of less than 0.2 mm , the wrist could not function reliably.

ACKNOWLEDGEMENT

Many people have supported me to carry out this research. They have provided a valuable help in the intellectual, spiritual, emotional and economic realms of my life during the past years. I would publicly thank De Montfort University and the Department of Mechanical and Manufacturing Engineering for providing an environment of learning, where I carried out my research work.

My sincere appreciation goes to Dr Keith Maycoack, my first supervisor, who guided my research by helping me staying on the right path. Also, he wisely gave me a confidence in my research abilities by giving me all the help and support I needed instead of all the help and support I thought I wanted.

Thanks to Professor Jeff Knight, the second supervisor, and the Head of Research and Mechanical and Manufacturing Engineering Department; for his supports throughout my stay at this university. Also, for his valuable advise on my research from time to time. Also, many thanks to Dr Hong Qiao who was my first supervisor before she moved to another job. Not to forget Dr H. Newlyn, Mr R. Lawrence, Mr B. Harris, Mr A. Gayretli and Mr A. Ahmed; all for their valuable time discussing my research work. Much more thanks goes to my family who gave me the spiritual and financial support to carry out this research, and finally, thanks to my wife who has been very patient with me in the last few years and gave me the belief and confidence that I can do more than I thought can do.

TITLE PAGE	i
ABSTRACT	ii
ACKNOWLEDGEMENT	iii
CONTENTS	iv
LIST OF FIGURES	ix
LIST OF TABLES	xiii
NOMENCLATURE	xiv
CHAPTER 1	1
1. INTRODUCTION	1
1.1 ASSEMBLY PROBLEMS	2
1.2 APPLICATION AND MOTIVATION	3
1.3 METHODOLOGY	3
1.4 THESIS ORGANISATION	4
CHAPTER 2	6
2. LITERATURE SURVEY	6
2.1 INTRODUCTION	6
2.2 INDUSTRIAL EXAMPLES	6
2.2.1 The Rover Engine Line	6
2.2.2 Robot System Builds Customised Printed Circuit Boards	7
2.2.3 Automatic Board Assembly	8
2.2.4 Acoustic Emission For Monitoring Assembly Operation	8
2.3 FINE-MOTION STRATEGIES	9
2.3.1 A Strategy For Peg-Hole Assembly Without RCC Or Force Sensor	10
2.3.2 The Pre-Image Strategy	10
2.4 COMPLIANT SYSTEMS	12

2.4.1	Passive Assembly Accommodation	12
2.4.1.1	Compliant wrists or work station	13
2.4.1.2	Air-stream assisted method	14
2.4.1.3	Magnetic force method	14
2.4.1.4	Vibratory motion method	15
2.4.2	Active Assembly Accommodation	16
2.4.2.1	Servoing with force sensors	16
2.4.2.2	Servoing with vision sensors	17
2.4.2.3	Servoing with proximity sensors	17
2.4.3	Passive-Active Assembly Accommodation	18
2.5	SUMMARY	21
 CHAPTER 3		22
3.	A NEW ASSEMBLY STRATEGY AND THE DOMINO EFFECT THEORY	22
3.1	INTRODUCTION	22
3.2	A NEW ASSEMBLY STRATEGY	23
3.3	THE DOMINO EFFECT THEORY	24
3.4	COMPARISON BETWEEN THE NEW STRATEGY AND THE DOMINO EFFECT THEORY	25
3.5	DOMINO EFFECT ANALYSIS	26
3.6	ANALYSIS OF THE NEW ASSEMBLY STRATEGY	27
3.6.1	Vertical Assembly	27
3.6.2	Horizontal Assembly	30
3.7	CONCLUSION	35
 CHAPTER 4		36
4.	3D ANALYSIS OF THE GEOMETRICAL PEG-HOLE INSERTION	36
4.1	INTRODUCTION	36
4.2	PRELIMINARY ANALYSIS	36
4.3	PEG-INTO THE HOLE	39
4.4	THE EFFECT OF THE TILT ANGLE ON THE INSERTION DEPTH	42
4.5	CONCLUSION	45

CHAPTER 5	46
5. DYNAMIC INVESTIGATION OF THE PEG-HOLE PROCESS	46
5.1 INTRODUCTION	46
5.2 THE FRICTION CONE	47
5.3 COMPLIANT MOTION	48
5.3.1 Stick-Slip Motion	49
5.4 INVESTIGATION OF THE DYNAMIC OF 3D INITIAL CONTACT BETWEEN THE PEG AND THE HOLE	50
5.4.1 Approach	50
5.4.2 Initial Contact Between The Peg And The Surface Of The Hole	51
5.4.2.1 Slipping or sticking occurrence	51
5.4.2.2 The possibility of three points of contact (3 POC)	54
5.4.2.3 The ideal wrist stiffness	56
5.4.3 Peg Is Inside The Hole: The Conditions For Successful Assembly	58
5.5 THE INSERTION FORCE DURING ONE/TWO-POINT CONTACT	67
5.6 WRIST KINEMATICS	68
5.6.1 Peg Diameter From Dynamical Consideration	69
5.6.2 Peg Diameter from Geometrical Consideration	71
5.7 DISCUSSION	73
5.8 CONCLUSION	73
CHAPTER 6	75
6. PEG-HOLE MODELLING AND SIMULATION	75
6.1 INTRODUCTION	75
6.2 BACKGROUND	76
6.3 MODELLING STAGES	77
6.3.1 Approach Stage	78
6.3.2 Initial Contact	79
6.3.3 Transition Stage	81
6.3.4 Transition From One To Two-Point Contact	84
6.3.5 Final Alignment	86

6.4	SIMULATION	87
6.5	CONCLUSION	102
CHAPTER 7		103
1.	THE CHAMFERLESS-VERTICAL-HORIZONTAL COMPLIANT WRIST (CVHRCC)	103
7.1	INTRODUCTION	103
7.2	WRIST DESCRIPTION	104
7.2.1	Wrist Operation	104
7.3	WRIST STIFFNESS	106
7.3.1	Wrist Angular Stiffness	107
7.3.2	Wrist Lateral Stiffness	110
7.4	MAXIMUM WRIST STIFFNESS	114
7.5	WRIST DESIGN	119
7.6	DISCUSSION	122
7.7	CONCLUSION	123
CHAPTER 8		124
8.	EXPERIMENTS AND DATA CORRELATION	124
8.1	INTRODUCTION	124
8.2	FIRST STAGE OF EXPERIMENTS	125
8.2.1	Experimental Rig	125
8.2.2	Experimental Procedure	125
8.3	SECOND STAGE OF EXPERIMENTS	130
8.3.1	Assembly Rig and Wrist Instrumentation and Calibration	130
8.3.2	Peg-hole Experiments	133
8.3.2.1	Further experiments	136
8.4	DISCUSSION	140
8.5	CONCLUSION	141
CHAPTER 9		142
9.	DISCUSSION	142

CHAPTER 10	147
10. CONCLUSION AND RECOMMENDATIONS	147
10.1 CONCLUSIONS	147
10.2 RECOMMENDATIONS	149
REFERENCES	150
APPENDIX 1	
EXPERIMENTAL DETERMINATION OF THE MOMENT OF INERTIA FOR THE CVHRCC	159
APPENDIX 2	
Peg-Hole Assembly Experiments	161
APPENDIX 3	
SUMMARY OF FINITE ELEMENT RESULTS	166
DRAWINGS & PUBLICATIONS	176

LIST OF FIGURES

Figure 1.1	Misalignment of parts during an assembly operation, (a) lateral error and (b) angular error	2
Figure 2.1	Basic idea for the pre-image concept	11
Figure 3.1	The new assembly strategy, main vertical stages	23
Figure 3.2	The new assembly strategy, main horizontal stages	24
Figure 3.3	Graphical representation for the domino effect theory	25
Figure 3.4	First domino in unstable position	26
Figure 3.5	Forces acting on the second domino	26
Figure 3.6	Vertical approach stages	27
Figure 3.7	Peg during second stage, position (a)	28
Figure 3.8	Peg during second stage position (c)	29
Figure 3.9	The peg during stages 3&4	30
Figure 3.10	Completion of the assembly operation	30
Figure 3.11	Horizontal approach stages	31
Figure 3.12	Peg during second stage, position (a)	32
Figure 3.13	Peg during second stage, position (c)	32
Figure 3.14	The peg during stages 3 & 4	33
Figure 3.15	Completion of the assembly operation	34
Figure 3.16	The steps of the new assembly strategy during the simulation programme	34
Figure 4.1	Peg and a hole in 3D space	37
Figure 4.2	Vertical projection of the peg tip over the hole	38
Figure 4.3	Peg and a hole in 3 different stages in the initial contact phase	39
Figure 4.4	General case, peg-hole in two-point of contact	40
Figure 4.5	A top view on the peg artificial cut and the hole	41
Figure 4.6	A top artificial view on the projection of the peg tip inside the hole	42
Figure 4.7	Peg is in a contact with the hole (a) two-point, (b) one-point of contact	43
Figure 4.8	Tilt angle versus insertion depth during two-point contact	44
Figure 4.9	Tilt angle versus insertion depth during one-point contact	44
Figure 5.1	The friction cone	47

Figure 5.2	Sticking (<i>a</i>) and sliding (<i>b</i>)	48
Figure 5.3	approach stage	50
Figure 5.4	Initial contact between the peg and the upper surface of the hole	52
Figure 5.5	3D space of point (1) and the impulsive force acting upon	53
Figure 5.6	Peg is in 3 point of contact with the hole	55
Figure 5.7	Schematic of peg-wrist during 3POC	57
Figure 5.8	Peg is inside the hole tilt angle is zero	59
Figure 5.9	Peg in two-point contact ($\vartheta = 0$)	60
Figure 5.10	Centre axis of the peg is tilted by ϑ	61
Figure 5.11	Peg is in line contact with the hole	62
Figure 5.12	Peg is in one-point contact	63
Figure 5.13	Peg is in one-point contact from the bottom	65
Figure 5.14	The jamming diagram (after Whitney)	66
Figure 5.15	The wrist model in 2D space	68
Figure 5.16	Peg is sitting inside the wrist	69
Figure 5.17	Peg diameter versus the wrist initial lateral deformation	70
Figure 5.18	Peg geometry	71
Figure 5.19	Peg diameter versus the wrist angular deformation	72
Figure 6.1	Concept of a system	76
Figure 6.2	General block diagram of the insertion process	77
Figure 6.3	Representation of peg-wrist during peg-in hole initial contact	77
Figure 6.4	A one-stage insertion process (no misalignments)	78
Figure 6.5	A simulation block diagram for peg-hole (no misalignments)	79
Figure 6.6	Reaction torque's acting on the FBD of the peg during two-point contact	79
Figure 6.7	The peg in two point contact with the hole during the initial contact stage	80
Figure 6.8	A simulation block diagram for the peg initial tilt	81
Figure 6.9	Peg is moving to the far side of the hole (transitional)	82
Figure 6.10	The FBD of the peg during the transition stage	82
Figure 6.11	Simulation block diagram for the peg transitional stage	83
Figure 6.12	left-side angular misalignment	84

Figure 6.13	The peg is in transition from one-to-two point contact	84
Figure 6.14	The FBD of the peg during transition stage	85
Figure 6.15	Integrator chain, simulation diagram for the peg during contact sliding	86
Figure 6.16	The peg tilting from two-point contact to zero angular misalignment	86
Figure 6.17	Simulation block diagram for the peg during two-point contact-completion stage	87
Figure 6.18	Simulation programme for the peg-in hole insertion process	89
Figure 6.19	Summary of the simulation process for initial error of 1.5 mm, $c = 0.2$ mm	90
Figure 6.20	Successful assembly for initial error of 1 mm, $c = 0.2$ mm	91
Figure 6.21	Successful assembly for initial error of 1 mm, $c = 0.2$ mm	91
Figure 6.22	Jamming, zero angular stiffness and 1 mm initial lateral error, $c = 0.2$ mm	92
Figure 6.23	Jamming, angular stiffness 5000 Nmm/rad and 1 mm initial error, $c = 0.2$ mm	92
Figure 6.24	Progress of the maximum angular tilt for given initial lateral misalignment and different clearances	93
Figure 6.25	Progress of the maximum lateral transition for given initial lateral misalignment and different clearances	94
Figure 6.26	Summary of the simulation process for initial angular misalignment, from 1° to 12°, $c = 0.2$ mm	95
Figure 6.27	Relation between the applied forces and the angle of tilt	95
Figure 6.28	Summary of the simulation process for initial angular misalignment, from 1° to 12°, $c = 0.2$ mm, the applied force is 100 N	96
Figure 6.29	Angular error, clearance and the possible 3 point of contact	97
Figure 6.30	Behaviour of angular tilt versus angular stiffness	98
Figure 6.31	Progress of the maximum lateral transition for given initial lateral misalignment and different clearances using wrist theoretical stiffness	100
Figure 6.32	Summary of theoretical results	101
Figure 6.33	Maximum angular tilt for different peg sizes, $c = 0.2$ mm	101
Figure 7.1	CVHRCC mechanism	105
Figure 7.2	Operational principles of the CVHRCC	106
Figure 7.3	Sketch of the experimental rig, CVHRCC during the angular stiffness measurements	107
Figure 7.4	CVHRCC on a milling machine, for angular stiffness determination	108

Figure 7.5	Sketch of experimental rig, CVHRCC during lateral stiffness measurements	110
Figure 7.6	CVHRCC on a milling machine, for lateral stiffness determination	111
Figure 7.7	Comparison between experimental, theoretical CVHRCC angular deflections	113
Figure 7.8	Comparison between experimental, theoretical CVHRCC lateral deflections	113
Figure 7.9	Sketch of peg-wrist during the test	114
Figure 7.10	The applied force versus the wrist angular stiffness	117
Figure 7.11	The applied force versus the wrist lateral stiffness	118
Figure 7.12	Scheme for the wrist design parameters	120
Figure 8.1	The assembly rig/machine	126
Figure 8.2	The success rate for the experimental positional error	128
Figure 8.3	CVHRCC performing assembly operation	129
Figure 8.4	Instrumentation of the CVHRCC and the assembly rig	130
Figure 8.5	Cross plate instrumentation and calibration	131
Figure 8.6	The calibration data for the cross plate	132
Figure 8.7	The success rate of range of pegs of different diameter	133
Figure 8.8	The success rate against range of lateral misalignment on the X axis	134
Figure 8.9	The success rate against range of lateral misalignment on the Y axis	134
Figure 8.10	The success rate against a variable angular misalignment	135
Figure 8.11	The success rate for 30 and 35 <i>mm</i> peg diameter	137
Figure 8.12	Peg diameter 15 <i>mm</i> and the clearance is 0.1 <i>mm</i>	138
Figure 8.13	Peg diameter 20 <i>mm</i> and clearance 0.1 <i>mm</i>	138
Figure 8.14	Peg diameter 25 <i>mm</i> and clearance 0.2 <i>mm</i>	139
Figure 8.15	Peg diameter 30 <i>mm</i> and clearance 0.2 <i>mm</i>	139
Figure 8.16	Peg diameter 35 <i>mm</i> clearance 0.2 <i>mm</i>	140

LIST OF TABLES

Table 2.1	Performance data for various assembly methods	20
Table 3.1	Similarities between the new assembly strategy and the domino effect theory	25
Table 5.1	Contact mode conditions	54
Table 5.2	Possible contact modes	60
Table 7.1	CVHRCC angular deflection data	109
Table 7.2	CVHRCC lateral deflection data	112
Table 7.3	First test, experimental data and wrist stiffness	116
Table 7.4	Second test, experimental data and wrist stiffness	116
Table 7.5	Third test, experimental data and wrist stiffness	116
Table 7.6	Fourth test, experimental data and wrist stiffness	117
Table 8.1	A summary of the assembly experiment	127
Table 8.2	The progress of the cross plate calibration	134

NOMENCLATURE

B	is the positional uncertainty ball with P as the centre of the tip of the peg
c	clearance between the peg and the hole
COC	centre of compliance
COM	centre of mass
$CVHRCC$	chamferless-vertical-horizontal remote centre compliance
e_0	initial lateral error
e_x and e_y	initial approach misalignment on the X and Y axes, or peg transition
e_g	is the lateral distance between the centre of the peg to that of the hole during peg-in hole one or two point contact
$F, F_{in}, F_{1...n}, F_{2...n}$	applied forces
F_{imp}	impulsive force
F_S	spring force
F_X	axial force
F_Z	insertion force
f, f_2', f_t	friction forces
f_1, f_2, f_3, f_4	reaction forces
f_n	normal force
f_r	resultant force/reaction force
g	gravitational acceleration
G	the goal (bottom of the hole)
h	distance between peg's tip and the hole surface before the start of the assembly
H	peg height
I	moment of the inertia
K_x	compliance lateral stiffness
K_g	compliance angular stiffness
l, l_1, l_2, l_i	distance from the applied force to the friction force (surface), or the insertion depth during one and two point contact
L_g	is the centre of rotation
m	the mass of the peg and the wrist
M, M_1, M_t	tilt moment
O_h	centre of the hole about its mouth

O_p	centre of the peg at the tip
P	point on the centre of the peg tip
r	peg's radius
R	hole radius, or sub-goal
RCC	remote centre compliance
s	rotational displacement
T	is the reaction torque
$W, W_{1,2}$	domino weight
μ	coefficient of friction
ϑ, ϑ_0	angle between the peg's tip and the hole's surface/axis, or the angular approach misalignment (initial angular error)
$\delta \vartheta$	angular deflection in radians
δe	the lateral approach misalignment
δx	is the lateral deflection of the peg due to the applied force and the sponge compression.
ϕ	the friction angle
ρ	material density

CHAPTER 1

INTRODUCTION

The cylindrical peg-in hole assembly operation is the most common task in assembly [S. P. Chan et al,1997]. In the past, this task was performed by humans, because of their ability to sense and adjust to changes in the products being assembled. However, the technological progress has led to more complex parts being designed, and produced in large quantities and having small clearances that has to be assembled in a short time. This fact has resulted in:

- an increase in the assembly time
- a decrease in the reliability and quality of products, due to the complexity and repetitive actions of assembly which causes tiredness to the workers
- an increase in the assembly cost, nearly 40% of manpower costs in production come from assembly

Hence, in the past decades research and development have shifted towards the robotic/automated assembly technologies [Y. Xu et al, 1990: H. Qiao, 1995]. However, the inaccuracy of an assembly robot in positioning an inserted peg into a hole, due to the uncertainty of the assembly environment, represents an obstacle in this area of automation. In addition, robotic assembly is not a simple task; solutions must be found for a number of problems, amongst which are:

- precision and repeatability in positioning the end effector
- motion in straight lines while maintaining fixed orientation of the end effector
- automatic end effector changing, or a versatile gripper
- rapid motion of the robot arm

To overcome these problems, complex and expensive equipment has been designed. Also, to help reduce the cost of assembly operation much attention has been focused on minimising the number of components that need to be assembled from one direction and to ensure that the remaining ones can be assembled as easily as possible (Design-for-Assembly, [G. Boothroyd, 1987 & 1988]).

Although robots and automated machines have liberated the human operator from hard and dangerous tasks, they still rely on the human operator for feeding them with parts and even undertaking the product inspection after the completion of assembly.

1.1 ASSEMBLY PROBLEMS

One critical problem that arises during component assembly is that small error in relative lateral position or angular position can produce large reaction forces. These forces can prevent successful completion of the assembly (jamming) and can cause damage to the parts and the robot.

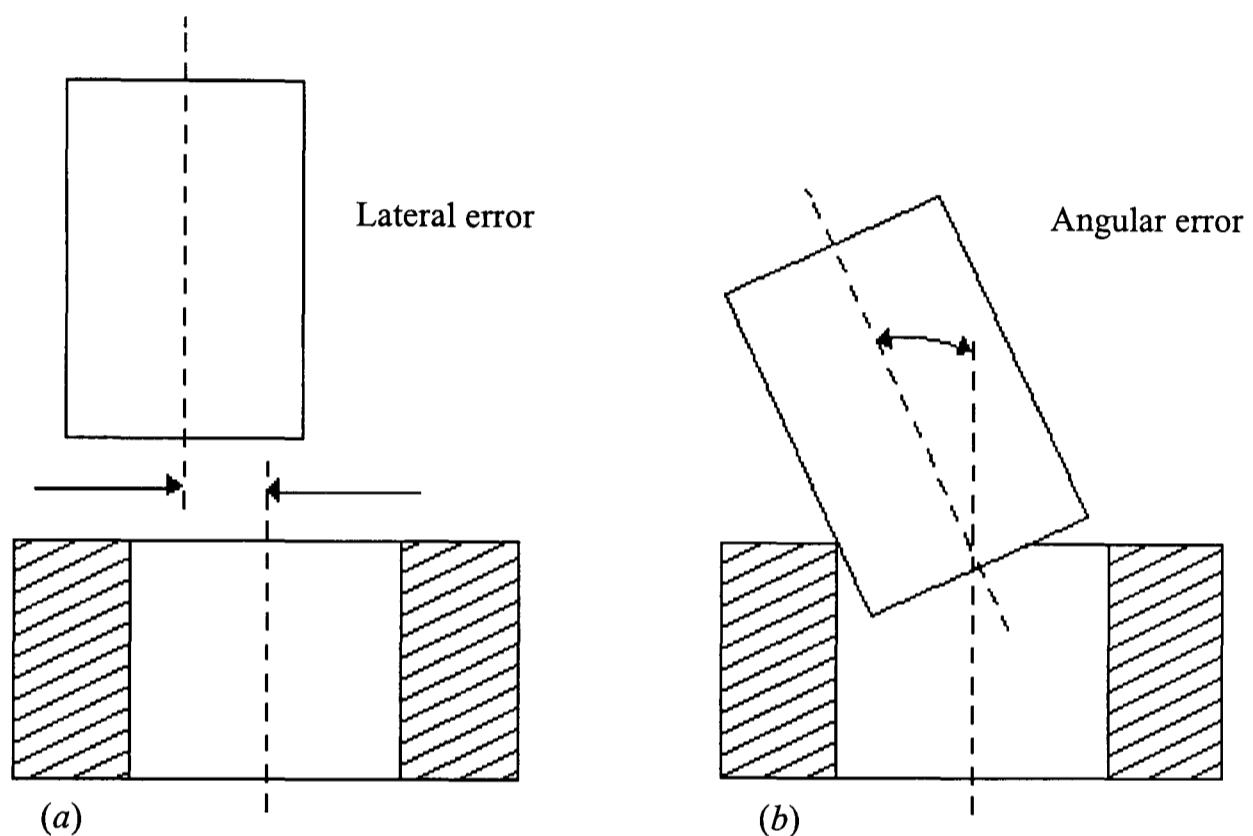


Figure 1.1 Misalignment of parts during an assembly operation, (a) lateral error and (b) angular error

Figure (1.1) shows a lack of precision in the location (1.1a lateral error) of the peg and in the angular orientation (1.1b angular error) of the peg. To overcome these errors, such misalignments must be corrected at the interface stage between the parts to be assembled, taking into account part properties such as clearance and mating geometry.

Considerable research has evolved in the past decades, which defines the two-dimensional mating of parts. Rigid parts, at least one compliantly held, have been assembled by researchers in Russia, Belgium, New Zealand, Japan and the Charles Stark Draper

Laboratory in the US [D. E. Whitney, 1982]. The common element in their experiments is the use of a chamfer on either of the mating parts to reduce the alignment problem between the mating parts. Also, in case of chamferless assembly, success usually comes from initially tilting the peg by a small angle; so considerable misalignment of the two parts can then be tolerated.

1.2 APPLICATION AND MOTIVATION

So far, most advanced mechanical/compliant assembly systems perform assembly operations with the aid of a chamfer on either of the peg or the hole. For this reason, to achieve an insertion process, the allowable positional misalignment between the mating parts should be restricted to the chamfer width-something that constrains the assembly system to that specific application. Moreover, to make a chamfer, the part has to be set up on the relevant machine for machining which takes time and cost money; this can result in an increase in the overall assembly cost.

The research presented in this thesis, aims at utilising the domino effect theory [W. Haskiya, 1997] for the robotic peg-hole application. The objective is to develop a passive compliant wrist that can accommodate effectively angular/lateral misalignment between chamferless cylindrical parts [W. Haskiya, 1998]. The wrist should function in the vertical as well as the horizontal directions. However, the sub-objective of this research can be summarised as follows:

1. To develop a mathematical model from 2D and 3D for a peg-hole assembly strategy [W. Haskiya, 1997 & 1999]
2. To demonstrate the new assembly strategy through a simulation process using Matlab-Simulink
3. The peg-hole experimental results should be at least of the same standing as those, with the use of a chamfer (see literature survey for results: chapter2, table 2.1)

1.1 METHODOLOGY

This research went through, in three stages:

- I. Literature survey: To stay updated on the latest in the area of robotic assembly, a thorough literature survey was carried out. Until the time of writing this thesis, it is

not reported yet on any assembly method/compliant wrist, that functions as the one reported in this research.

- II. Analysis and computer modelling: After comprehending the principles of the domino effect theory, the new assembly strategy was developed and presented in 2D and 3D space. Thereafter a mathematical model of the chamferless peg-in hole insertion process is developed. A computer simulation was made to establish peg-in hole theoretical limits of the insertion system.
- III. Design/construction of the assembly rig and experiments: Following the design stage, the wrist is built, and tested for finding its stiffness. Also, the wrist was stress analysed using Finite-Element-Analysis package (ALGOR). Thereafter, the compliant wrist and the assembly rig were made. Note, throughout the design and construction stages, consultations with local manufacturers were made. Also, chamferless peg-hole assembly experiments were performed in stages to test and achieve the research objectives.

1.2 THESIS ORGANISATION

The organisation of the thesis is as follows:

Chapter 2 This chapter is a literature survey. It presents the latest published research, about robotic assembly devices, methods and strategies used around the world that relates to the peg-hole assembly. In addition, advantages and disadvantages of each assembly technology are discussed.

Chapter 3 This chapter relates the domino effect theory to the robotic peg-in hole assembly application. Subsequently, a new assembly strategy is developed and analysed in 2D space.

Chapter 4 A 3D geometrical analysis of the chamferless peg-hole is described. To realise the geometric constraints of the peg-hole problem, and to establish the geometric conditions for a successful peg-hole insertion process.

Chapter 5 This chapter is a progression from chapter 4. It describes phenomena such as friction, compliant motion stick/slip and their effect on the insertion process (*e.g.* jamming/wedging). In addition, investigation of the dynamics of the assembly process, taking into account those phenomena, the forces and moments between the mating parts are presented.

Chapter 6 In this chapter, a modelling and simulation of the chamferless peg-hole insertion process is presented; to investigate and learn about the theoretical behaviour of the compliant wrist/assembly strategy. Also, to establish the required parameters for the assembly system (e.g. wrist stiffness, allowable misalignment etc,)

Chapter 7 This chapter describes the compliant wrist (Chamferless-Vertical-Horizontal Remote Centre Compliance CVHRCC); the experiments to find the wrist stiffness. In addition, the wrist design and stress analysis using FEA package is presented.

Chapter 8 Presents the experimental build-up and procedure for the chamferless peg-hole insertion process, and the data correlation.

Chapter 9 This is a discussion for the research method; shortcoming of the research, the extent of the research objective that have been achieved, etc.

Chapter 10 Conclusion and recommendation.

CHAPTER 2

LITERATURE SURVEY

2.1 INTRODUCTION

The peg-hole example has many applications in automated assembly [J. L. Nevins et al, 1980: D. E. Whitney, 1979], and therefore it is widely used in the robotic assembly industry [J. L. Nevins et al, 1978] e.g. bearing in housing, shafts in bearing and gear into a pump etc. Hence, much research [Y. Xu et al, 1990: M. A. Badger, 1983] and development have been undertaken in this area. Despite the programmability and the flexibility of assembly robots, they are not yet widely employed in assembly operations [K. Park et al, 1994]. The reason for this is their inaccuracy; in precision assembly, the clearance between the mating parts is normally lower than the accuracy of the assembly robots. Accordingly, any positional misalignments between the mating parts can lead to jamming, which can cause damage to the mating parts or the assembly robot itself. One of the industrial examples for solving the inaccuracy problem during clearance fit assembly, is to heat the female part (bearing), as a result the diameter is increased by the several micro-millimetre and then the insertion of the male part (shaft) becomes possible.

The following is the order of existing solutions for the assembly problems:

Section 2.2	industrial examples
Section 2.3	fine-motion strategies
Section 2.4	compliant systems
Section 2.5	summary

2.2 INDUSTRIAL EXAMPLES

A growing company, faced with a skilled labour shortage, and the need for consistently high quality products, naturally tends to consider automation for their product assembly as a means of tackling both these problems at the same time.

2.2.1 The Rover Engine Line

Rover-motors have introduced new engines called the K-series [A Motive, 1990]. The engines are made of aluminium casting. There are two types of the K-series: the K8 with

two valves per cylinder and the K16 with four valves per cylinder. The assembly of the engine head is carried out on different stations (automatic and semiautomatic). The mounting for the head is tilted to three different locations so the valve stem is vertical for each different insertion operation. A robot fits the sub-assemblies produced on different lines to the valve stem. First, a spring seat and seal are assembled, followed by a spring and finally a cup and cotter. At one station, Pragma robot with vision system is used to identify components by the optical character recognition of grading details on the parts; it picks the shell from a conveyor. Altogether, the robot assembles the two thrust washers and five sets of bearing shells to the block and ladder. Note that a sensor attached to the gripper detects the orientation of the oil hole in the shell, if the shell is not aligned then the robot corrects the alignment during the loading operation. However, at one station the assembly of the con rods to the pistons is not fully automated. The ends of the con rods are heated to 350° C in an induction unit and then inserted into the piston and aligned. The assembly of the piston and con rods to the engine block are done manually. Also, the sump is fitted manually.

One of the limitations of the Rover's assembly line is that it can not cope with horizontal assembly therefore parts have to be tilted after each vertical insertion to fit the other object from a different orientation. Also they still rely on manual assembly for parts of interference fit clearance, and complex components, but they have not yet automated this kind of assembly.

2.2.2 Robot System Builds Customised Printed Circuit Boards

Kent Modular Electronics (KME) [J. Hollingum, 1991] is a small company who makes colour and monochrome monitors for data display systems. The robot line makes the assembly of their printed circuit boards (PCB). An IBM 7576 robot with a total reach of 800 *mm* and a high-speed payload of 1 *kg* is used at one station. The robot picks a component and places it on the board. If it is not aligned, a pressure sensor attached to the gripper sends a signal to the control unit and then the robot moves a small distance from the nominal position and starts a search routine for the hole. The robot does ten insertion attempts and if it still fails to insert the component, then it makes another ten attempts and if it still fails, then it discards the component in a reject box and picks another component. If the problem persists then it stops and calls for help. Once the robot inserts the

component into the PCB, it updates the location of the X-Y co-ordinate for the next component. According to the company, the overall insertion time for each cycle is 3 seconds.

It can be said that the overall insertion time is long, even if taking into account the number of components that need to be inserted onto the PCB. Considering other options to overcome the robot inaccuracy would save the company time and money which is needed to survive in today's market.

2.2.3 Automatic Board Assembly

Another example to the assembly of printed circuit boards is the use of one gripper for all parts of different shapes. CHAD industries' [G. W. Holcomb, 1995] uses a system called CHAD OFM (Odd Form Master) which includes Adept robots with 3D compliant gripper and single pin clinch system. According to the company, this gripper is the only one in the world that is capable of handling all parts of different shapes, without having to make tooling or gripper changes. This is achieved by the gripper's ability to compensate for variations in each part to be inserted, complying three-dimensionally similar to the human hand when picking up different shaped parts. Instead of changing tooling, one simply changes the software to handle any mix of parts.

After all, in case of insertion failure, the system presented here has to resort to the search routine for the hole, the same as the one presented by the KME in the previous section. Moreover, it can be said about the assembly of printed circuit boards, since the boards contain multi-components of same shape/type, then why not have one assembly system which is capable of doing multi-insertion at one go?

2.2.4 Acoustic Emission For Monitoring Assembly Operation

The peg-in hole insertion process releases strain energy in the form of sound/stress waves, which is due to the peg and the hole contact. Hence, the term acoustic emission refers [C. R. Heiple et al, 1993: R. Penfold, 1994: G. Bright et al, 1995] to the elastic stress waves emitted during the engagement of the mating parts. A Puma MK II robot having Val II language is used for the peg-in hole insertion process. Several insertion attempts are carried out for different pegs. A condenser microphone is used to receive the sound waves

produced by the mating parts. The signal transmitted by the microphone is amplified and then processed by a dynamic signal analyser. The dynamic signal analyser converts the sound signal from the time domain to the frequency domain. The sound frequency component is displayed on a monitor, the process is repeated to find a mean frequency component for each process. So, in case of incorrect assembly, the frequency traces are different than the ones for correct assembly. Accordingly, the micro-computer detects that, and changes to the programme of the peg-hole insertion are made on-line. The values of the frequency traces for successful insertion process are used as references points for determining future incorrect insertion. If insertion fails, and values of the incorrect insertion are different to the ones stored for successful insertion, then the robot carries out a search for the exact location for the hole. If problems persists then the computer sounds an alarm and the assembly stops.

In addition to what already has been said about the shortcomings of the previous methods in terms of the search procedure for the hole in case of incorrect insertion, the utilisation of sound characteristics require special equipment which add to the overall cost of the insertion process. Also, authors did not give information about the overall insertion time, which is likely to be similar to the one in previous methods. More importantly, such method may not suit practical assembly operations, because of noise produced by the surrounding environment.

2.3 FINE-MOTION STRATEGIES

The principles of the fine-motion strategies are the utilisation of the geometric constraints of the mating parts to guide the assembled parts to their destination through the employment of an algorithm.

Bruno Dufay and Latombe [B. Dufay et al, 1984] has suggested a new approach for fine motion strategies, which is based on automatic robot programming. His system embodies a two-phase approach for building such programmes. A training phase produces traces of execution, and an induction phase transforms these traces into an executable programme. However, this approach is good for research purposes, not for practical use. It needs several improvements so it can be used with different mating parts without having to

retrain or by simplifying the editing of the rules of the programme, perhaps for a better on-line interaction with the human programmer.

Other assembly methods have been developed under this scheme (see next section). One method is known as a strategy for peg-hole assembly without RCC or force sensor. Another one is called the pre-image strategy. Other strategies can be also found in “Automatic Synthesis of Fine-Motion Strategies for Robots” (see section 2.3.2).

2.3.1 A Strategy For Peg-Hole Assembly Without RCC Or Force Sensor

This strategy [H. Qiao et al, 1994] is based on identifying the basic relationship between the peg-hole system and the movement of the peg and the contact forces during the mating process. This strategy can be divided into two stages:

- I search stage
- II insertion stage

The search stage is to get the peg engaged with the hole, and this can be achieved through a series of sub-goals. This starts from any allowable initial state and ends at the final goal that is the completion of the insertion action. This strategy can be used with chamferless mating parts. However, one of its limitations is the 2.5 seconds duration of the insertion action that is much longer than that in the compliant systems.

2.3.2 The Pre-Image Strategy

The pre-image strategy [T. Lozano et al, 1984] is “a set of points from which the goal can be attained in a single motion” (see figure 2.1). In other words, it is to identify a series of positions from where the tip of the peg can reach the bottom of the hole by a single motion. The direction of such motion can be represented as a unit velocity, and each unit velocity can compute one point at the tip of the peg, and such motion that reaches the goal by a single motion called the pre-image of the goal.

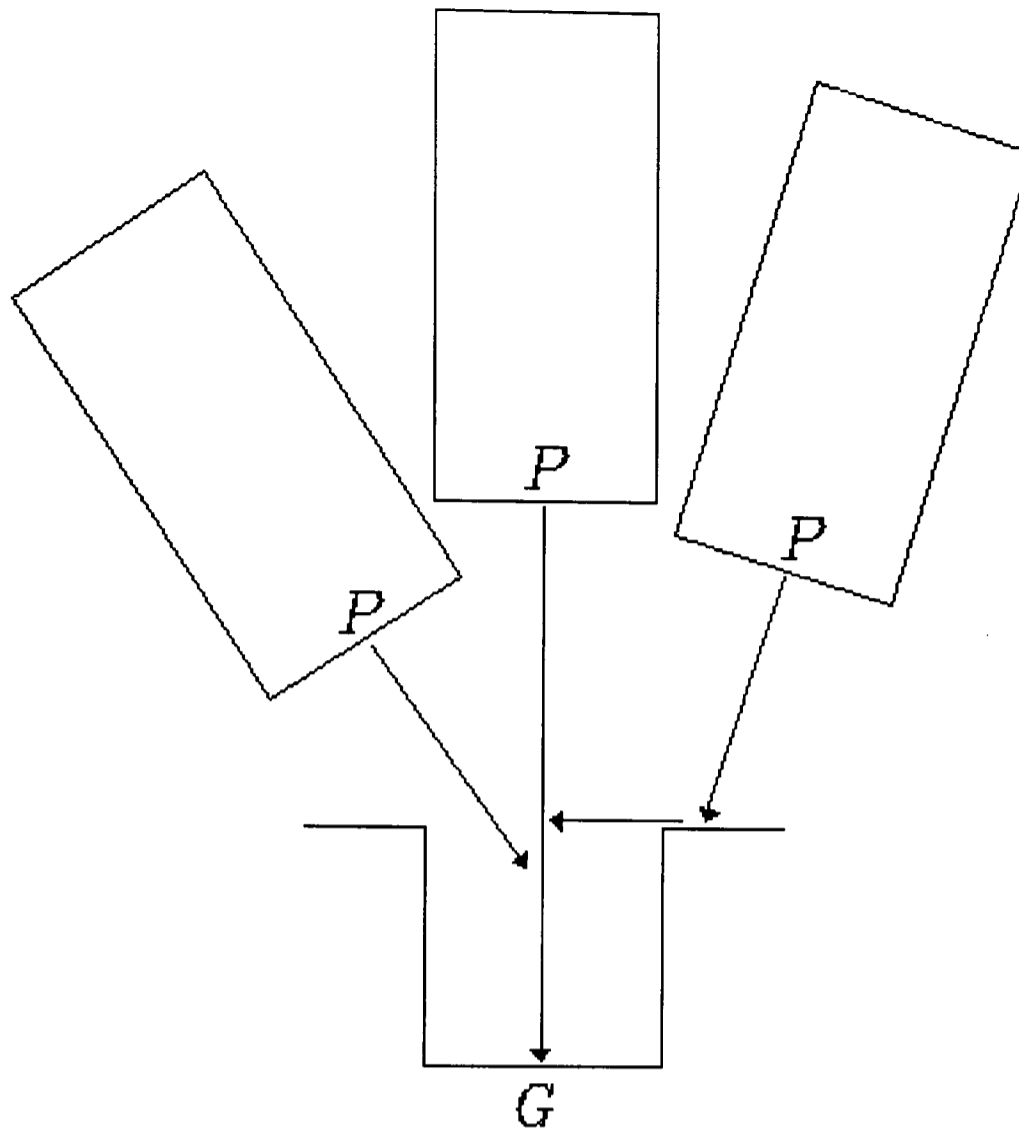


Figure 2.1 Basic idea for the pre-image concept [after T. Lozano et al]

When the current position of the peg contains no pre-image of the goal, then the same computation can be applied recursively. By using each of the existing pre-images as a possible goal. This process is called backward chaining [N. Nilson, 1980]. Each of the pre-images serves to define a new goal. This process is repeated until one of the pre-images contains the current position of P .

In short, the basic approach is to chain backward from the goal towards the current position, characterising at each step the range of positions that can reach the current goal in one motion. A full description of this strategy can be found in [N. Nilson, 1980].

Because of the need to search for the hole, it can be said that the insertion time is longer than that in compliant systems. Furthermore the disadvantages of this strategy and the previous one, is the need for different algorithm for each unsimilar insertion task.

2.4 COMPLIANT SYSTEMS

One question tends to arise when adopting compliant systems for solving assembly problems; Why is compliance needed in flexible assembly [K. W. Klaus, 1992]?

Flexible assembly in a modern production environment poses very specific problems. The need for flexibility is well established and is mainly due to the desire to bring the economic advantages of mass production into a changing marketplace, where the trend goes towards smaller batches, larger product variety and faster response to the customer's expectations. In fact, all assembly automation relies on some form of compliance in the system. Sometimes the imprecision in the assembly machine/robot is sufficient to overcome the misalignment, particularly when the products themselves do not need high precision.

Compliant system devices can be classified under three different techniques [J. H. Chao et al, 1987]:

2.4.1 passive accommodation

2.4.2 active accommodation

2.4.3 passive-active accommodation

See table 2.1 for compliant systems features.

2.4.1 Passive Assembly Accommodation

This method utilises the passive concept to accommodate misalignments between the mating parts. This is achieved by the elastic deformation of the compliant devices, under the influence of the reaction forces generated through the contact between the mating parts or other externally generated forces, such as air-stream force or magnetic force.

R. Stepourjine and Rouget [R. Stepourjine et al, 1983] has proposed an automatic insertion device for light robotic assembly parts made of light alloys or plastic, parts with peg diameter from 0.5 to 8 mm. The system consists of pneumatic cylinders, elastomeric cylindrical rods, gripper and gripper holder combined with a force sensor. The strategy based on inclining the inserted peg by bending the elastomeric rods through the pneumatic cylinders. Detecting the hole edges is achieved with the aid of spherical joints. When reaction forces arise, the force sensor sends a signal to the pneumatic cylinders in which the stored energy by the elastic rods is released causing the peg to be aligned into the hole.

The author claims the system was tested in inserting chamferless peg inside a hole, the clearance was 0.01 mm between the mating parts. However, the inclination of the peg and the approach motion is said to be under visual and force feedback.

Generally speaking, passive assembly devices/methods can be classified into four categories:

2.4.1.1 compliant wrists or work table

2.4.1.2 air or gas stream

2.4.1.3 magnetic force

2.4.1.4 vibratory motion

2.4.1.1 Compliant wrists or work station

A variety of compliance concepts have been proposed and developed [H. McCallion et al, 1979: S. Havilk, 1983: H. J. Warnecke et al, 1980: G. Belforte et al, 1982: A. Fakri et al, 1984] that utilise the concept of passive compliance. The most successful device in this category is the Remote Centre Compliance developed by the Charles Draker Laboratories [P. C. Watson et al, 1978] in the US. It was evaluated and tested by General Motors and used in several applications [J. D. Lane, 1980].

Remote Centre Compliance (RCC): The RCC is a passive compliant device [P. C. Watson, 1977: D. E. Whitney et al, 1979] mounted between the robot arm and the gripper, that enables peg-hole insertion without jamming or wedging, despite initial errors in the peg's position and orientation. The essential characteristic of the RCC is that the lateral and the angular errors are absorbed independently. This elimination is achieved by placing the centre of compliance at the tip of the peg.

A typical remote centre compliance device is made of a frame (matrix) and a set of flexing members (rotational and translational springs). One of its limitations is the need for chamfer on one of the mating parts and thus the allowable positional error is restricted to the chamfer width.

Work table: Due to problems caused by the previous devices (RCC's), such as vibration on positioning of the part, and large displacements generated by a small force, several

researchers [T. Arai et al, 1981] have proposed a work table concept. The work table is a compliant table that carries either of the mating parts. A typical compliance system consists of a rotational and translational spring. In the work table, the alignment is achieved by the structure compliance rather than the robot compliance.

2.4.1.2 Air-stream assisted method

In this method [F. Caliot et al, 1984; Y. A. Yakimovich, 1970], the alignment of the mating parts is achieved by the air-stream instead of the contact forces as with compliant devices. Here, the parts are fed into their corresponding holes and aligned by the air stream that passes through the corresponding holes and flows around the end of the parts.

As it has been said, the air stream produces the reaction forces necessary to align the peg into the hole, while in compliant devices the reaction forces are generated by the contact between the mating parts. This fact is considered as advantage for this method over compliant devices similar to the RCC, because large errors can be allowed; the reason for that it is not restricted to the chamfer width. Moreover, this method requires no chamfer.

2.4.1.3 Magnetic force method

In this method [V Mashinostroenya, 1976 & 1977] the alignment of the mating parts is achieved by magnetic forces that due to the magnetic fields. Therefore this method can be used only for ferromagnetic parts.

The device that generates the magnetic fields comprises of a DC electromagnet with poles and an AC electromagnet in the form of solenoid coil and a vibrating ring. The mating parts are magnetised by the supply to the electromagnet, then the peg moves towards the hole into the area of greater magnetic field strength. Since the peg is also subject to the effect of the alternating field, its magnetisation is reversed during each half cycle of the alternating current with the result that the poles at its ends are continuously changing. The peg located within the solenoid is vibrated by the alternating torque produced by the magnetic force, while the axial force simultaneously seeks to pull the peg into the central area of the field between the poles of the permanent magnet. The condition for the entry of the peg into the hole during the search period depends mainly upon the vibration amplitude and the angle of the intersection of the parts' axes.

One of the advantages of this method is that possible welding can be eliminated by the vibration of the mobile part. However, this method is limited to ferromagnetic parts.

2.4.1.4 Vibratory motion method

In this method the alignment of the mating parts is achieved by vibrating the peg with respect to the hole. The vibration is carried out by:

- Robot [St. Kaczanowski et al, 1981]
- vibrator fitted between the robot arm and the gripper [S. Kang et al, 1995; K Won et al, 1989]
- vibrator fitted to a work table [J. Warnecke et al, 1988]

The robot vibration is made possible by making small movements in the X-Y plane that causes the gripper to vibrate a device similar to the RCC structure; but its insertion principles are different. The alignment is achieved by the wrist vibration that commences after the initial contact between the mating parts, which is detected by a force sensor installed on one of the sides plate springs. When the initial positional errors are corrected, the insertion force is reduced and the wrist vibration stops. The final alignment is achieved by the wrist flexibility.

In the third version of the vibratory method, the alignment of the mating parts resorts to the search procedure for either of the peg or the hole. The robot's gripper holds one of the mating parts fixed, and a vibratory table holds the other part.

One of the disadvantages of the vibratory method is that the search for finding the desired inserting position must usually resort to a trial and error procedure, which consumes additional time to the net-time of the insertion process.

Advantages, disadvantages and applications of the passive accommodation

Advantages: Passive compliant devices can handle small misalignment between mating parts (allowable error less than 2 mm and 3° in case of chamfered parts) with a simple configuration and scheme in a short time compared to the active accommodation method.

Disadvantages: The allowable positioning error is restricted by the chamfer width in the case of peg-hole assembly. Compliance of wrist alone often produces a large insertion force that depends upon the initial error and the clearance ratio of the mating parts. Adaptability that accounts for changing work environments is limited.

Applications: Cylindrical parts (peg-hole), variable resistors, valve/ 4 cylinder engine, electric components, such as bearings in housings and shafts in bearings as in VCR.

2.4.2 Active Assembly Accommodation

Because of the limitations of passive compliant devices, much research and development has been made into the active assembly method [G. Hirzinger, 1985; S. Hopkins et al, 1988]. This method mostly employs force sensors to acquire information about the position of the mating states and uses the signals for position control of the robot end effector.

Considering sensing method, these can be classified into:

2.4.2.1 servoing with force sensors

2.4.2.2 servoing with vision sensors

2.4.2.3 servoing with proximity sensors

2.4.2.1 Servoing with force sensors

In this category there are:

- Hi-T hand
- programmable force controlled wrist
- active sensory table

Hi-T hand: It is a flexible wrist [T. Goto et al, 1974 & 1980; K. Takeyasu et al, 1976] instrumented with force sensors on its three axes (X-Y-Z). The wrist fits between the robot arm and its end effector. In this method the alignment of the mating parts is achieved by the search procedure which commences upon receiving the signal/s from the wrist.

One of the advantages of this wrist over passive compliant devices is that it can accommodate large initial errors between the mating parts, even in case of chamferless mating parts. However, this wrist yields much longer insertion time than passive compliant devices due to long search motion.

Programmable force controlled wrist: This device [V. Brussel et al, 1978 & 1979 & 1979 & 1980 & 1981 & 1983] has five degrees of freedom with no axial rotation and incorporates force sensors and programmable unit for position control. A DC motor via a servo loop actuates each axis. However, this wrist is quite complex and expensive (compared with passive, active devices).

Active sensory table: The system [K. Takeyasu et al, 1981] consists of a coarse motion robot, active working table and its motion controller. The table has 6 degrees of freedom and equipped with force sensors and fine motion actuators. The controller consists of a signal processing unit and a driving unit. The controller generates the fine motion needed for the active table to overcome initial positional misalignment between the mating parts based on the sensor's information obtained during the peg-hole contact.

2.4.2.2 Servoing with vision sensors

This method [K. McWalter, 1993: A. Sanderson et al, 1983] provides the ability to visualise position and orientation of characteristic features of the parts' image. Parts' image can be taken by two techniques:

Binary imaging: The binary imaging system is used for assembly of parts with a simple geometry. The problem with this method is that it can not provide a satisfactory solution for complex parts due to low image resolution of the extracted information regarding the position and orientation of the part.

Grey-level imaging: The concept of the grey-level imaging is the same as the binary method, except that this method provides a higher image resolution of the extracted information regarding the position and the geometry of the parts. The problem with this method that it requires a complex processing algorithm, thus it takes longer processing time than the previous method.

2.4.2.3 Servoing with proximity sensors

In this method [H. Hanafusa et al, 1976: J. Volmer et al, 1982: J. Draz et al, 1984] the alignment of the parts relative to the corresponding holes is achieved by the fine motion of

the robot or the gripper. The gripper's fine motion is provided by a pneumatic cylinder, which in turn is driven from the feedback signal of a set of pneumatic sensors.

The advantages of this method are that it does not require signal processing and control units, and it can accommodate larger positional errors than the force or the vision sensor techniques. However, the limitation of this technique is the need to reconfigure the location of the sensor for different part shape.

E. Paulos and Canny [E. Paulos et al, 1994] has suggested a self-calibrating peg-in hole insertion strategy using several simple proximity beam sensors. The key to the strategy is the use of a fixed sensor to localise both the mobile sensor and the peg, while the mobile sensor localises the hole. The author claims to have achieved successfully peg-in hole insertion process with a clearance of 25 microns.

Advantages, disadvantages and applications of the active assemble method

Advantages: handling comparably large positioning errors (than the passive accommodation) even in the case of chamferless parts. Also it can be used with different mating parts of different sizes and variable forces and moments.

Disadvantages: Usually they are complex and expensive (more costly than passive compliant devices), because of the need for using processing unit, therefore the insertion time is longer than that of the passive method. Also, difficult to compensate for small misalignments because of the high inertia of the robot arm.

Applications: Electrical motor (shaft/bearing), electrical leads in PC board holes, peg-hole applications.

2.4.3 Passive-Active Assembly Accommodation

This method is a technology that combines the advantages of both the passive and the active assembly methods. In this category there are various compliant devices[L. DeFazio, 1980: M. Jung et al, 1993: B Hakan et al, 1996: H. Chao et al, 1984]. A typical device is the Instrumented Remote Centre Compliance (IRCC).

The IRCC is a general-purpose tactile sensor having the fast error-absorption characteristics of a passive compliance and the measurement capabilities of a multi-degree-of-freedom sensor. The output can be used for contact detection, position and angle measurement, or force and torque measurement to aid the robot in the assembly operations. The IRCC is a normal remote centre compliance in which some or all of the internal deflections are instrumented with a suitable sensor.

The basic strategies of the IRCC are that angular/lateral misalignment between the mating parts is corrected by the RCC (within allowable forces and moments). At the same time a measurement of forces and moments/position and orientation is taken by the suitable sensor to correct for programming errors. When forces and moments are above the allowable value, the instrumented part of the IRCC measures those values and uses them to correct the position of the peg.

Advantages, disadvantages and applications of the IRCC

Advantages: The main advantages are that it can handle small and large positioning errors. Also the adaptability for changing work environment is not limited (as in the passive method), and chamfers are not needed in the case of peg-hole assembly.

Disadvantages: It is more expensive than the similar devices in the passive category. Also insertion time is longer than that in the passive method; this is due to the processing of signals to change the programme to minimise or overcome the positional error.

Applications: Shaft/bearing, gear pump, cylindrical objects as in peg-hole applications.

The following table summarises various assembly methods:

Table 2.1 Performance data for various assembly methods [J. H. Chao, 1987]

Assembly method	Clearance	Allowable positioning error	Chamfer required	Mating speed	Applications	Remarks
1. Compliant device						
RCC	0.01mm	$\epsilon = 1.0 \text{ mm}$ $\vartheta = 1.0^\circ$	yes	0.2 sec	cylindrical parts	commercially available
McCalion et al.	0.012-0.024 mm	$\epsilon = 1-2 \text{ mm}$ $\vartheta = 1.5-2.5^\circ$	yes	.	peg/hole	dependent upon length of the peg
Haaf	0.03 mm	$\epsilon < 1 \text{ mm}$ $\vartheta < 2^\circ$	yes	.	peg/hole	axial force sensor
Stepourjine	0.01 mm	$\epsilon = 0.6 \text{ mm}$ $\vartheta = 7^\circ$	no	.	peg/bore	force sensor used for detecting the contact
2. Air-stream method						
Mashinostroeniya	0.06 mm	$\epsilon < 3 \text{ mm}$	yes	.	variable resistors	96-100% successful
Calliot	0.04 mm	$\epsilon \leq 4 \text{ mm}$	yes	1.25 sec	valve/4 cylinder engine	compliant wrist
3. Vibratory method						
Jacobi	.	$\epsilon < 1.4 \text{ mm}$ $\vartheta < 1.0^\circ$	no	.	.	arbitrary shape
Hoffman	0.75 mm	.	no	0.25 sec	non-standard electric components	99.8% successful
4. Servoing with force sensors						
Hi-T hand	0.003-0.02 mm	$\epsilon < 2-3.5 \text{ mm}$	no	1.07-5 sec	electric motors (shaft and bearing)	insertion search based upon force pattern
Kasai	0.02 mm	.	no	3-10 sec	shaft and bearing	skill-acquisition capability
5. Servoing with visual sensor						
Mauri	0.4 mm	$\epsilon < 0.2 \text{ mm}$.	0.5 sec	electrical leads in PC boards holes	lead pitch: 5-25.4 mm
Baird	0.5 mm	$\epsilon < 2 \text{ mm}$ $\vartheta < 0.8^\circ$	yes	6 sec	loudspeaker/a mounting pin	95% successful
Agin	.	$\epsilon < 1.3 \text{ mm}$	no	5 sec	bolting	visual servo accuracy: 0.76 mm
Shirai	3 mm	.	no	10 sec	square box/hold	.
Fehrenbach	.	$\epsilon < 0.8 \text{ mm}$	no	1.0-5.5 sec	DIPS in PC board holes	dependent on hole size
6. Servoing with proximity sensor						
Volmer	0.01 mm	$\epsilon < 2 \text{ mm}$	yes	.	shaft/bearing	smooth surface
Jacobi	0.01-0.04 mm	$\epsilon < 3 \text{ mm}$	no	0.1 sec	gear pump	parts of arbitrary shape
7. Servoing with displacement sensor						
Sweizer	0.05-0.15 mm	$\epsilon < 5 \text{ mm}$	no	1 sec	peg/hole	non- contracting inductive sensor
8. Assembly-oriented robot						
Liegeois	0.03 mm	$\epsilon < 10 \text{ mm}$ $\vartheta = 2^\circ$	no	1.5 sec	peg/hole	elastic cable-driven manipulator

ϵ : initial lateral error, ϑ : initial angular error.

As shown in table 2.1, assembly technologies 1 to 3 are passive methods, 4 to 7 are active methods and the last one is the assembly oriented robot. Also, the same table includes all the relevant features for each method. So, the use of the relevant technique, will be based on the assembly application.

2.5 SUMMARY

In this chapter, the relevant assembly methods have been introduced. Arguments can be made for the use of any of those methods. In regard to the fine motion strategies, it can be said that with some more development on the software (programming) and the teaching side of the machine, a better on-line interaction will be produced between the assembly machine/robot and the operator to suit any part size and shape. In reference to the passive and active methods, the choice tends to be coloured by the preferences of the individuals and their confidence in the technological solutions. Mechanical arrangements are better understood to the user (Passive compliant devices - mechanisms such as the RCC). However, they need a strict specification in regard to the parts to be assembled (Chamfer, no chamfer, size and shape etc,) due to the fact that they have a fixed centre of rotation. Also, the change to different components may result in hardware changes. Besides, robots using passive systems need to take the flexibility of the compliance into account for the planning of their own motion. On the other hand, active system methods must include the imperfections of the robot and its actuators. Therefore, by instrumenting the proper joints/parts a certain degree of decision can be made, by using the data in different context interpretation. Where a detailed resolution of the interaction forces can provide a monitoring facility of the whole mating process. Although the need for the advantages of both passive and active methods has led to the development of the passive-active technology, improving the applicability and performance of the assembly system has resulted in more elaborated and expensive devices.

Following this literature review, the goal is to make a passive compliant wrist, having the advantages of passive devices (RCC's), that can operate without a chamfer on either of the mating parts. Clearance between the peg and the hole is in the range of passive and active devices (0.01-3 mm). With mating time less than that for RCC devices (Active systems have mating time of over 2 sec.). Furthermore, the wrist has to operate from both, vertical and horizontal directions.

CHAPTER 3

A NEW ASSEMBLY STRATEGY AND THE DOMINO EFFECT THEORY

3.1 INTRODUCTION

In chapter (2), assembly devices and strategies to overcome the jamming problem during the peg-hole insertion process were presented and classified into three different groups:

- I. Passive accommodation
- II. Active accommodation
- III. Passive-Active accommodation

The purpose of this chapter is to present a new assembly strategy. The difference between this strategy and other strategies is that all of these methods adopt the top-down assembly approach, and in some cases the mating parts must have a chamfer to facilitate the assembly operation. The approach presented here is a new strategy for chamferless peg-hole assembly from X/Y/Z directions. This strategy was born out of the Domino Effect Theory, in which the transition of one domino from angular tilt to axial slip was implemented in this assembly strategy.

The structure of this chapter is as follows:

- | | |
|-------------|--|
| Section 3.2 | is a presentation of the new assembly strategy |
| Section 3.3 | is an explanation of the domino effect theory |
| Section 3.4 | is a comparison between the new assembly strategy and the domino effect theory |
| Section 3.5 | is domino effect analysis |
| Section 3.6 | is the analysis of the new assembly strategy |
| Section 3.7 | is the conclusion |

3.2 A NEW ASSEMBLY STRATEGY

The new assembly strategy is a passive method, which is made up of a sequence of positions in which the peg has to pass through to get to its destination (the hole). Unlike other strategies such for Inoue or Cervera and Pobil [H. Inoue, 1979; A. P. del Pobil et al, 1994], this technique requires no search procedure. Since the path of the peg is corrected by the reaction forces that arise during engagement with the hole. Also, it applies to assembly operations in which the mating parts have no chamfer. Besides, it works from vertical as well as the horizontal direction. The assembly operation itself requires no rotation around X/Y/Z axes (insertion axis), and it consists of the following stages (see figure 3.1 and 3.2):

1. approach
2. peg contacts the upper surface of the mating part
3. peg tilts into the mouth of hole
4. peg moves to the far side of the hole
5. peg is aligned (completion of the insertion process)

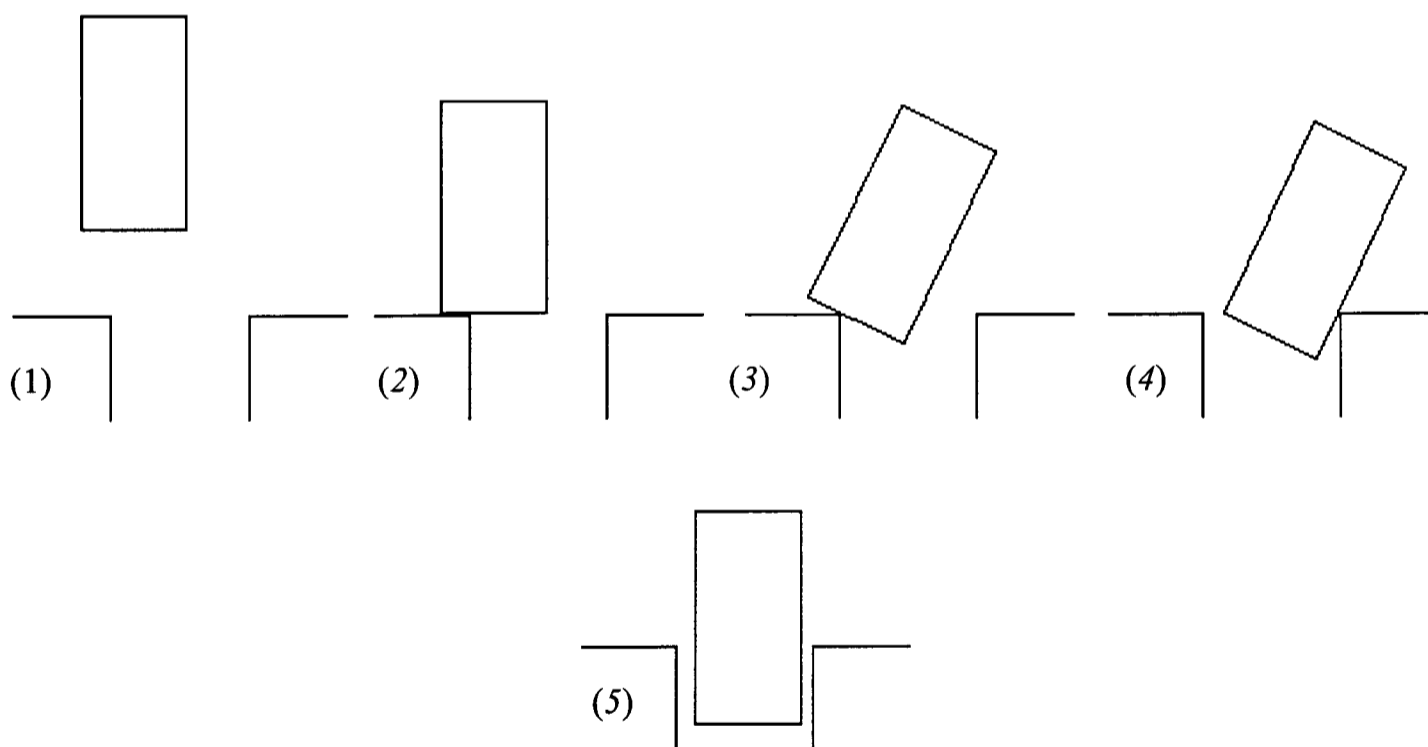


Figure 3.1 The new assembly strategy, main vertical stages

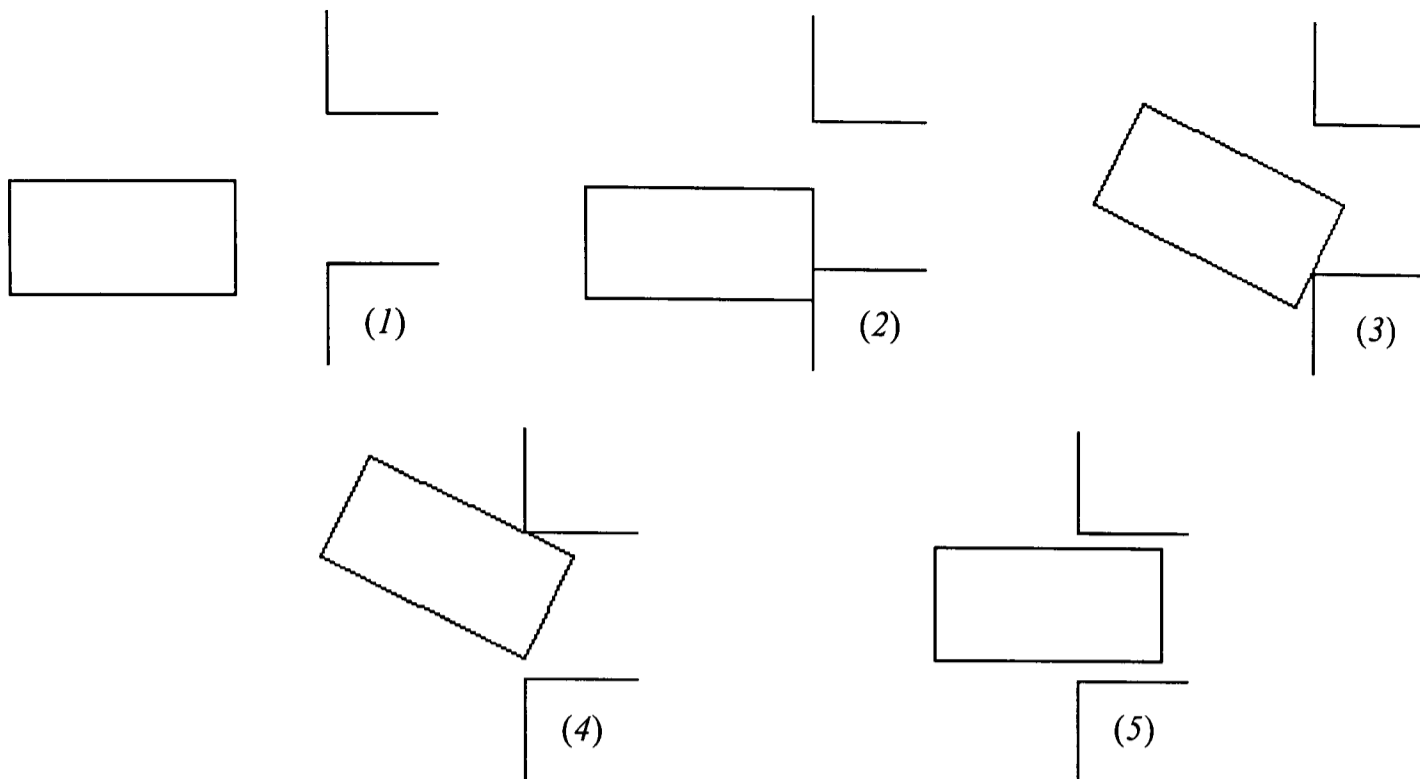


Figure 3.2 The new assembly strategy, main horizontal stages

3.3 THE DOMINO EFFECT THEORY

The domino effect theory is a generic term, which is used in Engineering, Science, Business and even in Politics.

In mechanics, the domino phenomena starts off with a series of domino's standing near each other (see figure 3.3). Each one of which is initially in an equilibrium position. Perturbation of one domino so that it tilts to an unstable equilibrium position and falls over and generates a force (tilting moment) on the next domino which in turn becomes unstable and falls. As a result of this process a large number of domino's will finally have fallen over each one then occupying another equilibrium position.

Figure (3.3) describes the domino effect theory while the last domino is sitting between two surfaces, and it is free to slide:

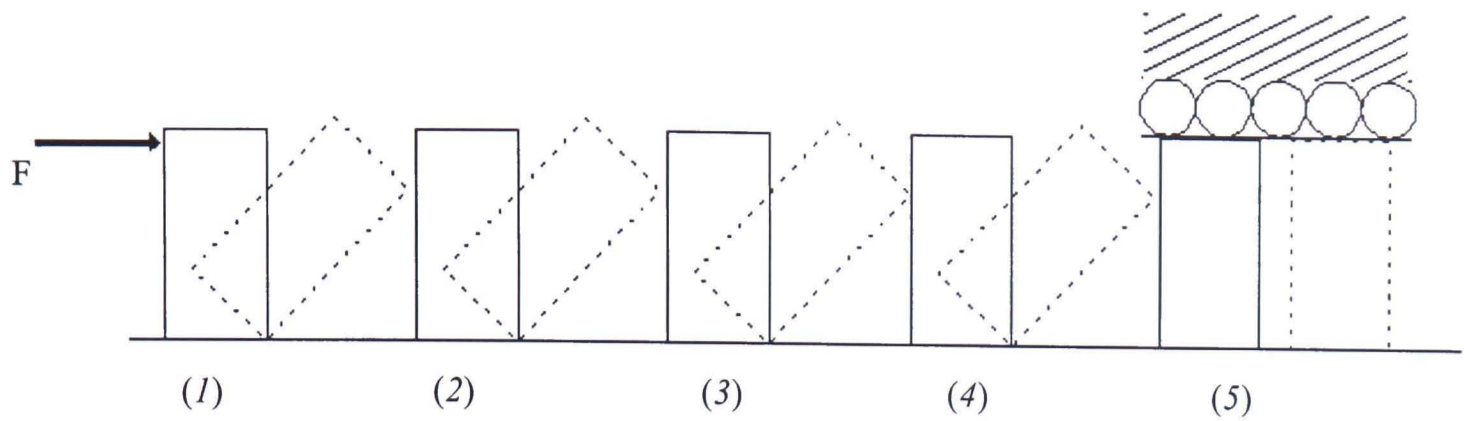


Figure 3.3 Graphical representation for the domino effect theory

3.4 COMPARISON BETWEEN THE NEW STRATEGY AND THE DOMINO EFFECT THEORY

To establish a relationship between the new strategy and the domino effect theory a minimum of two similar stages is required. Another look at figure (3.1-3.3) will show (see table 3.1):

Table 3.1 Similarities between the new assembly strategy and the domino effect theory

Category	New strategy Vertical assembly	New strategy Horizontal assembly	Domino effect theory
Similar stages	3 & 4	3 & 4	2, 3, 4 & 5

In the new strategy, the similarity between the vertical and the horizontal chamferless assembly is shown in figure (3.1 & 3.2). The important stages are (3) and (4). In both categories, stage (3) is caused by a moment, which is generated by the reaction force. Also in both categories, stage (4) caused by a lateral motion generated by an additional compliance. The difference between the vertical assembly and the horizontal assembly is that in the horizontal assembly the device holding the peg being inserted has to be stiff enough to withstand the bending moment (possible deflection of the peg) which caused by the gravitational force (weight).

In the domino effect theory, stage (3, figure 3.3) can be any stage other than the first and the last, and it is caused by the tilting moment. While the last stage (5), is caused by a lateral motion (pushing force) of the previous stage. As shown in table (3.1), stages (3 & 4)

in the new assembly strategy and the domino effect theory are similar. Both are the result of a reaction moment and an axial force.

3.5 DOMINO EFFECT ANALYSIS

To tilt the first domino (see figure 3.4),

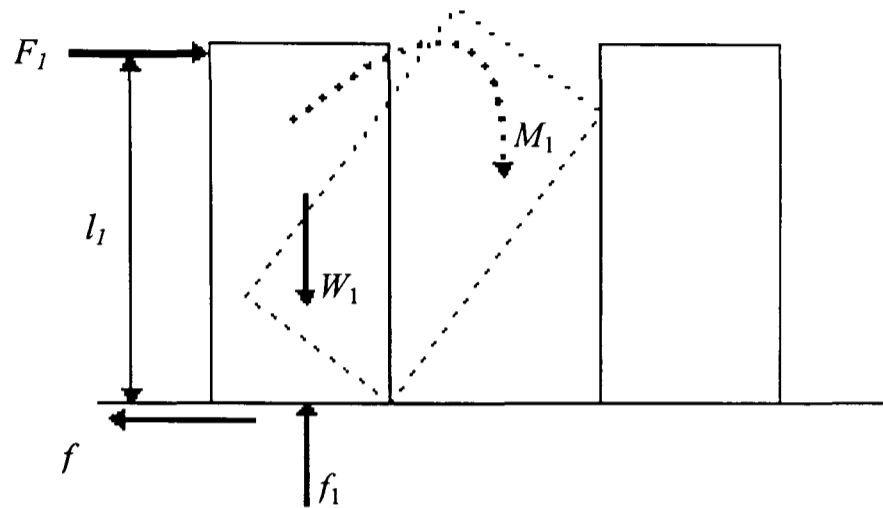


Figure 3.4 First domino in unstable position

The required tilting moment is

$$M_1 = F_1 \times l_1 \quad (3.1)$$

and the forces acting on the second domino can be shown as in figure (3.5),

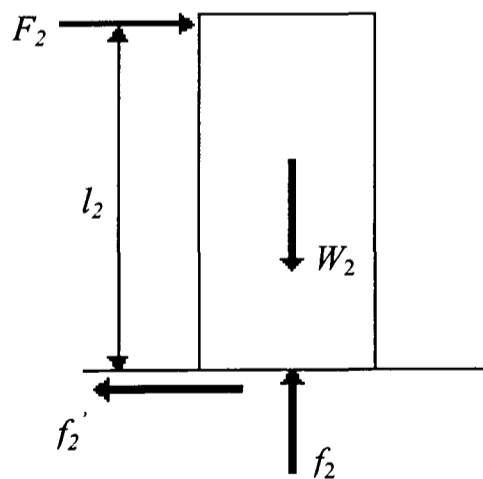


Figure 3.5 Forces acting on the second domino

To tilt the second domino

$$M_2 = F_2 \times l_2 \quad (3.2)$$

and it is assumed that $l_1 > l_2 > \dots > l_i$. Then for a general case, the required tilting moment is

$$M_i = F_i \times l_i \quad (3.3)$$

Eq. (3-3) shows that the tilting moment is decreasing, which is due to the decrease in the location (l) of the reaction force. For that reason, this chain of reaction (domino effect) is going to stop at one stage.

3.6 ANALYSIS OF THE NEW ASSEMBLY STRATEGY

The analysis of this strategy will be divided into two sections. Note that the pivoted point at which the peg rotates is approximate and not the actual one (the actual point will be dealt with in chapter 6).

3.6.1 Vertical Assembly

As shown in section (3.2), this strategy consists of (5) stages of which the last three are generated by reaction forces.

Stage 1

Approach, as shown in figure (3.6), the peg could approach the hole from 3 different positions;

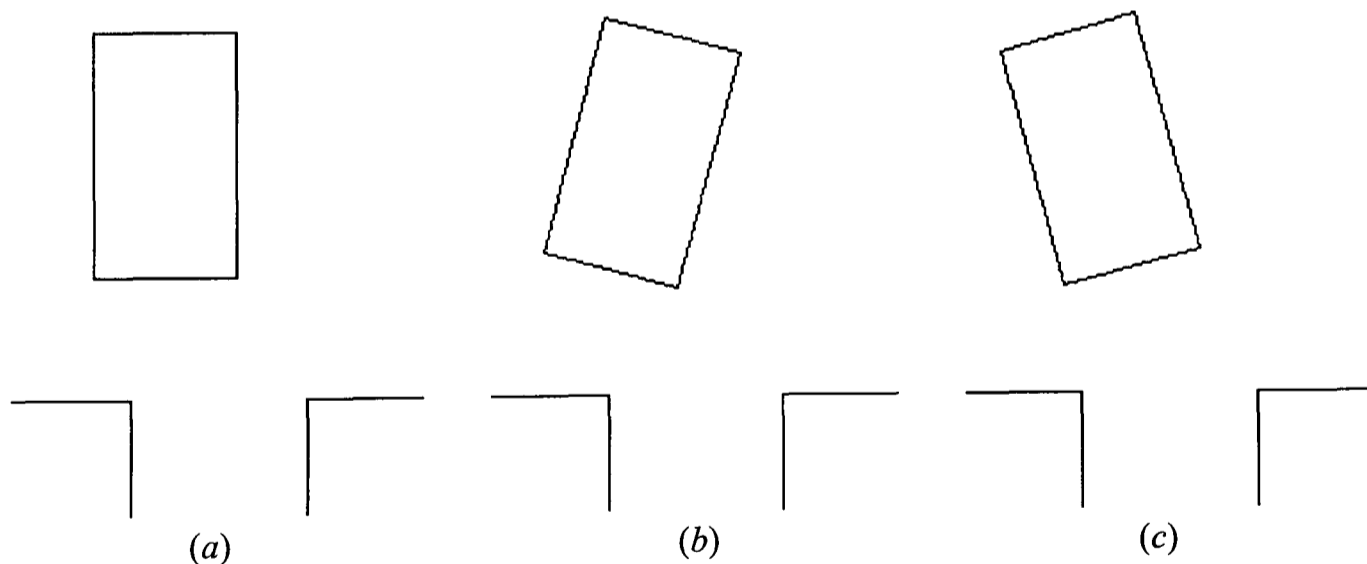


Figure 3.6 Vertical approach stages

Stage 2:

Peg touches the upper surface of the mating part;

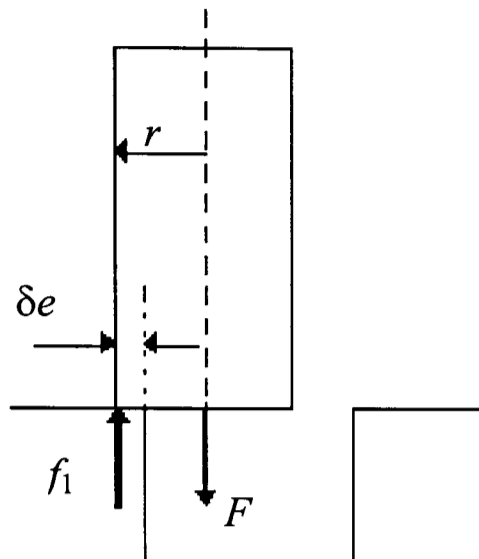


Figure 3.7 Peg during second stage, position (a)

Position (a): The condition for this stage is described in figure (3.7), which is $\delta e < r$ and the initial required moment (tilt) is

$$M = F(r - \delta e) \quad (3.4)$$

Position (b): This position is the same as that in stage (3).

Position (c), as shown in figure (3.8), this position consists of two sub-positions:

- I. aligning the peg to the top surface as in position (a)
- II. proceeding to stage (3)

In the first sub-position the following relationship must be fulfilled:

$$M = F \cos \vartheta \times r \quad (3.5)$$

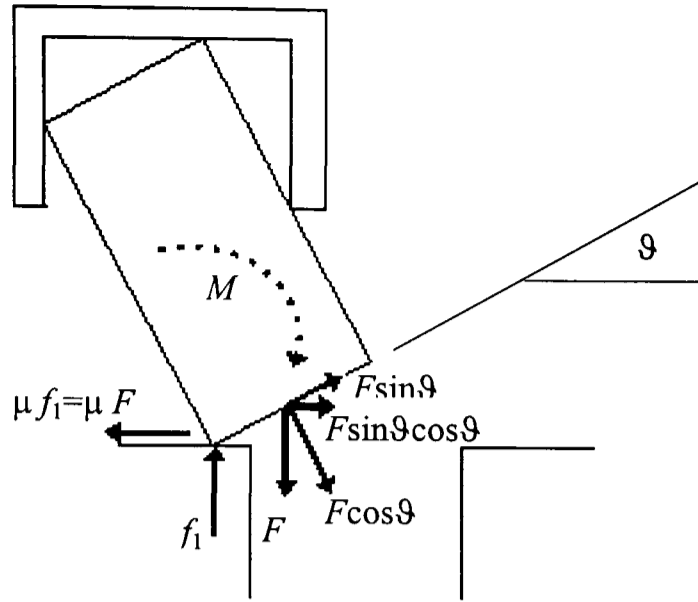


Figure 3.8 Peg during second stage position (c)

and

$$F \sin \vartheta \cos \vartheta > \mu F \quad (3.6)$$

Where F is the applied force, ϑ is the angular misalignment between the peg and the hole and μ is coefficient of friction. Therefore,

$$\sin \vartheta \cos \vartheta > \mu \quad (3.7)$$

Note that in this stage, it's assumed that the peg tilt and movement occur at an equal pace.

Stage 3 & 4

As shown in figure (3.9), once stage (2) is achieved, the peg tilts into the hole's mouth and moves to the far side of the hole; The tilt moment at any time during stage (3) is

$$M = F \cos \vartheta (r - \delta e) \quad (3.8)$$

Then, in order to move the peg to the far side of the hole, the relationship should be:

$$F \sin \vartheta > f \quad (3.9)$$

therefore

$$\tan \vartheta > \mu \quad (3.10)$$

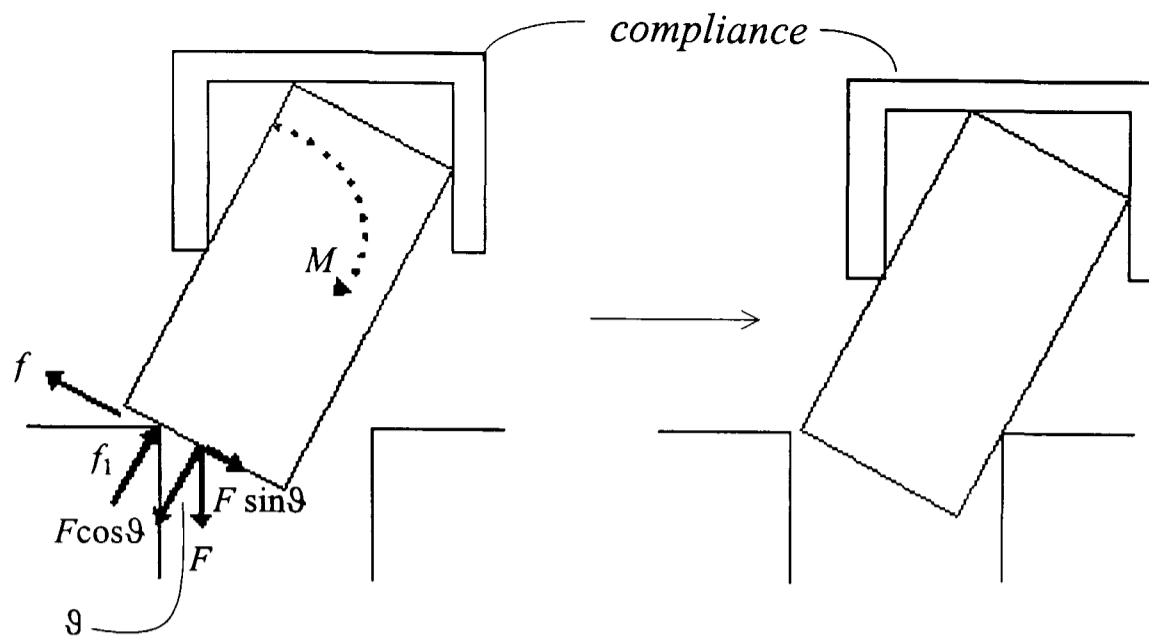


Figure 3.9 The peg during stages 3&4

Once the peg has moved to the far side of the hole (stage 4), then the insertion problem is reduced to jamming/wedging occurrence. Fulfilling the conditions of jamming/wedging avoidance will achieve stage (5). See chapter (5).

stage 5

Completion of the assembly operation;

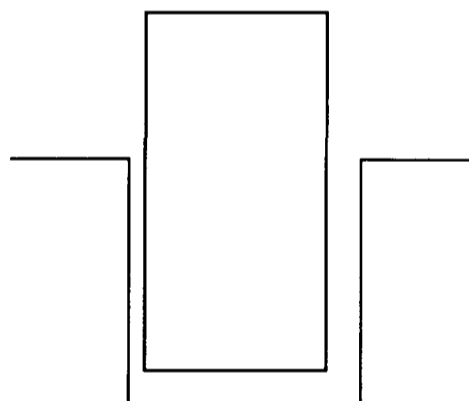


Figure 3.10 Completion of the assembly operation

3.6.2 Horizontal Assembly

This analysis is based on the assumption that the device, which holds the peg, is sufficiently stiff, and therefore the gravitational force has no effect on the peg's state during any stage of the assembly operation. In addition, the mass of the peg is too small to cause binding.

Stage 1

Approach, the peg could approach the hole in 3 different positions, they are shown in figure (3.11);

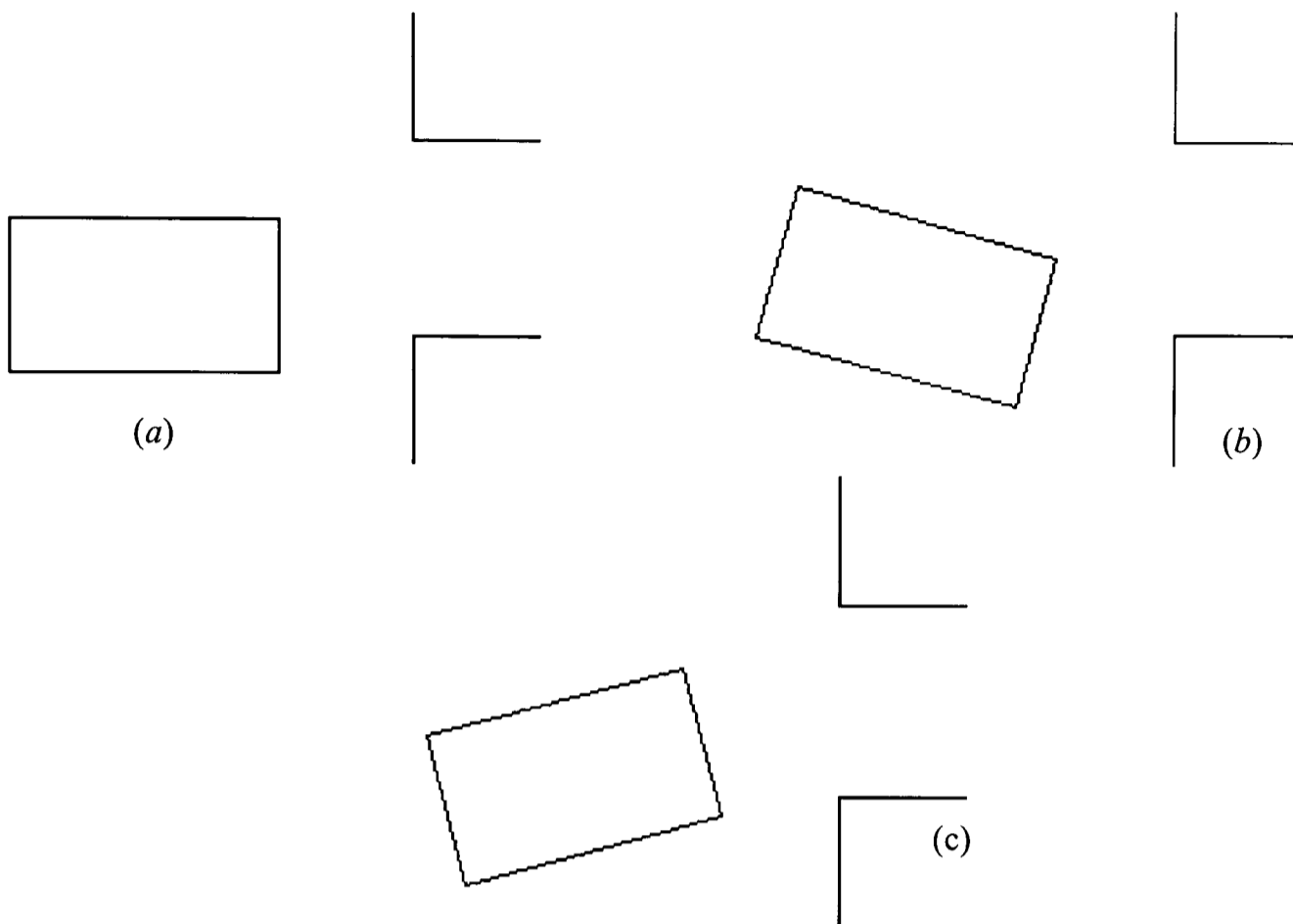


Figure 3.11 Horizontal approach stages

Stage 2

Peg touches the out-side surface of the mating part;

Position (a): The condition for this stage is shown in figure (3.12), which is $\delta e < r$ and the initial required moment is

$$M = F(r - \delta e) \quad (3.11)$$

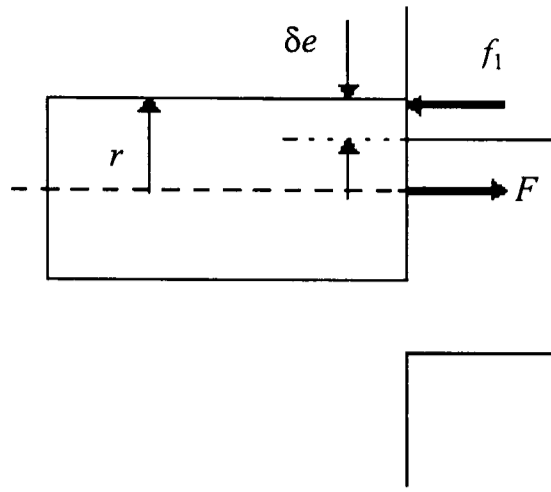


Figure 3.12 Peg during second stage, position (a)

Position (b): This position is the same as that in stage (3).

Position (c): This position consists of two subpositions that shown in figure (3.13)

- I. aligning the peg to the side surface of the hole as in position (a)
- II. proceeding to stage (3)

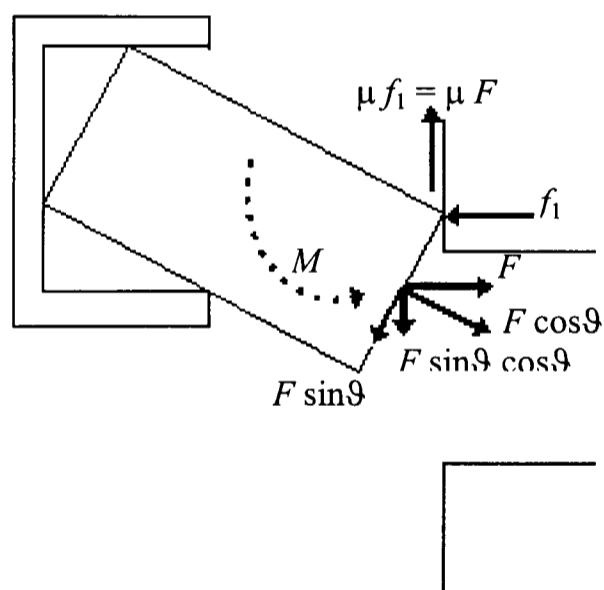


Figure 3.13 Peg during second stage, position (c)

In the first subposition the following relationship must be fulfilled:

$$M = F \cos \vartheta \times r \quad (3.12)$$

and

$$F \sin \vartheta \cos \vartheta > \mu F \quad (3.13)$$

therefore

$$\sin \vartheta \cos \vartheta > \mu \quad (3.14)$$

Stage 3 & 4

As described in figure (3.14), once stage (2) is achieved, the peg tilts into the hole's mouth and moves to the bottom side of the hole;

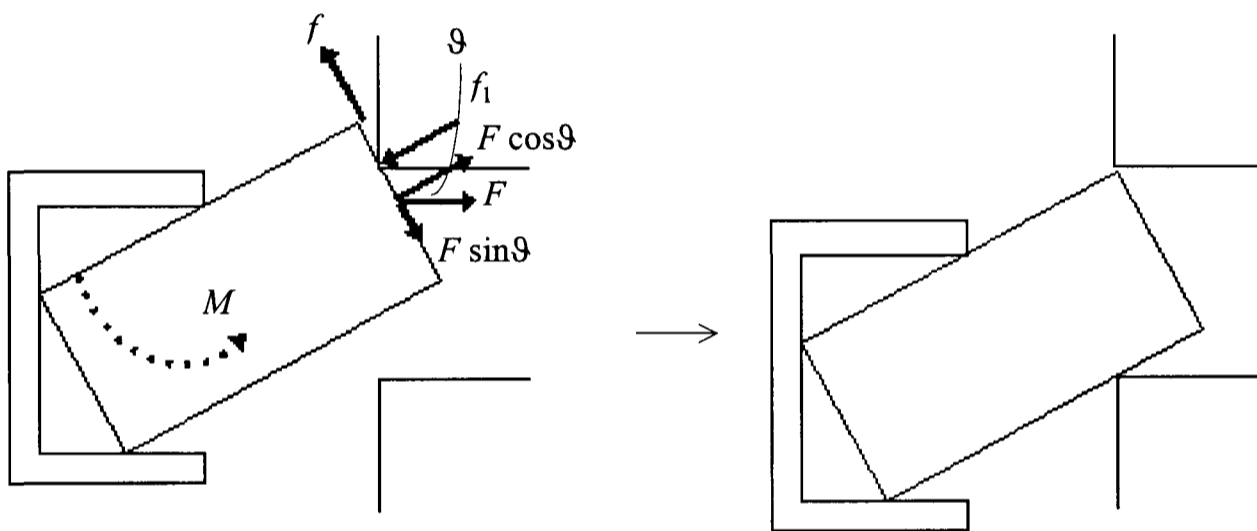


Figure 3.14 The peg during stages 3 & 4

The moment at any time during stage (3) is

$$M = F \cos \vartheta (r - \delta e) \quad (3.12)$$

Then in order to move the peg to the bottom side of the hole, the relationship should be:

$$F \sin \vartheta > \mu F \cos \vartheta \quad (3.13)$$

therefore

$$\tan \vartheta > \mu \quad (3.14)$$

Once the peg is in stage (4), assembly problems are reduced to jamming/wedging occurrence. Fulfilling the conditions of jamming/wedging avoidance will complete stage (5).

stage 5

Figure (3.15) shows the completion of the insertion action;

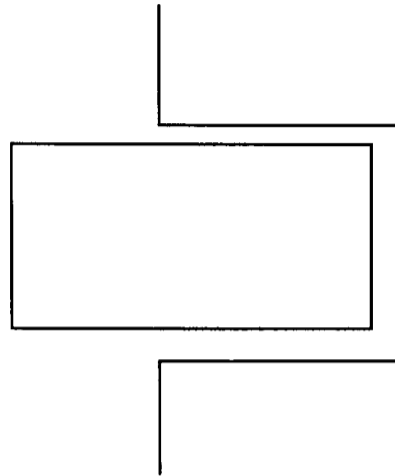


Figure 3.15 Completion of the assembly operation

To summarise the new assembly strategy, figure (3.16) presents both, vertical and horizontal assembly stages with the sequence of occurrence.

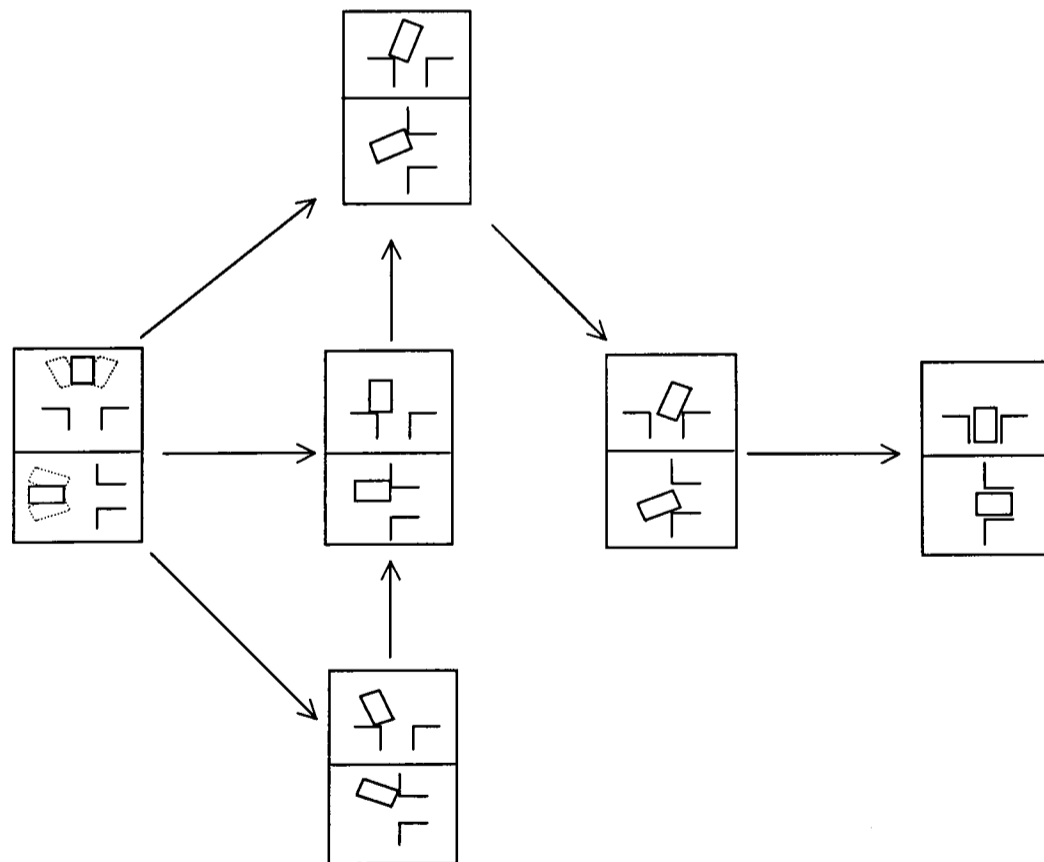


Figure 3.16 Summary of the steps of the new assembly strategy

3.7 CONCLUSION

This chapter has led to the following conclusions:

1. Some principles of the new strategy are based on those for the domino effect theory.
2. The new assembly strategy is suitable for vertical/horizontal chamferless mating parts.
To ensure a successful vertical/horizontal assembly the relationship $\sin\theta\cos\theta > \mu$ must be fulfilled during the initial tilt and $\tan\theta > \mu$ during the transition stages.
3. Horizontal chamferless assembly has same conditions as those of the vertical assembly, in addition to that, the device which holds the peg being inserted has to be sufficiently stiff to withstand a possible deflection.

CHAPTER 4

3D ANALYSIS OF THE GEOMETRICAL PEG-HOLE INSERTION

4.1 INTRODUCTION

A great deal of analysis of the peg-hole problem has evolved over recent years [T. Tsuruoka et al, 1997: E. Gustavson, 1985: A. Kirz et al, 1996: D. Pham, 1983: D Whitney, 1986]. Provided in 2 or 3 dimensional space, these analysis assumed a chamfer on either of the mating parts, and where there is no chamfer, an assembly strategy was constructed and analysed. Such assembly strategies have to have either feed back from sensors or an algorithm for each different insertion task.

In chapter (3), a passive assembly strategy for chamferless peg-hole assembly operation was presented, and briefly analysed in 2 dimensional space. Consequently, the objective of this chapter is to analyse the peg-hole insertion of that strategy in the 3 dimensional space. However, for ease of presentation the analysis is divided into two parts, geometric analysis and force analysis. The 3D-force analysis will be dealt with in the next chapter. From this point on the aim will be to establish the geometric constraints of the 3D peg-hole problem and the geometric conditions for successful insertion of the peg into the hole.

The structure of this chapter is as follows:

- Section 4.2 deals with a general case, where the peg is away from the hole.
- Section 4.3 describes the peg when it is inside the hole.
- Section 4.4 shows the effect of the tilt angle on the insertion depth.
- Section 4.5 is a conclusion.

4.2 PRELIMINARY ANALYSIS

This stage of the analysis provides the 3D geometrical conditions of the peg and the hole for successful insertion, starting from the initial stage where the peg is away from the hole. As shown in figure (4.1), the peg's centre axis is misaligned by ϑ with respect to the Z axis, both centre points of the peg and the hole (O_h & O_p) are placed at the X-Y plane to define the initial lateral misalignment e_x and e_y between the peg and the hole.

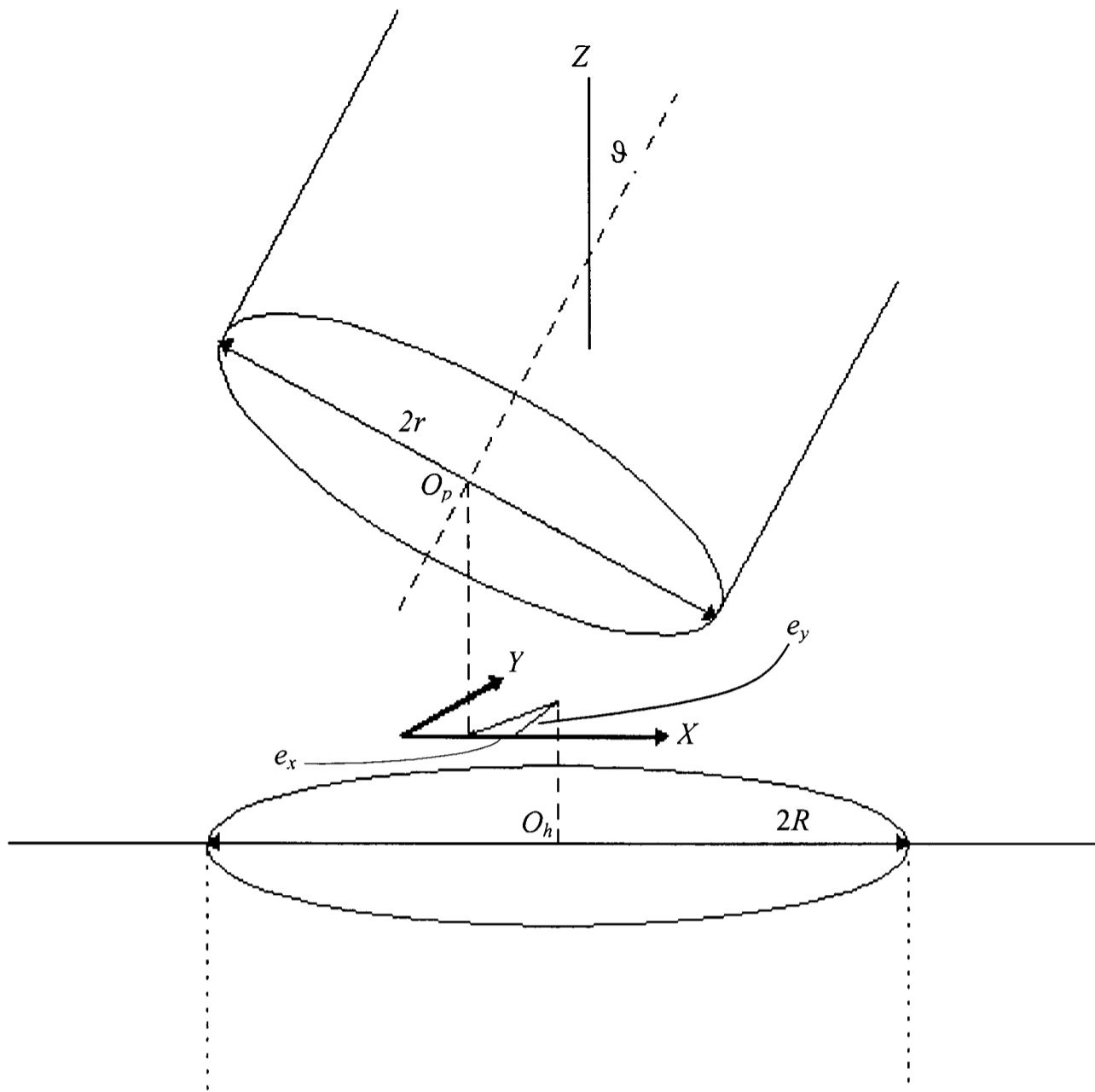


Figure 4.1 Peg and a hole in 3D space

So, the vertical projection of the peg tip over the hole of figure (4.1) is shown in figure (4.2).

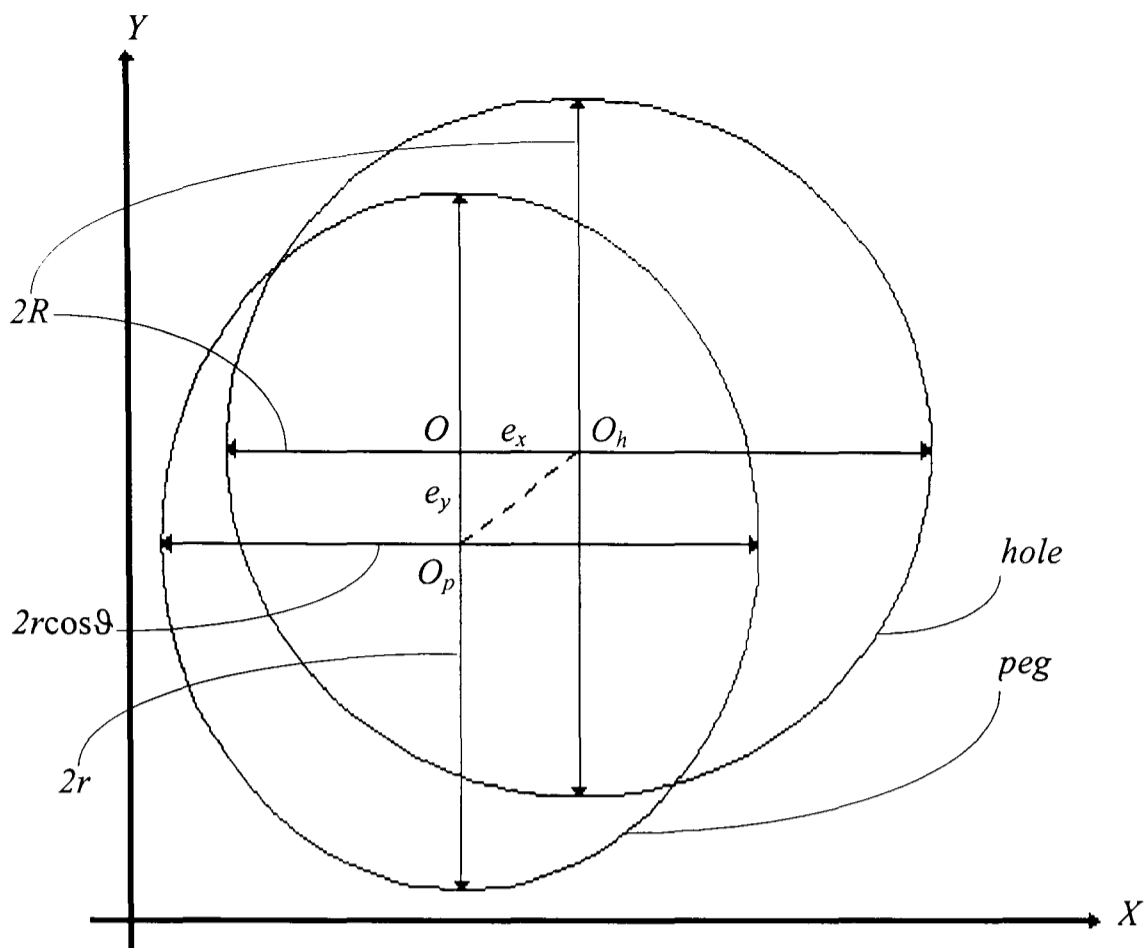


Figure 4.2 Vertical projection of the peg tip over the hole

As shown in figure (4.2), to enable the peg to enter the mouth of the hole, the following conditions must be fulfilled:

$$\begin{aligned} r \cos \vartheta + e_x &\leq R \\ r + e_y &\leq R \end{aligned} \quad (4.1)$$

from the X and the Y directions respectively. From eq. (4.1) the following relationships are derived about the X axis:

$$\begin{aligned} \vartheta &\leq \cos^{-1} \left(\frac{R - e_x}{r} \right) \quad \text{or} \\ e_x &\leq R - r \cos \vartheta \end{aligned} \quad (4.2)$$

and about the Y axis

$$e_y \leq R - r \quad (4.3)$$

In equations (4.1) through (4.3), it can be noticed that a decrease in the clearance between the peg and the hole ($c = R - r$) will dissatisfy the conditions given in those equations. Therefore the peg will not enter the hole. Also, an increase in the clearance will ease the insertion process, as described in those equations.

Also in equations (4.1) through (4.3), the outcome of any stage of the insertion process depends upon the value of the variables e_x , e_y , \mathcal{G} .

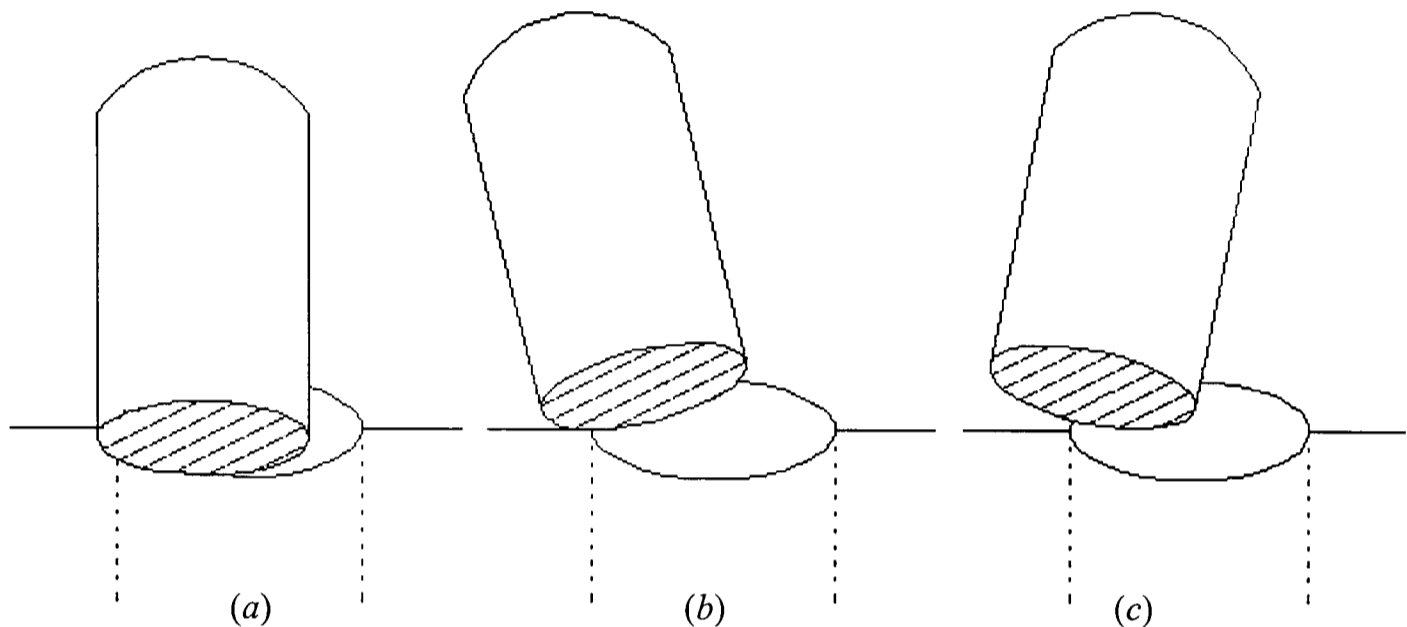


Figure 4.3 Peg and a hole in 3 different stages in the initial contact phase

Figure (4.3) shows 3 different stages in the initial contact process between the peg and the hole. These stages are a result of:

	$\mathcal{G} = 0$	$\mathcal{G} < 0$	$\mathcal{G} > 0$
(a)	$e_x \geq 0$ $e_y \geq 0$	(b) $e_x \geq 0$ $e_y \geq 0$	(c) $e_x \geq 0$ $e_y \geq 0$

It should be understood that once the peg has passed stages *a* through *c* of figure (4.3), by satisfying the previous conditions, it should enter the hole through one-two or in some cases three-point of contact (see chapter 5), otherwise jamming could occur.

4.3 PEG-INTO THE HOLE

The analysis in this section is based on the fact that the geometric conditions of section (4.2) are satisfied, and the peg is already in either one or two-point contact with the hole.

Thus the aim of this analysis is to determine the geometrical conditions for successful assembly while the peg is inside the hole.

Once the peg is in contact with the inside of the hole, the geometric uncertainty of the positional misalignment becomes similar to the 2D analysis. Because the point/s of contact will always lie in one plane, either the X-Z or Y-Z plane.

During either one or two-point of contact; the peg will slide down the hole if the tilt angle θ between the peg and the hole becomes smaller. For a general case see figure (4.4),

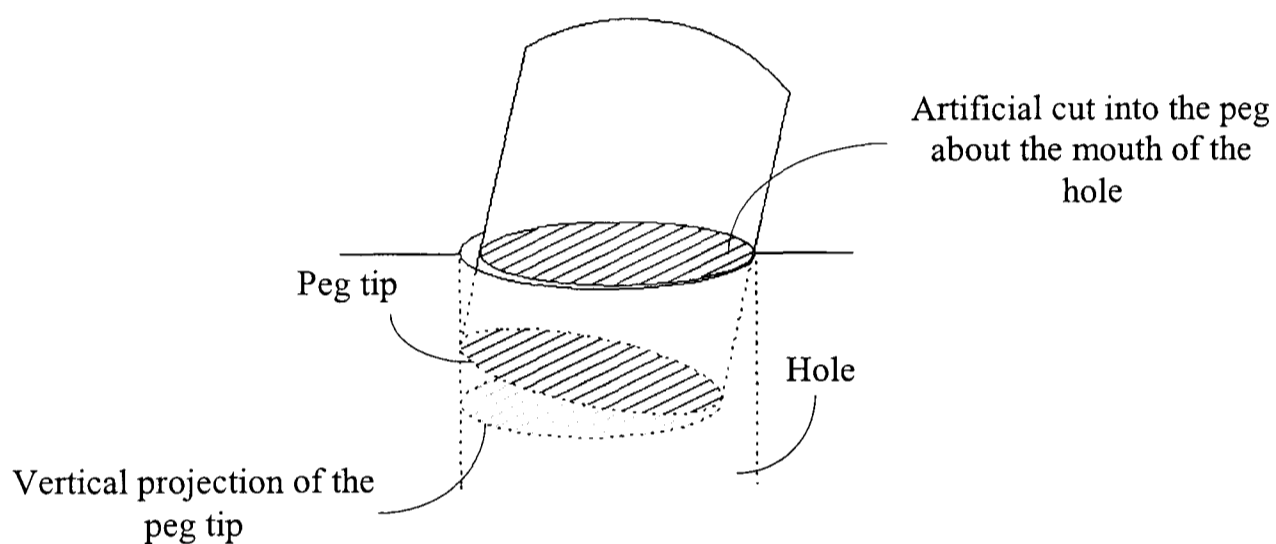


Figure 4.4 General case, peg-hole in two-point of contact

One-point of contact case: With reference to figure (4.4), and assuming contact between the peg and the hole on the top right hand side only, the plan view is shown in figure (4.5):

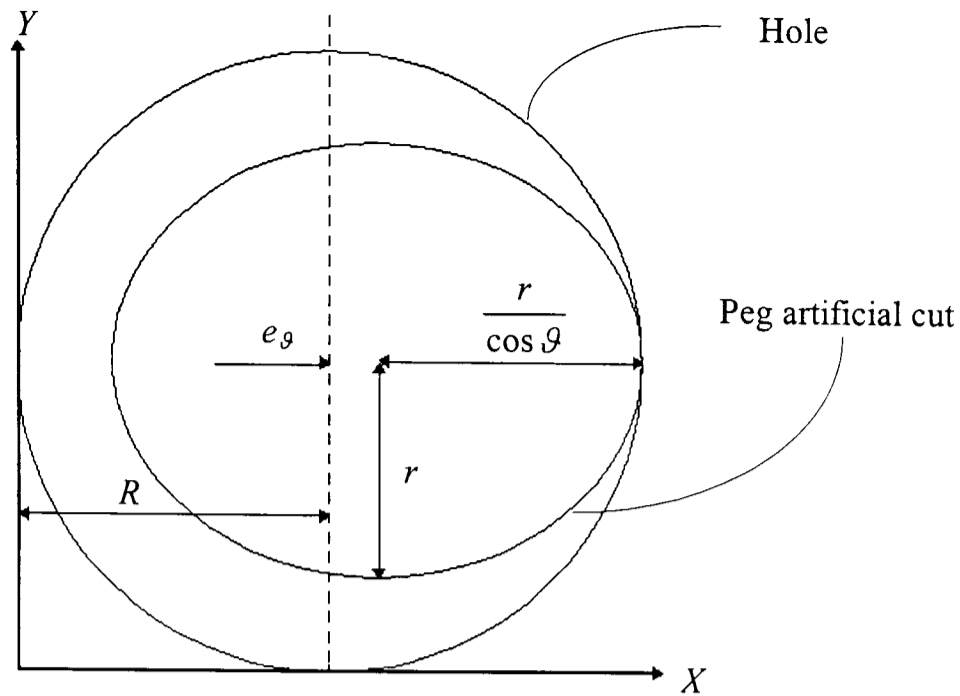


Figure 4.5 A plan view on the peg artificial cut and the hole

From figure (4.5) the following condition are drawn:

$$e_g + \frac{r}{\cos \vartheta} = R$$

$$e_g = R - \frac{r}{\cos \vartheta} \quad (4.4)$$

$$\vartheta = \cos^{-1} \left(\frac{r}{R - e_g} \right)$$

It can be seen in eq. (4.4), the e_g is dependent on ϑ , thus decreasing the tilt angle will decrease e_g which will facilitate the insertion process.

However, if the one-point contact is on the bottom left hand side of the hole (figure 4.4) then the analysis will be similar to that for two-point contact.

Two-point of contact case: Another look at figure (4.4) where there is two-point of contact, though this time looking at the projection of the peg tip inside the hole will appear as in figure (4.6):

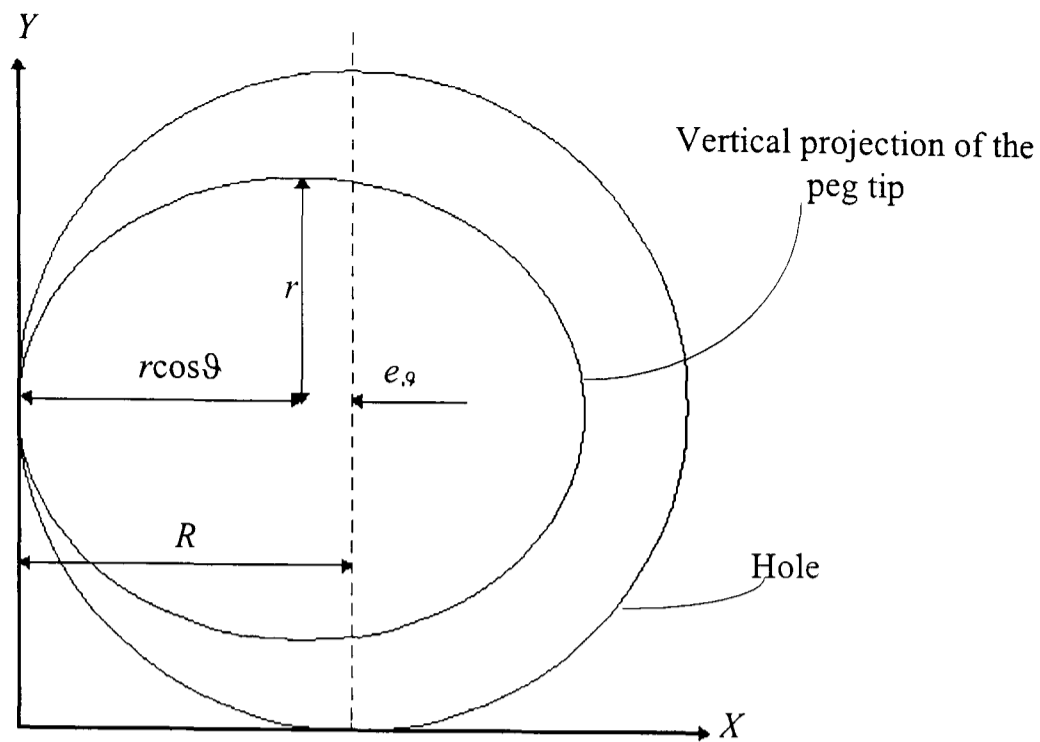


Figure 4.6 A top artificial view on the projection of the peg tip inside the hole

As with the one-point contact case, of figure (4.6) the following conclusions are drawn:

$$\begin{aligned}
 r \cos \theta + e_g &= R \\
 e_g &= R - r \cos \theta \\
 \theta &= \cos^{-1} \left(\frac{R - e_g}{r} \right)
 \end{aligned}
 \tag{4.5}$$

Again, as in eq. (4.4), for either the bottom left hand side one-point contact or for two-point contact, the insertion process is dependent on the tilt angle. However, this time satisfying eq. (4.5) may lead to the completion of the insertion process.

4.4 THE EFFECT OF THE TILT ANGLE ON THE INSERTION DEPTH

In this section the insertion depth of the peg during one and two-point of contact with the hole will be analysed. The final equations will be plotted on a graph to give a clear picture of the effect of the tilt angle on the insertion depth and consequently on the insertion process. In figure (4.7), the peg is in 3D space contact with the hole. Once in one and then in two-point contact.

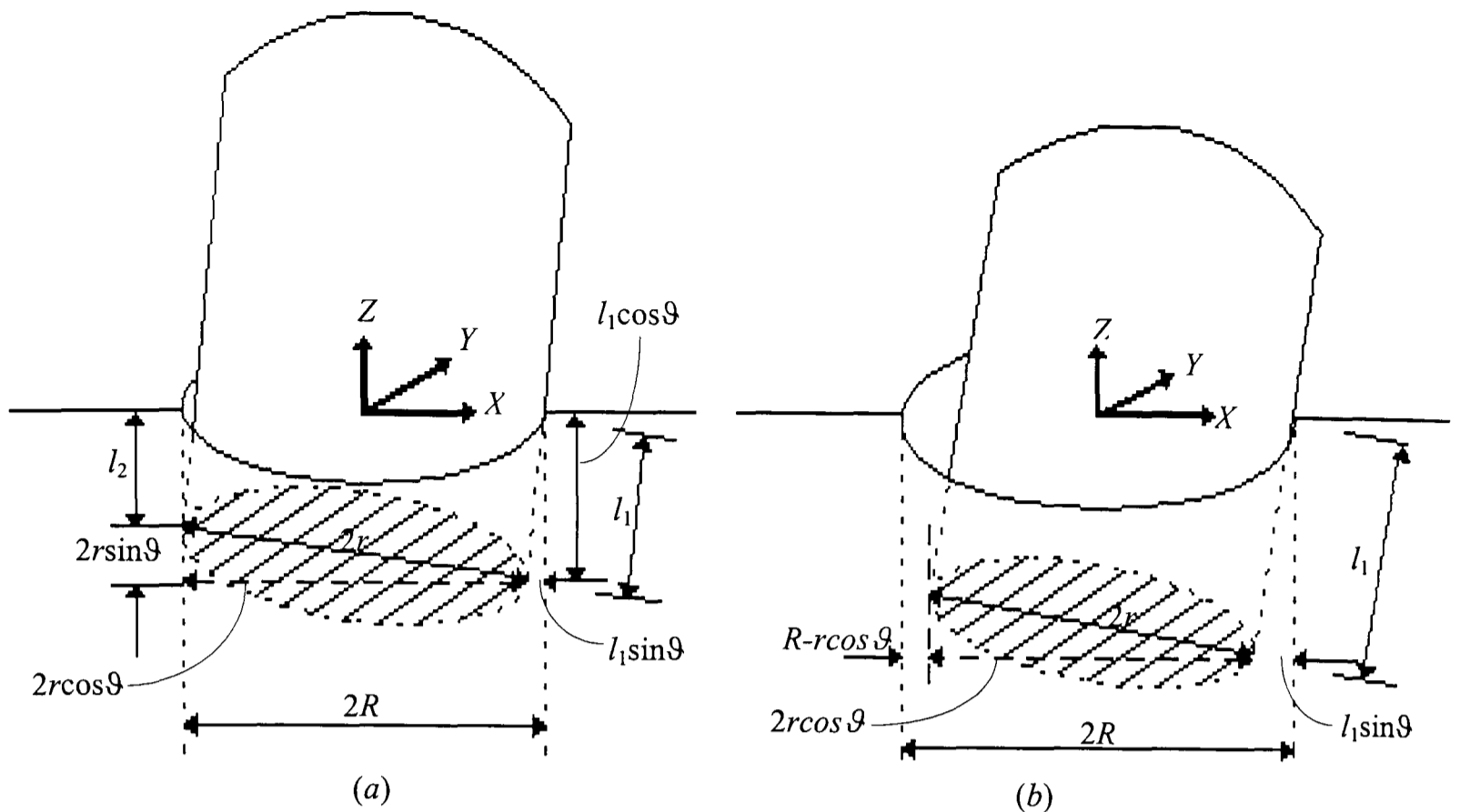


Figure 4.7 Peg is in a contact with the hole (a) two-point, (b) one-point of contact

In figure (4.7), the centre of the peg and the centre of the hole are assumed to coincide. Also in figure (4.7), it can be noticed that the dimensions lying in the X-Z plane as in 2D space. The reason for that is that in 3D space, when mating cylindrical parts, the contact points will lie always on one plane either X-Z or the Y-Z. Also in figure (4.7a), for two-point contact the following geometrical equation can be written:

$$l_1 = \frac{2R - 2r \cos \vartheta}{\sin \vartheta} \quad (4.6)$$

$$l_2 = \left(\frac{2R - 2r \cos \vartheta}{\sin \vartheta} \right) \cos \vartheta - 2r \sin \vartheta$$

Where l_1 : one point contact insertion depth and l_2 : two point contact insertion depth. For one-point of contact (figure 4.7b)

$$l_1 = \frac{R - r \cos \vartheta}{\sin \vartheta} \quad (4.7)$$

To show the effect of the tilt angle on the insertion depth during one and two point contacts, both equations (4.6 and 4.7) were plotted and presented in figure (4.8 and 4.9). In both graphs the clearance between the peg and the hole is assumed to be 0.2 mm , and the radiuses of the peg and the hole, $r = 9.8 \text{ mm}$ and $R = 10 \text{ mm}$ respectively.

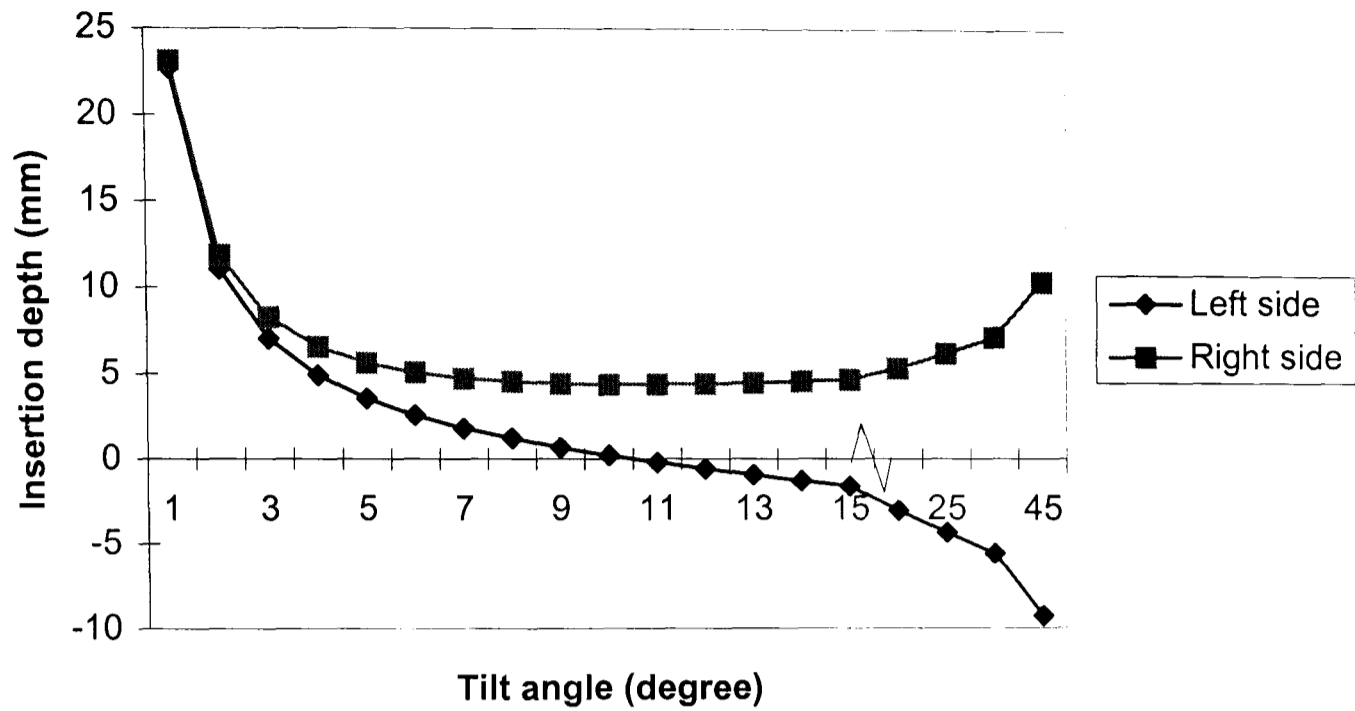


Figure 4.8 Tilt angle versus insertion depth during two-point contact

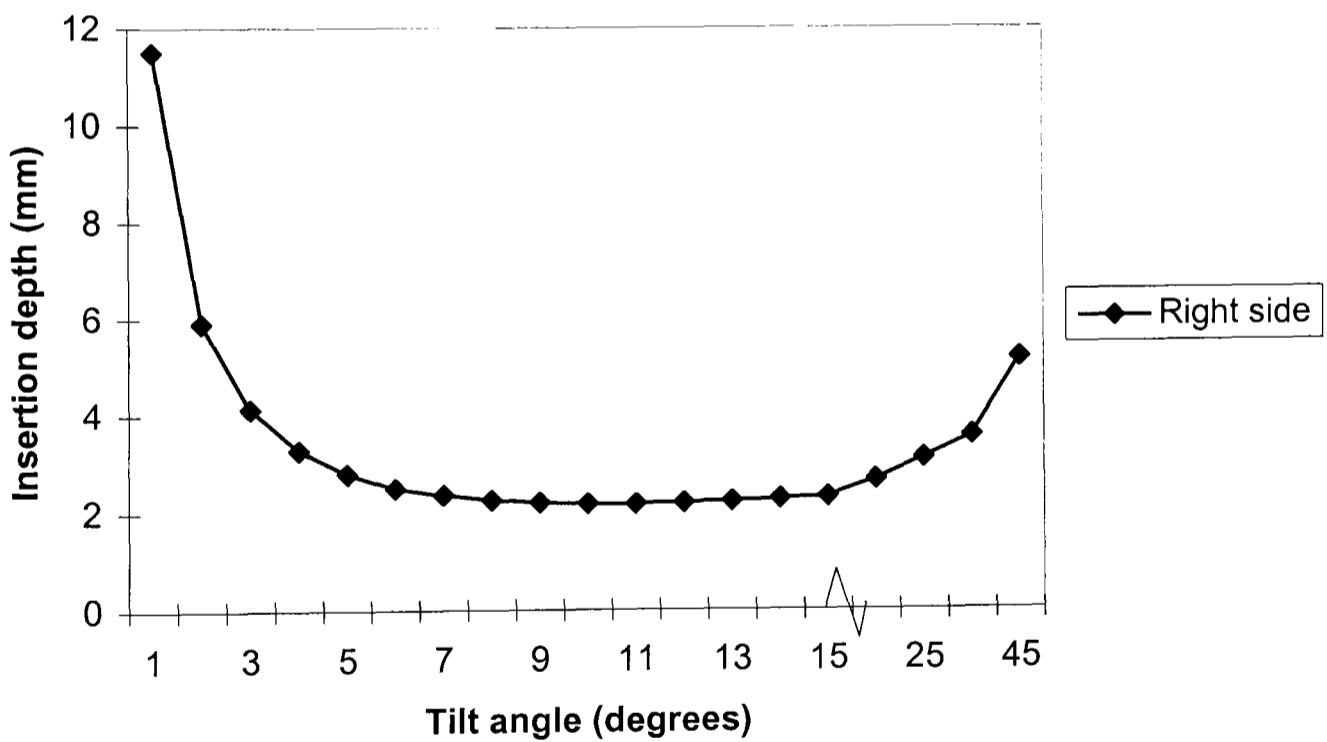


Figure 4.9 Tilt angle versus insertion depth during one-point contact

In figure (4.8), during two-point of contact between the peg and the hole, the increase in the value of the tilt angle decreases the insertion depth. As a result of this when the tilt angle is over 10° the peg attempts to get out of the hole. Although, the right side of the peg slides into the hole and as a result of that the peg contacts the hole in one point, the insertion depth of this point (right hand side) increases until a stage where the peg gets completely out of the hole.

Also, in the chart of figure (4.9), during one-point of contact the increase in the value of the tilt angle decreases the insertion depth. However, from 15° upwards, the insertion depth starts to increase. The reason for this change in the insertion depth is that from 15° , the peg moves from the one-point of contact to two-point of contact with the hole.

4.5 CONCLUSION

As stated in the introduction, from the geometrical point of view, the 3D geometrical analysis has given a better understanding of the chamferless peg-in hole assembly. However, it is inappropriate to base or to construct assembly strategies or even to give a definite solution to the peg-hole problem in 3 dimensional space before considering other factors, which are involve in the assembly process such as forces, friction and wrist stiffness etc. At this stage, a more general 3D analysis for the peg-hole problem can be made on the ground of the geometry. In the next chapter the dynamics of the peg-in hole insertion process will be analysed.

CHAPTER 5

DYNAMIC INVESTIGATION OF THE PEG-HOLE INSERTION PROCESS

5.1 INTRODUCTION

In previous chapters, the assembly strategy was presented and analysed in 2D space, followed by a 3D geometrical analysis, which dealt with the geometrical aspects of the insertion process, rather than the dynamic ones. The objective is to investigate the dynamics of the assembly process of the new strategy, taking into account the friction between the mating parts and the forces, moments involved in the insertion process.

The friction between two surfaces/points as a result of the compliant motion stick-slip phenomena can determine the success or failure of each stage of the insertion process. In this instance, the friction can be considered in the form of the friction cone, and the compliant motion stick slip; are detailed. Once the peg is in initial contact with the top surface of the hole, several problems are raised and analysed in the 3D view. After that, the peg moves inside the hole in one/two point contact, the fact that the contact between the peg and the hole is in one plane, reduces the investigation to a 2D space problem.

The structure of this chapter is as follows:

Section 5.2 describes the friction cone.

Section 5.3 presents the compliant motion and explains the stick-slip phenomena.

Section 5.4 is a dynamic investigation of the insertion process.

Section 5.5 shows the insertion force during one/two-point contact.

Section 5.6 is wrist kinematics

Section 5.7 is a general discussion of this work.

Section 5.8 is a conclusion.

One major point of this work, is that for a given positional misalignment and other parameters/variables (dimensions, forces etc,) the success or failure of the insertion process can be determined in theory.

5.2 THE FRICTION CONE

When two objects such as cylindrical peg and a hole are in contact, and providing that the point of contact is governed by dry friction or Coulomb friction, the reaction force (f_r), as a result of the applied mass/force is the sum of both the normal force (f_n) and the friction force (f_t). The maximum value of the tangential component (friction force) of the reaction force is,

$$f_{t_{\max}} = \mu f_n \quad (5.1)$$

Where the coefficient of friction μ is static; Equation (5.1) can also be represented graphically (figure 5.1). This graphical representation of the frictional reaction forces known as the friction cone [E. Caine, 1982]. Where the half angle of the cone is called the friction angle (ϕ), and it is given by the relation,

$$\phi = \tan^{-1} \mu \quad (5.2)$$

A set of vectors at this angle (contact point) to the normal defines the friction cone, and the perpendicular bisector of the cone is perpendicular to the contact point/surface. The interior of the cone specifies the possible range of reaction forces that one object can exert on another through one point of contact in the presence of friction.

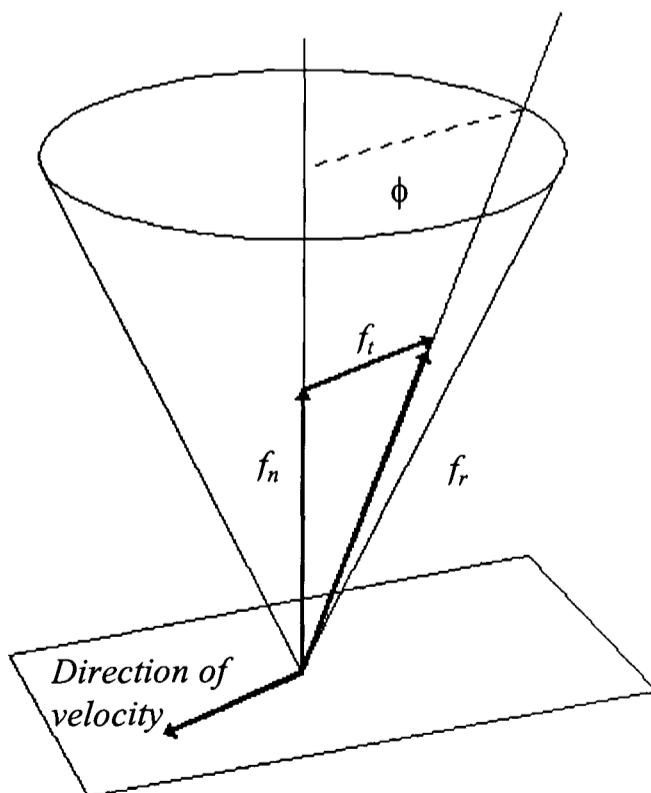


Figure 5.1 The friction cone

Another way to interpret the friction cone is to consider an applied force F (see figure 5.2). If the applied force points into the cone, then the tangential component of the reaction force will cancel the tangential component of the applied force and the object will not move (figure 5.2 *a*), for this case $\tan \phi < \mu$. However, for $\tan \phi > \mu$, the applied force lies outside the cone, and the friction force nullifies only a portion of the applied force and leaving a net force (F_{net}) parallel to the contact surface that causes the object to slide (figure 5.2 *b*). When the applied force lies at the edge of the cone, the object is on the verge of slipping and $\tan \phi = \mu$.

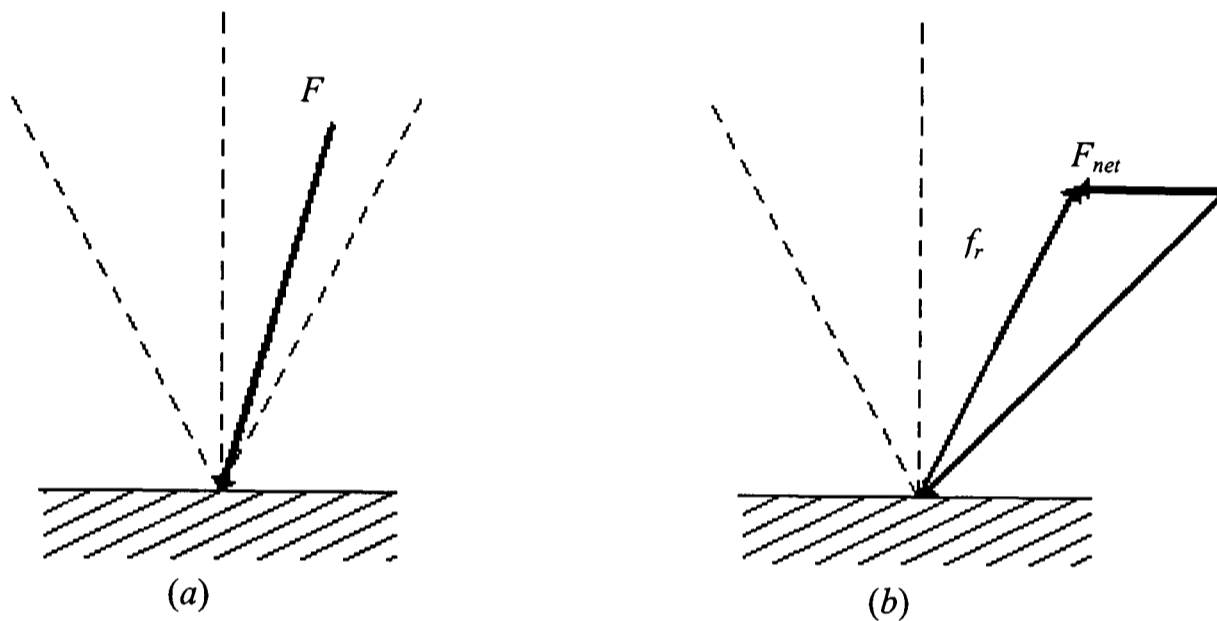


Figure 5.2 Sticking (*a*) and sliding (*b*)

5.3 COMPLIANT MOTION

In robotic assembly operation of peg-in hole there are two types of motion:

- position controlled motion,
- compliant motion.

The first type of motion is used primarily in the active assembly methods, where the motion of the peg is monitored by active sensors, and the trajectory of the peg to achieve the insertion is corrected through the feedback of the relevant sensors.

On the other hand, in the compliant motion the trajectory of the inserted peg is corrected by the reaction forces that arise during the contact between the peg and the hole. In

practice, every linkage in the robot is compliant to some extent and this compliance is in universal use.

To realise the effect of the compliant motion as producing sliding condition; sliding means that the moving object confines its motion to be tangent to the constraining surface. When there is no contact between the peg and the hole, the direction of the motion will be along the commanded velocity.

5.3.1 Stick-Slip Motion

As further to what was cited about the compliant motion, when the peg contacts the upper surface of the mating part, there are two possibilities, stick or slip on the surface of the hole could occur. Based on the initial contact velocity and the angular orientation of the peg and the coefficient of friction between the peg and the hole surfaces, the outcome will be determined.

To understand the role of friction during contact between the peg and the hole, imagine two pieces of metal one above the other. To slide the top part, a pushing force is needed, and it should be larger than the sum of the microscopic frictional forces acting on each individual point of contact between the two parts. However, if the surfaces are very smooth then there are more points of contact and therefore a higher frictional resistance is generated. But for rough surfaces, there are fewer points of contact between the two surfaces and consequently the sum of the microscopic frictional forces is less than that for a smooth surface. So this time a smaller pushing force is needed to slide the upper part.

In addition to what was cited about sticking and sliding, with reference to figure (5.2), if the angle of the force vector to the surface normal is less than ϕ , then no motion will result. If the angle of the force vector to surface normal is greater than ϕ , sliding will occur. In other words, if the velocity at the contact point is equal to zero then sticking occurs, but if only the normal velocity is equal to zero then slipping occurs.

Now, having presented the friction cone, compliant motion and the stick slip phenomena's, more in depth analysis for the new assembly strategy can be made.

5.4 INVESTIGATION OF THE DYNAMICS OF 3D INITIAL CONTACT BETWEEN THE PEG AND THE HOLE

As presented in chapter (3) the insertion process consists of 5 stages. However, in this investigation for ease of analysis, the 5 stages are divided into 3 major stages:

5.4.1 Approach

5.4.2 Initial contact between the peg and the upper surface of the mating part

5.4.3 Peg is inside the hole, one or two point of contact

5.4.1 Approach

The force balance of figure (5.3) is,

$$\begin{aligned} \sum F &= m(a - g) \\ v_i &= \sqrt{2ah} \end{aligned} \quad (5.3)$$

Where v_i is the initial contact velocity when the peg contacts the hole surface, m is the combined mass of the peg and the wrist, and h is the distance before the peg contacts the hole. In eq. (5.3) the acceleration a is constant, and it is assumed that there is no relative movement between the gripper/wrist (gripping force) and the peg.

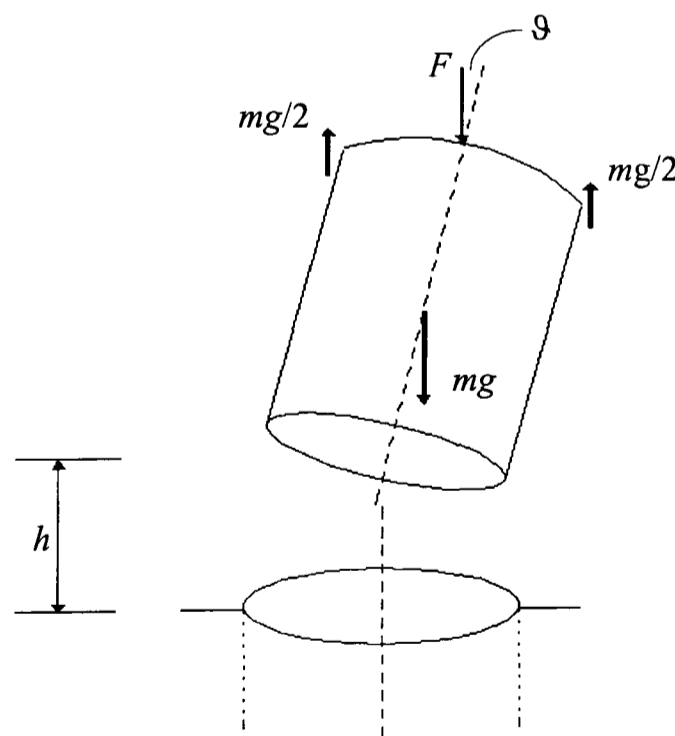


Figure 5.3 Approach stage

It can be seen that in eq. (5.3), the relationship between the insertion force and the insertion velocity is proportional, which means that any change in either value will affect the outcome of the next stage.

5.4.2 Initial Contact Between The Peg And The Upper Surface Of The mating part

The investigation of this section will provide an analysis for predicting slipping or sticking occurrence and the possible 3 points of contact between the peg and the hole.

5.4.2.1 Slipping or sticking occurrence

The contact modes between the peg and the upper surface of the hole are determined by factors such as the friction and its inconsistency, and the effect of impact and the conversation of energy etc. Although the last two phenomena are beyond the scope of this investigation, it is worth to mention here some of the other work in this area. Mason and Wang [Y. Wang et al, 1987] propose a thorough investigation of impact model for removing frictional inconsistency. Also Featherstone [R. Featherstone, 1986] has addressed the impact inconsistency in the presence of friction. For the representation of friction in 3D space and also energy conservation, see Michael Erdman [M. Erdmann, et al, 1994 & 1988].

So, the goal of the following investigation is to determine the outcome mode (sticking/slipping) after the initial contact between the peg and the upper surface of the hole. To simplify the analysis, it is assumed that the coefficient of friction is static and constant between the peg and the hole. Also it is assumed that the forces during the collision (contact) are impulsive F_{imp} , and these forces are much greater than the applied forces.

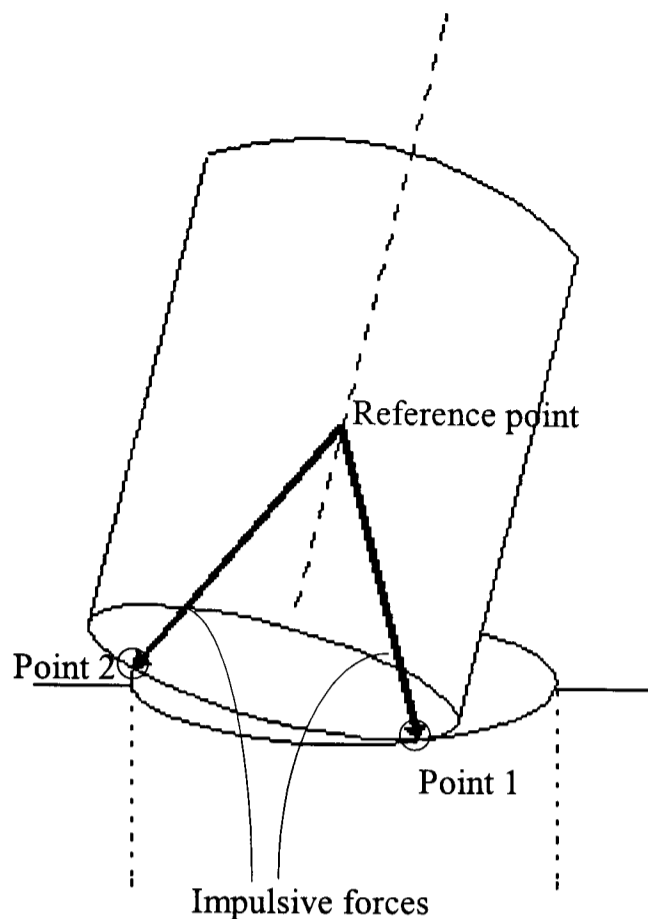


Figure 5.4 Initial contact between the peg and the upper surface of the hole

As shown in figure (5.4), there are two points of contact which are affected by impulsive forces. In 3D space it is convenient to choose the reference point of an impulsive force for an object (peg) at its centre of mass. Now, it is possible to use Coulomb's law of friction/friction cone, to determine whether sticking or slipping will occur. Points (1, 2) of figure (5.5) are acted upon an equal impulsive force. Therefore the analysis will concentrate on just point (1) and the outcome should be correct for point (2) as well. The configuration space of the impulsive force acting on point (1) is shown in figure (5.5):

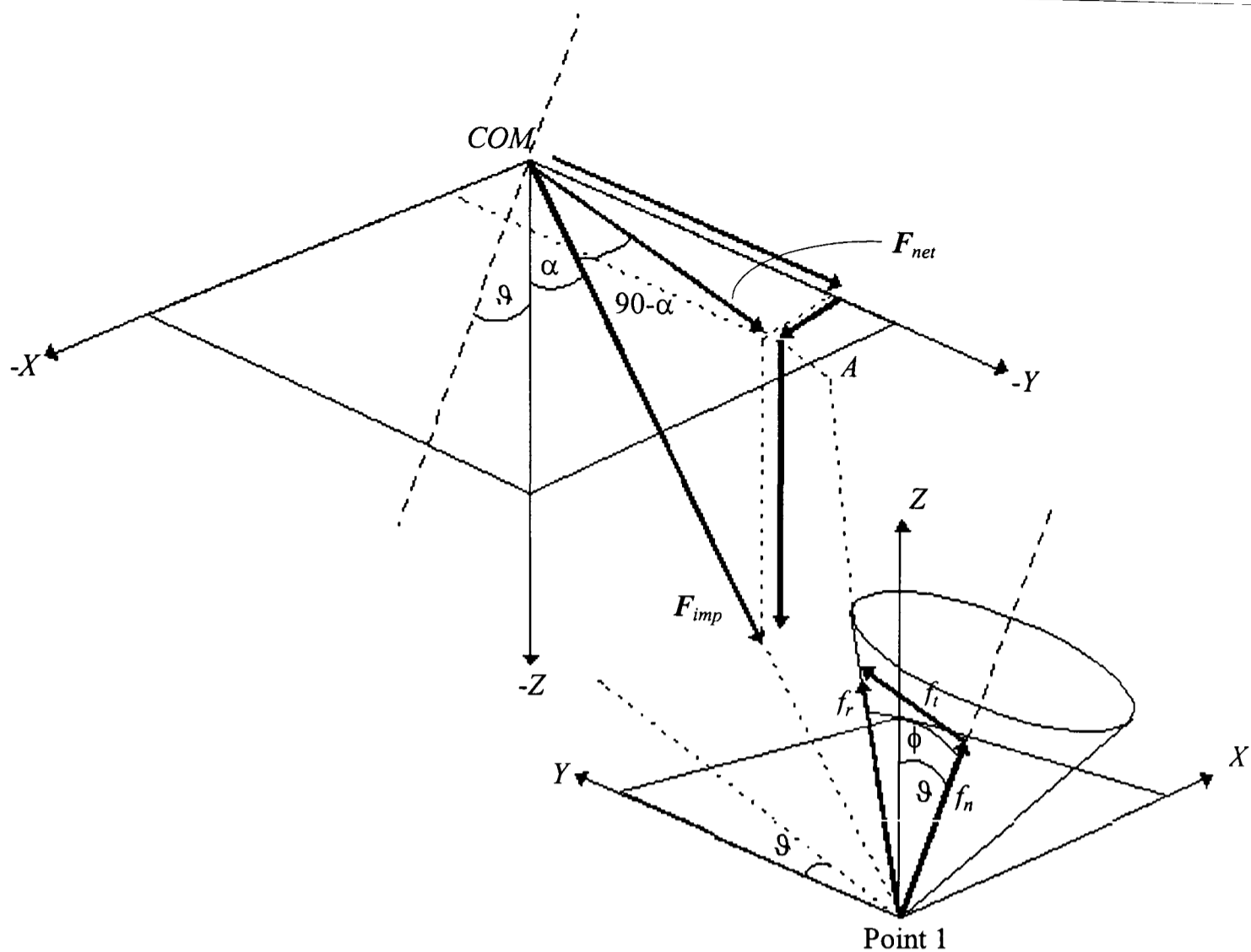


Figure 5.5 3D space of point (1) and the impulsive force acting upon

In figure (5.5), and at point (1), the reaction force f_r is the sum of the normal force f_n and the friction force f_t . Also in figure (5.5), it can be seen that the impulsive force points out of the friction cone which means that the peg will slide along the constrained surface of the hole (tangential to the contact point). Also, it is seen that the impulsive force and the reaction force lie in the same plane. Therefore to calculate the magnitude of the impulsive force,

$$\begin{aligned}
 \mathbf{J} &= \int \mathbf{F}_{imp} dt \quad \text{or,} \\
 \mathbf{J} &= m\mathbf{v}_f + m\mathbf{v}_i \quad \text{and,} \\
 \mathbf{J} &= \Delta\mathbf{P} = \mathbf{P}_f - \mathbf{P}_i
 \end{aligned}
 \tag{5.4}$$

Where \mathbf{J} is the impulse of the force or the change in momentum ($\Delta\mathbf{P}$), \mathbf{v}_f and \mathbf{v}_i are the final velocity after the break of contact and the initial velocity. dt is the duration of the contact. Since this duration is short ($\Delta t \Rightarrow 0$), the dt is used, then rearranging eq. (5.4) will reveal eq. (5.5),

$$\mathbf{F}_{imp} = \frac{\Delta \mathbf{P}}{dt} = \frac{m(v_f - v_i)}{dt} \quad (5.5)$$

$$\mathbf{F}_{imp} = m a_f$$

Where a_f is the breaking acceleration from the sticking to the slipping stage. A comparison between eq. (5.3) and eq. (5.5) shows that the difference between the two forces involved is the acceleration. Where in eq. (5.3) the acceleration is constant, but in eq. (5.5) is not, but large enough to overcome and break the contact between the peg and the upper surface of the mating part.

In regard to point (2), the magnitude of the impulsive force is equal to that in eq. (5.5), which is equal to that acting on point (1).

For a general case, to determine the contact mode, have a look at the plane (COM, A, point 1) of figure (5.5); it can be said that

$$\mathbf{F}_{imp} - f_r = \mathbf{F}_{net} \text{ which is slipping, but if} \quad (5.6a)$$

$$\mathbf{F}_{imp} - f_r = 0 \text{ then the peg is on the verge of slipping, for} \quad (5.6b)$$

$$\mathbf{F}_{imp} < f_r \text{ the peg will stick.} \quad (5.6c)$$

Table (5.1) summarises the results of this investigation for this section:

Table 5.1 Contact mode conditions

Slipping	Verge of slipping	Sticking
$\vartheta < (\pi/2) - \phi$ or $\vartheta + \alpha > \phi$	$\vartheta = (\pi/2) - \phi$ or $\vartheta + \alpha = \phi$	$\vartheta > (\pi/2) - \phi$ or $\vartheta + \alpha < \phi$
$(\tan\phi > \mu)^*$	$(\tan\phi = \mu)^*$	$(\tan\phi < \mu)^*$

- Refer to the friction cone section.

5.4.2.2 The possibility of three points of contact (3 POC)

When using passive compliant devices for inserting a peg into a hole, it is difficult to cope with three point of contact between the mating parts, due to the insufficient compliance of the wrist about the insertion axis. Where the need for rotation and motion to overcome this mode of contact is greater than in other phases of the assembly. Hence, the goal is to avoid

having 3 POC. Such mode of contact is a geometrical relation rather than force/moment relation. Because of that, identifying the variables (allowable angular error, lateral error etc.) during that stage of the insertion process will facilitate the design of an assembly task for avoiding this mode of contact.

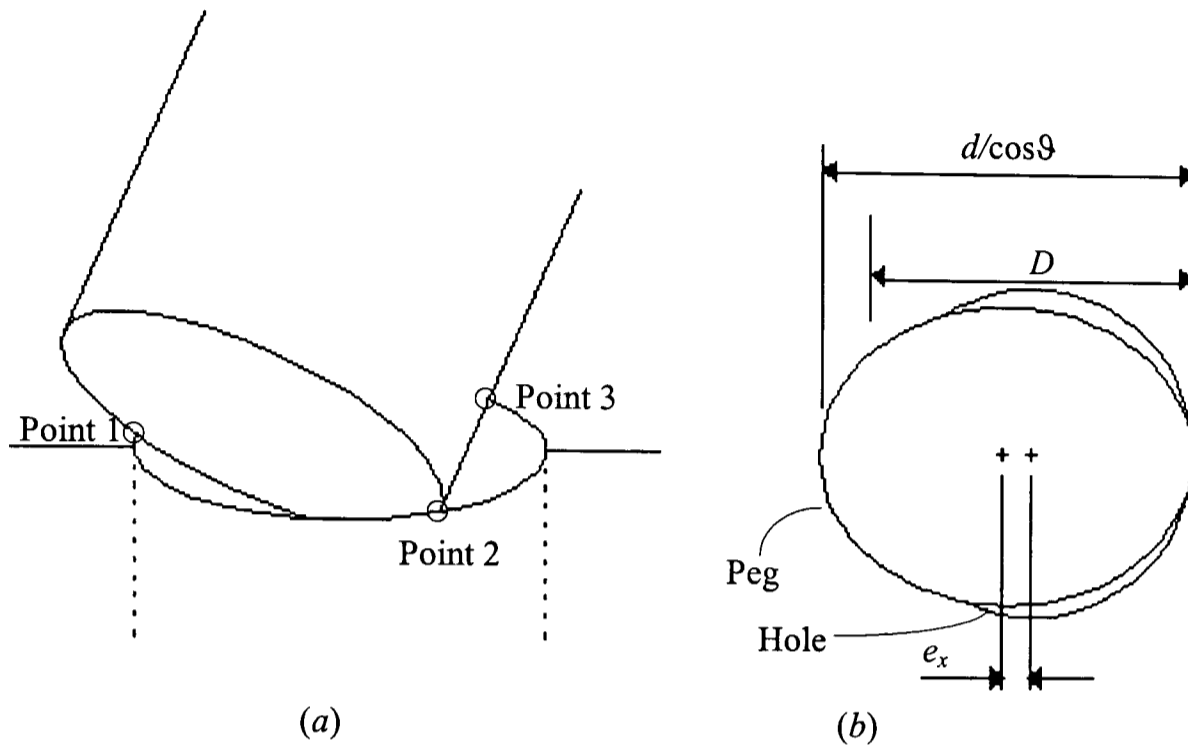


Figure 5.6 Peg is in 3 point of contact with the hole

As shown in figure (5.6a), the peg is in contact with the hole in 3 different points, and this satisfies $d/\cos\theta$ larger than D . Where d and D are the peg and the hole diameters and θ is the angular misalignment between the peg and the hole.

To avoid 3 point of contact, the following relation must be satisfied:

$$\frac{d}{\cos\theta} \leq D \quad (5.7)$$

In regard to the contact at point (3) it will exist until the one or two point of contact break and the peg slides down the hole.

The clearance between the peg and the hole is $c = R-r$, putting this relation in eq. (5.7) will give the maximum allowable clearance to avoid 3 POC (eq. 5.8),

$$c \geq \frac{(1 - \cos\theta)r}{\cos\theta} \quad (5.8)$$

In figure (5.6b), to avoid 3POC, $d/\cos\vartheta$ must be either smaller or equal to D . In the first case,

$$e_x = R - \frac{r}{\cos\vartheta} \quad (5.9)$$

this is the allowable lateral error along the X axis, which will not cause 3 POC.

Substitute $c = R-r$ in eq. (5.9)

$$\vartheta = \cos^{-1}\left(\frac{r}{r+c+e_x}\right) \quad (5.10)$$

And in the second case where $e_x = 0$, the

$$\vartheta = \cos^{-1}\left(\frac{r}{r+c}\right) \quad (5.11)$$

Both equations (5.10 & 5.11) give the range of admissible angular error in which 3 POC can be avoided.

5.4.2.3 The ideal wrist stiffness

The equilibrium equations that describe the peg sliding in during 3 POC, assuming that the peg is moving at a uniform velocity (figure 5.7) are then given by

$$F_z = 2f + \mu f_3 \quad \text{because } (f = f_1 = f_2) \quad (5.12)$$

$$F_x = 2\mu f + f_3 \quad (5.13)$$

$$M_3 = F_z r + F_x l \quad (5.14)$$

Where the F_x is the lateral force, which is a result of the lateral stiffness times the lateral deflection of the wrist.

Substitute eq. (5.12) into eq. (5.13)

$$f_3 = \frac{F_x - \mu F_z}{1 - \mu^2} \quad (5.15)$$

Equating eq. (5.14) to the moment where the peg is rotating (centre of rotation, point O),

$$F_z r + F_x l = \left(\frac{F_x - \mu F_z}{1 - \mu^2} \right) (l + \mu r) \quad (5.16)$$

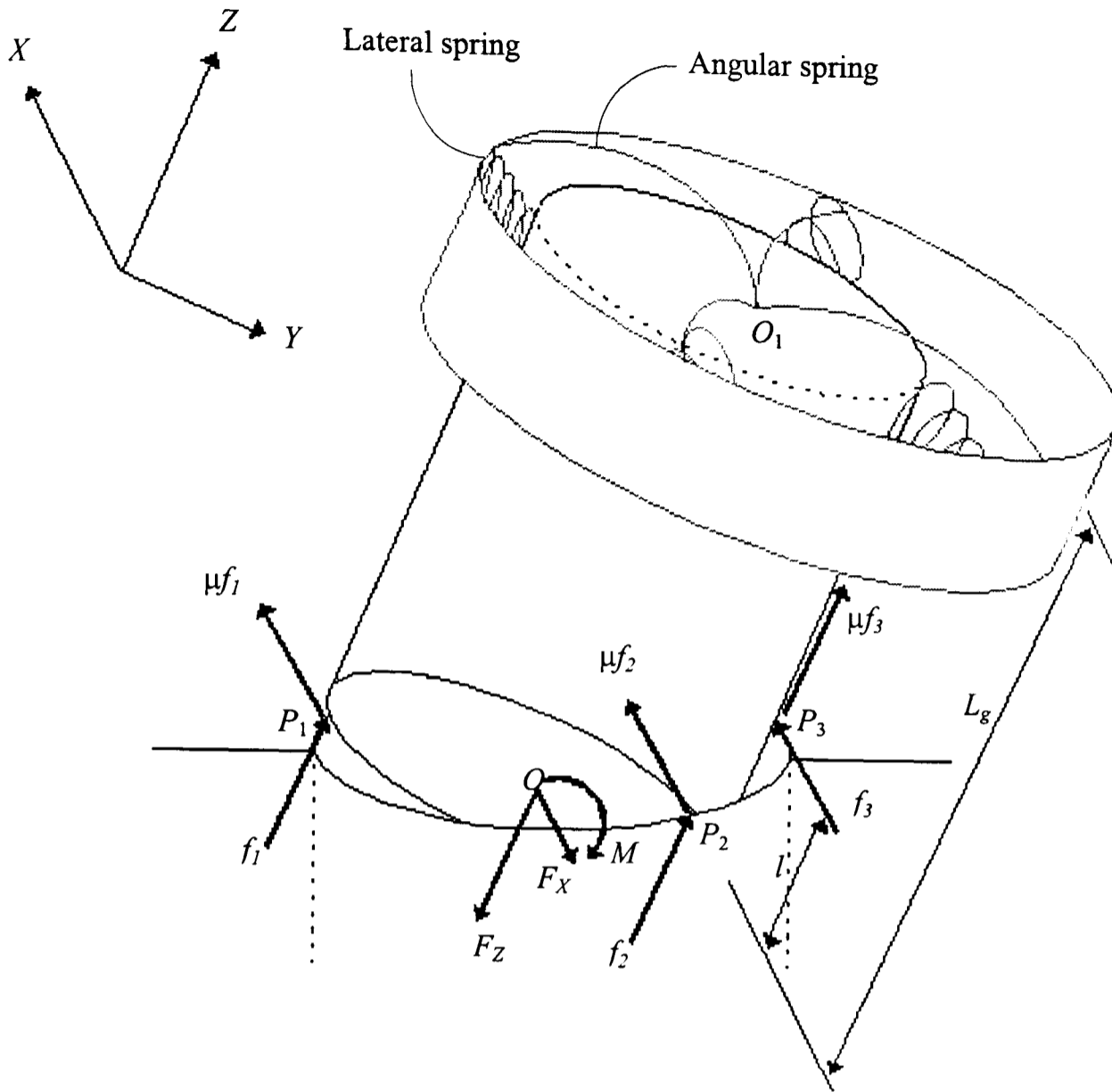


Figure 5.7 Schematic of peg-wrist during 3 POC

Eq. (5.16) yields the relation between the insertion and the lateral forces:

$$\frac{F_x}{F_z} = \frac{1}{\mu} \quad (5.17)$$

Considering both the compliant wrist and the inserted peg as one object during 3 POC (figure 5.7), the moment in the wrist is equal to the moment anywhere on the peg.

Now, to find the optimum stiffness (ideal) that will enable the wrist to overcome the 3 POC mode, equating the moment at the wrist to that at the third contact point between the peg and the hole, then

$$K_x(e_{x_0} - e_x)L_g - K_\theta(\theta - \theta_0) = F_z r + F_x l \quad (5.18)$$

Where L_g is the centre of rotation or the distance from the wrist to the point in space where the peg rotates. Also,

$$K_X(e_{x_0} - e_x) = -F_X \quad (5.19)$$

Substitute eq. (5.17 & 5.19) into eq. (5.18)

$$\begin{aligned} -|K_g| &= \frac{\frac{F_Z}{\mu}(L_g + \mu r + l)}{\vartheta - \vartheta_0} \quad \text{or} \\ -|K_g| &= \frac{F_X(L_g + \mu r + l)}{\delta \vartheta} \end{aligned} \quad (5.20)$$

Where $\delta \vartheta = \vartheta - \vartheta_0$

The ideal lateral wrist stiffness, can be found from the relation (eq. 5.19)

$$\begin{aligned} K_X &= \frac{-F_X}{\delta e_x} \quad \text{or} \\ K_X &= \frac{-\frac{F_Z}{\mu}}{\delta e_x} = -\frac{F_Z}{\mu \delta e_x} \end{aligned} \quad (5.21)$$

Where $\delta e_x = e_{x_0} - e_x$; Both equations (5.20 & 5.21) give the ideal wrist stiffness to overcome the 3 POC mode. Note that the δe_x and the $\delta \vartheta$ are correspond to those displacements of the peg and they are equal.

5.4.3 Peg Is Inside The Hole: The Conditions For Successful Assembly

Once the wrist-peg overcome the 3 POC mode, the peg will either slide in or will contact the hole in one/two-point, which may cause jamming or wedging occurrence, if jamming/wedging avoidance conditions are not met.

Jamming, defined as a condition in which the peg will not move during insertion action, because the forces and moments applied to them through the supports are in the wrong proportions.

Geometrically [S. Simunovic, 1975 & 1979] this will happen when the applied force by the insertion device is inside the friction cone (refer to figure 5.1 & 5.2). Consequently jamming could occur during both one and two point contact (at least in theory). To overcome jamming, the direction of the insertion force must be changed so that the resultant force can lie outside the friction cone. This is achieved by removing the peg from the hole and changing its orientation and then to reinsert it into the hole.

Wedging is a condition in which the reaction forces are inside their friction cones and acting along the same line and thus movement can not occur. Wedging is worse than jamming because removal of the insertion force will not remove the reaction forces. Unlike jamming, the cause is geometric rather than ill-proportioned forces. Wedging occurs when the insertion depth (during two-point contact) is smaller than the coefficient of friction times the peg diameter. Also, the tilt angle should be smaller than the ratio clearance over coefficient of friction.

Now, to determine whether an assembly will succeed or fail, it is necessary to consider the forces acting on the mating parts. Also, it is assumed that the friction is consistent all over between the peg and the hole. In figure (5.8), the peg is in equilibrium and slides down the hole in a uniform velocity, it is assumed that the angle of tilt between the peg and the hole is zero. The possible contact modes shown in figure (5.8) could be any of those of table 5.2. As shown in chapter (4) section (4.3 & 4.4), once the peg is inside the hole then the problem can be treated as 2D rather than 3D, therefore from now on the analysis is 2D.

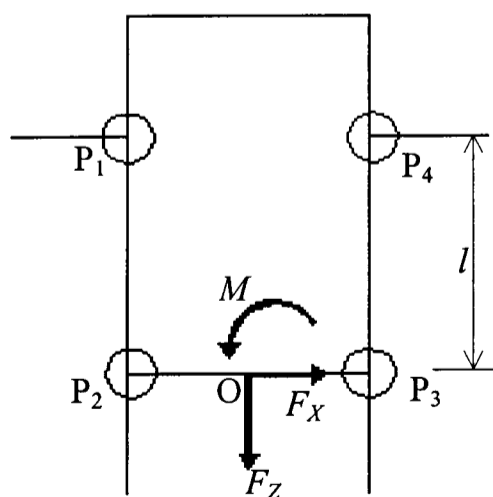


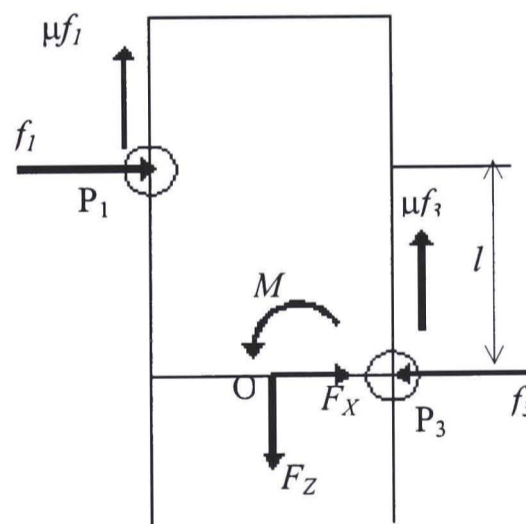
Figure 5.8 Peg is inside the hole and tilt angle is zero

Table 5.2 Possible contact modes

One-point Contact	Two-point Contact	Line Contact
P ₁	P ₁ & P ₂	P ₁ & P ₂
P ₂	P ₄ & P ₃	P ₄ & P ₃
P ₃	P ₁ & P ₃	
P ₄	P ₄ & P ₂	
		P ₁ & P ₂ & P ₄ & P ₃

Where P₁, P₂, P₃ and P₄ are points of contact. In this analysis, situation of P₁ & P₂ & P₄ & P₃ will not be dealt with because it is a surface contact (interference fit) which occurs when the peg is completely inside the hole or with the completion of a successful assembly process.

Starting with two-point contact, then the equilibrium equations that describe the peg sliding in during P₁ & P₃ (figure 5.9) are then given by,

Figure 5.9 Peg in two-point contact ($\vartheta = 0$)

$$\begin{aligned}
 F_x &= f_3 - f_1 \\
 F_z &= \mu(f_1 + f_3) \\
 M_O &= f_1 l - \mu r(f_3 - f_1)
 \end{aligned}
 \tag{5.22}$$

solving eq. (5.22) will result in

$$\frac{M}{rF_z} = \frac{l}{2r\mu} - \frac{F_x}{F_z} \left(\frac{l}{2r} + \mu \right) \quad (5.23)$$

So far the tilt angle has been ignored ($\vartheta = 0$). But if the tilt angle is not zero, then as in figure (5.10) the X-Z axes is tilted by ϑ , and the rotational displacement of the peg is denoted by (s), which the peg makes with respect to the hole, in radians it is $s = \vartheta r$. Theoretically, point (O) in figure (5.10 & 5.9) will remain in the same position even after the tilt (Centre of rotation is at the peg tip.). Therefore the change in the moment about point (O) can be expressed in terms of s and ϑ in place of r then put $r = \frac{s}{\vartheta}$ into eq. (5.23),

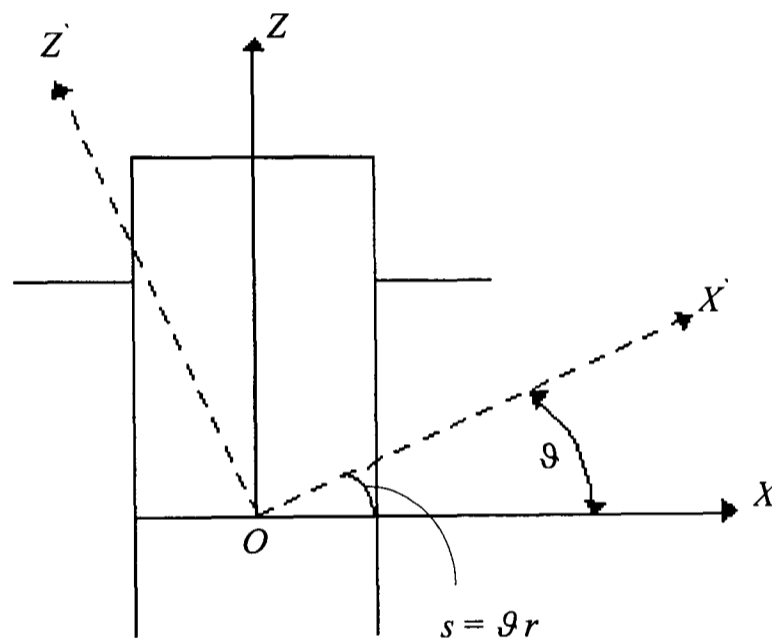


Figure 5.10 Centre axis of the peg is tilted by ϑ

$$\begin{aligned} \frac{M\vartheta}{sF_z} &= \frac{\vartheta l}{2s\mu} - \frac{F_x}{F_z} \left(\frac{\vartheta l}{2s} + \mu \right) \\ \frac{M\vartheta}{F_z} &= \frac{\vartheta l}{2\mu} - \frac{F_x}{F_z} \times \frac{\vartheta l}{2} - \frac{F_x}{F_z} \times \mu s \\ \frac{M\vartheta}{F_z} &= \frac{l\vartheta}{2\mu} - \frac{F_x}{F_z} \left(\frac{l\vartheta}{2} + \frac{\mu s}{1} \right) \end{aligned} \quad (5.24)$$

Define

$$\lambda = \frac{l\vartheta}{2\mu} \quad (5.25)$$

then eq. (5.24) can be expressed as

$$y = mx + b \quad (5.26)$$

that is a straight line, where

$$\begin{aligned} y &= \frac{M\theta}{F_z} \\ x &= \frac{F_x}{F_z} \\ m &= -\mu(\lambda + s) \\ b &= \lambda \quad \text{and if the peg was tilted to the other side then} \\ b &= -\lambda \end{aligned} \quad (5.27)$$

To finish the derivation one must consider all the possible contact modes, half of which will suffice for illustration. Note, all of the moments have been taken about the centre of the peg tip if not otherwise stated. For figure (5.11) contact mode P₁ & P₂,

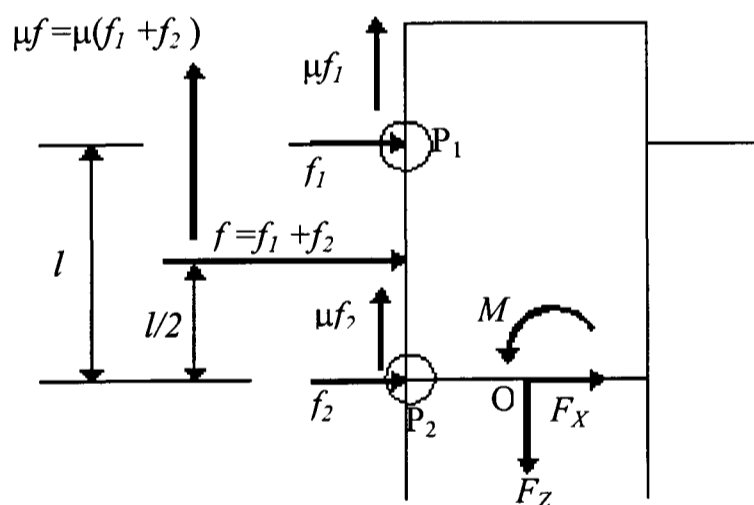


Figure 5.11 Peg is in line contact with the hole

the equilibrium equations are

$$\begin{aligned} F_x &= -f \\ F_z &= \mu f = -\mu F_x \\ \frac{F_x}{F_z} &= -\frac{1}{\mu} \end{aligned} \quad (5.28)$$

and

$$M = f \left(\frac{l}{2} + \mu r \right) = -F_x \left(\frac{l}{2} + \mu r \right) \quad (5.29)$$

When tilting the peg by ϑ , the line contact between the peg and the hole becomes one-point contact either P_1 or P_2 , which depends upon the direction of the tilt. In eq. (5.29), the insertion depth $l/2$ becomes l , and put $r = \frac{s}{\vartheta}$ into eq. (5.29)

$$\begin{aligned} M &= -F_x \left(l + \mu \times \frac{s}{\vartheta} \right) \\ \frac{M\vartheta}{F_z} &= -\frac{F_x}{F_z} \times \vartheta \left(l + \mu \times \frac{s}{\vartheta} \right) \\ \frac{M\vartheta}{F_z} &= +\frac{1}{\mu} (l\vartheta + \mu s) \\ \frac{M\vartheta}{F_z} &= 2\lambda + s \end{aligned} \quad (5.30)$$

and for the other side of the peg (P_3 & P_4), one should get

$$\begin{aligned} \frac{F_x}{F_z} &= \frac{1}{\mu} \quad \text{and} \\ \frac{M\vartheta}{F_z} &= -(2\lambda + s) \end{aligned} \quad (5.31)$$

The one-point contact mode (P_1); in figure (5.12)

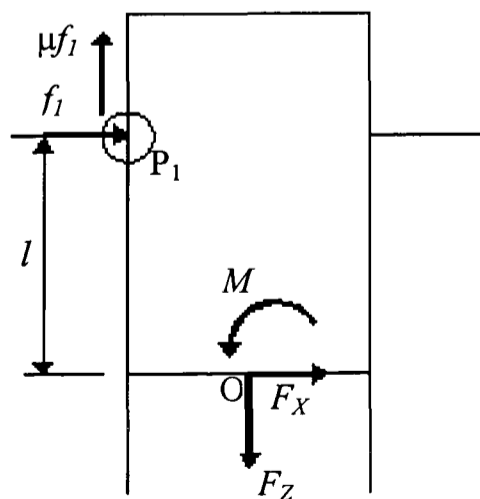


Figure 5.12 Peg is in one-point contact

the equilibrium equations are:

$$\begin{aligned} F_x &= -f_1 \\ F_z &= \mu f_1 = -\mu F_x \\ \frac{F_x}{F_z} &= -\frac{1}{\mu} \end{aligned} \quad (5.32)$$

and

$$M = f_1(l + \mu r) = -F_x(l + \mu r) \quad (5.33)$$

When tilting the peg by ϑ , then substitute $r = \frac{s}{\vartheta}$ into eq. (5.33)

$$\begin{aligned} M &= -F_x \left(l + \mu \times \frac{s}{\vartheta} \right) \\ \frac{M\vartheta}{F_z} &= -\frac{F_x}{F_z} \times \frac{l\vartheta}{1} - \frac{F_x}{F_z} \times \frac{\vartheta \mu s}{\vartheta} \\ \frac{M\vartheta}{F_z} &= -\frac{F_x}{F_z} (l\vartheta + \mu s) \\ \frac{M\vartheta}{F_z} &= \frac{1}{\mu} (l\vartheta + \mu s) \\ \frac{M\vartheta}{F_z} &= \frac{l\vartheta}{\mu} + s \\ \frac{M\vartheta}{F_z} &= 2\lambda + s \end{aligned} \quad (5.34)$$

and for the other one-point contact (P₄), one should get

$$\begin{aligned} \frac{F_x}{F_z} &= \frac{1}{\mu} \quad \text{and} \\ \frac{M\vartheta}{F_z} &= -(2\lambda + s) \end{aligned} \quad (5.35)$$

For the bottom one-point contact (P₂) of figure (5.13),

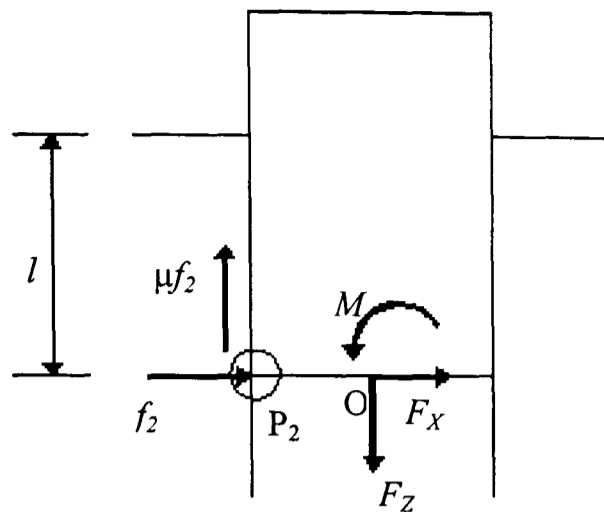


Figure 5.13 Peg is in one-point contact from the bottom

the equilibrium equations are

$$\begin{aligned} F_x &= -f_2 \\ F_z &= \mu f_2 = -\mu F_x \\ \frac{F_x}{F_z} &= -\frac{1}{\mu} \end{aligned} \quad (5.36)$$

and

$$M = \mu f_2 r = -\mu r F_x \quad (5.37)$$

when tilting the peg by ϑ , then substitute $r = \frac{s}{\vartheta}$ into eq. (5.37)

$$\begin{aligned} M &= -\mu \frac{s}{\vartheta} F_x \\ \frac{M\vartheta}{F_z} &= -\mu s \times \frac{F_x}{F_z} \\ \frac{M\vartheta}{F_z} &= s \end{aligned} \quad (5.38)$$

and for the other one-point contact (P_3), one should get

$$\begin{aligned} \frac{F_x}{F_z} &= \frac{1}{\mu} \quad \text{and} \\ \frac{M\vartheta}{F_z} &= -s \end{aligned} \quad (5.39)$$

The results of this analysis are summarised in figure (5.14). The jamming parallelogram (figure 5.14) may be interpreted as follows, combination of F_X , F_Z and M falling on the parallelogram's edges describe equilibrium sliding in. Outside the parallelogram lie combination which jam the peg either in one (which is unlikely to happen during assembly operation) or two-point contact. Inside the parallelogram, the peg is in disequilibrium sliding or falling in. Note that the vertical dotted lines (points P_1 & P_2 , P_3 & P_4) describe a line contact.

Also, as λ approaches zero, that is, the insertion depth is small compared to the radius of the peg, the parallelogram collapses to a line from $1/\mu$, $-s$ on the right to $-1/\mu$, s on the left. Thus the initiation of two-point contact, the no-jam region is quite small, and the possibility of jamming is high. Jamming is most likely to occur during insertion tasks with very small tolerances, because the smaller the tolerances, the smaller the insertion depth at which two-point contact occurs.

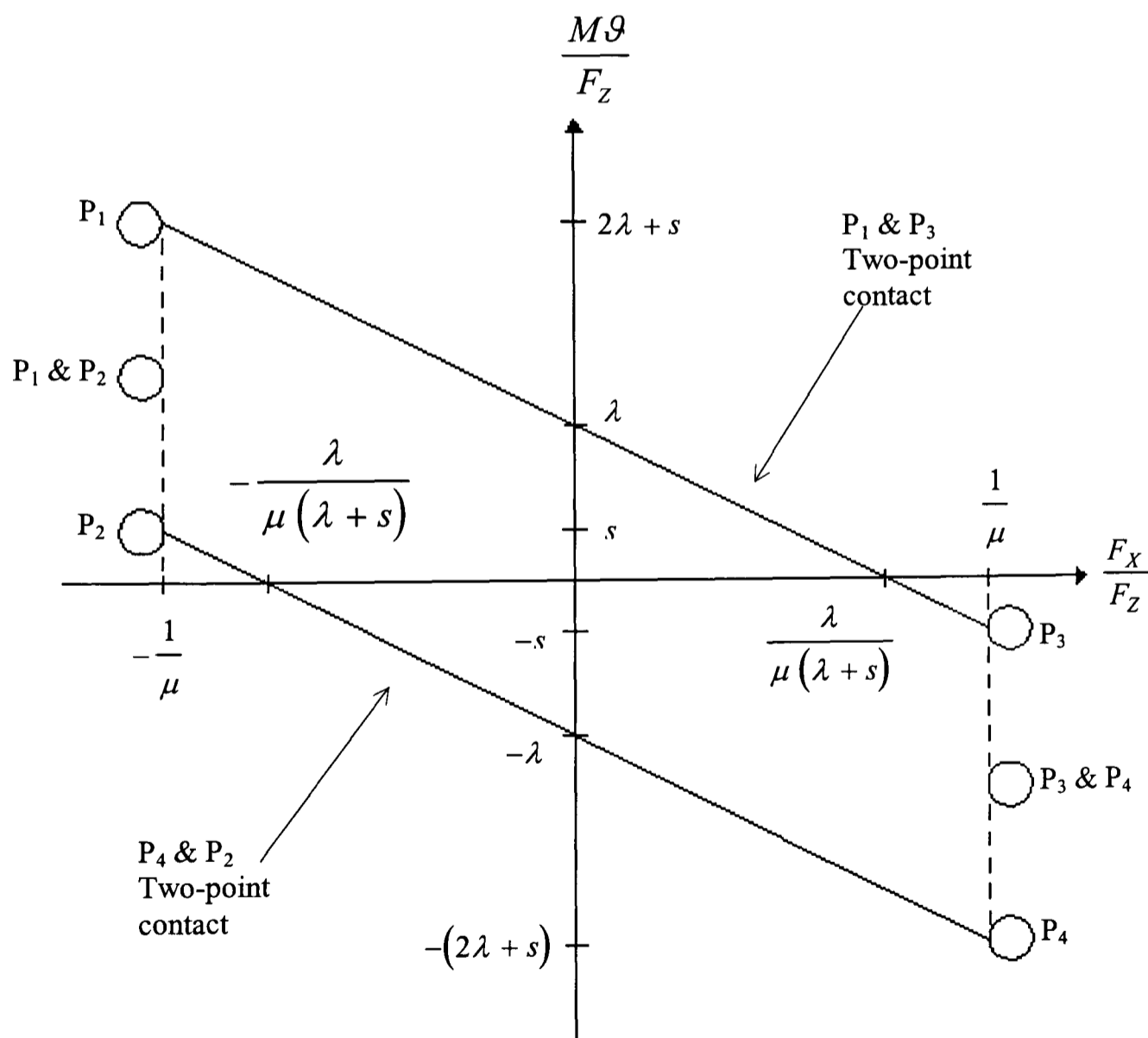


Figure 5.14 The jamming diagram [after Whitney, 1986]

5.5 THE INSERTION FORCE DURING ONE/TWO-POINT CONTACT

The applied/insertion force during the assembly process assumed to be zero when no contact between the peg and the hole. For one-point contact, earlier it was found that during sliding mode of the peg the relation between the lateral and the insertion force is

$\frac{F_x}{F_z} \leq \frac{1}{\mu}$, and from eq. (5.33) for one-point contact the lateral force is given by

$$F_x = -\frac{M}{l + \mu r} \quad (5.40)$$

The moment inside the wrist is the same as that about the contact point/s between the peg and the hole ($M = K_x \delta e_x L_g - K_g \delta \vartheta$); Combining these relations will give

$$F_{z1} = -\mu \left(\frac{K_x \delta e_x L_g - K_g \delta \vartheta}{l + \mu r} \right) \quad (5.41)$$

Also, during two-point contact the previous relations are still valid, therefore putting these relations into eq. (5.23) for two-point contact, one should obtain

$$F_{z2} = -\frac{K_x \delta e_x L_g - K_g \delta \vartheta}{r} \quad (5.42)$$

However, in ideal conditions the $L_g = 0$, because as mentioned earlier RCC's devices tempt to locate their support point at the tip of the peg (point O, in figures 5.7-5.13), then eq. (5.47 & 5.48) will become

$$F_{z1} = \frac{\mu K_g \delta \vartheta}{l + \mu r} \quad (5.43)$$

and

$$F_{z2} = \frac{K_g \delta \vartheta}{r} \quad (5.44)$$

Both equations may be interpreted thus; the larger the angular misalignment, the larger insertion force is needed and vice versa.

5.6 WRIST KINEMATICS

Since the wrist movement is restricted to one plane, it has 2 degrees of freedom, laterally and angularly. To understand the kinematics of the wrist, it is modelled in 2D space shown in figure (5.15) (refer to CVHRCC assembly drawing number 11 in appendix 3).

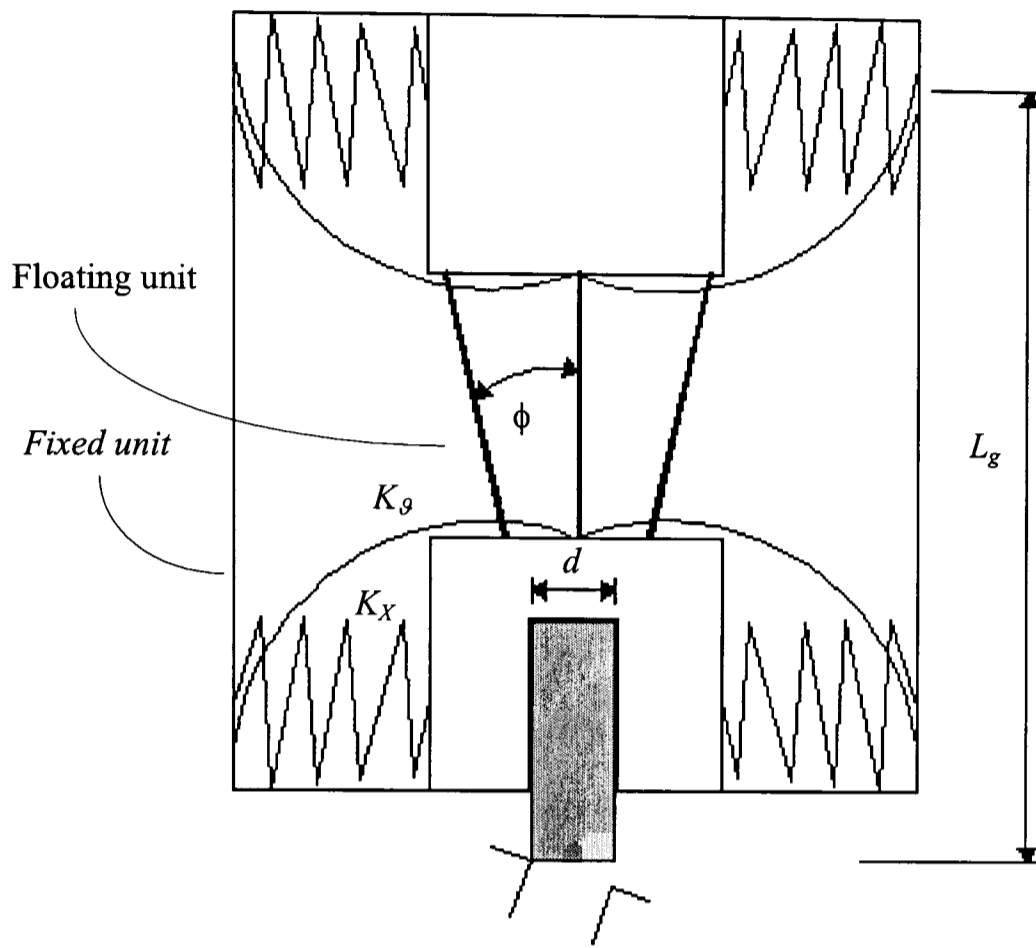


Figure 5.15 The wrist model in 2D space

As shown in figure (5.15), the springs represent the rubber that provides the lateral and angular deformations. Also in figure (5.15), it can be seen that the wrist has two main units, the fixed and the floating units. The movements of the wrist are achieved by the lateral and angular deflection of the floating unit. To realise the kinematics of the wrist, the parameters e_x , ϑ and d has to be derived from the wrist other features such as K_x , K_θ , L_g and ϕ . In this chapter the peg diameter is to be determined, other parameters will be dealt with in the next chapter. The peg diameter that fits inside the wrist can be determined in 2 different ways:

1. Dynamically, in terms of peg mass and spring stiffnesses etc.
2. Geometrically, in terms of jamming avoidance.

5.6.1 Peg Diameter From Dynamic Considerations

In the first case, look at figure (5.16), the peg is assumed to be supported laterally.

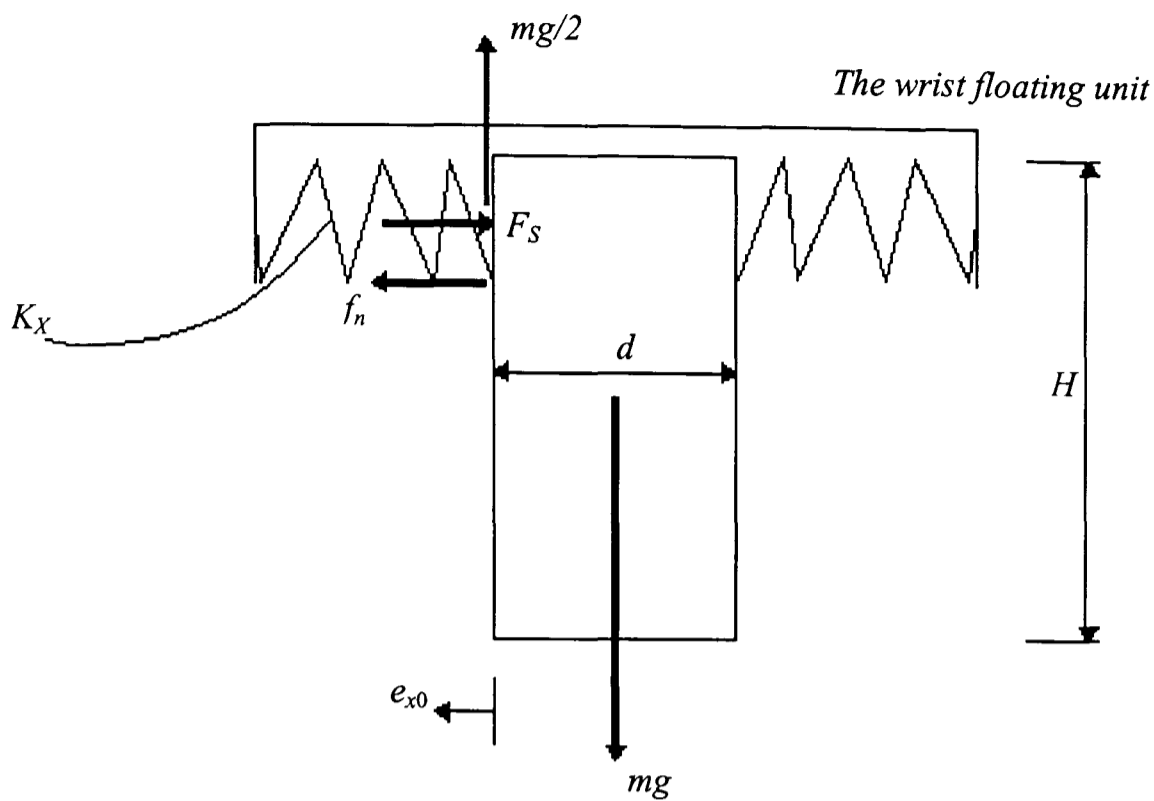


Figure 5.16 Peg is sitting inside the wrist

In figure (5.16), e_{x0} is the spring initial deformation, which is due to the peg mass and diameter. The equilibrium equation that describe the peg inside the wrist is:

$$K_x e_{x0} = f_n \quad (5.45)$$

since

$$f_n = \frac{mg}{2\mu} \quad (5.46)$$

then put eq. (5.46) into eq. (5.45)

$$K_x e_{x0} = \frac{mg}{2\mu} \quad (5.47)$$

Also, the mass is equal to the density times the peg volume

$$m = \rho V \quad (5.48)$$

substitute eq. (5.48) into eq. (5.47) gives

$$K_x e_{x0} = \rho \times \frac{\pi d^2}{4} \times H \times \frac{g}{2} \times \frac{1}{\mu}$$

$$d = \sqrt{\frac{8 \mu K_x e_{x0}}{\rho \pi H g}} \quad (5.49)$$

and to get the peg diameter in millimetres equation (5.49) can be written as

$$d = \sqrt{\frac{8 \times 10^3 \mu K_x e_{x0}}{10^{-3} \rho \pi H g}} \quad (5.50)$$

Now, equation (5.50) was simulated with different values and presented in figure (5.17). Note, the coefficient of friction between rubber and steel is 1, and the density for steel is $7.85 \times 10^{-3} \text{ Kg/m}^3$, the peg length H is 67 mm , and the lateral stiffness is 1.5 N/mm .

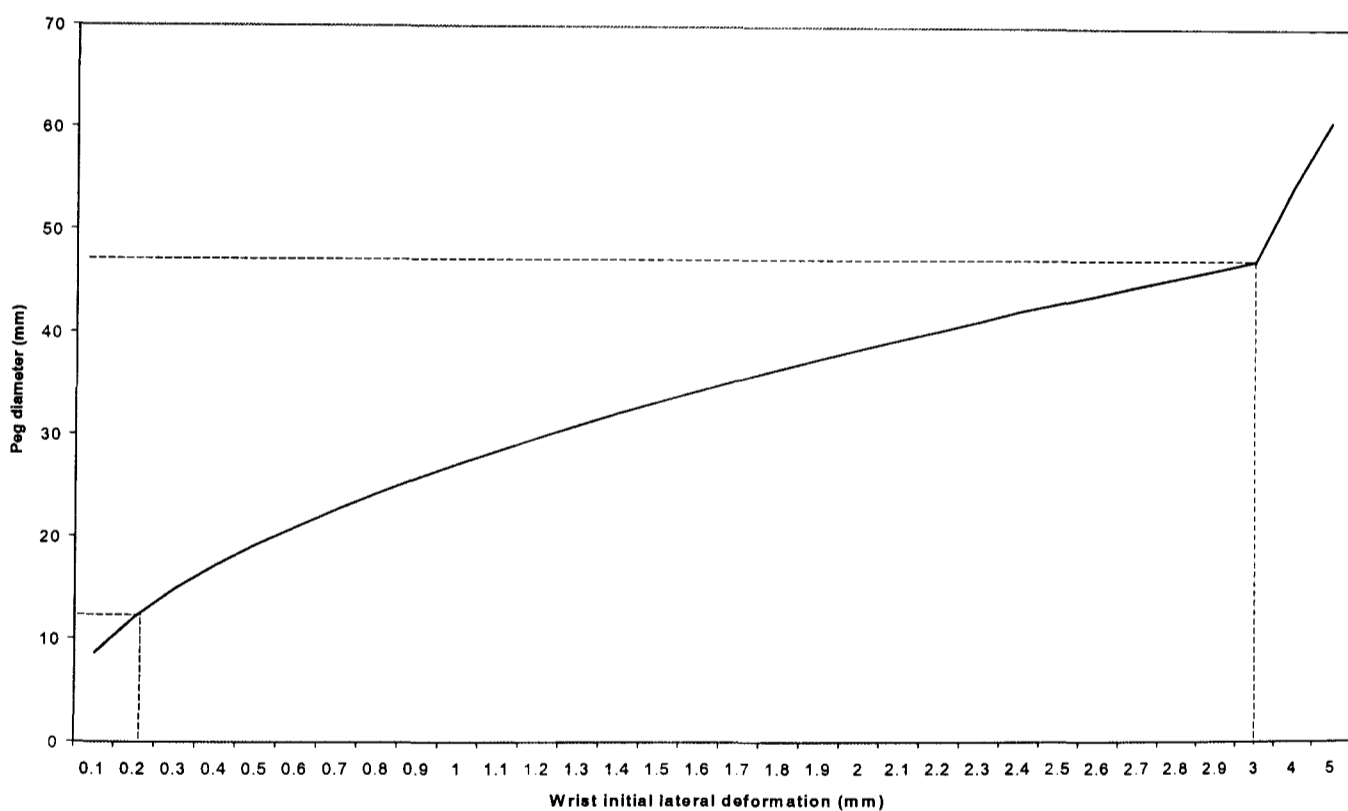


Figure 5.17 Peg diameter versus the wrist initial lateral deformation

In robotic/automated assembly of peg-hole, most passive techniques as well as the CVHRCC are supposed to accommodate up-to 3 mm allowable error (refer to table 2.1 in chapter 2). It is assumed that the actual lateral misalignment between the peg and the hole

is larger than the initial deformation then, in figure (5.17), this corresponds to a peg diameter of over 45 mm. However, technically the wrist can not accommodate a diameter of over 40 mm (see section 5.6.2, and refer to the wrist drawings in appendix 3). Also, the smallest practical allowable error is over 0.2 mm, which corresponds to a peg diameter of over the 10 mm.

5.6.2 Peg Diameter from Geometrical Consideration

In the second case, to determine the peg diameter geometrically; under jamming avoidance conditions the insertion force must lie within the friction cone angle $\pm\phi$. Also, the angular misalignment must be smaller than the friction angle. Look at figure (5.18),

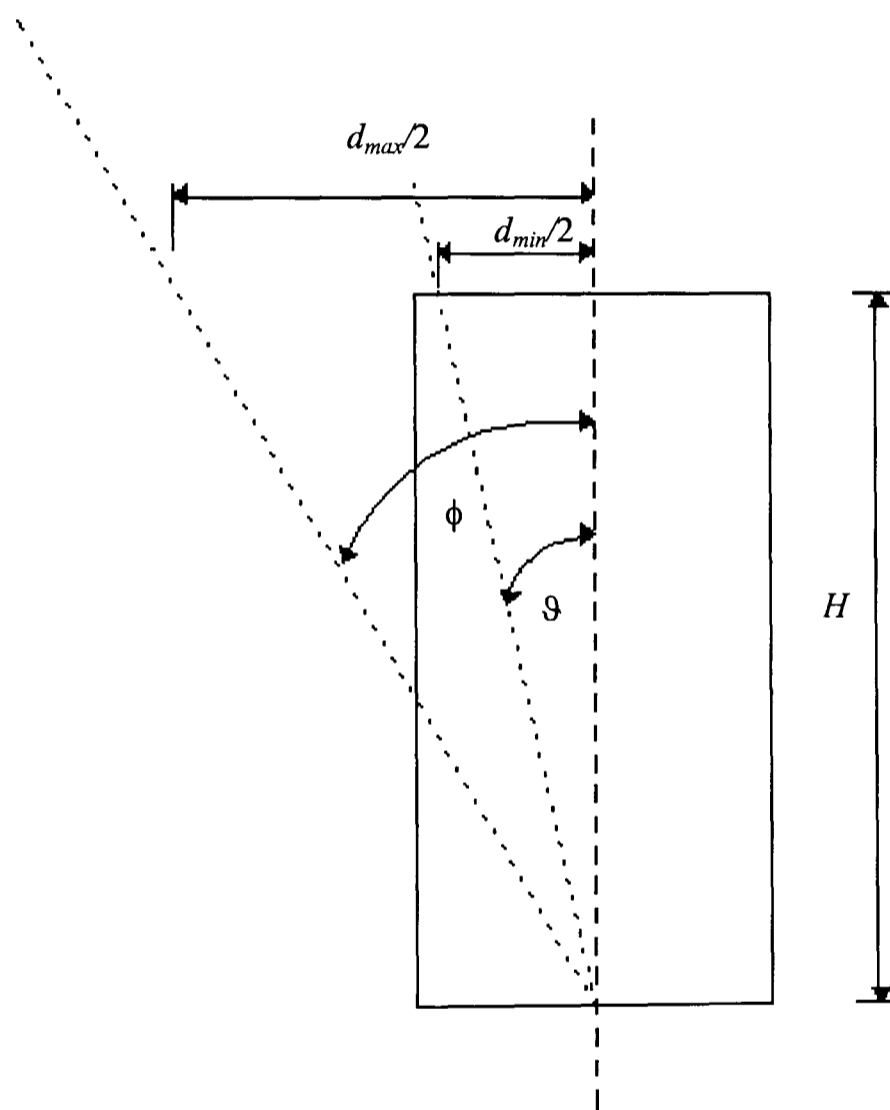


Figure 5.18 Peg geometry

In figure (5.18),

$$\frac{d_{\max}}{2} = H \tan \phi \quad (5.51)$$

and

$$\frac{d_{\min}}{2} = H \tan \vartheta \quad (5.52)$$

In eq. (5.51), the friction angle is 12° , this will give a maximum diameter of over 30 mm . In eq. (5.52), it is normal to have an initial angular misalignment of up-to 5° , this will give a minimum diameter of over 15 mm . Another look at the results of the dynamic calculations of the peg diameter will show small difference between the minimum and maximum diameter in both methods.

Now, to determine the allowable angular deformation of the CVHRCC, look at figure (5.18). Geometrically it can be said that the maximum angular error which the wrist can tolerate is

$$\vartheta_{\max} = \tan^{-1} \left(\frac{d/2}{H} \right) \quad (5.53)$$

Equation (5.53) is plotted with various data and presented in figure (5.19).

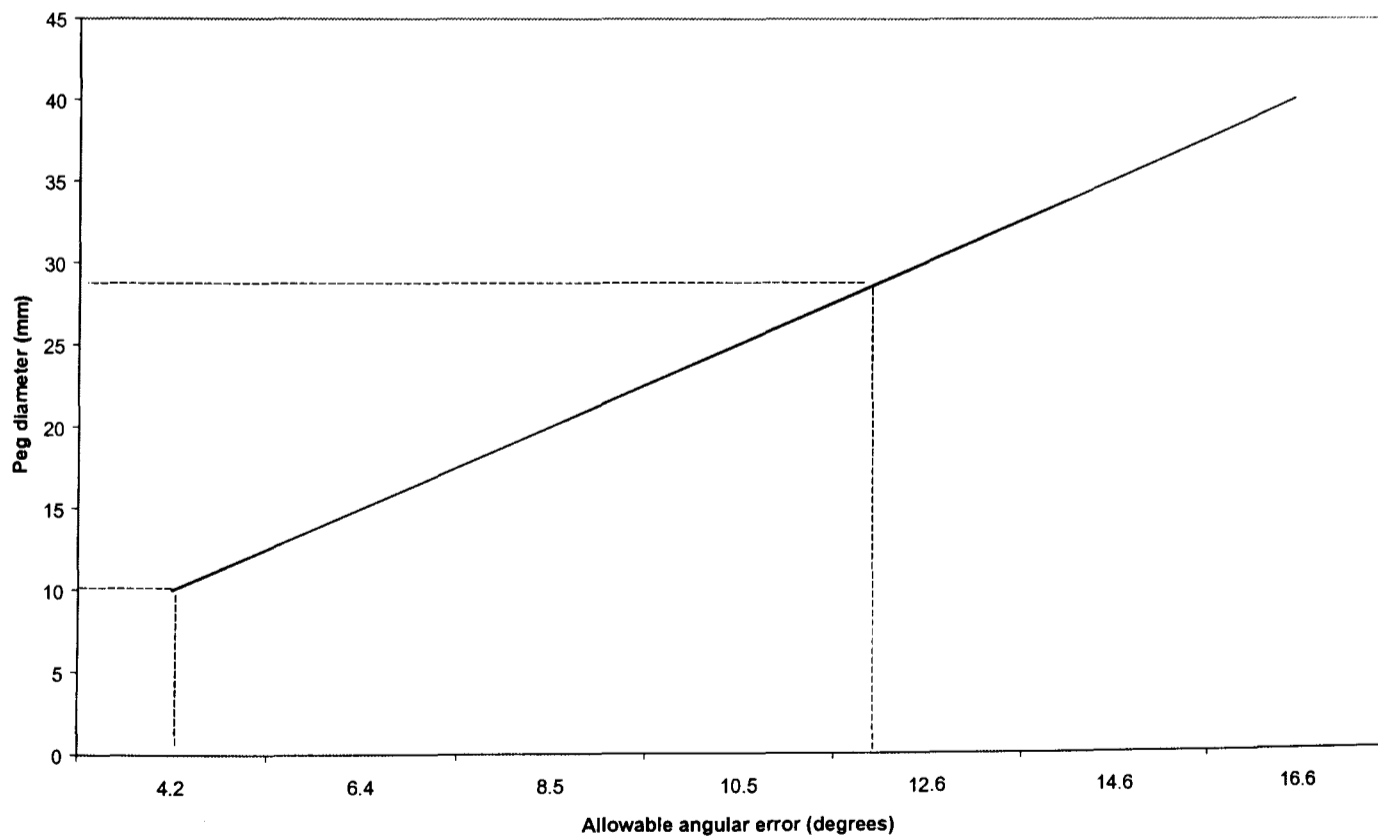


Figure 5.19 Peg diameter versus the wrist angular deformation

Since the allowable error should be less than 12° (refer to the friction angle), in figure (5.19) this corresponds to a peg diameter of less than 30 mm . Note that these results are in terms of the geometrical conditions for jamming avoidance. Also in figure (5.19), it can be seen that for a minimum peg diameter of 10 mm the wrist can accommodate an initial angular misalignment of over 4° .

5.7 DISCUSSION

In this chapter, the dynamic investigation of the chamferless peg-in hole insertion process was detailed and analysed (Note: main discussion will be discussed in chapter 9). The peg approach, and initial contact with the hole in presence of friction and the possible stick-slip occurrence, demonstrated the need for a larger acceleration during the contact than the approach stage, to enable the peg not to stick, but to slip (break contact). To achieve that, two conditions must be met:

1. The tangent of the friction angle has to be smaller than the coefficient of friction.
2. The impulsive force has to be larger than the applied force.

Once the peg gets into the mouth of the hole; 3 POC could occur. Since this is a geometrical relation, it is advisable to have the parameters/variables involved within the prescribed range given in equations (5.8 to 5.11). The reason for that is that RCC devices tend to accommodate angular/lateral errors independently, where the 3POC needs a device with the flexibility to accommodate both errors at the same time (Perhaps a vibrational wrist could achieve this!).

Also, the kinematics results for the wrist movement have shown that the wrist can accept a range of peg diameters from 15 to 35 mm .

5.8 CONCLUSION

The major points of this chapter are as follows:

1. To avoid jamming or sticking, $\tan\phi < \mu$
2. During the initial contact stage between the peg and hole, the following conditions summarise the outcome stage,

$$\mathbf{F}_{imp} - f_r = \mathbf{F}_{net} \quad \text{slipping occur}$$

$$\mathbf{F}_{imp} - f_r = 0 \quad \text{the peg is on the verge of slipping}$$

$$\mathbf{F}_{imp} < f_r \quad \text{the peg will stick}$$

3. To avoid 3 point of contact, the allowable clearance must be $c \geq \frac{(1 - \cos \vartheta)r}{\cos \vartheta}$

4. To avoid jamming during one/two point contact, one must maintain

$$\left| \frac{M\vartheta}{F_z} + \frac{\mu(1 + \lambda)F_x}{F_z} \right| < \lambda \quad \text{and}$$

$$\left| \frac{F_x}{F_z} \right| < \frac{1}{\mu}$$

5. Theoretically, the CVHRCC can accept a range of peg diameters from 15 *mm* to 35 *mm*.

CHAPTER 6

PEG-HOLE MODELLING AND SIMULATION

6.1 INTRODUCTION

In previous chapters, the chamferless peg-hole insertion process was discussed and analysed geometrically and dynamically. The geometric and dynamic equations that were derived to establish the successful conditions for the insertion process are to be validated in this chapter. Rossitza Setchi and Bratanov [R. Setchi et al, 1998] have suggested a 3D simulation programme for the peg-in hole insertion process. The approach considers the insertion process as a sequence of discrete events, and models the process as a transition from one contact situation to another. Rossitza Setchi et al claim that this simulation is a tool for developing insertion strategies and devices for a specific application such as chamferless mating parts. However, throughout the modelling stages it was assumed that the inserted peg is supported by a compliant wrist device (RCC). This assumption contradicts the fact that RCC devices cannot accommodate positional errors between chamferless mating parts [D Whitney et al, 1979].

In this chapter, the objective of the modelling and simulation is to validate a new assembly strategy of a chamferless peg-in hole process for prescribed positional misalignments, for given system features, such as applied forces, moments, wrist stiffness and dimensions of the mating parts. A further objective is to examine the behaviour of the assembly system (wrist-peg-hole) by using different values of friction, clearances and stiffnesses. Also, this simulation could be used as a tool for future assembly-systems design.

It is assumed that the insertion process is subject to a mixture of viscous and friction damping. The viscous effect is negligible for there is little air resistance on the insertion process. In this chapter, the friction is assumed to be constant.

The structure of this chapter is as follows:

Section 6.2 is a background for the modelling-simulation process.

Section 6.3 modelling each sub-process of the insertion process individually.

Section 6.4 the simulation process

Section 6.5 conclusion

The software used to simulate the peg-hole insertion process is Matlab (Simulink). The simulation results have demonstrated the insertion process and revealed the wrist stiffness and the initial positional misalignment region, which allows the wrist to overcome such errors.

6.2 BACKGROUND

In this model the insertion process is treated as 3D problem until the peg enters the hole (one/two-point contact), where the contact between the peg and the hole occurs just in one plane reducing the problem to 2D space. Also, note that the co-ordinate axes system of the peg and that of the hole are in the same plane. Now, the insertion process is divided into sub-processes, where each sub-process occurs independently. In some of the sub-processes, the input is the output of the previous process.

The concept of the modelling system is shown in figure (6.1), where the input is a pressure force provided by the piston, or the torque generated by the reaction forces. The system is the wrist or springs and the peg, and the output is the final peg position in each sub-process.

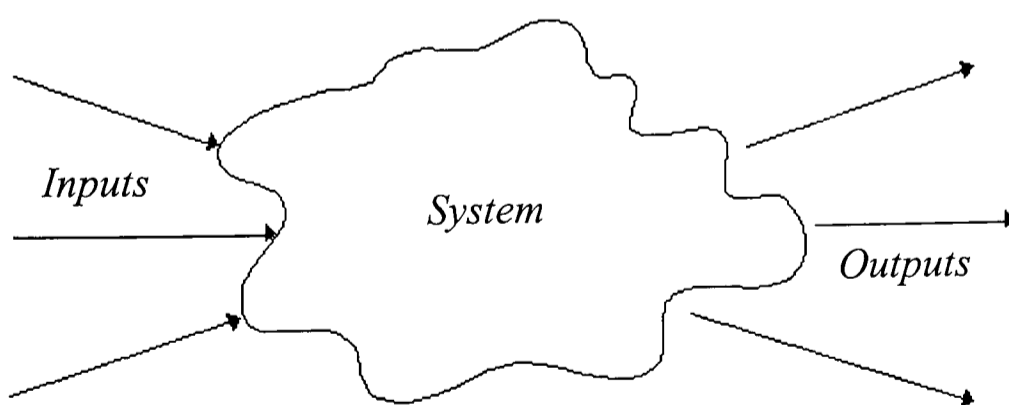


Figure 6.1 Concept of a system

Figure (6.2) shows a simulation block diagram for the insertion process. The pneumatic piston applies a constant force that drives the peg downward. If there is misalignment, reaction forces will arise and cause the springs to deflect. This deflection is fed to the

summing point in the form of a reaction force to accommodate the misalignment. The process is repeated until the peg is completely inside the hole.

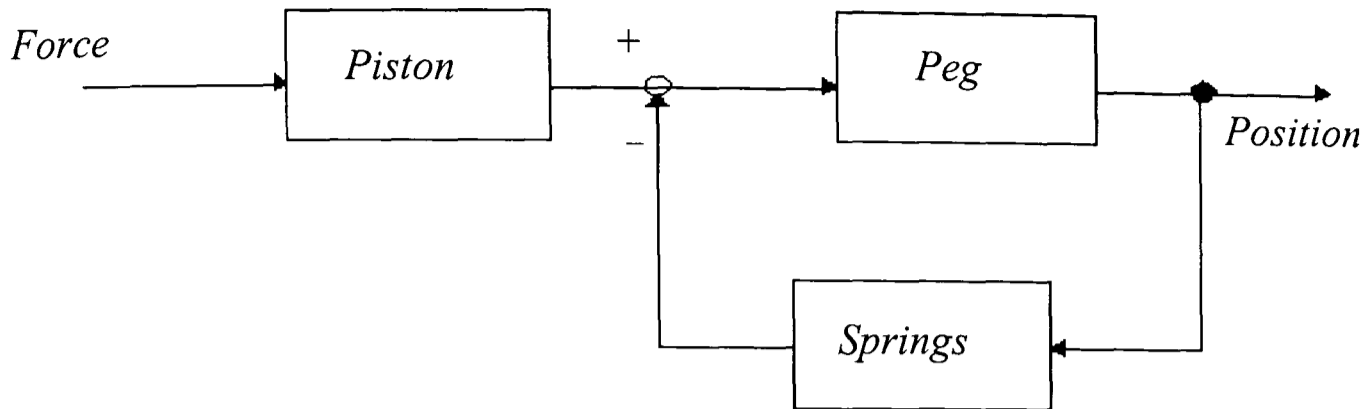


Figure 6.2 General block diagram of the insertion process

In figure (6.3), the springs represent the compliant wrist. So, note that since the peg and the wrist moves as one object (there is no relative movement between the peg and wrist), and the mass of the peg is negligible compared to that of the wrist, the moment of inertia used in this analysis is for the wrist.

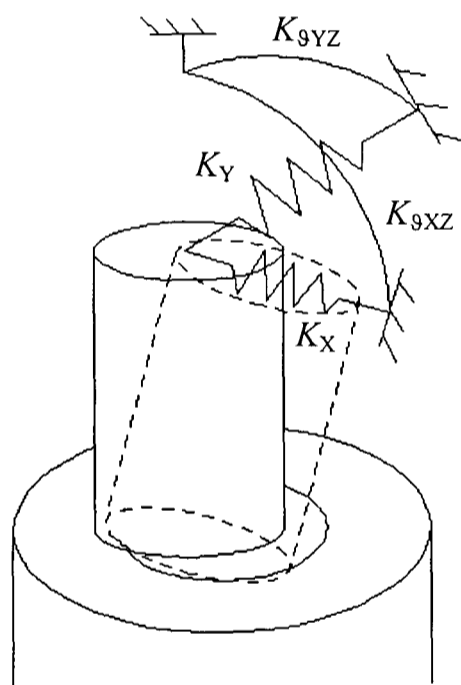


Figure 6.3 Representation of peg-wrist during peg-in hole initial contact

6.3 MODELLING STAGES

In this section, the insertion process is divided into 5 sub-processes:

- 6.3.1 Approach stage (no positional errors between the mating parts).
- 6.3.2 Initial contact between the peg and the top surface of the mating part (angular error).
- 6.3.3 Transition stage where the peg moves to the far side of the hole.
- 6.3.4 Peg moves from one-point of contact with the hole to two-point of contact.

6.3.5 Alignment stage where the peg breaks the two-point of contact and slides down the hole.

6.3.1 Approach Stage

As shown in figure (6.4), it is assumed that the peg is above the hole and there is no positional misalignment.

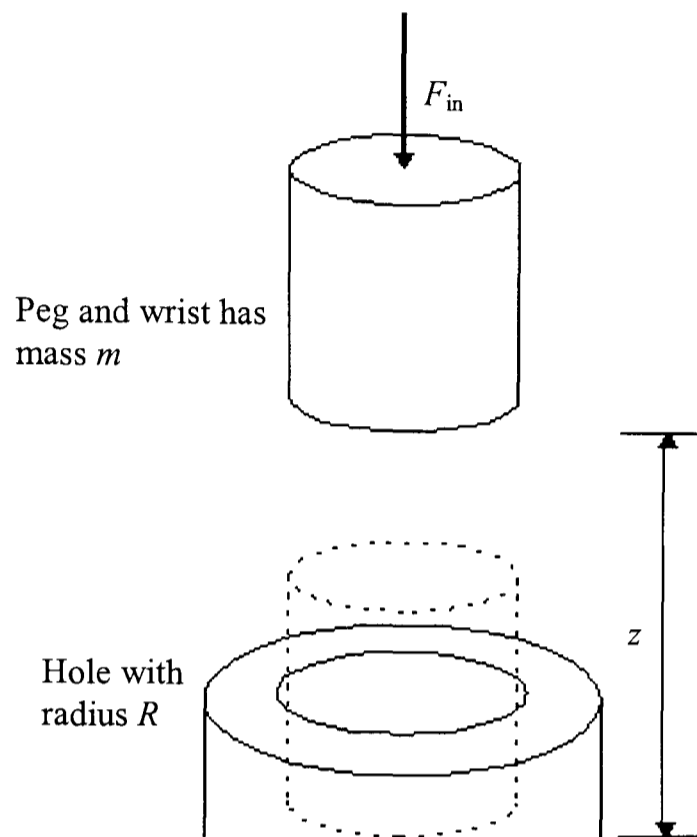


Figure 6.4 A one-stage insertion process (no misalignments)

Output z is the distance the peg has to travel to get into the hole. This stage is described by the differential equation:

$$F_{in(t)} = m \frac{d^2 z}{dt^2} \quad (6.1)$$

To find the output z , eq. (6.1) can be expressed in the s-domain, for zero initial condition yielding:

$$F_{in(s)} = ms^2 Z_{(s)} \quad (6.2)$$

$$Z_{(s)} = F_{in(s)} \frac{1}{ms^2}$$

The simulation block diagram that describes this insertion process is shown in figure (6.5).

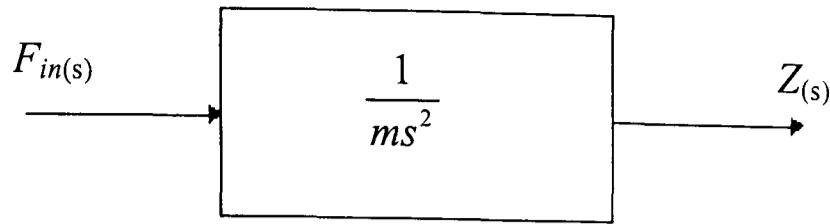


Figure 6.5 A simulation block diagram for peg-hole (no misalignments)

On the other hand, when there is an initial lateral misalignment between the peg and the hole, it will result in a reaction force during the initial contact, which causes either of the springs $K_{\theta XZ}$ or $K_{\theta YZ}$ to compress (see figure 6.3). The output z will be the vertical distance from the bottom surface of the peg to the upper surface of the hole.

6.3.2 Initial Contact

Looking back at figure (6.3), during the initial contact between the peg and the hole the reaction force generates a torque that tilts the peg into the mouth of the hole. Note that in 3D space, during contact between the bottom of the peg and the upper surface of the hole, the springs will react in one plane either the X-Z or the Y-Z plane, despite the fact that the system has 4 degrees of freedom (2 transitional and 2 rotational). Also in figure (6.3), the lateral springs have lateral stiffness of K_X and K_Y which are equal, and angular stiffness of $K_{\theta XZ}$ and $K_{\theta YZ}$ which are also equal. Note that in this sub-process only one angular spring provides the torque to tilt the peg, either $K_{\theta XZ}$ or $K_{\theta YZ}$. Also, their angular deflection is in the same plane and direction.

The free body diagram (FBD) of the peg during this stage is shown in figure (6.6).

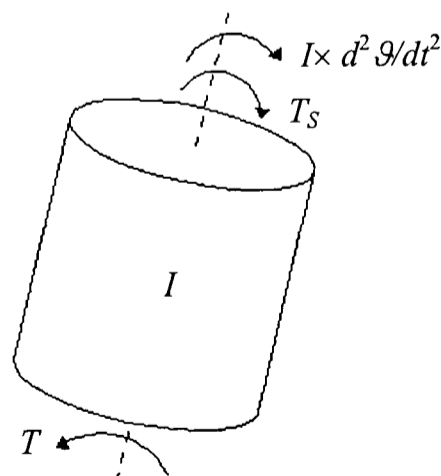


Figure 6.6 Reaction torque acting on the FBD of the peg during two-point contact

The dynamic differential equation of Newton's 2nd law that describes this sub-process is,

$$T_{(t)} = I \frac{d^2 \mathcal{G}}{dt^2} + K_{\mathcal{G}XZ} \mathcal{G}$$

$$T_{(t)} = I \frac{d^2 \mathcal{G}}{dt^2} + K_{\mathcal{G}} \mathcal{G} \quad \text{since } K_{\mathcal{G}XZ} = K_{\mathcal{G}YZ}, \text{ they are denoted by } K_{\mathcal{G}} \quad (6.3)$$

The output \mathcal{G} is the angular deflection of the springs, which corresponds to the angular tilt of the peg. $d^2 \mathcal{G}/dt^2$ is the angular acceleration, and I is peg/wrist moment of the inertia about either X or Y axis, and it was determined experimentally (see appendix 1). T is the reaction torque at the contact points between the peg and the hole. In figure (6.7), e is the lateral distance between the centre of the peg to the contact points.

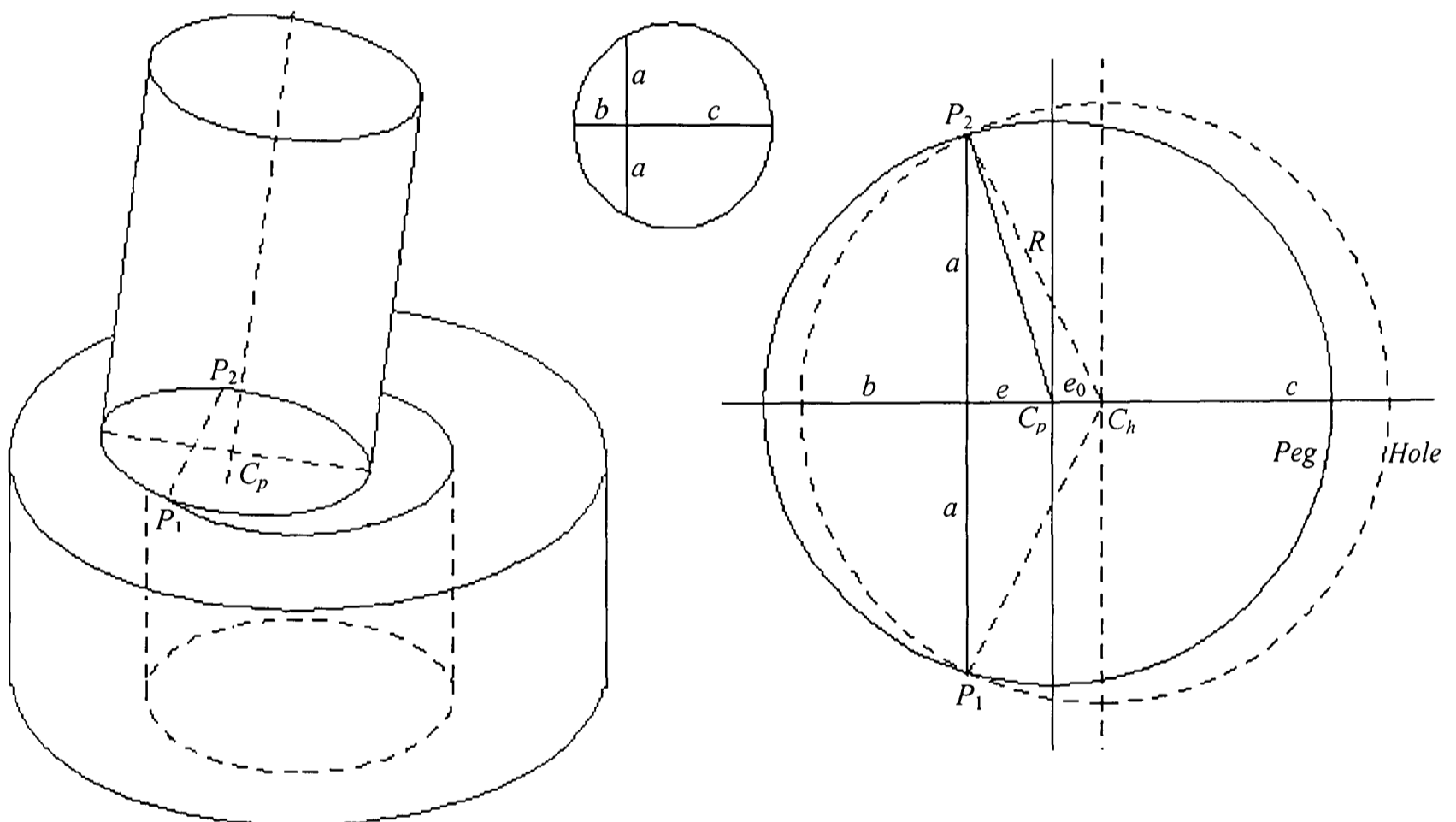


Figure 6.7 The peg in two point contact with the hole during the initial contact stage

In figure (6.7, the peg circle) there are the followings relations:

$$\begin{aligned}
a^2 &= bc \text{ also,} \\
a^2 &= R^2 - (e + e_0)^2 \text{ and,} \\
b &= r - e \\
c &= r + e \text{ then} \\
R^2 - (e + e_0)^2 &= (r - e)(r + e) \text{ this should give} \\
e &= \frac{R^2 - r^2 - e_0^2}{2e_0}
\end{aligned} \tag{6.4}$$

Then, the reaction torque is given by:

$$T = F_{in} \times \cos \vartheta \times e = F_z \times e = F_z \times \frac{R^2 - r^2 - e_0^2}{2e} \tag{6.5}$$

To find the output ϑ , substitute eq. (6.5) into eq. (6.3), then the system differential equation (eq. 6.3) can be expressed in the s-domain method for zero initial condition then,

$$\begin{aligned}
T_{(s)} &= Is^2 \vartheta + K_g \vartheta \\
T_{(s)} &= \vartheta (Is^2 + K_g) \\
\vartheta_{(s)} &= T_{(s)} \frac{1}{Is^2 + K_g}
\end{aligned} \tag{6.6}$$

The simulation diagram that describes this equation is,

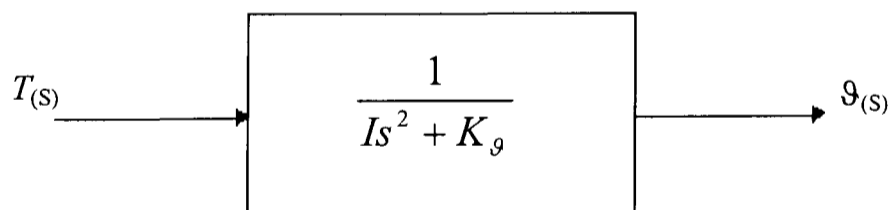


Figure 6.8 A simulation block diagram for the peg initial tilt

6.3.3 Transition Stage

In this stage the peg moves to the far side of the hole by a distance e_x (output), which corresponds to the spring K_x compression (of figure 6.3), and this is shown in figure (6.9).

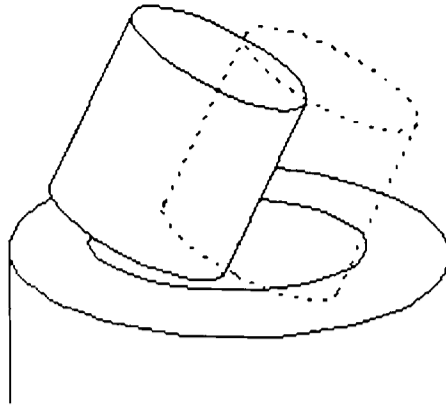


Figure 6.9 Peg is moving to the far side of the hole (transitional)

The forces acting on the free body diagram (FBD) of the peg are shown in figure (6.10),

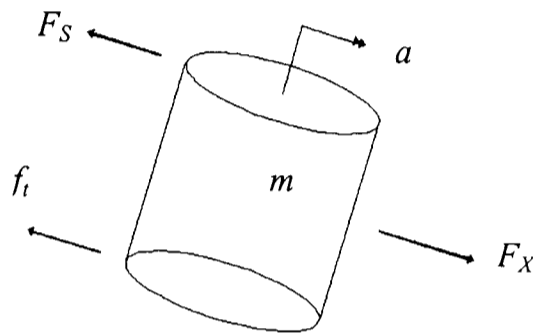


Figure 6.10 The FBD of the peg during the transition stage

Newton's 2nd law for this system is:

$$F_x - F_s - f_t = ma \quad (6.7)$$

Where the input F_x is the axial force, F_s is the spring force, and f_t is the friction force. Note that

$$f_t = \mu f_n = \mu F_z \quad (6.8)$$

Where f_n is the normal force. Then putting the relations $F_x = F_z \tan \theta$ and $F_z = F_{in} \cos \theta$ into eq. (6.7) should give:

$$\begin{aligned}
 F_{z(t)} \tan \vartheta - \mu F_{z(t)} &= m \frac{d^2 e_x}{dt^2} + K_x e_x \\
 F_{in(t)} (\sin \vartheta - \mu \cos \vartheta) &= m \frac{d^2 e_x}{dt^2} + K_x e_x
 \end{aligned}
 \tag{6.9}$$

Expressing the system differential equation in the s-domain method for zero initial condition, yields:

$$\begin{aligned}
 F_{in(s)} (\sin \vartheta - \mu \cos \vartheta) &= ms^2 e_x + K_x e_x \\
 e_{x(s)} &= F_{in(s)} (\sin \vartheta - \mu \cos \vartheta) \frac{1}{ms^2 + K_x}
 \end{aligned}
 \tag{6.10}$$

The simulation block diagram for this stage is shown in figure (6.11),

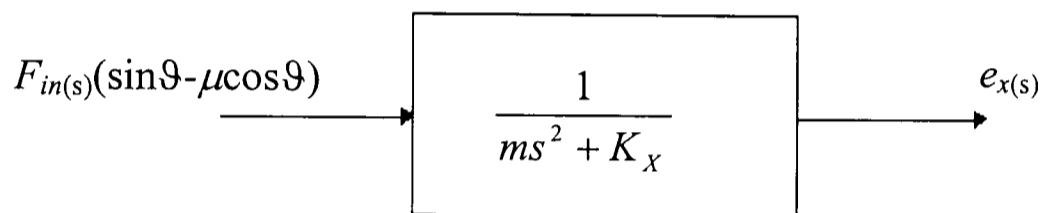


Figure 6.11 Simulation block diagram for the peg transitional stage

However, if the peg approaches the hole with negative initial angular misalignment (figure 6.12), then during contact between the mating parts, the input is the torque generated from the reaction forces and the output is ϑ . Note that to accommodate this initial misalignment, the springs should react in one plane, either the rotational springs $K_{\vartheta XZ}$ or $K_{\vartheta YZ}$. The differential equation that describes this stage is

$$\begin{aligned}
 T_{(t)} &= I \frac{d^2 \vartheta}{dt^2} + K_{\vartheta} \vartheta \\
 T_{(t)} &= I \frac{d^2 \vartheta}{dt^2} + K_{\vartheta} \vartheta
 \end{aligned}
 \tag{6.11}$$

Which is the same as eq. (6.3), except ϑ is negative and, the torque is (refer to chapter 3, figure 3.8),

$$T = F_{in} \cos \mathcal{G} \times r = F_z \times r \quad (6.12)$$

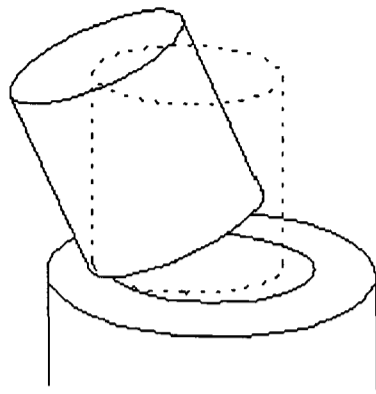


Figure 6.12 left-side angular misalignment

The simulation block diagram for this stage is the same as that for eq. (6.3) apart from the value of T , which is given in eq. (6.12).

6.3.4 Transition From One To Two-Point Contact

The next stage is where the peg slides into the hole and two-point contact occurs (see figure 6.13). In this stage the insertion system will continue in providing the peg with the vertical motion (sliding-in) while maintaining the one-point contact with the hole until a stage where the peg changes from one to two point contact with the hole.

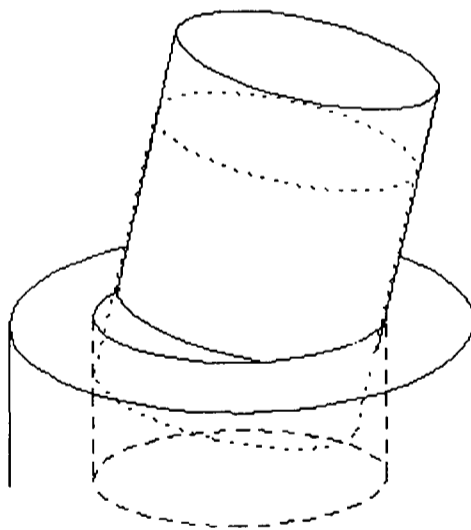


Figure 6.13 The peg is in transition from one-to-two point contact

The forces that act on the FBD of the peg are shown in figure (6.14). Note that the line of action of all forces lies in the X-Z plane, something that reduces the 3D problem to 2D.

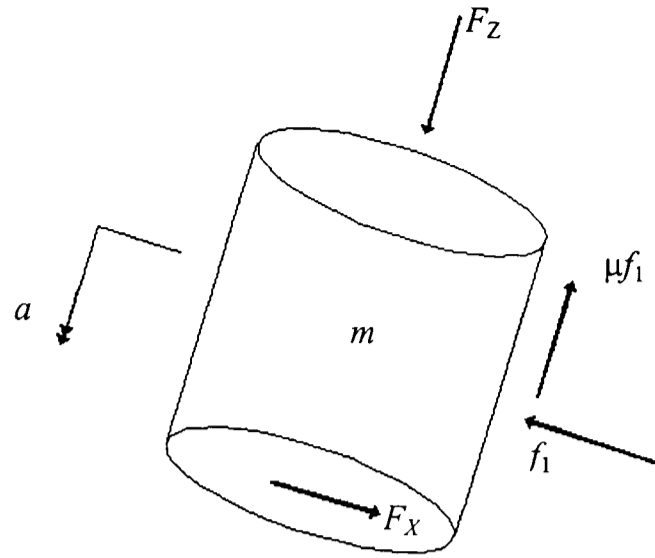


Figure 6.14 The FBD of the peg during transition stage

The following equation is derived from Newton's 2nd law (see figure 6.14):

$$F_z - \mu f_1 = ma \quad (6.13)$$

Also in figure (6.13), the following relation exist:

$$f_1 = F_x \quad (6.14)$$

Then putting the relations of eq. (6.14) into eq. (6.13), should give the system dynamic equation, which is:

$$F_{z(t)} - \mu F_{x(t)} = m \frac{d^2 z}{dt^2} \quad (6.15)$$

$$F_{in(t)} (\cos \vartheta - \mu \sin \vartheta) = m \frac{d^2 z}{dt^2}$$

Now, eq. (15) is expressed in the s-domain method should give:

$$F_{in(s)} (\cos \vartheta - \mu \sin \vartheta) = ms^2 Z_{(s)} \quad (6.16)$$

$$Z_{(s)} = F_{in(s)} (\cos \vartheta - \mu \sin \vartheta) \frac{1}{ms^2}$$

The simulation block diagram for this stage is shown in figure (6.15).

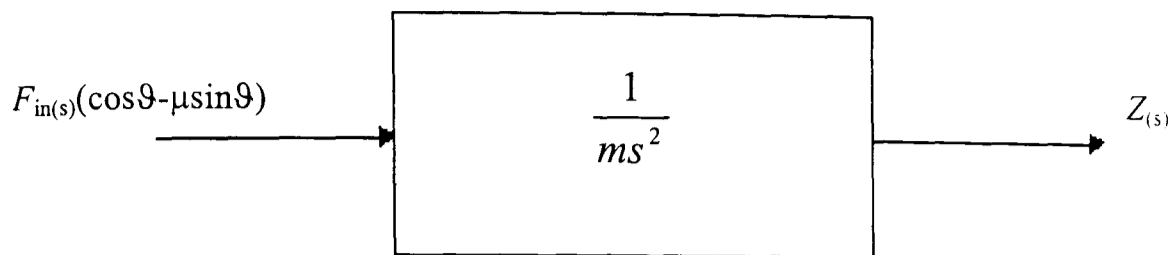


Figure 6.15 Simulation block diagram for the peg during one-point contact sliding

3.5 Final Alignment

The final stage is where the peg is in two-point contact with the hole (figure 6.16). The input is the torque generated by the reaction forces due the two-point contact. The output is the angular tilt. In the final alignment, the angular tilt becomes zero degrees. It is assumed that once the peg is inside the hole and the angular error is zero, this is a success, and hence becomes the end of the insertion process.

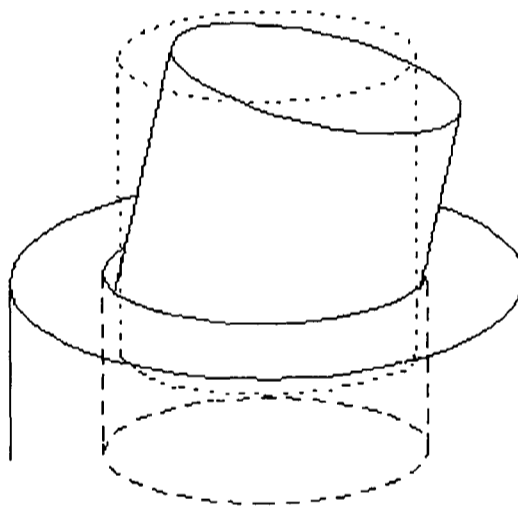


Figure 6.16 The peg tilting from two-point contact to zero angular misalignment

As before, on the FBD of the peg of figure (6.16), the forces acting on it are all lying in one plane. The actual diagram is the same as that of figure (6.6).

Newton's 2nd law for this system is:

$$T_{(t)} - T_{S(t)} = I \frac{d^2 \theta}{dt^2} \quad (6.17)$$

Where $T_{(t)}$ is the input and \mathcal{G} is the output of the system. In eq. (6.17) the input $T_{(t)}$ is equal to the moment at the wrist (refer to eq. 5.18, recovery torque) and it is shown in eq. (6.18).

$$T_{(t)} = K_g \times \mathcal{G}_{(t)} \quad (6.18)$$

Rearranging eq. (6.17 and 6.18) and then transferring into the s-domain method,

$$\begin{aligned} T_{(t)} &= I \frac{d^2 \mathcal{G}}{dt^2} + K_g \mathcal{G} \\ T_{(s)} &= Is^2 \mathcal{G}_{(s)} + K_g \mathcal{G}_{(s)} \\ \frac{\mathcal{G}_{(s)}}{T_{(s)}} &= \frac{1}{Is^2 + K_g} \quad \text{or} \\ \mathcal{G}_{(s)} &= T_{(s)} \frac{1}{Is^2 + K_g} \end{aligned} \quad (6.19)$$

To complete the insertion process, the output \mathcal{G} (in eq. 6.19) has to become zero. This is achieved when the spring/wrist tilts the peg to the other side until contact between the mating parts is broken from both sides, and no reaction forces exist. Also, it is assumed that once the peg is inside the hole with zero angular misalignment, peg sliding could continue until the desired insertion depth without risking jamming/wedging occurrence.

The simulation block diagram that describes the final stage of the insertion process is shown in figure (6.17).

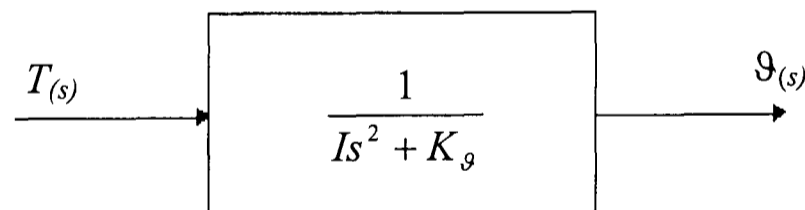


Figure 6.17 Simulation block diagram for the peg during two-point contact-completion stage

6.4 SIMULATION

A simulation programme was designed to simulate the insertion process model of that developed in this chapter. The software used to simulate the insertion process is Matlab-Simulink, and the default parameters were as follow:

For the wrist, various values were used for angular and lateral stiffness,

$$K_X = 0 \text{ to } 10 \text{ N/mm}$$

$$K_g \text{ or } K_a = 0 \text{ to } 10000 \text{ Nmm/rad}$$

For the peg-hole and wrist:

$m = 3.10 \text{ Kg}$ this is the mass of the wrist, mass of the peg is negligible

$$R = 10 \text{ mm}$$

$I \cong 0.0035 \text{ Kg.m}^2$ (see appendix 1 for experimental determination of the moment of inertia for the wrist)

The initial lateral and angular misalignments between the mating parts were,

$$e_{x0} \text{ or } e = 1.5 \text{ mm}$$

$$g_0 = 3^\circ$$

Coefficient of friction, $\mu = 0.2$

$$c = 0.2 \text{ mm}$$

A constant force used as input, it is equal to 500 N.

Figure (6.18) shows a schematic of the simulation programme designed to simulate the wrist during chamferless peg-in hole insertion process.

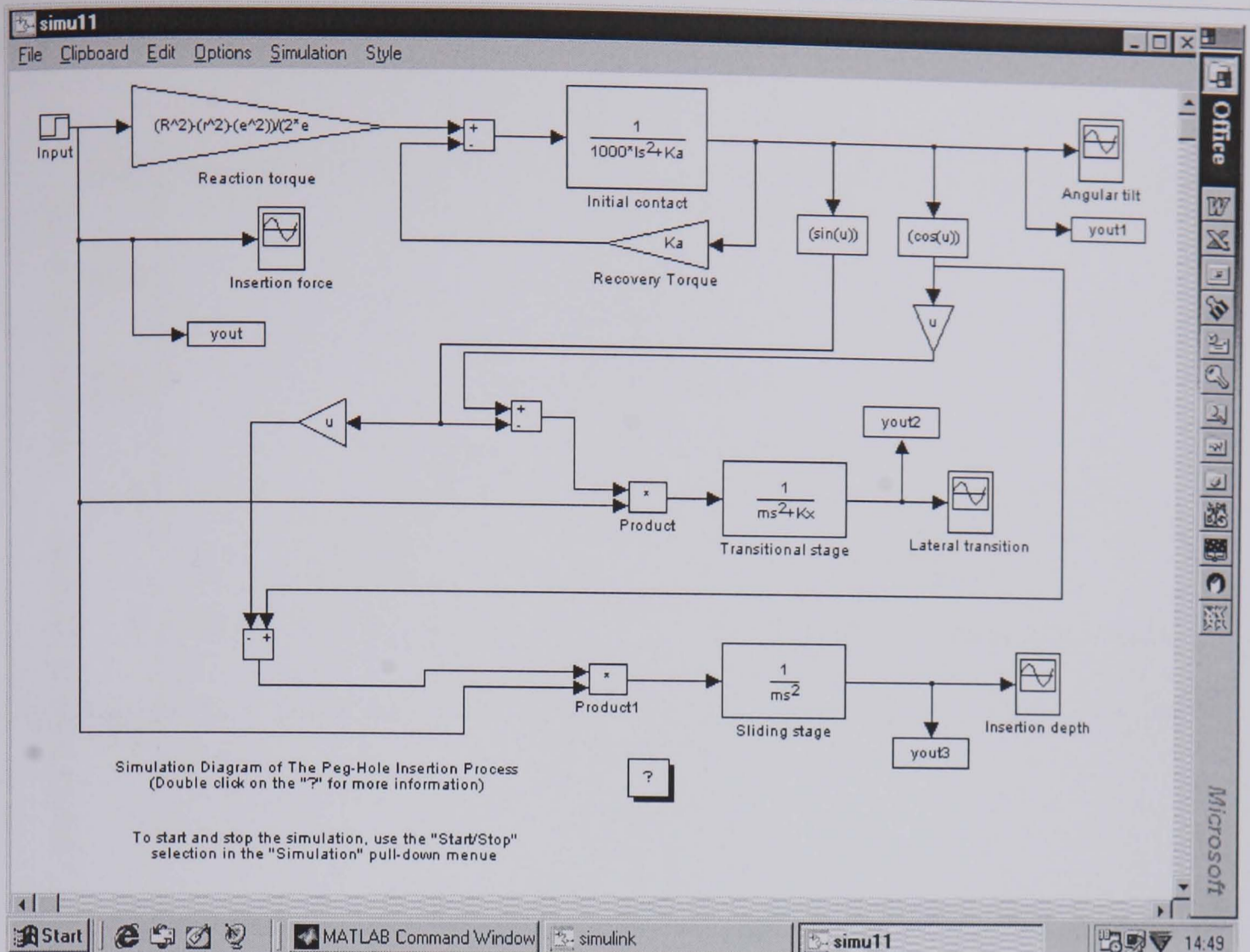


Figure 6.18 Simulation programme for wrist during the peg-in hole insertion process

The principles of the programme presented in figure (6.18) are the same as those for figure (6.2). Note that either the initial angular or the initial lateral misalignment must not be zero at all times. In figure (6.18), the applied force is in the form of a step-input which provides the system with a constant force/signal to run the transfer function blocks, that were derived from the mathematical models of the insertion process. The input force generates a reaction torque (eq. 6-5), which is in turn, fed into the initial contact transfer function block (eq. 6.6). The output is an angular tilt. The angular tilt is fed into function blocks to create $\sin(\theta)$ and $\cos(\theta)$ which in turn is fed into the system to generate the input forces needed for each of those stages (refer to equations 6.10 and 6.16) to slide the peg laterally and then to slide it down inside the hole to form one or two point of contact (refer to eq. 6.19). At the same time the recovery torque does the final alignment (refer to eq. 6.18). The scope blocks throughout the programme are to monitor the progress of the simulation process.

Figure (6.19) is a summary of a successful insertion attempt.

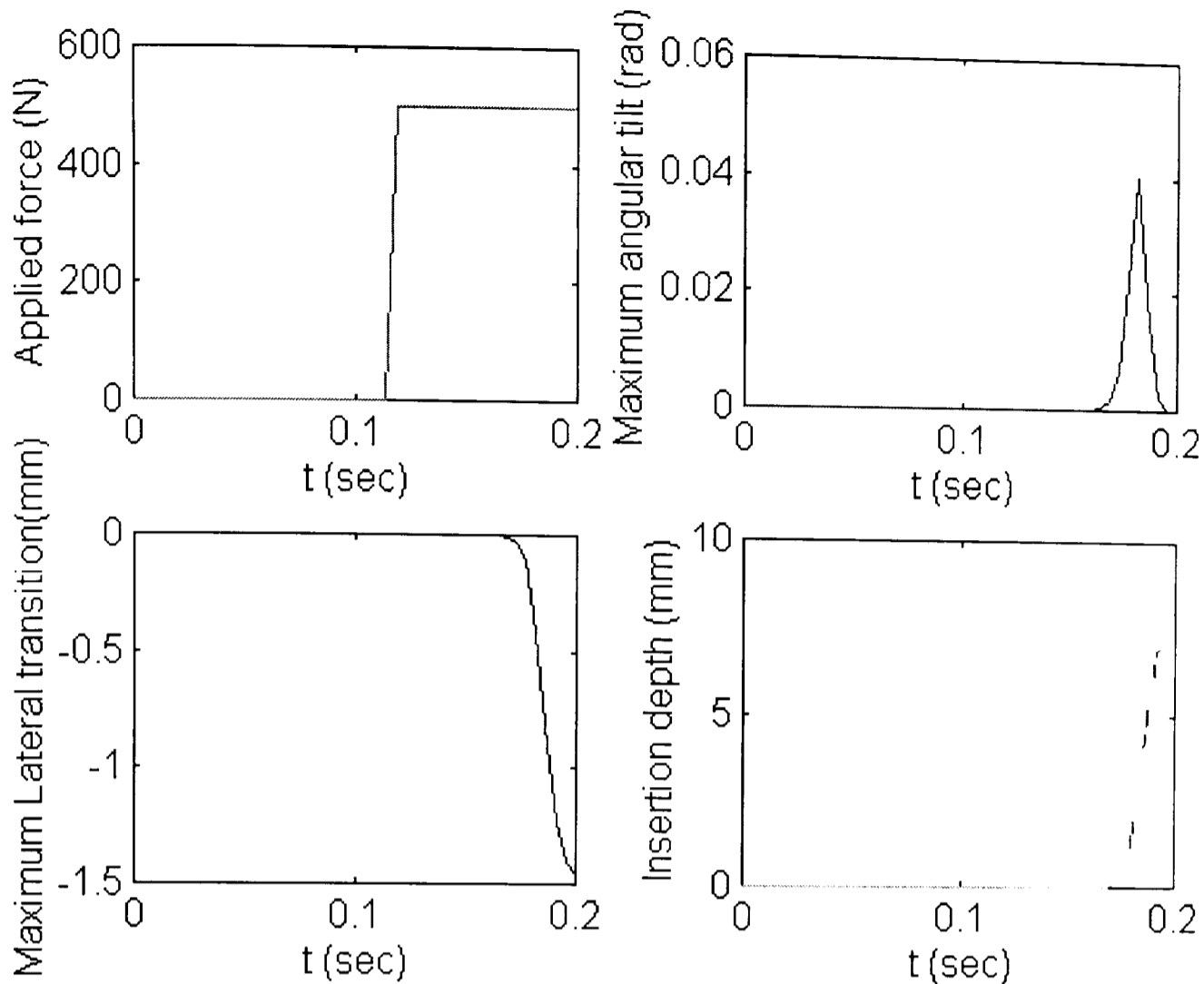


Figure 6.19 Summary of the simulation process for initial error of 1.5 mm, $c = 0.2$ mm

As shown in figure (6.19), for a given force of 500 N, the wrist can tilt the peg inside the hole to about 2.5° and then slides the peg to about 1.4 mm. After that, the peg moves from one-to-two point contact with the hole. At the same time the wrist tends to align the peg with the hole. Note that in the maximum lateral transition graph, the results indicate that to overcome the initial lateral misalignment the wrist has to slide the peg axially to a distance of at least the value of the initial positional misalignment. Since the clearance between the mating parts is 0.2 mm, the 1.4 mm lateral movement of the peg becomes sufficient to overcome the 1.5 mm initial lateral misalignment.

Also, figures (6.20 and 6.21) present successful assembly examples. Figures (6.22 and 6.23) present jamming occurrence due to insufficient wrist stiffness. In both figures (6.20-21), the wrist tilts the peg inside the hole 5° and 13° and then the peg moves to the far side of the hole to overcome the initial lateral errors, and slides down the hole to form one and two point contact. To complete insertion, the wrist aligns the peg inside the hole.

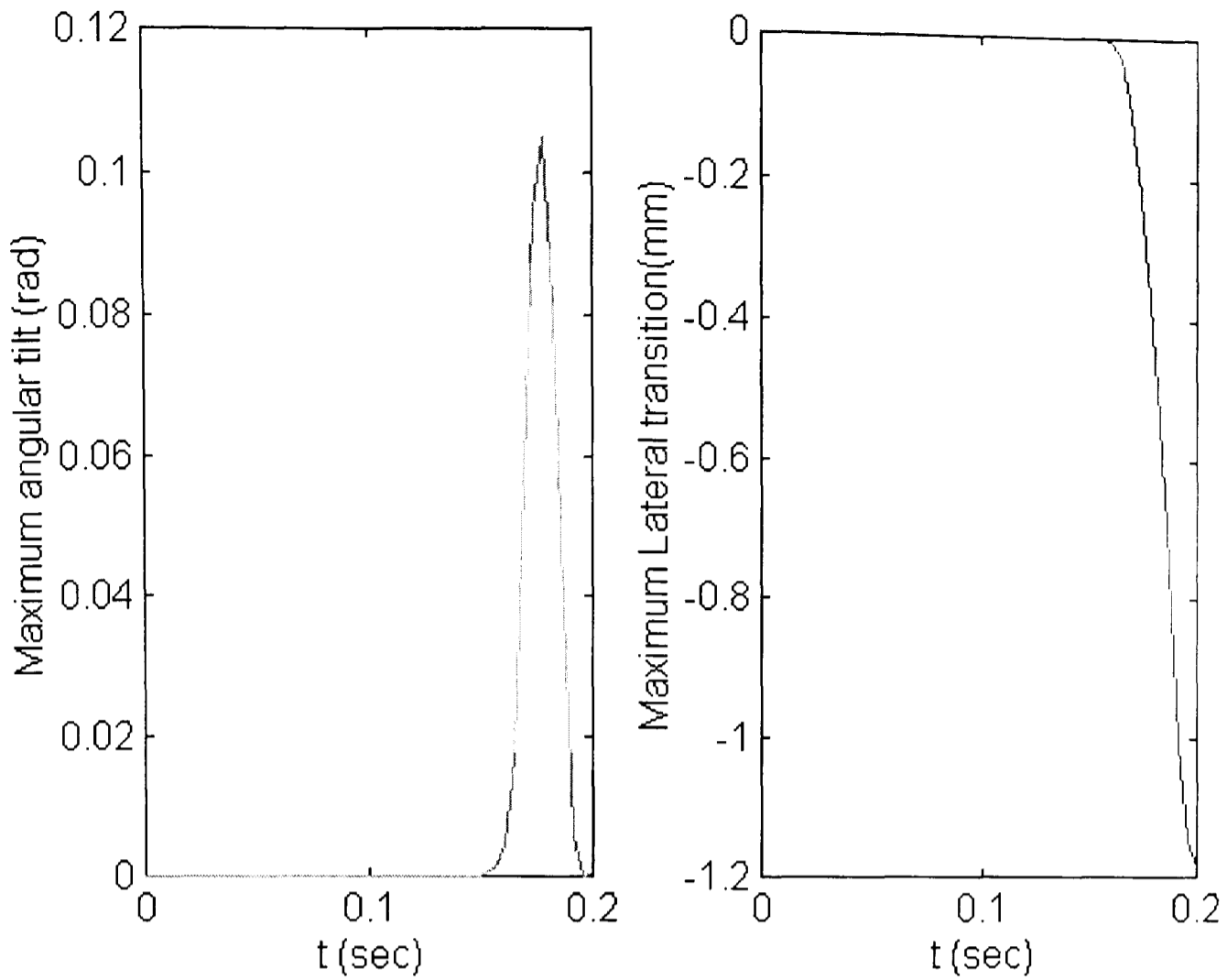


Figure 6.20 Successful assembly for initial error of 1 mm, $c = 0.2$ mm

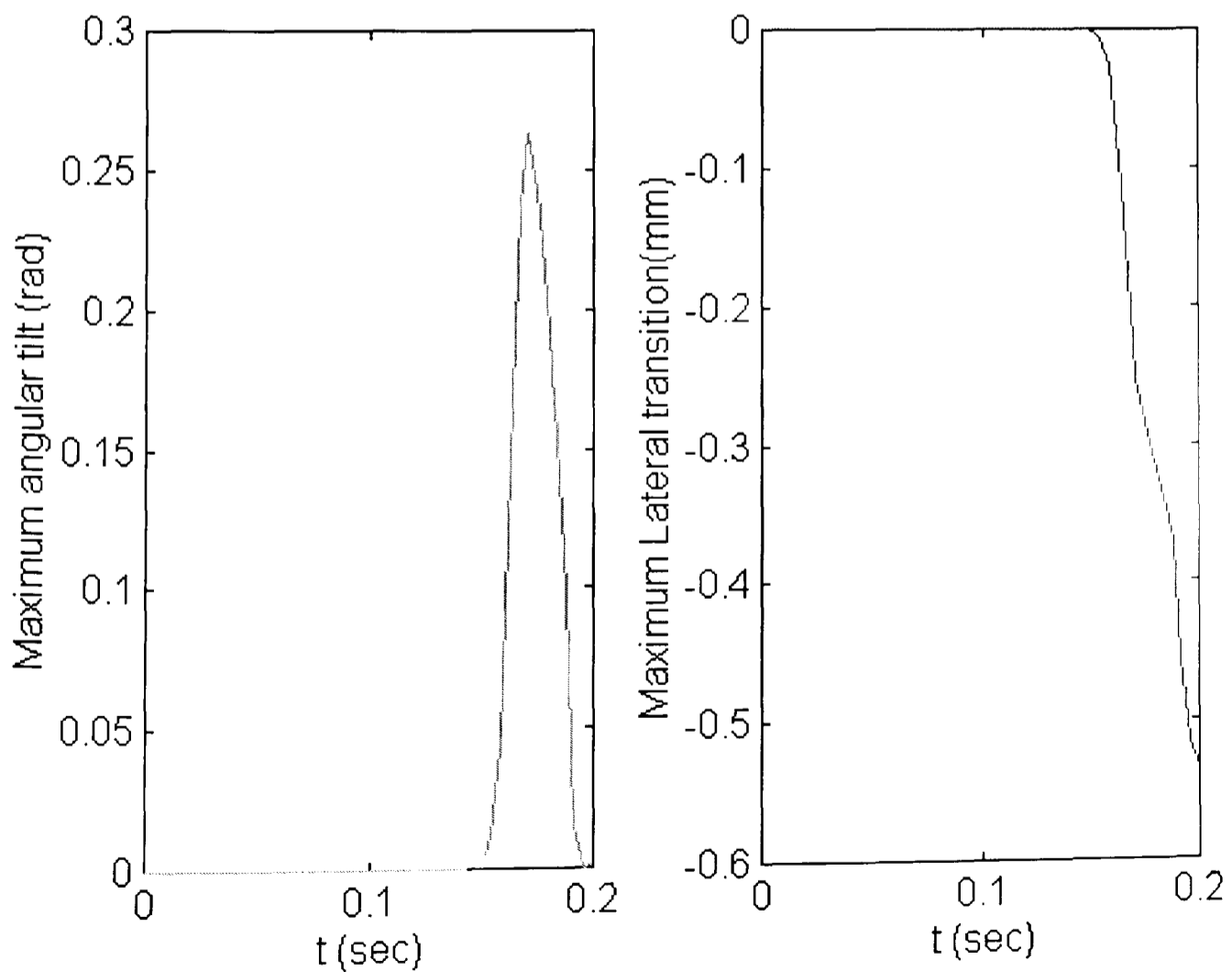


Figure 6.21 Successful assembly for initial error of 0.5 mm, $c = 0.2$ mm

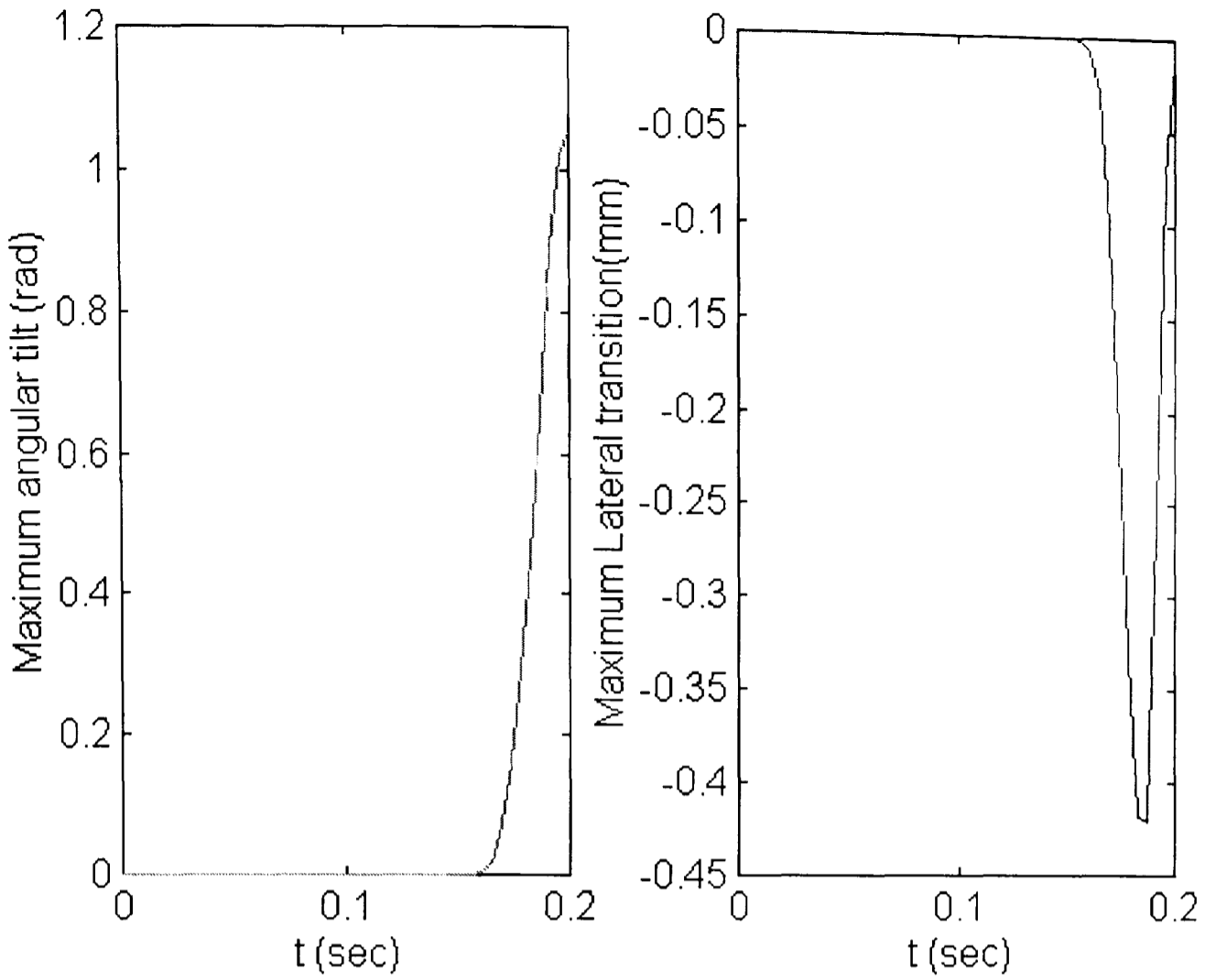


Figure 6.22 Jamming, zero angular stiffness and 1 mm initial lateral error, $c = 0.2$ mm

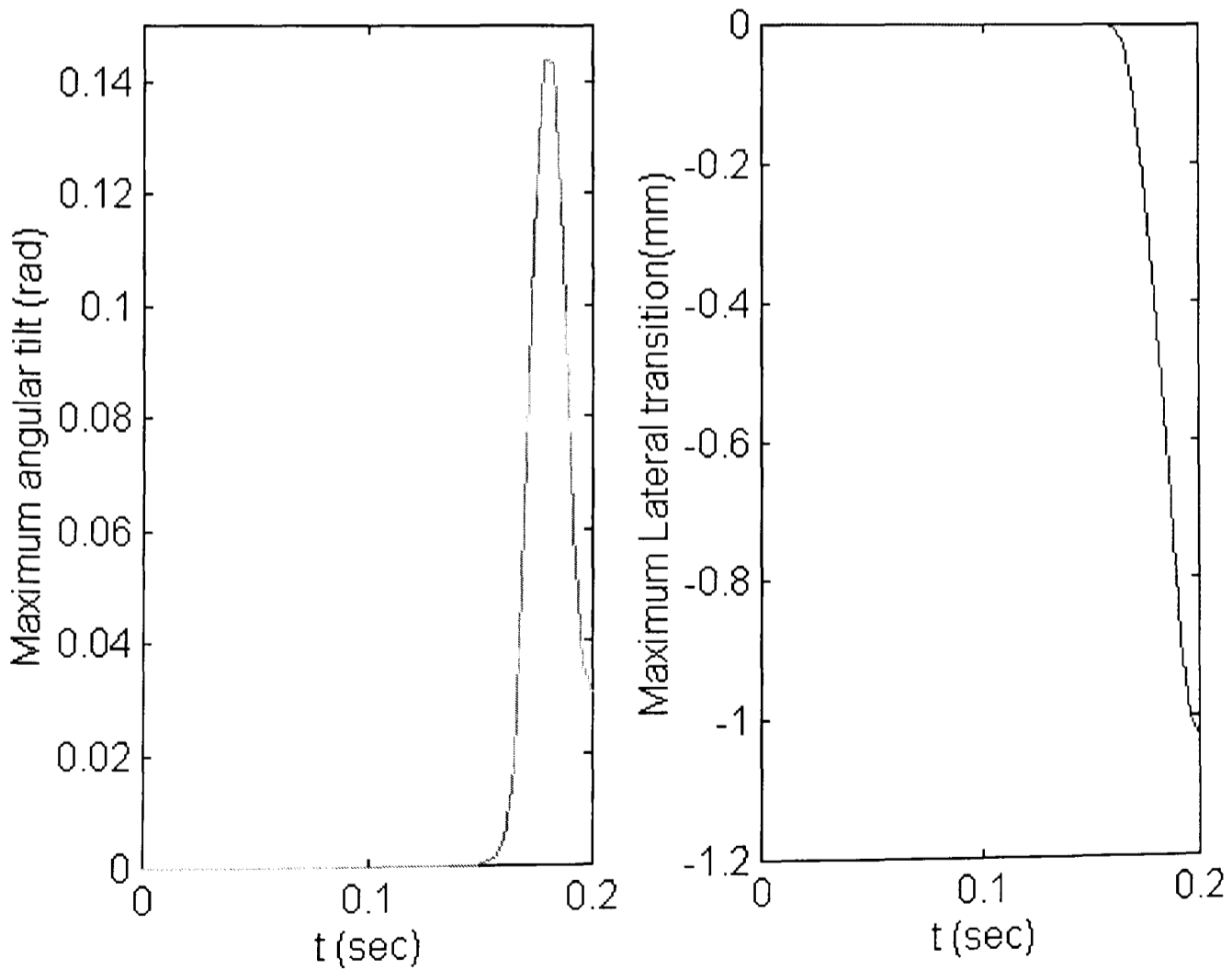


Figure 6.23 Jamming, angular stiffness 5000 Nmm/rad and 1 mm initial error, $c = 0.2$ mm

As shown in figure (6.22), for zero angular stiffness and 1 mm initial lateral error, the wrist tilts the peg to over 50°, and moves the peg to over 0.4 mm but does not keep it in position. However, in figure (6.23) for 5000 Nmm/rad angular stiffness and 1 mm initial error, the wrist tilts the peg to over 8 degrees and moves the peg laterally over the 1 mm. But in this case the wrist could not recover the peg during the final alignment stage (final angular tilt must become zero).

Now, to evaluate the simulation model, different clearances were used for variable initial lateral misalignment. The results are shown in figure (6.24 and 6.25).

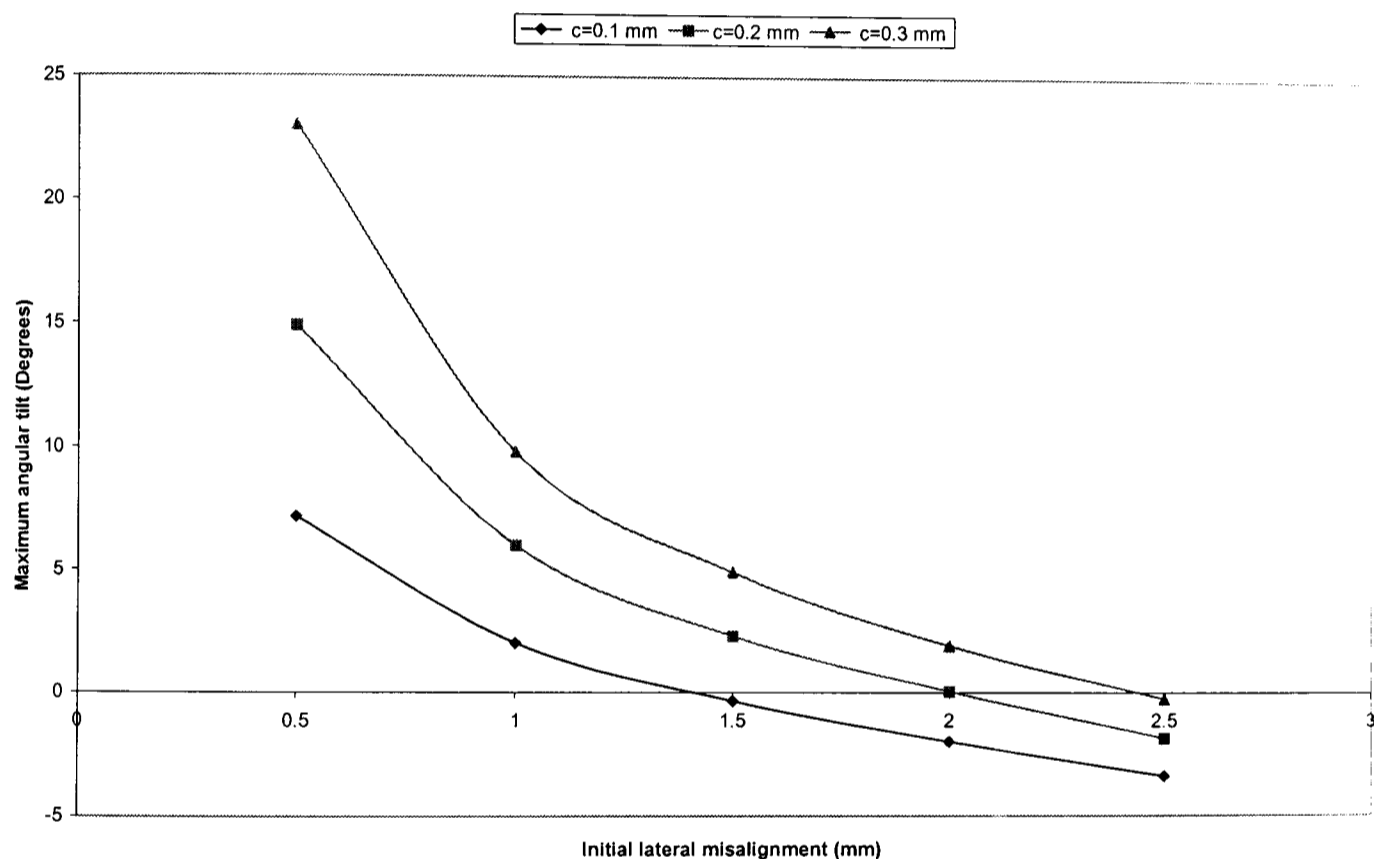


Figure 6.24 Progress of the maximum angular tilt for given initial lateral misalignment and different clearances

In figure (6.24), for 0.5 mm initial error and a clearance of over 0.2 mm, this results in a large angular tilt (over 15°) during the simulation process, which will cause a 3POC jamming. On the other hand in figure (6.25), initial lateral error of over 1.5 mm leads to insufficient lateral transition to overcome the initial lateral error, therefore jamming occurring is inevitable.

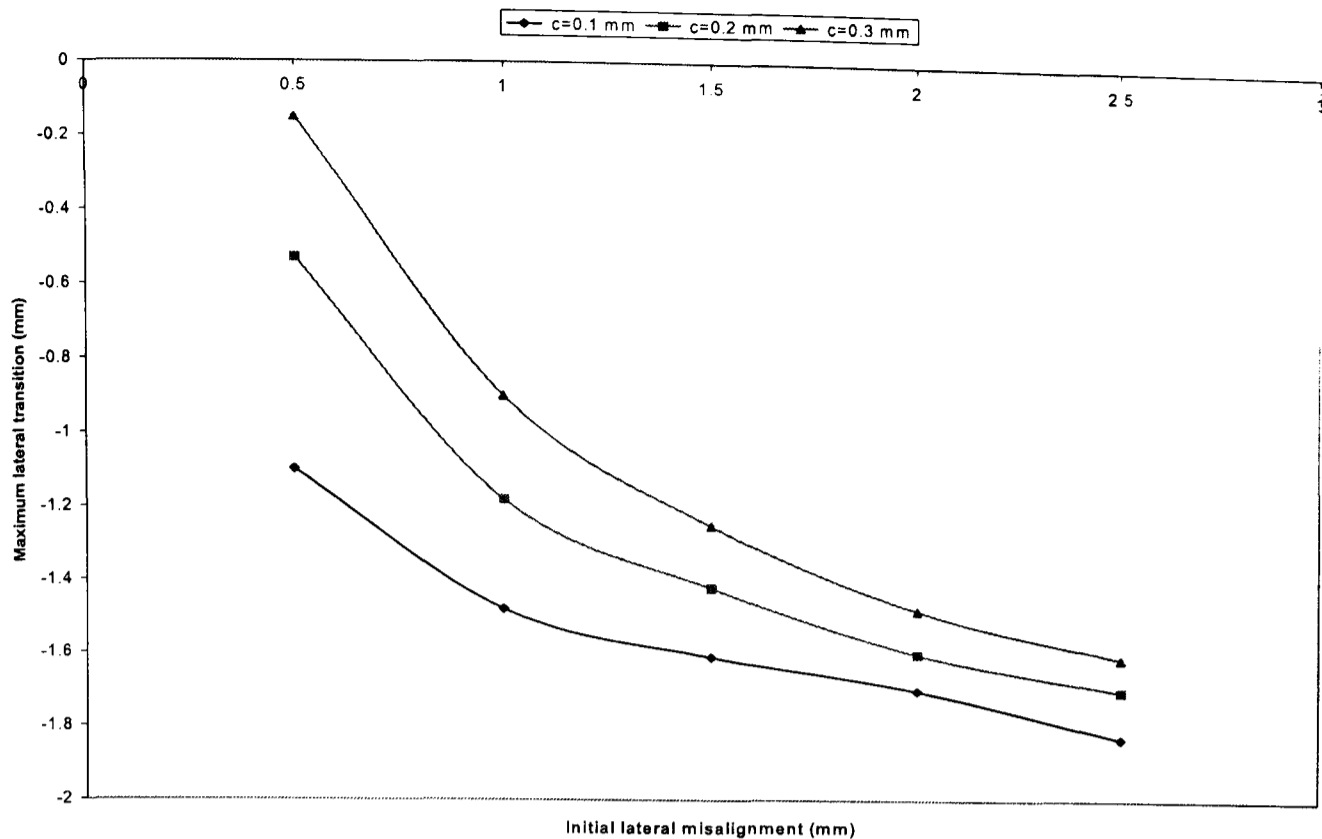


Figure 6.25 Progress of the maximum lateral transition for given initial lateral misalignment and different clearances

So far, the initial angular misalignment in the presence of initial lateral misalignment was ignored because it has little effect on the insertion process. However, if there is a situation where the initial lateral misalignment is zero, and the initial angular misalignment is not zero, then the reaction torque given in eq. (6.5) would become:

$$T = F_{in} \cos \vartheta \times r \quad (6.20)$$

Which is the same as eq. (6.12) except that ϑ is positive. So putting eq. (6.20) in the simulation programme would give the results shown in figure (6.26).

The results presented in figure (6.26) indicate a complete jamming occurrence. To understand the reasons behind that, one should refer to the principles of remote compliance devices. It is known that RCC's accommodate angular errors within the range of their friction angle. In the case of the CVH-RCC the friction angle is 12° , therefore both of ϑ_0 and ϑ_{max} must be smaller than 12° otherwise jamming occurring is inevitable. To

understand the effect or the relation between the friction angle, ϑ_0 and ϑ_{max} have a look at figure (6.27).

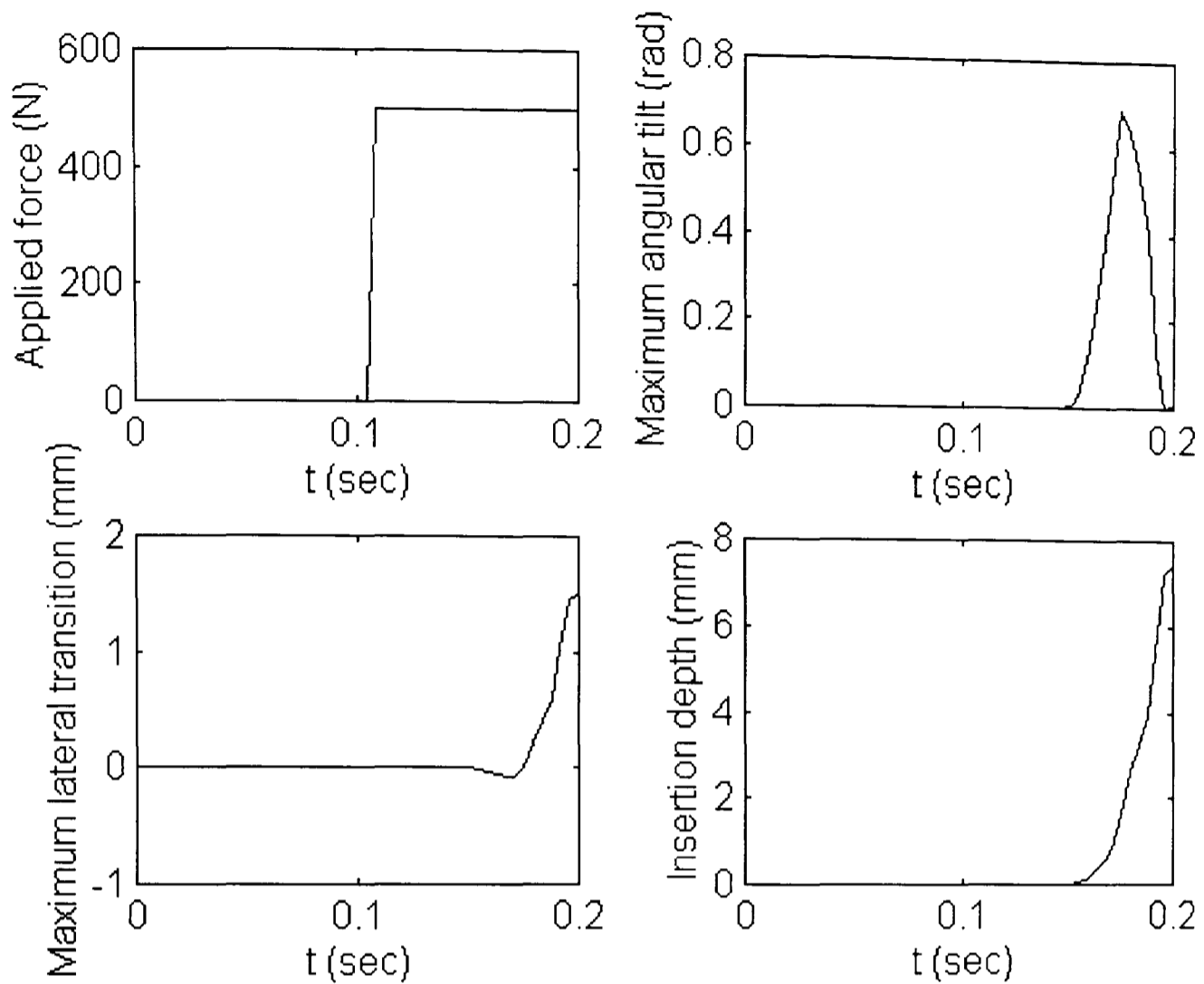


Figure 6.26 Summary of the simulation process for initial angular misalignment, from 1° to 12° , $c = 0.2 \text{ mm}$

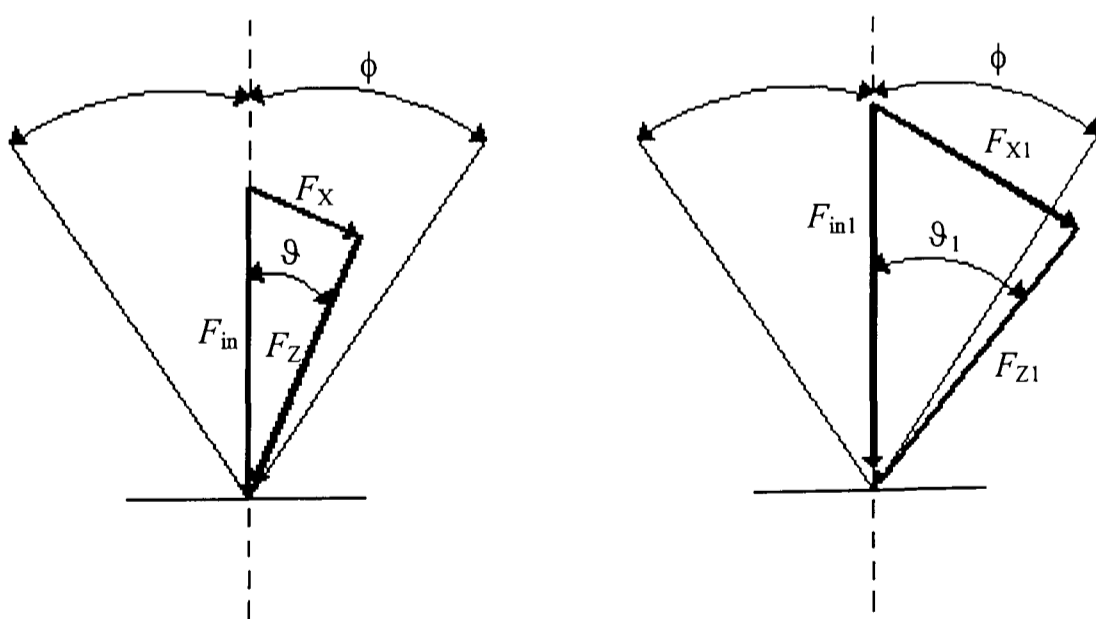


Figure 6.27 Relation between the applied forces and the angle of tilt

As shown in figure (6.27), by increasing the applied force, the F_z , F_x and reaction torque will be increased and as a result, the angular tilt increases and thus the insertion force F_z will lie outside the friction cone and the outcome is jamming. Since the only parameter that can be controlled is the applied force (F_{in}), in the actual simulation programme, decreasing the applied force will give the results shown in figure (6.28).

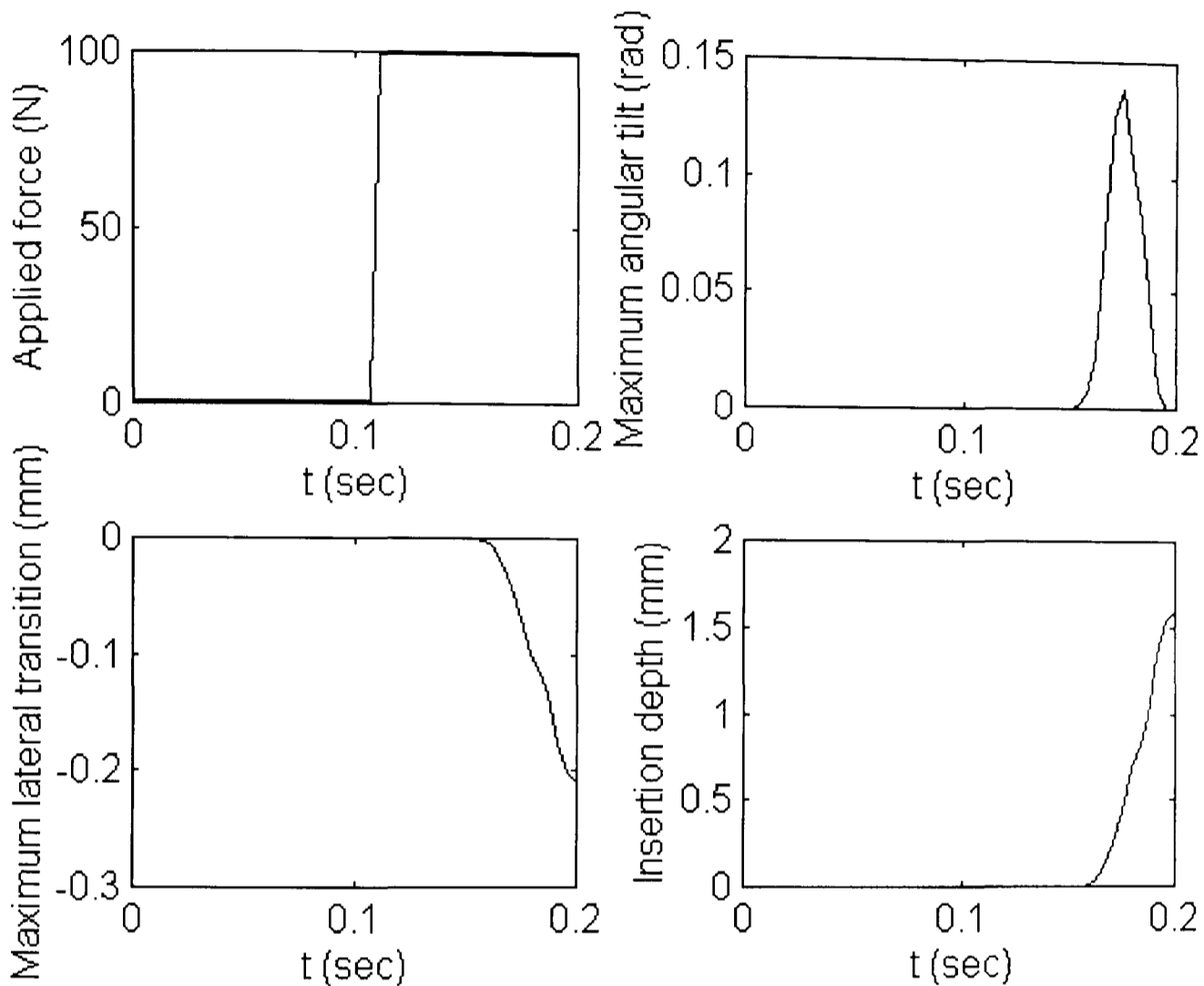


Figure 6.28 Summary of the simulation process for initial angular misalignment, from 1° to 12° , $c = 0.2 \text{ mm}$, the applied force is 100 N

Figure (6.28), presents same insertion process with 100 N applied force; the outcome is successful assembly. However, one point can be noticed in both figures (6.27 and 6.28) is that the initial angular misalignment has same effect on the simulation process, whether it is small or large. Hence, to determine whether jamming could occur based on the initial angular error, then one should consider the relation $r/\cos\vartheta \leq R$ (see eq. 5.7). So, variable angular misalignments were substituted into eq. (5.7) along with different clearances, and the data generated was plotted in figure (6.29).

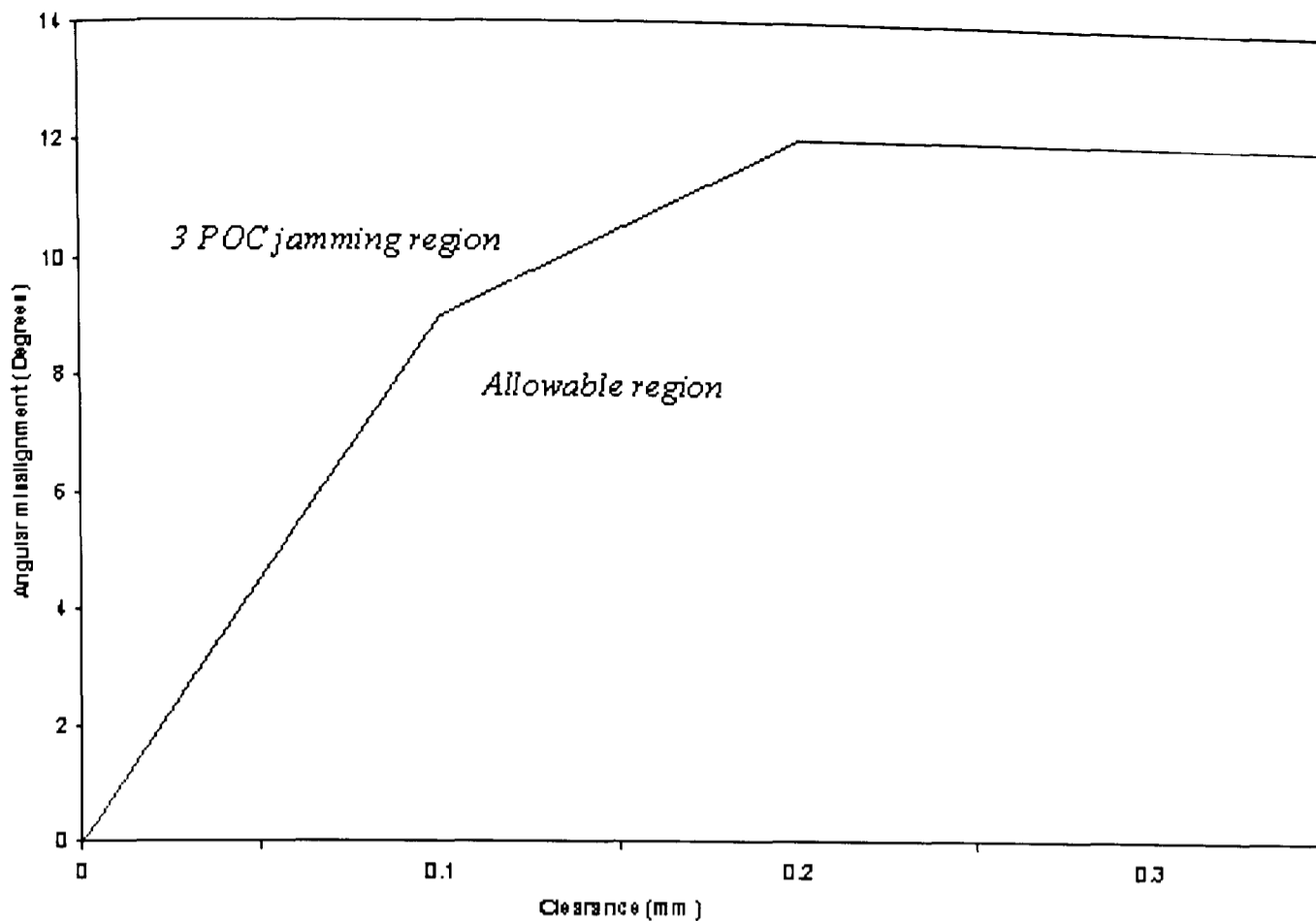


Figure 6.29 Angular error, clearance and the possible 3 point of contact

In order to avoid jamming, in figure (6.29) and for a given clearance the initial angular misalignment or the maximum angular tilt should correspond to that particular clearance at the trend line, otherwise jamming occurring is inevitable.

Now, after finding the region of the allowable initial positional misalignment, the theoretical wrist stiffness has to be determined. To find the angular stiffness, for 0.2 mm clearance, the range of the initial lateral misalignment which will give maximum angular tilt without causing jamming is 0.5 to 1.5 mm. These values were put in the simulation programme and assuming that the default value of the lateral stiffness is zero, revealed the results shown in figure (6.30).

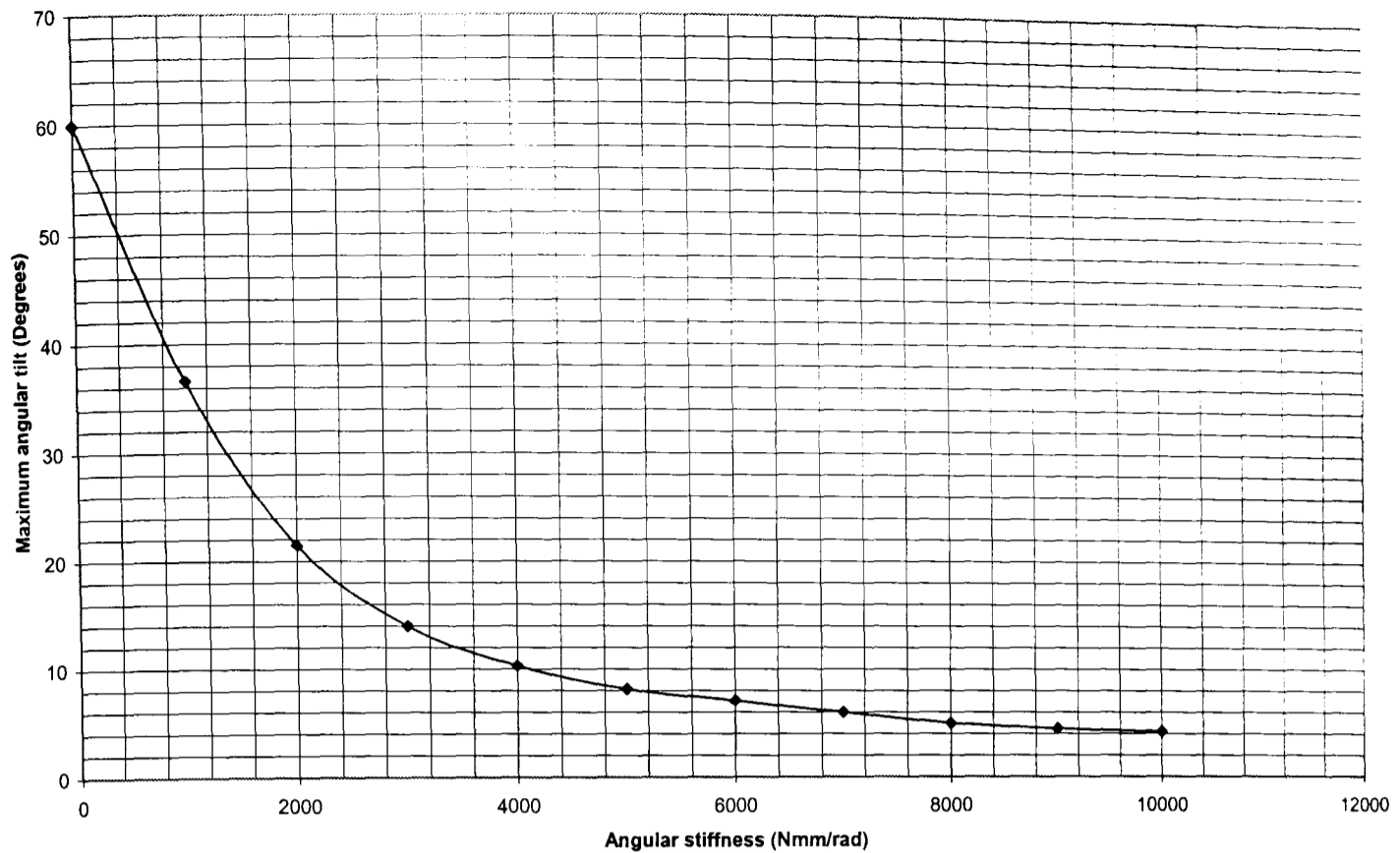


Figure 6.30 Behaviour of angular tilt versus angular stiffness

In figure (6.30), for variable angular stiffness, different values of the maximum angular tilt were generated. During the simulation process, the angular stiffness that led to successful assembly is between 6800 *Nmm/rad* to 7500 *Nmm/rad*. On the chart of figure (6.30) this corresponds to maximum angular tilt of 6.2° and 5.5° respectively. Also, during the simulation process for angular stiffness of 6800-7500 *Nmm/rad* the maximum lateral transition was -1.15 *mm* and -1.2 *mm* respectively. To find the wrist theoretical lateral stiffness, refer to figure (5.7), assuming that the peg is in contact with the hole at points P_1 and P_2 (for lateral transition). Then taking moments about point O_1 , which is the centre of the wrist, should give:

$$F_x L_g - f \times \frac{R^2 - r^2 - e^2_0}{2e_0} - \mu f L_g = K_g \vartheta \quad (6.21)$$

Also,

$$\begin{aligned} \mu f &= F_x \\ f &= \frac{F_x}{\mu} \end{aligned} \quad (6.22)$$

Substitute eq. (6.22) into eq. (6.21) should give:

$$\frac{F_x}{\mu} \times \frac{R^2 - r^2 - e_0^2}{2e_0} = K_g \mathcal{G} \quad (6.23)$$

Then substitute eq. (5.19, $F_x = K_x e_x$) into eq. (6.23) should give:

$$K_x = \frac{2K_g \mathcal{G}_{\max} \mu e_0}{e_{\max} (R^2 - r^2 - e_0^2)} \quad (6.24)$$

Also, the lateral stiffness should have theoretical, minimum and maximum values. The same as the theoretical angular stiffness for which the minimum and maximum angular tilt and lateral transition (5.5° to 6.2° and -1.2 mm to -1.15 mm) are achieved. Now, substituting the minimum and maximum values of angular stiffness, angular tilt and lateral transition in addition to the initial value of the positional misalignment (1 mm : This is the allowable value for the RCC. Also this is the value in which successful assembly is achieved during the simulation process for different clearances.), should give:

$$K_{x \min} \cong 82 \frac{N}{mm} \text{ and}$$

$$K_{x \max} \cong 86 \frac{N}{mm}$$

However, this value of lateral stiffness is much larger than the ones were used in the simulation programme (84 N/mm as opposed to 2 N/mm). So, this time the new values of the wrist theoretical stiffness (7150 Nmm/rad and 84 N/mm) were put in the simulation programme and same process for generating figure (6.25) is repeated to generate figure (6.31).

A comparison between figure (6.25) and figure (6.31) shows that there is a decline in the lateral transition for a prescribed initial lateral error. In fact, the results of figure (6.25) indicate a maximum lateral transition which the wrist could achieve in order to overcome the initial lateral error. In figure (6.31) the results indicate the actual value which the wrist could achieve to overcome the initial lateral error without having to move the peg more than the value of the initial lateral error. Because the actual value plus the clearance should become sufficient to overcome the initial lateral error.

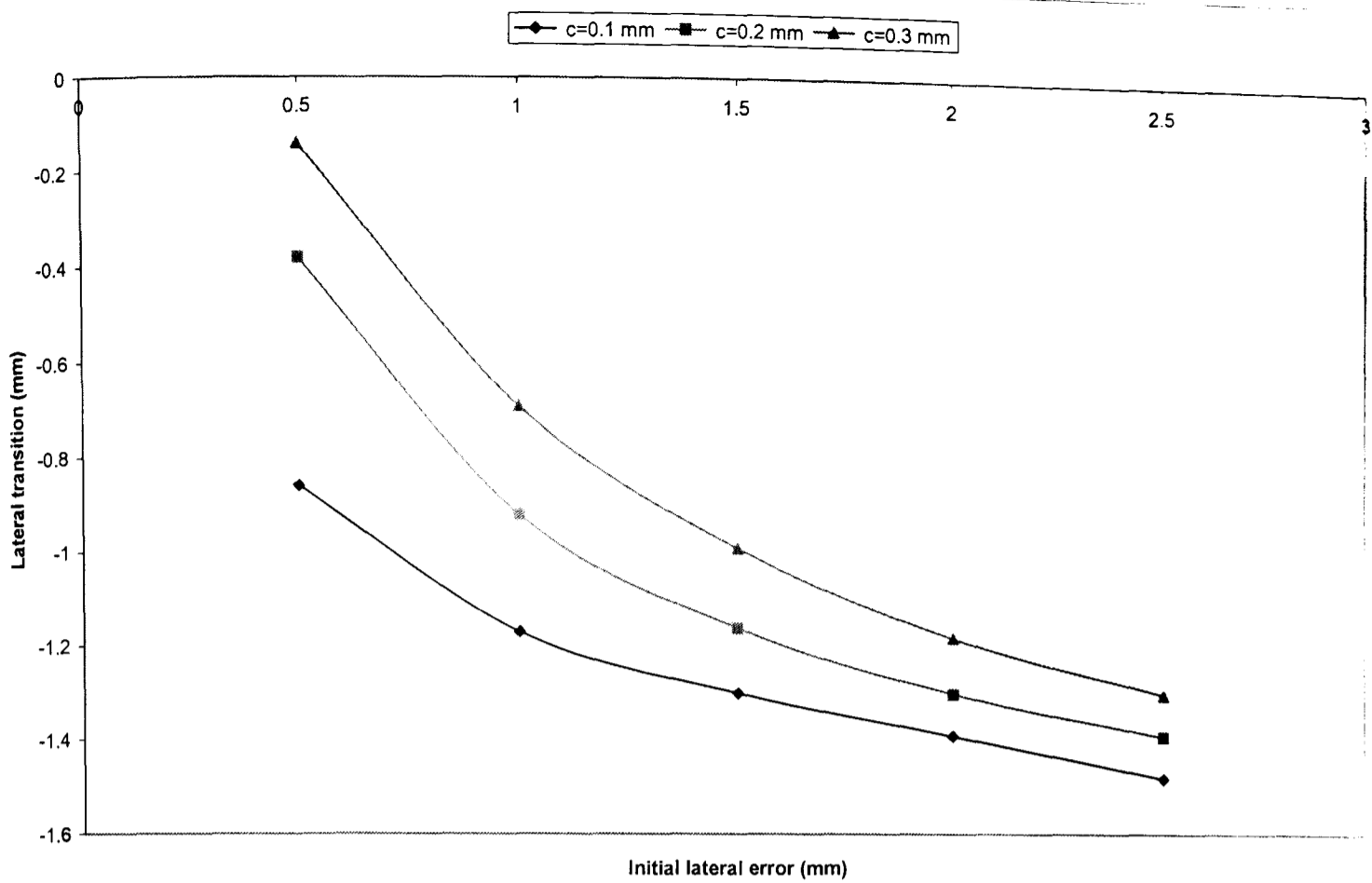


Figure 6.31 Progress of the maximum lateral transition for given initial lateral misalignment and different clearances using wrist theoretical stiffness

To summarise figure 6.31, to avoid jamming:

For

$c = 0.1 \text{ mm}$	$e_0 < 1.5 \text{ mm}$
$c = 0.2 \text{ mm}$	$e_0 < 1.2 \text{ mm}$
$c = 0.3 \text{ mm}$	$0.5 \text{ mm} < e_0 < 1 \text{ mm}$.

Now to summarise the relation between the wrist stiffness, allowable errors, and clearance for successful assembly, the previous results are presented in figure (6.32):

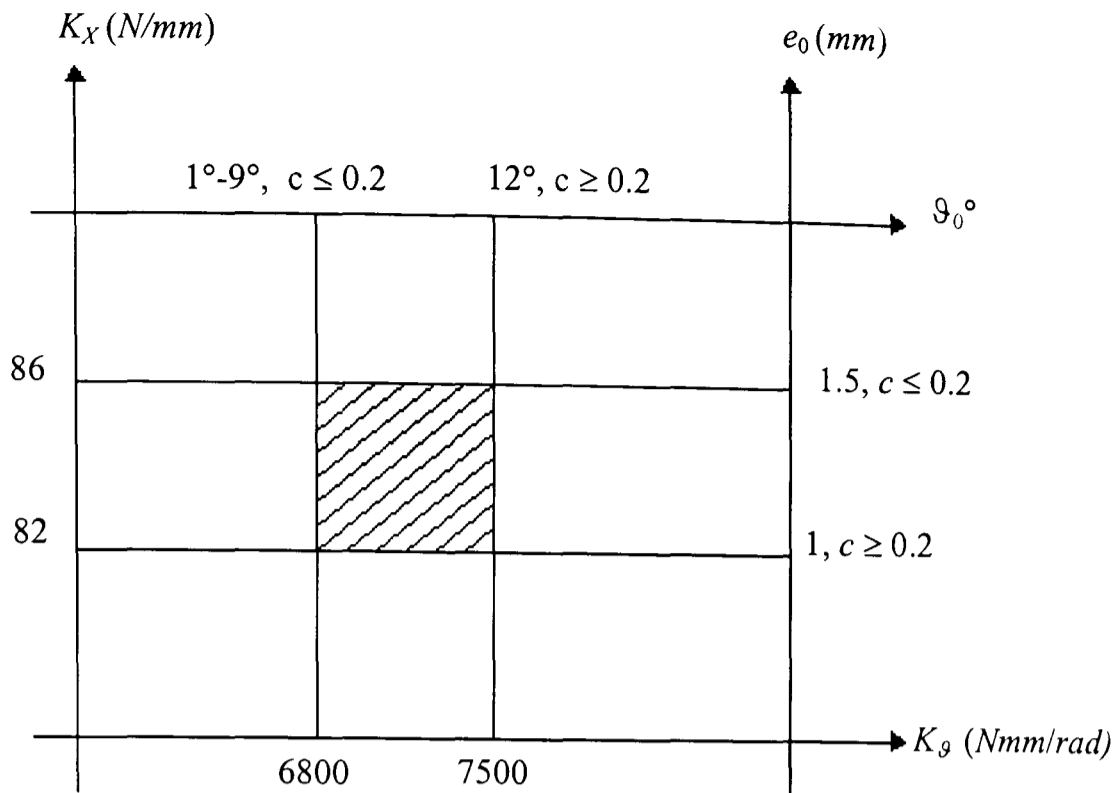


Figure 6.32 Summary of theoretical results

Now to show the effect of the peg size on the insertion process, the theoretical values of the wrist stiffness were entered into the simulation programme to generate data for the initial lateral error versus the maximum angular tilt for different peg radiuses (see figure 6.33).

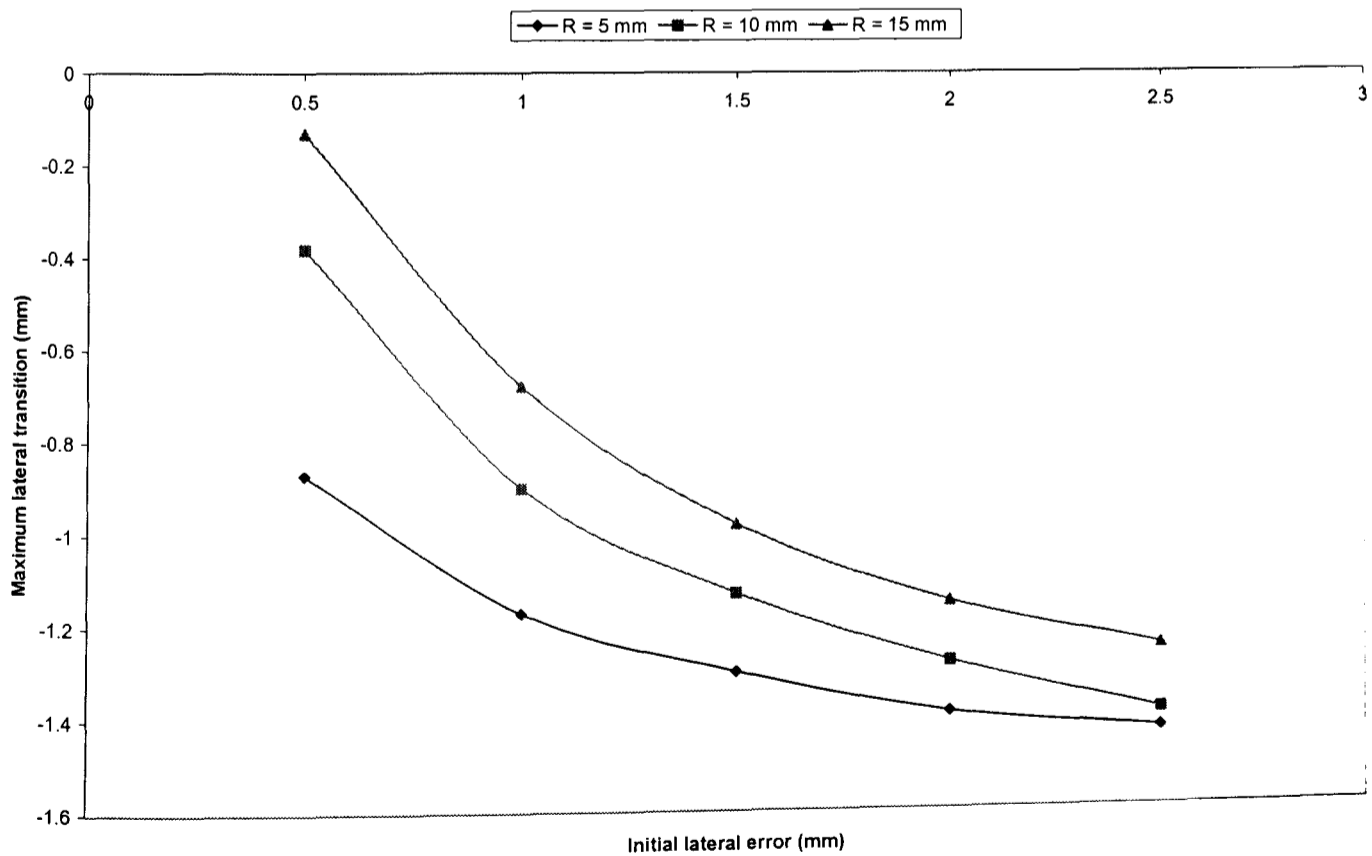


Figure 6.33 Maximum angular tilt for different peg sizes, $c = 0.2 \text{ mm}$

As shown in figure (6.33) for a peg of radius 15 *mm*, the wrist could not overcome the initial lateral misalignment at all times. For radius of 5 *mm*, the initial lateral misalignment should be up-to 1.5 *mm* to enable the wrist to accommodate, and for radius of 10 *mm*, the initial lateral misalignment should be up-to 1 *mm*.

6.5 CONCLUSION

In this chapter a mathematical model of the chamferless peg-in hole insertion process using a passive compliant wrist is presented. Subsequently, a Matlab-Simulink simulation programme for this model has been designed. The results of the simulation programme presents some recommendations for avoiding jamming, the design of the inserted peg and hole, and the wrist. These recommendations are summarised as follow:

1. Wrist stiffness should be: angular stiffness 6800 *Nmm/rad* to 7500 *Nmm/rad*, and the lateral stiffness 82 *N/mm* to 86 *N/mm*.
2. For $c \leq 0.2$ *mm*, the initial angular misalignment $\vartheta_0 \leq 9^\circ$, and when $c \geq 0.2$ *mm* then the initial angular tilt $9^\circ \leq \vartheta_0 \leq 12^\circ$.
3. For $c \leq 0.2$ *mm*, the initial lateral misalignment 1 *mm* $\leq e_0 \leq 1.5$ *mm*, and when $c \geq 0.2$ *mm*, then the initial lateral misalignment 0.5 *mm* $\leq e_0 \leq 1$ *mm*, otherwise jamming could happen (see chapter 9, for discussion and explanation).
4. The wrist should accept a peg from 5 to 10 *mm* radius.

CHAPTER 7

THE CHAMFERLESS-VERTICAL-HORIZONTAL COMPLIANT WRIST (CVHRCC)

7.1 INTRODUCTION

There have been many devices and strategies developed to accommodate positional errors between chamferless mating parts during an assembly operation (see chapter 2). The difference between those devices and the device presented here is that these devices adopt either the passive –active technique or the active technique to accommodate positional errors between chamferless mating parts. This approach is quite complex and expensive compared to the device presented in this chapter which was designed to operate passively.

The purpose of this chapter is to present a new compliant wrist that was designed for chamferless peg-in hole assembly from vertical and horizontal directions. The wrist stiffness should be within the boundary of the theoretical stiffness presented in chapter 6.

The structure of this chapter is as follows:

- Section 7.2 describes the wrist and how it functions.
- Section 7.3 presents a series of experiments that were carried out to measure the wrist deflection; to determine the wrist minimum stiffness which corresponds to the wrist stiffness when the peg is inside the hole in either one or two point contact.
- Section 7.4 describes the testing procedure for finding the wrist maximum stiffness
- Section 7.5 provides the design procedure and shows the wrist stress analysis using a finite element package (Algor: FEA).
- Section 7.6 presents a general discussion of this work.
- Section 7.7 is a conclusion.

The experimental determination of the wrist stiffness showed that the CVHRCC has a low stiffness compared to other devices in its category, but it can accommodate the same range of positional errors between chamferless mating parts during an assembly operation. The

finite element analysis of the wrist has validated the wrist structural design. However, due to the large weight of the CVHRCC (4 Kg); some weight was removed from it, from around the bottom and the top major units after it had been built (see figure 7.1).

7.2 WRIST DESCRIPTION

The Chamferless-Vertical-Horizontal remote centre compliance (CVHRCC) is a modification of the remote centre compliance (RCC) model (refer to section 2.4.1.1, chapter 2). CVHRCC differs from the RCC in that it can function with chamferless mating parts and from both the vertical and the horizontal directions. CVHRCC is a passive compliant wrist mounted between the robot arm/assembly machine and the end effector that enables peg-in hole assembly without jamming or wedging, despite initial errors in the peg position and orientation.

An essential characteristic of the CVHRCC is the ability to provide the peg being assembled with two different points for rotation (see next section) at the insertion axis, which enables it to accommodate positional errors even in the case of no chamfer on either of the mating parts. Also, the independent accommodation of the lateral and the angular error is achieved by placing the centre of compliance near the tip of the peg.

CVHRCC is made of two major units, the fixed unit and the floating unit. The fixed unit is a frame made of 2 aluminium plates mounted parallel to each other and connected by 3 steel rods. The top plate is attached to the robot/assembly machine end effector, while the bottom plate contains the floating unit. The floating unit is located inside a sandwich of soft rubber (sponge) and it is made of 2 aluminium plates connected with 3 converged steel rods, and one vertical centre steel rod. The bottom plate of the floating unit contains an internal sandwich of sponge for grasping the part to be assembled (see figure 7.1).

7.2.1 Wrist Operation

As shown in figure (7.2), CVHRCC places the centre of compliance (COC) near the tip of the peg (point O). This enables the peg to rotate about the insertion point in case of angular/lateral misalignment to correct that error. Also in figure (7.2), when the reaction force F_1 arises, it causes the peg to rotate about point O (COC) and at the same time it tilts the upper side of the peg (point A) into the sponge sandwich in the tilt direction (point B).

The peg tilt, results in another axial reaction force, in the direction of the tilt, which causes both the sponge sandwich and the peg to move to the side where there are fewer forces applied from the hole on the peg.

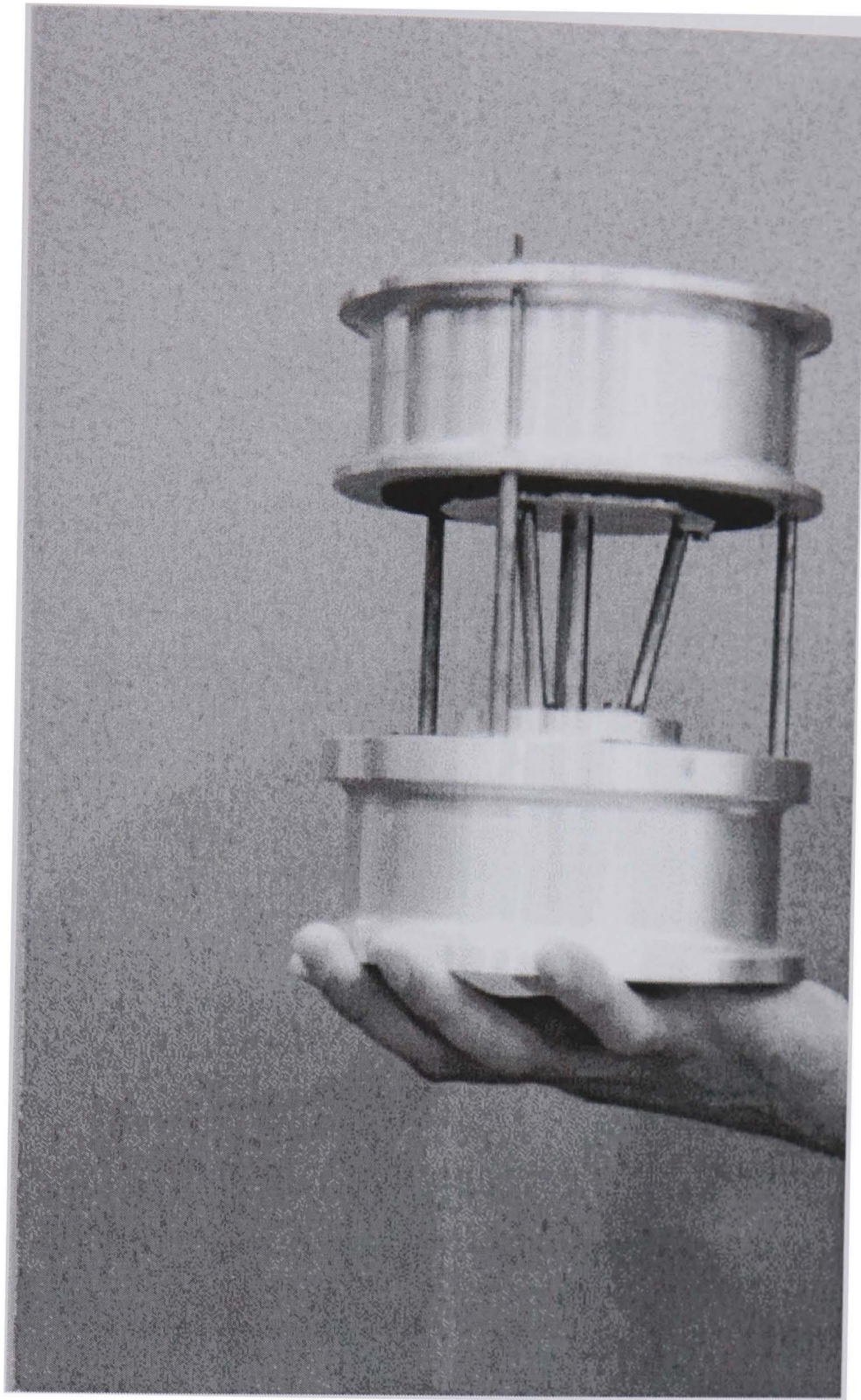


Figure 7.1 CVHRCC mechanism

Since the CVHRCC floating unit is inside a sandwich of sponge, and it weighs only 791 g. during horizontal assembly it causes the sponge sandwich to compress in the gravitational direction. This compression is designed to be small. CVHRCC can achieve the peg-in hole insertion process from the horizontal direction, provided that the positional error to be accommodated is less than the deflection of the assembly machine in the vertical direction.

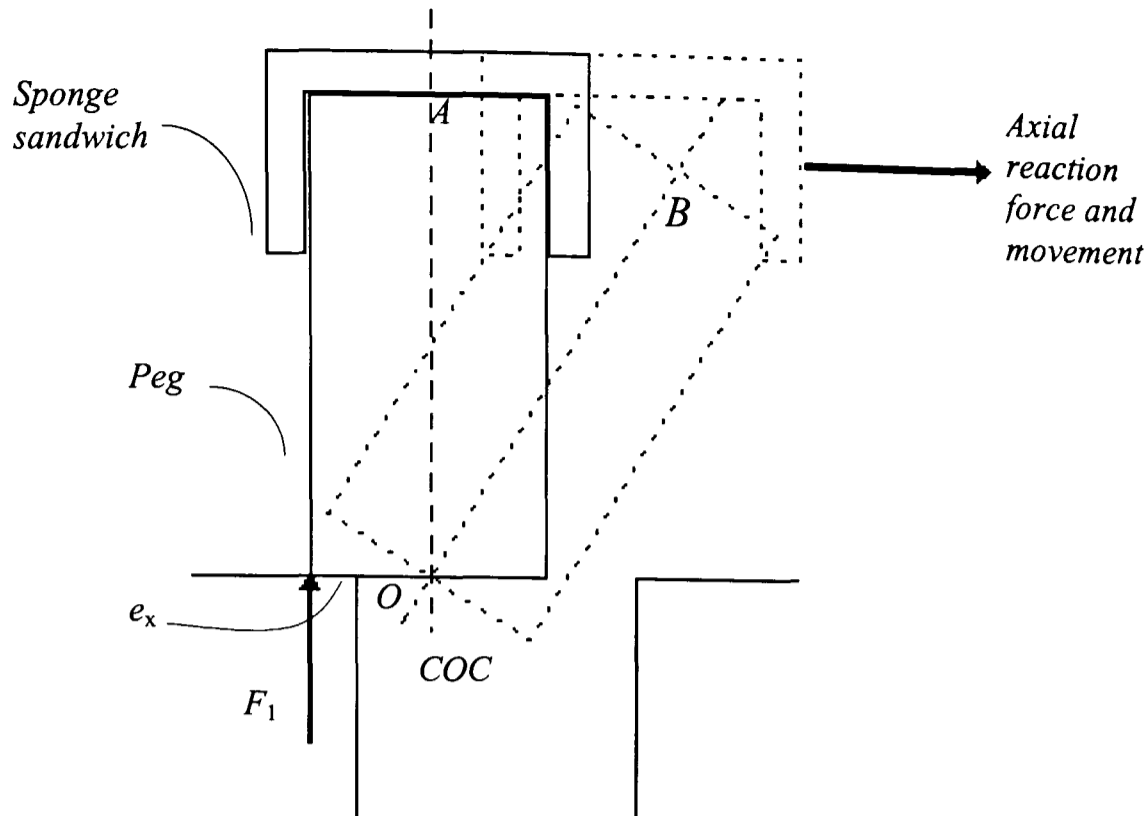


Figure 7.2 Operational principles of the CVHRCC

7.3 WRIST STIFFNESS

During the peg-in hole insertion process, there are small and large forces that act on the inserted peg. Small forces act on the peg while it is in one or two point contact with the hole. At that stage, the rubber attempts to manipulate the peg inside the hole, rather than both wrist structure and rubber. Therefore in this section experiments will be carried out to work out the minimum wrist stiffness. On the other hand, during the initial engagement between the peg and the hole, large reaction forces arise which cause both the wrist structure and rubber to manipulate the peg to the next stage of the insertion process. Testing for finding out the wrist maximum stiffness of this stage is presented in section 7.4.

To find the angular and the lateral wrist minimum stiffness, the CVHRCC was placed on a three axis milling machine. Two separate experiments were carried out to measure CVHRCC angular and lateral deflections. The angular and the lateral stiffness were calculated from the values of the wrist deflections.

Six angular deflection measurements were carried out, the mean measurement of each load was recorded, the angular stiffness of each mean measurement was calculated and the

subtotal was found. The mean angular stiffness of the wrist was the average of the subtotal angular stiffnesses.

Also, six lateral deflection measurements were carried out, a mean measurement for each load was made, and the lateral stiffness of each mean measurement was calculated and subtotal was found. The wrist lateral stiffness was the mean/average of the subtotal lateral stiffnesses.

7.3.1 Wrist Angular Stiffness

CVHRCC was mounted on a milling machine, and a rig as shown in figures (7.3 and 7. 4) was constructed. An angular force in the form of a variable weight hung at the edge of a beam used to create the angular deflection (see figure 7.4).

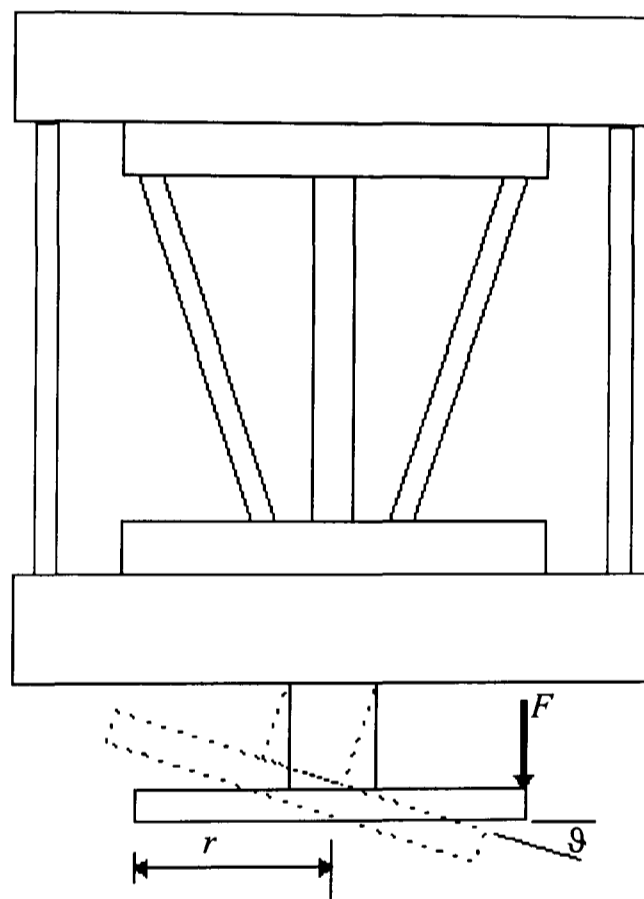


Figure 7.3 Sketch of the experimental rig, CVHRCC during the angular stiffness measurements

A Vernier height gauge used to measure the deflection of the beam at its edge. The gauge zero/reference point in the vertical direction was 168.30 mm from the table of the milling machine. The gauge measurement was the gauge reading less the 168.30 mm . The $\sin \theta$ for the beam/wrist angular deflection was the gauge measurement over the beam radius ($r = 90$

mm from the point of the applied force). Note that the accuracy of the Vernier height gauge is ± 0.01 mm.

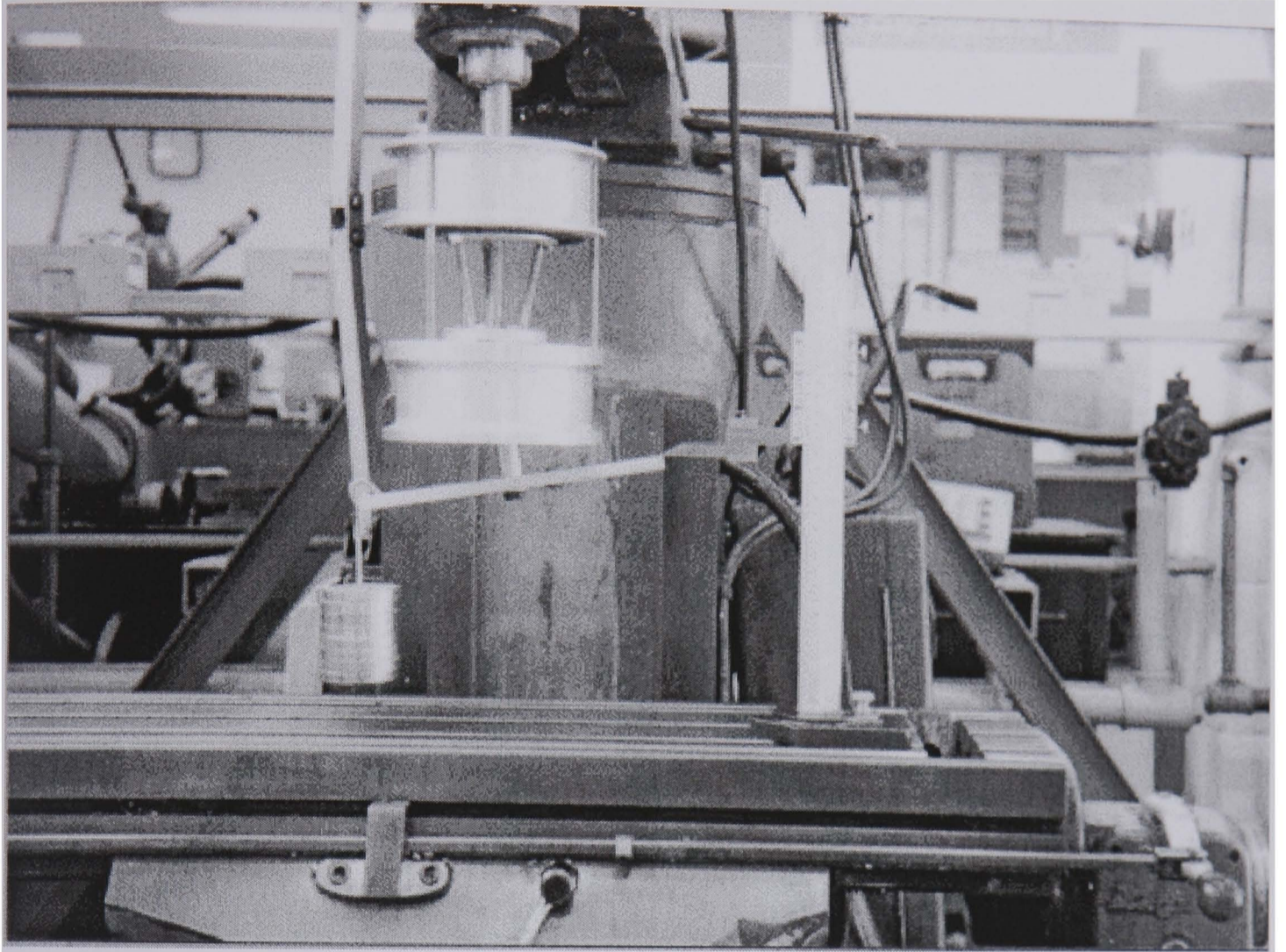


Figure 7.4 CVHRCC on a milling machine, for angular stiffness determination

Table 7.1 Shows experimental data, which was taken during the angular stiffness experiment.

Table 7.1 CVHRCC angular deflection data

Load (N)	Test #1 mm	Test #2 mm	Test #3 mm	Test #4 mm	Test #5 mm	Test #6 mm	Mean (mm)	Mean (degrees)	Theor. mean (degrees)	Mean (rad)	Ang. st. Nmm/rad	Mean Ang. st. Nmm/rad
0	0	0	0	0	0	0	0	0	0	0	0	
0.5	0.88	0.5	0.5	0.4	0.8	0.8	0.6466	0.352	0.537	0.0061	7317.073	
1	1.8	1.42	1.36	1.2	1.9	1.8	1.58	0.862	1.074	0.015	6000	
1.5	3.1	2.5	2.4	2.3	3.18	3.04	2.7533	1.502	1.611	0.026	5192.307	
2	4.35	3.4	3.44	3.38	4.34	4.3	3.8683	2.111	2.148	0.0368	4891.304	
2.5	5.82	4.62	4.7	4.66	5.7	5.9	5.2333	2.856	2.686	0.0498	4518.072	
3	7.1	5.7	6.02	6.1	7.1	7.3	6.5533	3.578	3.223	0.0624	4326.923	
3.5	8.54	7	6.7	7.4	8.66	8.9	7.8666	4.296	3.76	0.0749	4205.607	
4	10.12	8.5	8.7	8.8	10.2	10.34	9.4433	5.159	4.297	0.09	4000	
4.5	11.3	9.8	10	10.1	11.7	11.8	10.783	5.894	4.834	0.103	3932.038	
5	12.52	11.2	11.4	11.2	13.1	13.14	12.093	6.613	5.371	0.115	3913.043	
											48296.37	4829.637037
											037	4800
												Nmm/rad

Note: The actual wrist angular stiffness is based on the sponge stiffness.

The angular stiffness of each mean measurement was calculated from the following equation (of figure 7.3):

$$K_{\theta} = \frac{F \times r}{\delta \theta} \quad (7.1)$$

The wrist angular stiffness is the mean stiffness of each mean measurement and was found to be $4800 \frac{Nmm}{rad}$.

The fact that the wrist angular stiffness is smaller than that of other devices in its category ($30 \times 10^3 - 60 \times 10^3 \frac{Nmm}{rad}$), provides it with more flexibility to accommodate angular errors. Moreover, the wrist flexibility does not cause the peg being assembled to vibrate, because this type of sponge does not tend to vibrate after it is compressed.

7.3.2 Wrist Lateral Stiffness

Again, CVHRCC was mounted on a milling machine (figure 7.5 and 7.6). A lateral force in the form of a variable weight suspended through a string over a pulley applied at the tip of the peg.

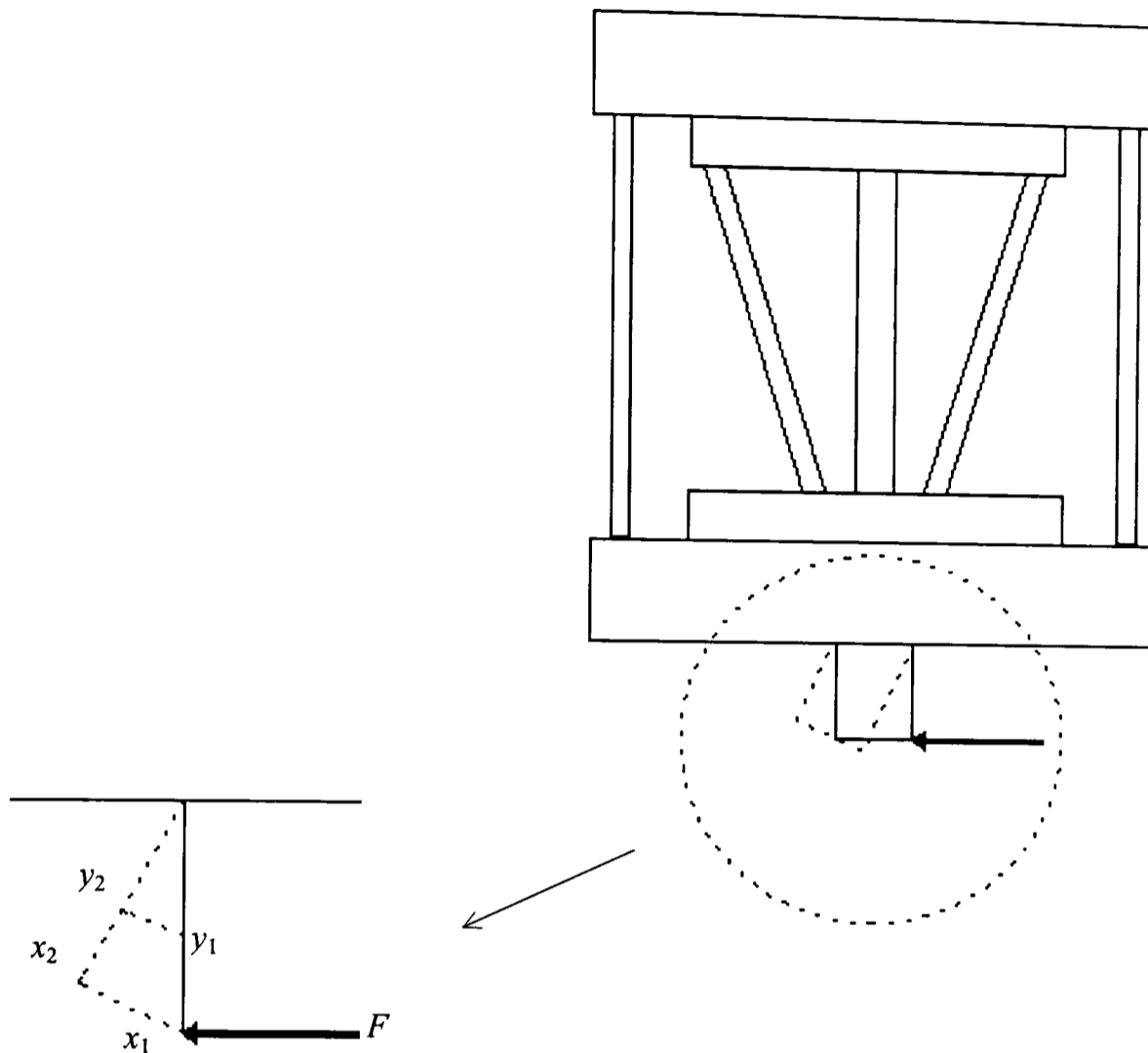


Figure 7.5 Sketch of experimental rig, CVHRCC during lateral stiffness measurements

A dial gauge measured the peg deflection in millimetres from point x_1 to x_2 (δx) was used. In figure (7.5), for ease of calculations, the distance δx is assumed to be a straight line. Note, the accuracy of the dial gauge is ± 0.01 mm.

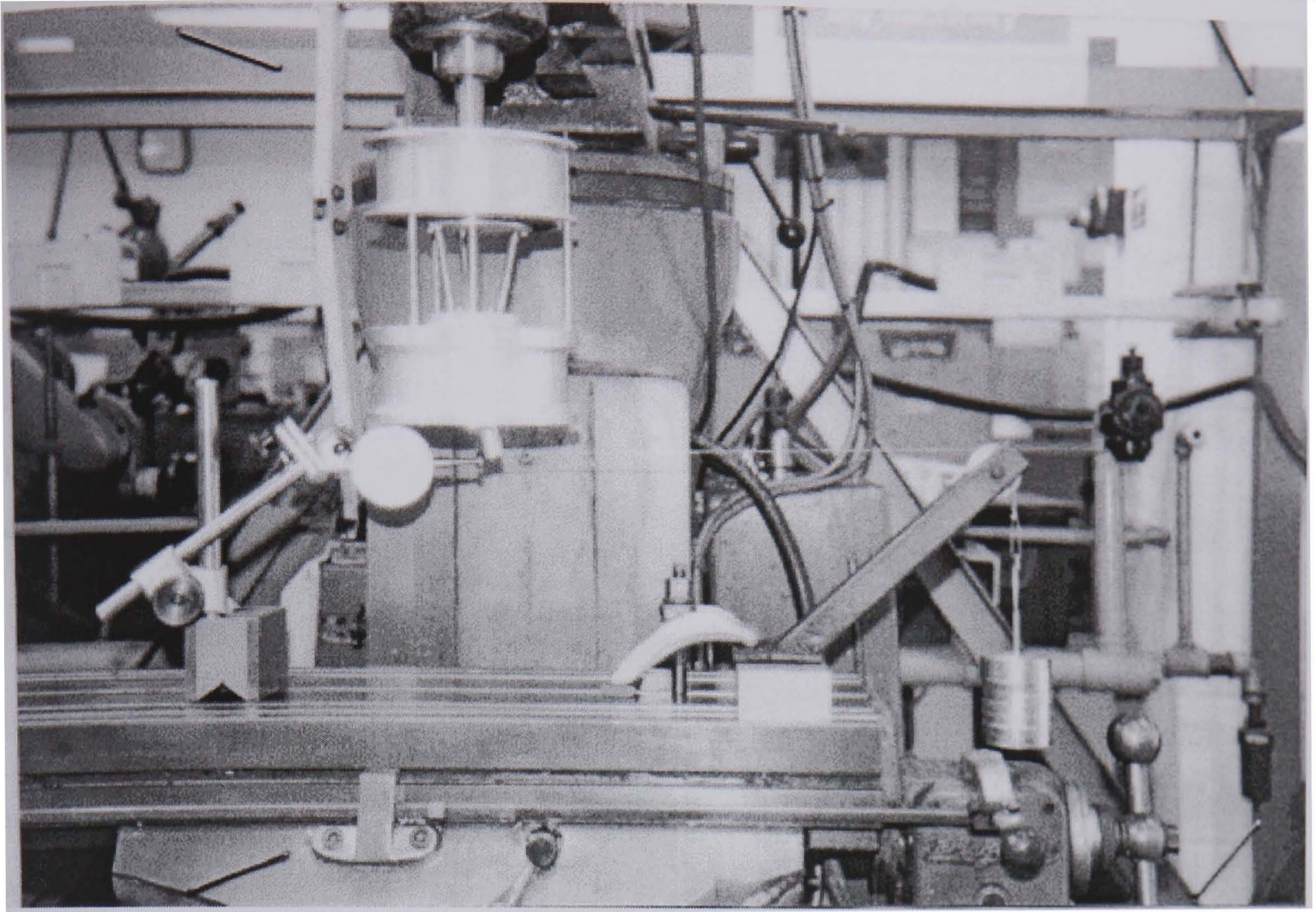


Figure 7.6 CVHRCC on a milling machine, for lateral stiffness determination

The reason why δx was chosen but not δy , is that δx is located near the point where the CVHRCC places its centre of compliance.

The following equation was used to calculate the lateral stiffness for each mean measurement (refer to figure 7.5):

$$K_x = \frac{F}{\delta x} \quad (7.2)$$

As shown in table 7.2, during the measurement process several problems were encountered, among which are the compressibility of the sponge and the starting position of the peg. The first problem was overcome by turning the wrist through 120° periodically. To ensure that the starting position of the peg is the same for every measurement, an alignment from the operator was made before and after each deflection.

Table 7.2 shows experimental data, which was taken during the lateral stiffness experiment. As can be seen in table 7.2 the wrist lateral stiffness is 1.5 N/mm , this value is far less than that for other devices of the same category ($4.5\text{-}10 \text{ N/mm}$). As stated earlier with respect to the angular stiffness, this low stiffness does not cause the wrist/sponge to vibrate, because this kind of sponge has one phase recovery after removing the applied force.

Table 7.2 CVHRCC lateral deflection data

Load (N)	Test #1 mm	Test #2 mm	Test #3 mm	Test #4 mm	Test #5 mm	Test #6 mm	Mean (mm)	Theoretical mean meas. (mm)	Lat. st. (N/mm)	Mean lat. st. (N/mm)
0	0	0	0	0	0	0	0	0	0	
0.5	0.2	0.053	0.14	0.18	0.09	0.18	0.1405	0.333333	3.558718	
1	0.45	0.3	0.485	0.49	0.595	0.45	0.461666	0.666666	2.166065	
1.5	0.79	0.8	0.82	0.79	0.96	0.74	0.816666	1	1.836734	
2	1.27	1.17	1.185	1.12	1.33	1.19	1.210833	1.333333	1.651755	
2.5	1.66	1.55	1.515	1.5	1.71	1.66	1.599166	1.666666	1.563314	
3	2.23	1.92	1.83	1.81	2.085	2.08	1.9925	2	1.505646	
3.5	2.53	2.5	2.29	2.24	2.55	2.59	2.45	2.333333	1.428571	
4	2.9	2.92	2.83	2.75	3	3.07	2.911666	2.666666	1.373783	
4.5	3.36	3.35	3.34	3.19	3.42	3.49	3.358333	3	1.339950	
5	3.98	4.31	3.9	3.59	3.96	4.12	3.976666	3.333333	1.257334	
5.5	4.33	4.71	4.5	4.29	4.49	4.48	4.466666	3.666666	1.231343	
									18.91321	1.576101
										4
										Lat. st. =1.5 N/mm

Note: The actual wrist lateral stiffness is based on the sponge stiffness.

In figures (7.7 and 7.8), the charts demonstrate the relationship between the applied force and the wrist actual and theoretical deflections. Where the theoretical lines were made from the value of the mean angular stiffness and the mean lateral stiffness, which were put in equations (7.1 and 7.2) respectively. Also in figure (7.7 and 7.8), it can be seen that up to 3 N the wrist experimental deflections are almost similar to the theoretical ones. Thereafter the actual deflections are higher than the theoretical ones, the reason for that is that the higher the applied force becomes, the larger the sponge is compressed and therefore the less efficient the wrist recovers.

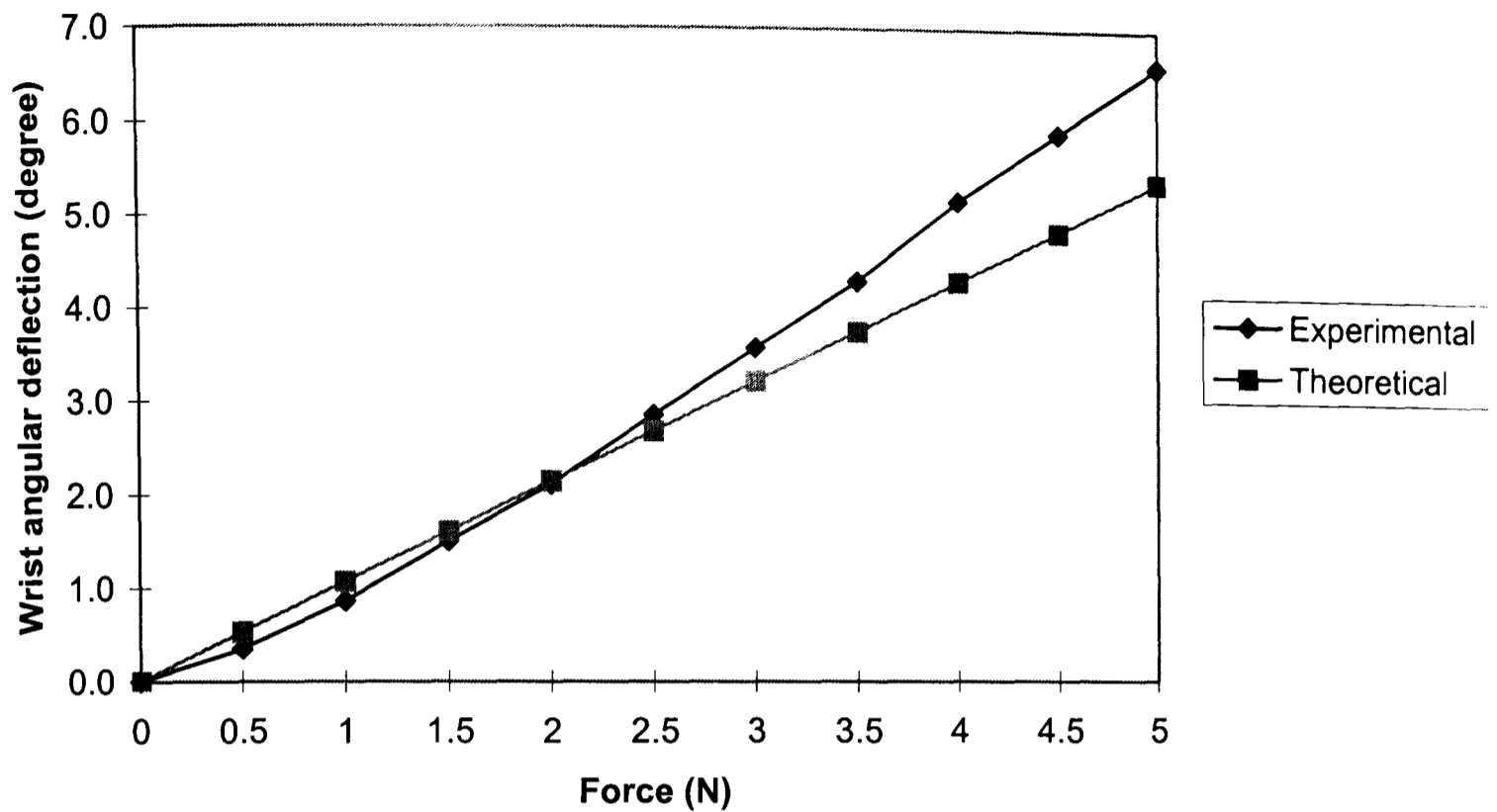


Figure 7.7 Comparison between experimental, theoretical CVHRCC angular deflection

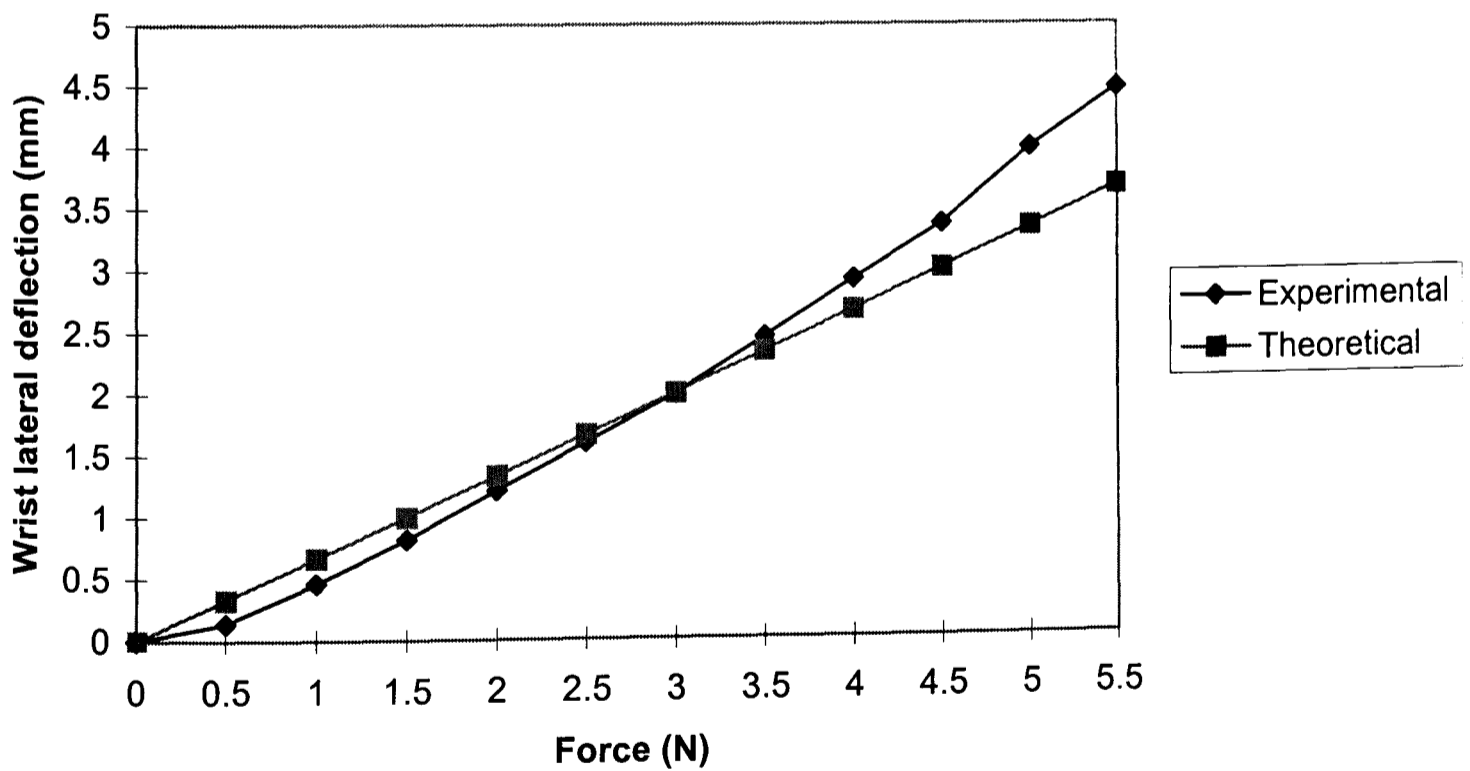


Figure 7.8 Comparison between experimental, theoretical CVHRCC lateral deflection

7.4 MAXIMUM WRIST STIFFNESS

In section 7.3, the minimum angular and lateral wrist stiffness was found. However that stiffness is correct for a situation where the peg is already inside the hole in either one or two point contact. In this section the maximum wrist stiffness is to be determined based on the movement of both, the rubber and the wrist structure as a result of the peg deflection. Thus, a 30 mm peg is attached to the wrist and the wrist is mounted on a Mays Tensile Testing Machine. Then, the bottom surface of the peg is confined to a square metal block (the peg just touching the surface of the block). So the peg overlaps the block by 1 mm (see figure (7.9) and also refer to figure 3.7 in chapter 3).

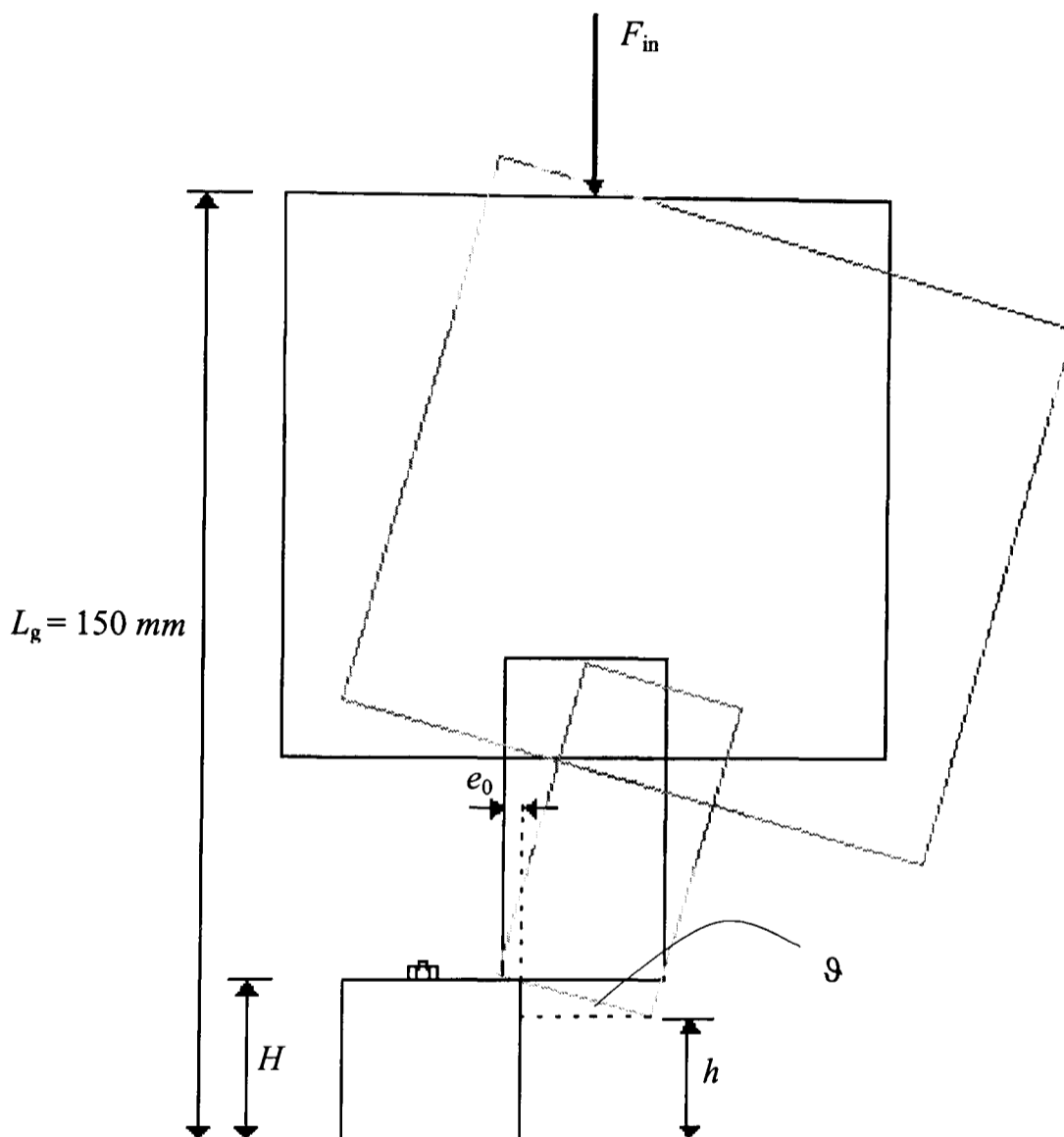


Figure 7.9 Sketch of peg-wrist during the test

Four experiments are carried out to measure the vertical distance from the table surface to the lowest point at the peg bottom surface. The applied force is from 100 to 500 N. As shown in figure (7.9), a Vernier height gauge is used to measure the vertical distance h . Then the angle ϑ is given in the relation:

$$\sin \vartheta = \frac{\Delta h}{d - e_0} \quad (7.3)$$

To find the wrist angular stiffness, a moment is taken about the centre point of the bottom surface of the peg that shown in figure (7.9), it yields:

$$\begin{aligned} F_z(r - e_0) &= K_x e_x L_g - K_\vartheta \vartheta \\ F_{in} \cos \vartheta (r - e_0) &= F_{in} \sin \vartheta L_g - K_\vartheta \vartheta \\ K_\vartheta &= \frac{[L_g \sin \vartheta - \cos \vartheta (r - e_0)]}{\vartheta} \end{aligned} \quad (7.4)$$

Also, there is the relation,

$$K_x = \frac{F_x}{e_x} = \frac{F_{in} \sin \vartheta}{e_0} \quad \text{providing that } e_0 = e_x \quad (7.5)$$

Using eq. (7.3 to 7.5), the value of the angular tilt and wrist stiffness is determined and placed in tables 7.3 to 7.6.

Table 7.3 First test, experimental data and wrist stiffness

$F_{in}(N)$	H (mm)	h (mm)	Δh (mm)	ϑ°	K_ϑ Nmm/rad	K_x N/mm
100	38	36.5	1.5	2.96	16053	7
150	38	36.25	1.75	3.45	16395	12
200	38	36	2	3.95	14021	18
250	38	36	2	3.95	13178	23
300	38	35.5	2.5	4.94	4771	34
350	38	35.5	2.5	4.94	4186	40
400	38	35.5	2.5	4.94	6363	45

Mean stiffness = 10710 Nmm/rad and, 26 N/mm

Table 7.4 Second test, experimental data and wrist stiffness

$F_{in}(N)$	H (mm)	h (mm)	Δh (mm)	θ°	K_θ Nmm/rad	K_X N/mm
100	38	36	2	3.95	7010	9
150	38	35.75	2.25	4.45	5958	15
200	38	35.75	2.25	4.45	7944	21
250	38	35.5	2.5	4.94	3977	29
300	38	35.5	2.5	4.94	4771	35
350	38	35.5	2.5	4.94	5567	40
400	38	35.25	2.75	5.44	1589	50

Mean stiffness = 5260 Nmm/rad and, 28 N/mm

Table 7.5 Third test, experimental data and wrist stiffness

$F_{in}(N)$	H (mm)	h (mm)	Δh (mm)	θ°	K_θ Nmm/rad	K_X N/mm
100	38	36.5	1.5	2.96	16054	7
150	38	36	2	3.95	7907	14
200	38	35.5	2.5	4.94	3181	23
250	38	35.5	2.5	4.94	3977	29
300	38	35.5	2.5	4.94	4771	35
350	38	35.25	2.75	5.44	1390	44
400	38	35.25	2.75	5.44	1589	51

Mean stiffness = 5553 Nmm/rad and, 29 N/mm

Table 7.6 Fourth test, experimental data and wrist stiffness

$F_{in}(N)$	H (mm)	h (mm)	Δh (mm)	θ°	K_θ Nmm/rad	K_X N/mm
100	38	36	2	3.95	7010	9
150	38	35.75	2.25	4.45	5958	15
200	38	35.75	2.25	4.45	7944	21
250	38	35.75	2.25	4.45	9930	26
300	38	35.5	2.5	4.94	4771	35
350	38	35.5	2.5	4.94	5567	40
400	38	35.25	2.75	5.44	1589	51

Mean stiffness = 6110 Nmm/rad and, 28 N/mm

From the data presented in tables 7.3-6, the mean wrist stiffness is found to be:

Angular stiffness, $K_\theta = 6900$ Nmm/rad

Lateral stiffness, $K_X = 30$ N/mm

To show the behaviour of the wrist stiffness in the presence of different applied forces, the data presented in tables 7.3 to 7.6 is plotted and presented in figures (7.10 and 7.11).

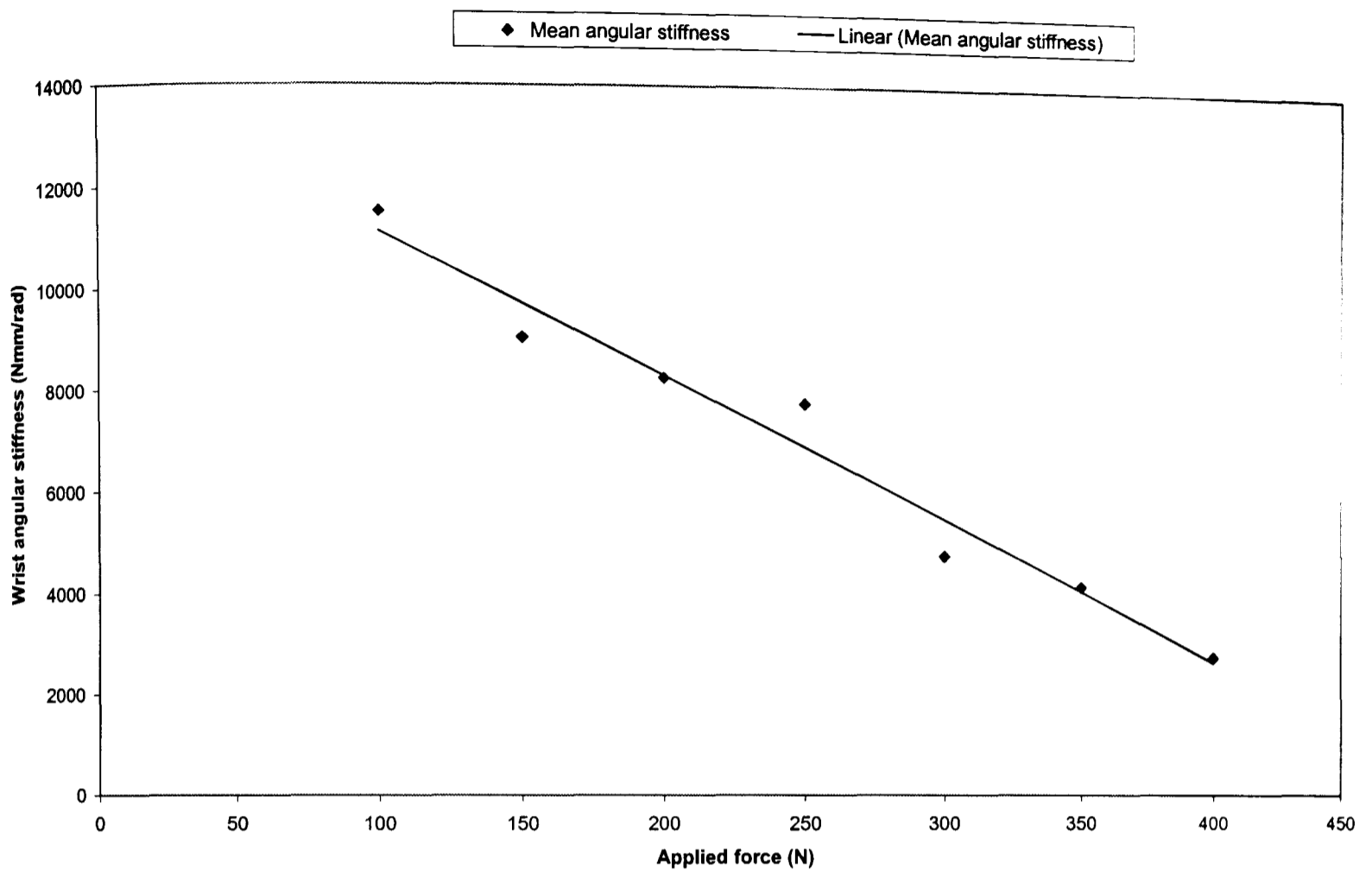


Figure 7.10 The applied force versus the wrist angular stiffness

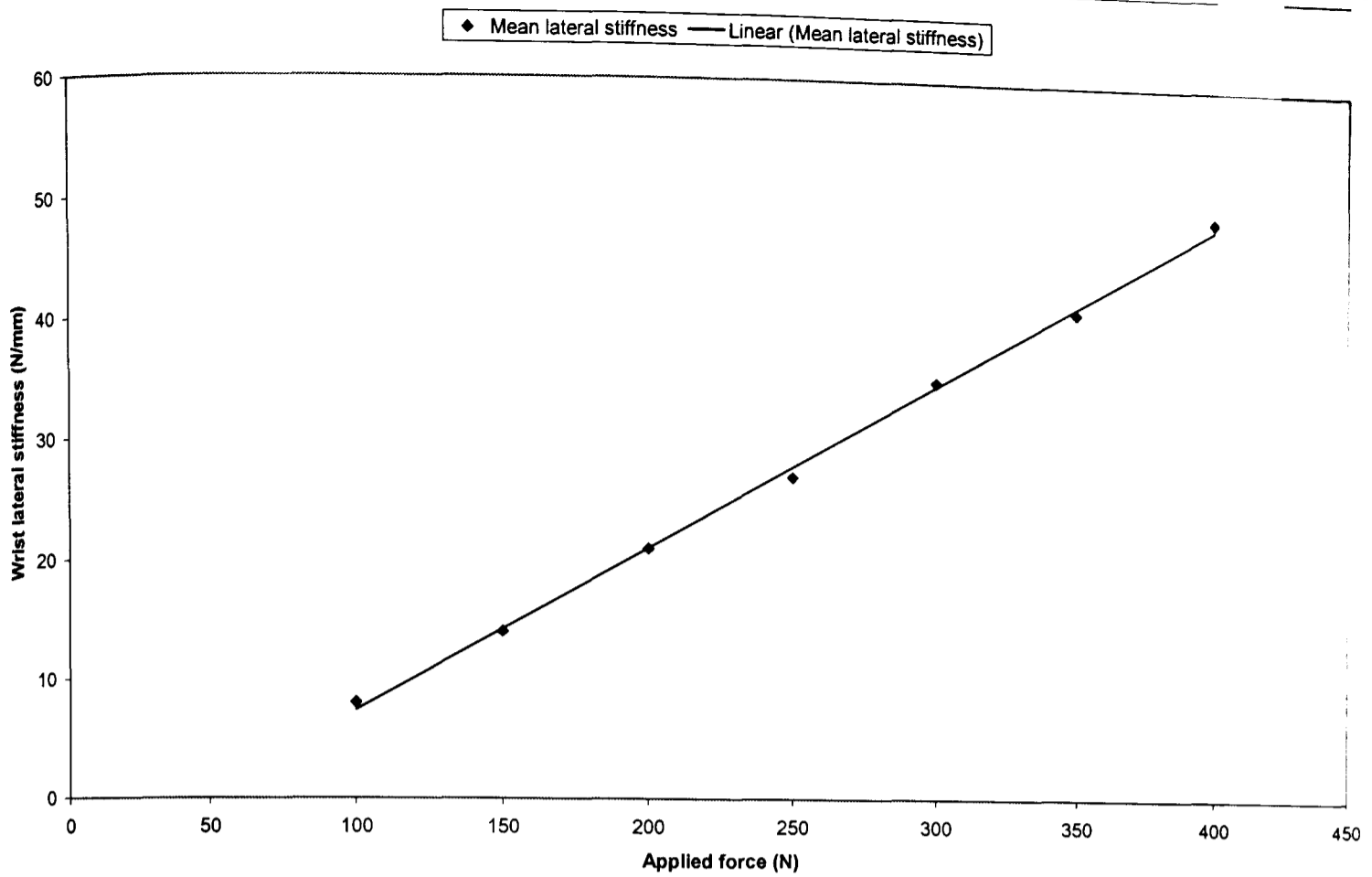


Figure 7.11 The applied force versus the wrist lateral stiffness

As shown in figure (7.10), the larger the applied force becomes, the larger the peg tilts and accordingly the more flexible the wrist becomes (the angular stiffness decreased). On the other hand, in figure (7.11) the increase in the magnitude of the applied force, results in a larger lateral stiffness. Because the lateral force increases as a result of the increase in the peg angular tilt (refer to eq. 7.5).

7.5 WRIST DESIGN

The requirements are to have a wrist mechanism that adopts the passive technology to accommodate errors between chamferless mating parts during an assembly operation from vertical and horizontal directions. The wrist should have a projection of 150 *mm* of its centre of compliance and should have stiffness within the boundary of the theoretical one. Also, the wrist has to accommodate positional errors within the theoretical limits (refer to theoretical results in chapter 6). Also, the wrist should accommodate a peg of variable diameter.

The wrist design covers:

- the dimensions of the elements which make the wrist,
- and the wrist/components stress analysis using Algor-FEA.

The dimensions of the wrist elements were based on the size of a general RCC model. The dimensions were chosen to be (see figure 7.12):

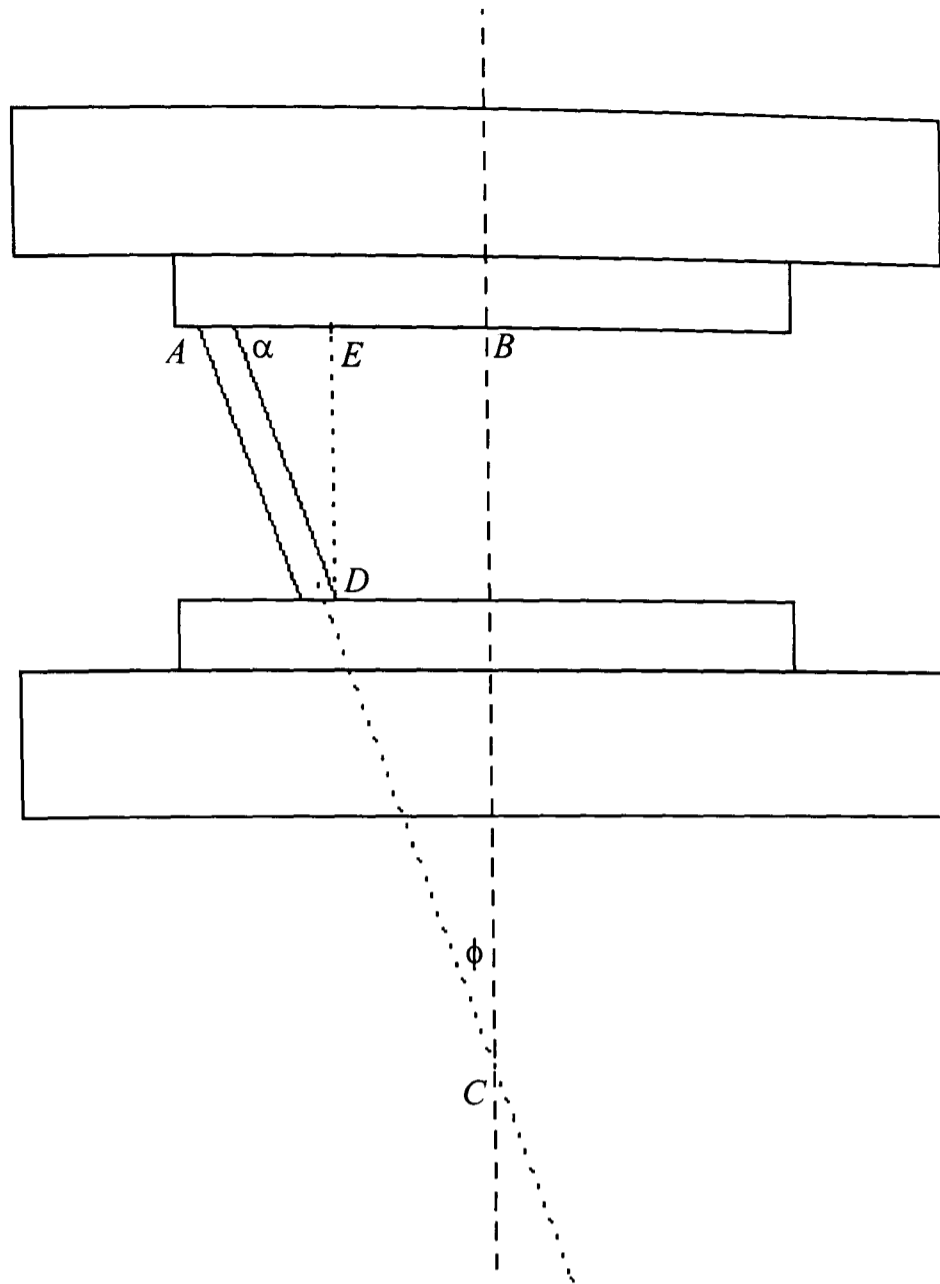


Figure 7.12 Scheme for the wrist design parameters

$$BC = 150 \text{ mm}$$

$$DE = 60 \text{ mm}$$

Based on

$$\mu = 0.15 \quad (\text{coefficient of friction})$$

and

$$\phi = 12^\circ$$

$\tan \phi$ must be larger than coefficient of friction, otherwise jamming could occur while the wrist is in use. To verify that, the above values were checked as follow:

$$\tan 12^\circ \cong 0.21 > 0.15$$

therefore the above values are valid.

For

$$\alpha = 78^\circ$$

In triangle ABC

$$AB = \frac{BC}{\tan 78} = \frac{150}{\tan 78} \cong 31.88 \text{ mm} \quad (7.6)$$

In triangle ADE

$$AD = \frac{DE}{\sin \alpha} = \frac{60}{\sin 78} \cong 61.34 \text{ mm} \quad (7.7)$$

The wrist dimensions were chosen to be

$$L_g = 150 \text{ mm}$$

$$\phi = 12^\circ$$

$$\alpha = 78^\circ$$

$$AB = 31.88 \text{ mm}$$

$$DE = 60 \text{ mm}$$

$$AD = 61.34 \text{ mm}$$

Based on the values of the wrist theoretical stiffness (refer to chapter 6), the wrist sponge thickness was chosen through personal communication with several rubber manufacturers and consultants amongst, (Metalastic LTD. Leicester). Based on this advice the sponge thickness was chosen as in the design drawing section (see appendix 3).

The wrist stress analysis; the objective of this investigation is to verify the stresses inside the wrist and the possible failure of any of the wrist components subjected to different forces. Due to the limited capabilities in the Algor software, which was discovered in the final stages of the FEA; modelling the CVHRCC as a whole model was not possible. Therefore, the model was simplified and broke into seven major components (see drawings in appendix 3), and each component was converted into 3D bricks. Note that this analysis assumed the critical case, when the rubber fails and large reaction forces exist.

The bottom plate of the fixed unit is shown in figure (1, appendix 3). It is fully constrained, and subjected to several forces starting from 50 to 500 N and 50 to 500 N in the Y and the Z directions-where possible collision with the inside plate could happen. According to the FEA results, the maximum stress is far less than the allowable stress for aluminium. Also, the worst deformation at any node is:

$$DX = -1.164e-010 \text{ mm}, DY = 1.080e-090 \text{ mm}, DZ = -9.770e-012 \text{ mm}$$

Therefore, these deformations are negligible and there is no risk of whatsoever of material failure.

Again, looking at the FEA results figures (1 to 10, in appendix 3), and in particular the one in figure (7), where the rod was subjected to different reaction forces (50-500 N). The maximum stress in the steel rod is over 350 N/mm^2 and the deformation at the worst node in that area is:

$$DX = 5.267e-011 \text{ mm}, DY = 6.965e-007 \text{ mm} \text{ and } DZ = 1.951e-007 \text{ mm. These deformations are still negligible.}$$

7.6 DISCUSSION

The CVHRCC mechanism was built as a prototype for research and experimental use. The two types of measurements that were carried out on it for finding the minimum and maximum lateral and angular stiffness have yielded stiffness values, which coincide with the theoretical ones that were obtained in chapter 6.

As stated earlier, the capability to rotate the peg being inserted into a hole about its centre of rotation so it can align itself to the hole in case of a positional error, has made the CVHRCC unique among other devices in its category (passive compliant devices). Normally, other devices combine more than one technique to accommodate positional errors between chamferless mating parts. There have been no reports to date of writing the thesis up, of any other device in that category with the ability to work in the horizontal direction, unlike the CVHRCC which was designed and built for this purpose (Further discussing is presented in chapter 9.)

One problem was encountered after CVHRCC was built is that it weighed about 4 Kg including the sponge, therefore some material from around the top and the bottom plates were taken out reducing the weight to 3.1 Kg. Also, despite the inability of Algor-FEA in modelling the CVHRCC as one unit, it was proved that the structure of the CVHRCC is strong enough to withstand against reaction forces, which may arise in case of failure of the rubber. Note, after completing the FEA using Algor, other packages were discovered that can do modelling and simulation and thereafter stress analysis for solid parts and assembly parts (product made of several parts). These packages are: MARC K7.3, ANSYS FEA and Unigraphics (UG V16).

7.7 CONCLUSION

This chapter has led to the following conclusions:

1. CVHRCC is a passive wrist, which utilises its flexibility to operate with chamferless mating parts from vertical and horizontal direction.
2. The CVHRCC characteristics are:
 - the centre of compliance is projected at a distance of 150 mm,
 - minimum stiffness: angular stiffness $4.8 \times 10^3 \text{ Nmm/rad}$, and $1.5 \times 10^3 \text{ N/mm}$ lateral stiffness,
 - maximum stiffness: angular stiffness $6.9 \times 10^3 \text{ Nmm/rad}$, and 30 N/mm lateral stiffness.
 - weight is 3.10 Kg.

CHAPTER 8

EXPERIMENTS AND DATA CORRELATION

8.1 INTRODUCTION

It is already been said that the peg-in hole example is the most common task in assembly. To support that, here are some case-studies: Kondoleon [A. Kondoleon, 1976] has examined ten products such as a refrigerator compressor, an electric jigsaw, an induction electric motor, a toaster-oven, a bicycle brake and the automobile alternator etc. Three principal directions to insert components into each other has been identified (X-Y-Z axes), and the most frequent task was the cylindrical peg-in hole task. Other study by General Motors [P. Lynch, 1976] found that 90% of the components used in the assembly of an automobile weigh less than 2 Kg. Moreover, the round peg-in hole tasks using a chamfer on either of the mating parts are the most frequent in the assembly of metal products with machined or cast parts.

So, the objective of this chapter is to present a series of experiments that have been carried out to test the CVHRCC in real assembly environment of chamferless pegs and a hole of different sizes and from different directions. Also, to compare the experimental results with the theoretical ones obtained in previous analysis.

The structure of this chapter is as follows:

Section 8.2 is the first stage of experiments.

Section 8.3 is the second stage of experiments include the wrist-rig instrumentation

Section 8.4 is a general discussion of this work and its shortcomings.

Section 8.5 is the conclusion.

A series of peg-hole assembly experiments were carried out to test the CVHRCC. The results have shown that the CVHRCC could accommodate over 2 mm and 3° allowable positioning error between mating parts with clearance of 0.3 mm. Although the experimental results have shown some agreement with the theoretical ones, the assembly of chamferless mating parts with small clearance (tolerance H7/h6) has a success rate of under 40%. Also, from the horizontal direction still some improvement is needed.

8.2 FIRST STAGE OF EXPERIMENTS

In this stage of experiments, the CVHRCC was tested in an assembly operation of chamferless mating parts. Several pegs of different diameters and a hole made of carbon steel with coefficient of friction 0.2 (commercial steel has a coefficient of friction from 0.1 to 0.2) to be used. At this stage of the research, the objective of these experiments is to demonstrate the capabilities of the CVHRCC from vertical and horizontal directions, and also, to examine its success rate.

8.2.1 Experimental Rig

At this stage, it is not advisable to mount the CVHRCC on an assembly robot for experimental use, because of the high risk in causing damage to the robot in case of the occurrence of jamming. Therefore an alternative to the assembly robot has to be found.

A basic assembly machine was built for providing the CVHRCC with motion and the insertion force needed to achieve the peg-in hole insertion process. As shown in figure (8.1) the assembly rig comprises of a platform made of extruded aluminium, and a cylinder mounted on top of it for providing the necessary forces and motion to perform an assembly operation. A fixture for aligning the hole laterally was made and mounted at the bottom of the platform. Also an electro-pneumatic valve with 2 regulators for controlling the assembly speed, connected the cylinder to the air supply station. A power supply device used to provide the voltage necessary for switching the system on and off.

8.2.2 Experimental Procedure

CVHRCC was connected to the piston rod and a constant pressure of 4 bar used to provide the motion. A supply of 12 V was used to power the system. A micrometer was used to create different initial lateral misalignments for each insertion action. The accuracy of the micrometer was ± 0.01 mm. Also, a Vernier protractor was used for creating the initial angular misalignment. The accuracy of the Vernier protractor was ± 5 min ($\cong 0.08^\circ$). The assembly operations were performed from the vertical and the horizontal directions. The assembly operations from the vertical direction were carried out on 4 stages:

1. In the first stage a 16 mm peg diameter with a 16.75 mm hole diameter were tested with a varied initial lateral error $\delta e = 0.4, 0.6, \dots 2.00$ mm, and the initial angular error was

- from 0 to 5°. The clearance between the peg and the hole was 0.375 mm. In this stage 50 insertion actions were performed and just twice the peg missed the hole (jammed).
2. In the second stage a 16.30 mm peg diameter with a 16.75 mm hole was tested. The clearance between the peg and the hole was 0.225 mm. This time, due to the small clearance and difficulties in pre-aligning the peg to the hole before the start of the insertion actions, a fixed lateral error of 2 mm and angular error of 3° were used. In this stage 50 insertion attempts were performed and just 15 times the peg missed the hole.

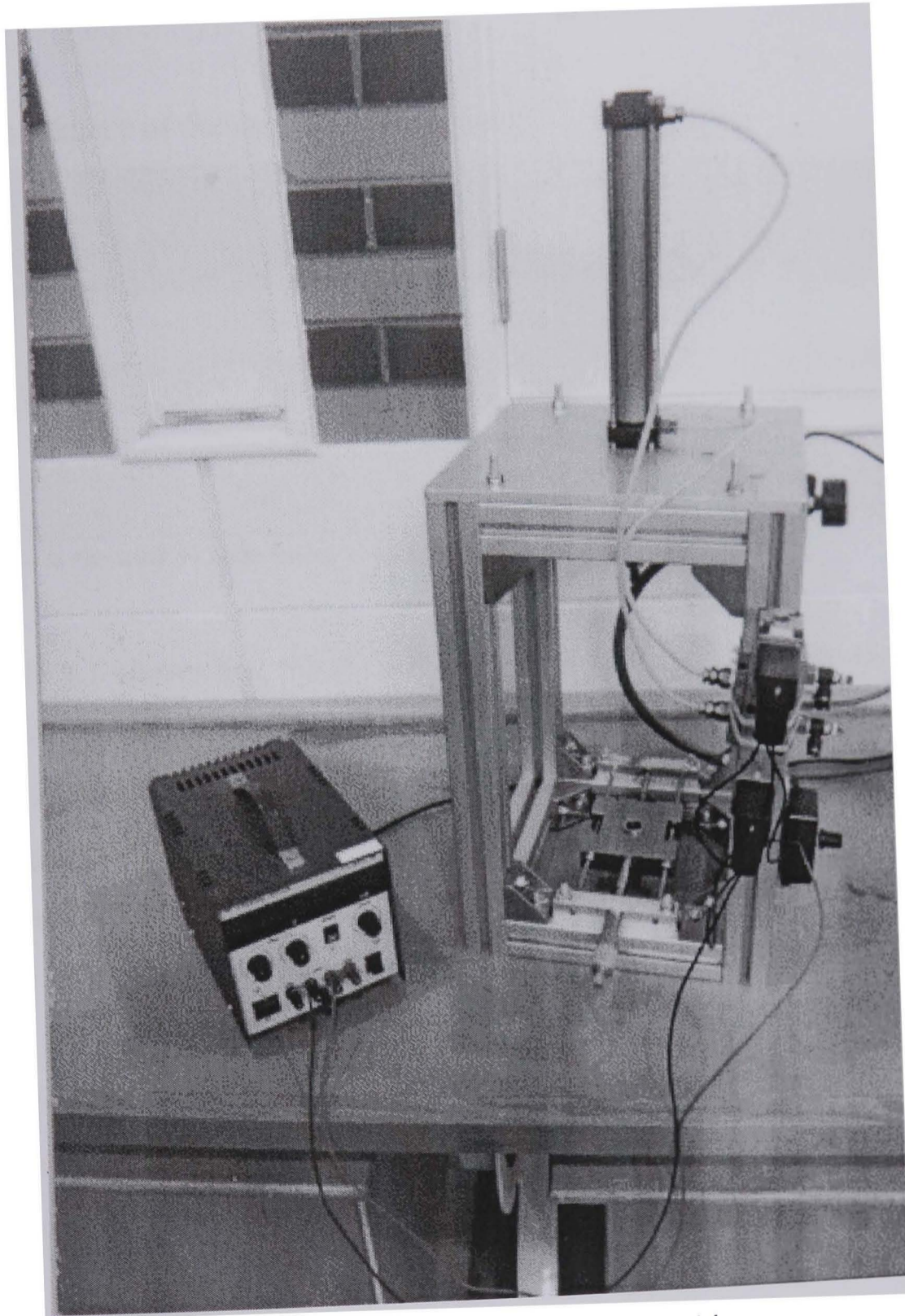


Figure 8.1 The assembly rig/machine

3. In stage three and four 16.50 and 16.70 mm pegs were tested with a 16.75 mm hole respectively. The clearance was 0.125 and 0.025 mm respectively. Again as in the second stage and for the same problems, a fixed lateral error of 1.5 mm and a 3° initial angular error were used. For 0.125 mm clearance the peg missed the hole 25 times of 50 attempts, but for 0.025 mm the peg did not enter the hole at all.

Figure (8.3) shows the CVHRCC during action. Also, table 8.1 is a summary of the 4 stages in which the assembly experiments went through.

Table 8.1 A summary of the assembly experiment

<i>Clearance (mm)</i>	<i>Initial lateral error (mm)</i>	<i>Initial angular error (degrees)</i>	<i>Success rate (%)*</i>
0.025	1.5	-	0
0.125	1.5	3	50
0.225	2	3	70
0.375	0.4 - 2	0 - 5	96

* The success rate is the total of tasks being succeeded over the total inserted tasks.

A look at table 8.1 shows that the CVHRCC works better with clearances larger than 0.3 mm. The reason for this is that the rubber that holds the peg is designed to hold a peg of a certain diameter, the larger the peg becomes the more tight the rubber gets, and results in a larger initial positional error prior to the start of the assembly process. Table 8.1 is also presented in a chart to give a better understanding of the experiments being carried out; this is shown in figure (8.2). As shown in figure (8.2), the success rate for a clearance 0.375 mm is the highest. However, when the initial angular error exceeded the 3°, 10 attempts were carried out and the peg could not enter the hole. Note that for this clearance the peg missed the hole twice, when the angular error is 2°. Also, for clearance 0.025 mm the peg could not enter the hole at all, even when the angular and lateral initial errors were zero.

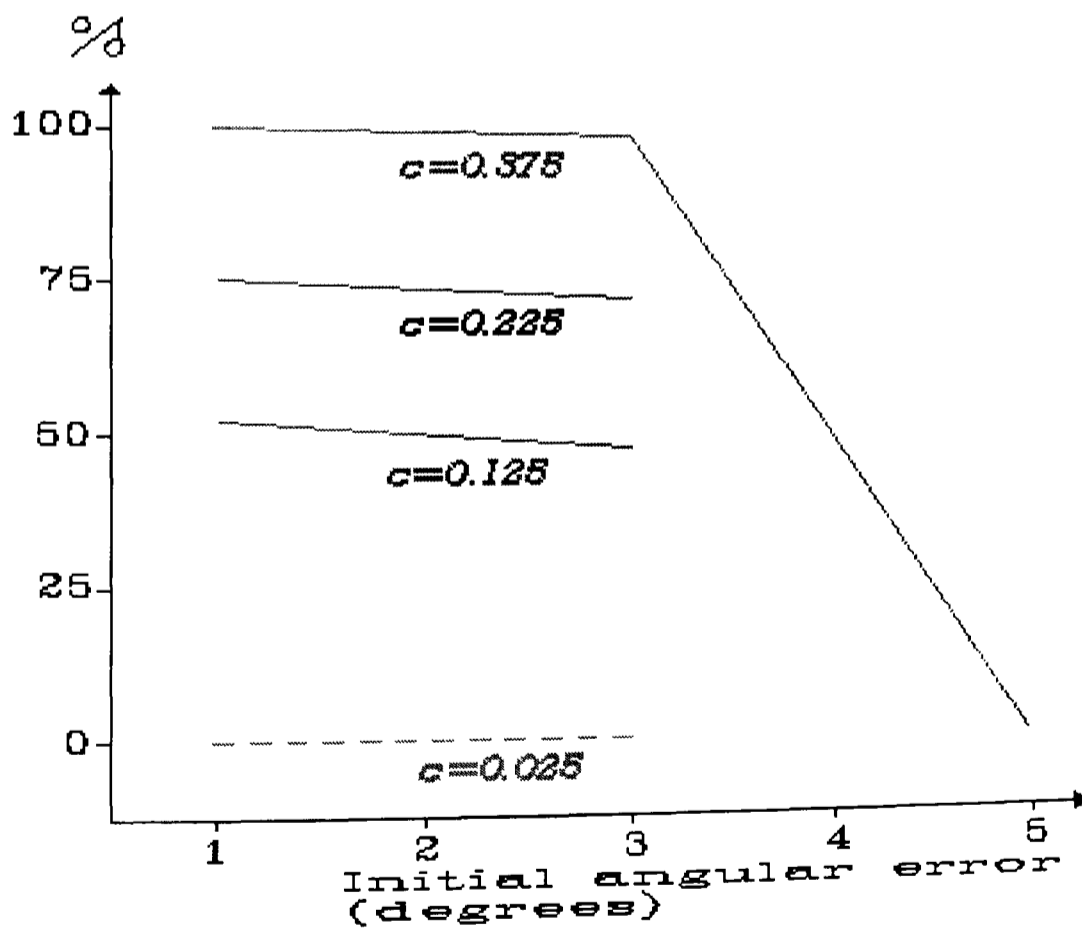
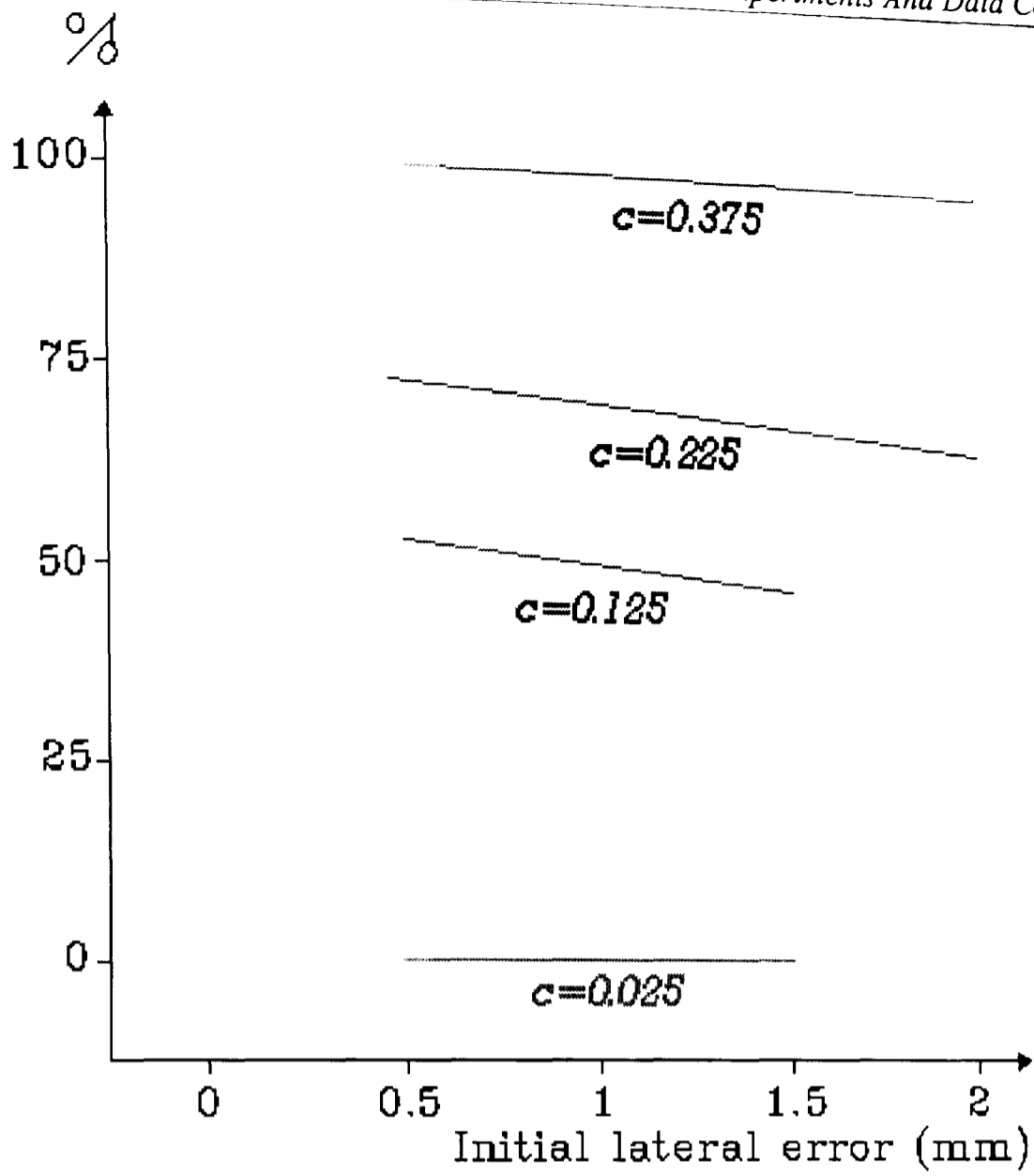


Figure 8.2 The success rate for the experimental positional error

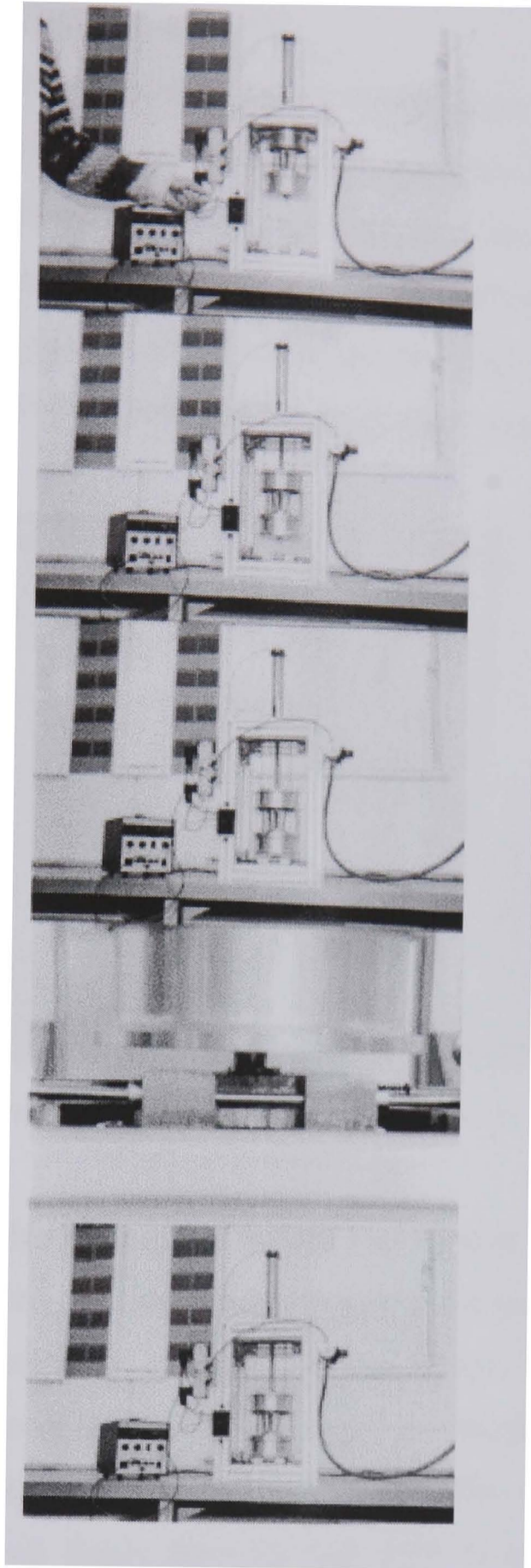


Figure 8.3 CVHRCC performing assembly operation

In horizontal assembly, several attempts were carried out. However, due to the gravity, the piston rod that drives the peg into the hole has bent (up-to 5 mm at the end of the rod). This is because of the weight of the wrist; the results that have been achieved can not be considered at this stage of the research.

8.3 SECOND STAGE OF EXPERIMENTS

In this stage of the assembly experiments, a range of pegs/holes with diameters from 15 to 35 millimetres and different clearances will be tested. However, this time the assembly rig and the wrist are to be instrumented with strain gauges (see figure 8.4) to provide a feedback information in terms of the insertion force to understand the behaviour of the peg-wrist during an insertion process. In addition, the force information from the insertion process should validate and give an understanding to the new assembly strategy.

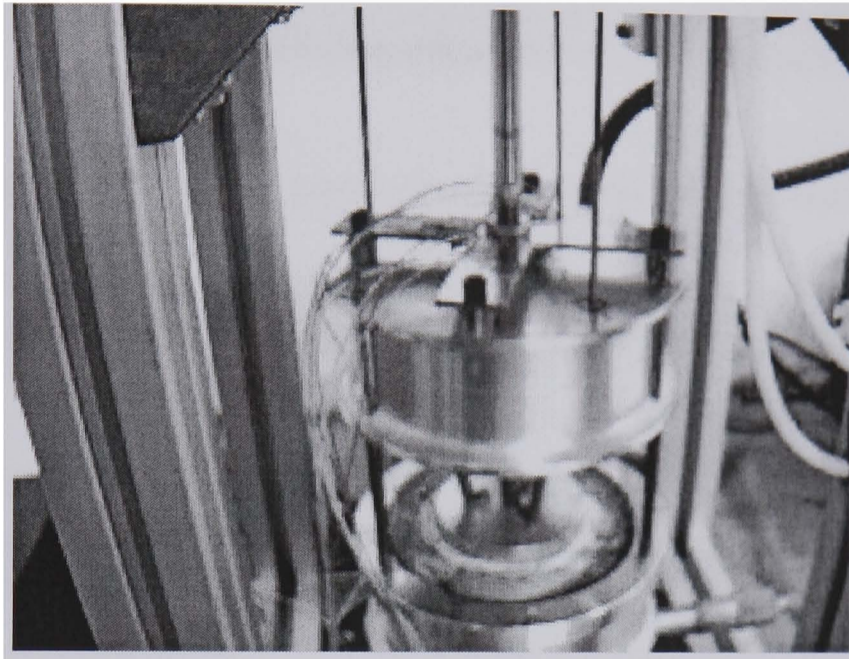


Figure 8.4 Instrumentation of the CVHRCC and the assembly rig

8.3.1 Assembly Rig, Wrist Instrumentation And Calibration

A cross plate made of mild steel was instrumented with strain gauges. On two arms of the plate, four gauges were connected in a full Wheatstone-bridge, two gauges on each arm, one on top and one on bottom of the arm. The top gauges should react under tension and the bottom gauges should react under compression loads. The cross plate thickness is 2 mm. The cross plate was fixed firmly from its four arms to a circular plate. A weight carrier was suspended through the plate centre hole, and weight units of 5 Kg each applied to it. See figure (8.5) for plate instrumentation and calibrations.

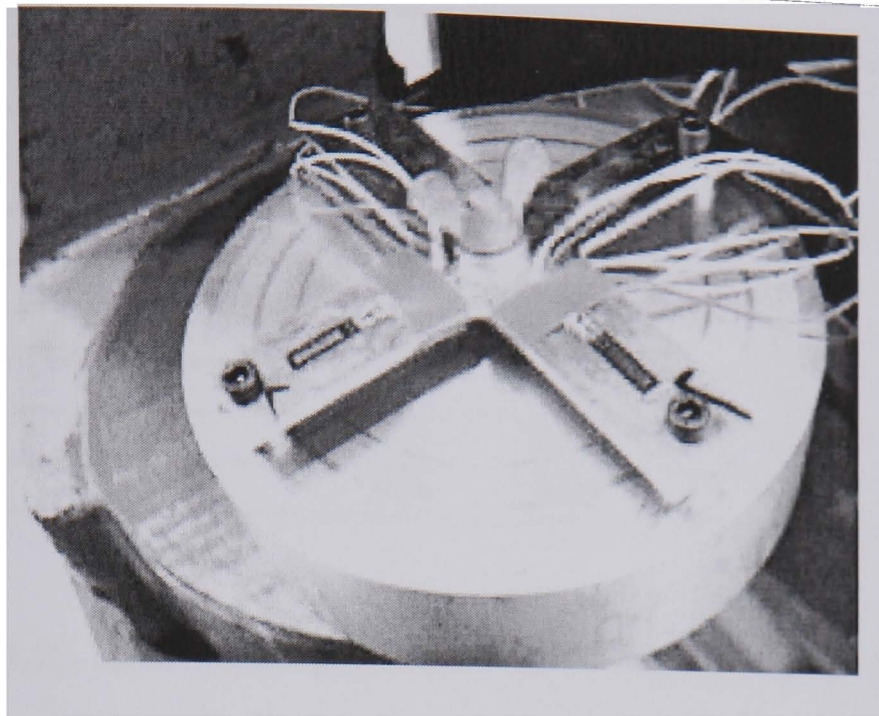


Figure 8.5 Cross plate instrumentation and calibration

Table 8.2 includes the progress of the calibration process for the instrumented cross plate.

Table 8.2 The progress of the cross plate calibration

Cross plate calibration: load vs. micro-strain			
	Test #1		
Load (Kg)	with load	Without load	Mean micro-strain
0	0	0	0
5	120	-0.2	61
10	238	114	176
15	357	230	293.5
20	475	348	411.5
25	592	465	528.5
30	709	581	645
35	823	700	761.5
40	936	816	876
	Test #2		
Load (Kg)	With load	Without load	Mean micro-strain
0	0	0	0
5	118	-1	59.5
10	237	115	176
15	355	231	293
20	473	349	411
25	588	466	527
30	706	583	644.5
35	820	700	760
40	934	817	875
	Test #3		

Load (Kg)	With load	Without load	Mean micro-strain
0	0	0	0
5	117	-1	59
10	236	115	175.5
15	351	233	292
20	470	349	409.5
25	587	466	526.5
30	703	583	643
35	818	699	758.5
40	933	816	874.5

As shown in table (8.2), three tests were carried out to calibrate the cross plate with the full bridge. An average micro-strain reading was made for each test, and for the three tests. This data is presented and plotted in figure (8.6). Also in figure (8.6), the nearest two points on the line were found and the slope for these points was determined (the two points correspond to the 25-30 Kg load of the same figure). Accordingly, the calibration equations is:

$$\text{Insertion force} = \frac{\text{Micro - strain reading}}{23.36} \times 9.81 \quad (8.2)$$

Equations (8.2) gives the value of the insertion force (in Newton's) which could arise during any stage of the insertion process during contact between the mating parts.

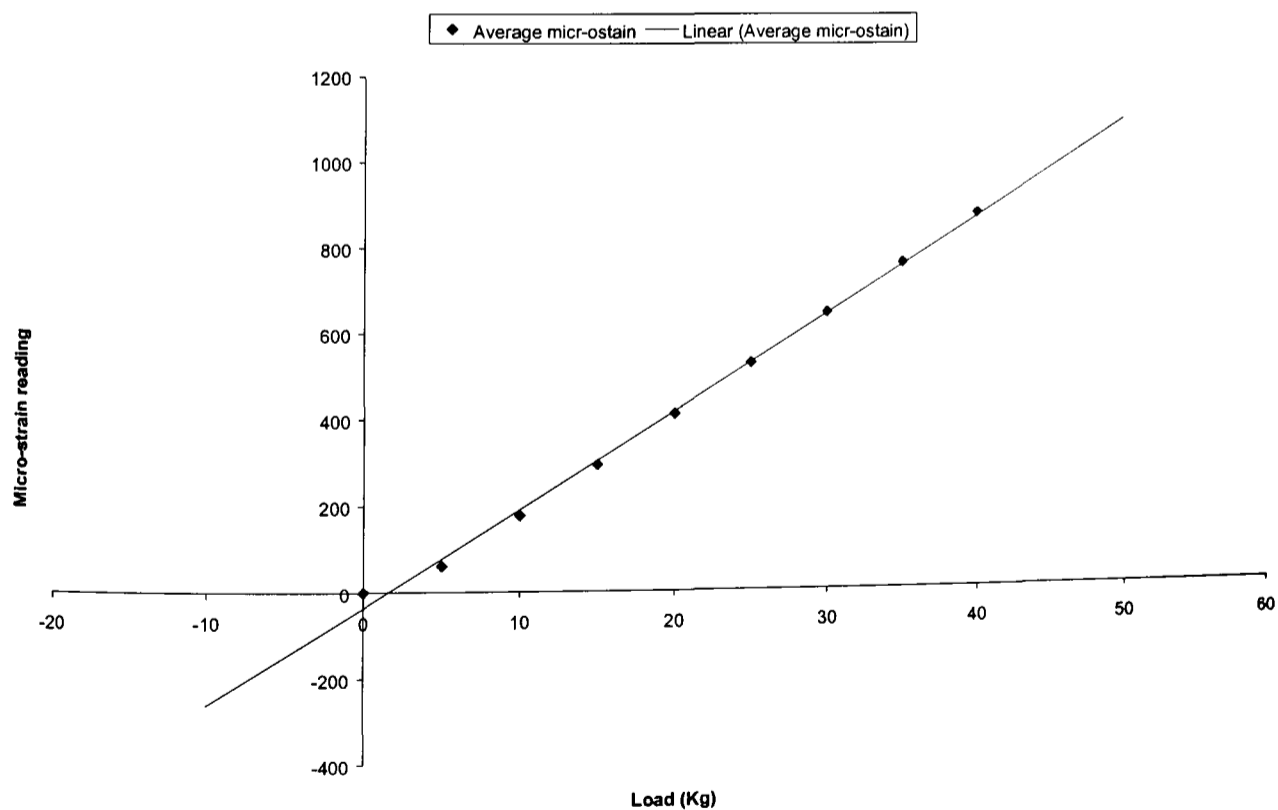


Figure 8.6 The calibration data for the cross plate

8.3.2 Peg-Hole Experiments

In this stage of the assembly experiments pegs with diameter 15 to 35 mm were tested with holes of the same diameters (Note that the peg diameter where it sets inside the rubber is constant and is 16 mm). The pegs length is 67 mm. The clearance between the pegs and the holes were 0.2 and 0.1 mm. In addition, a clearance of transition fit of H7/h6 was used. Each diameter and clearance was tested 5 times in total, to see the progress of the experiments refer to table 1 in appendix 3. The data taken during the experiments is presented statistically in figures (8.7 to 8.10).

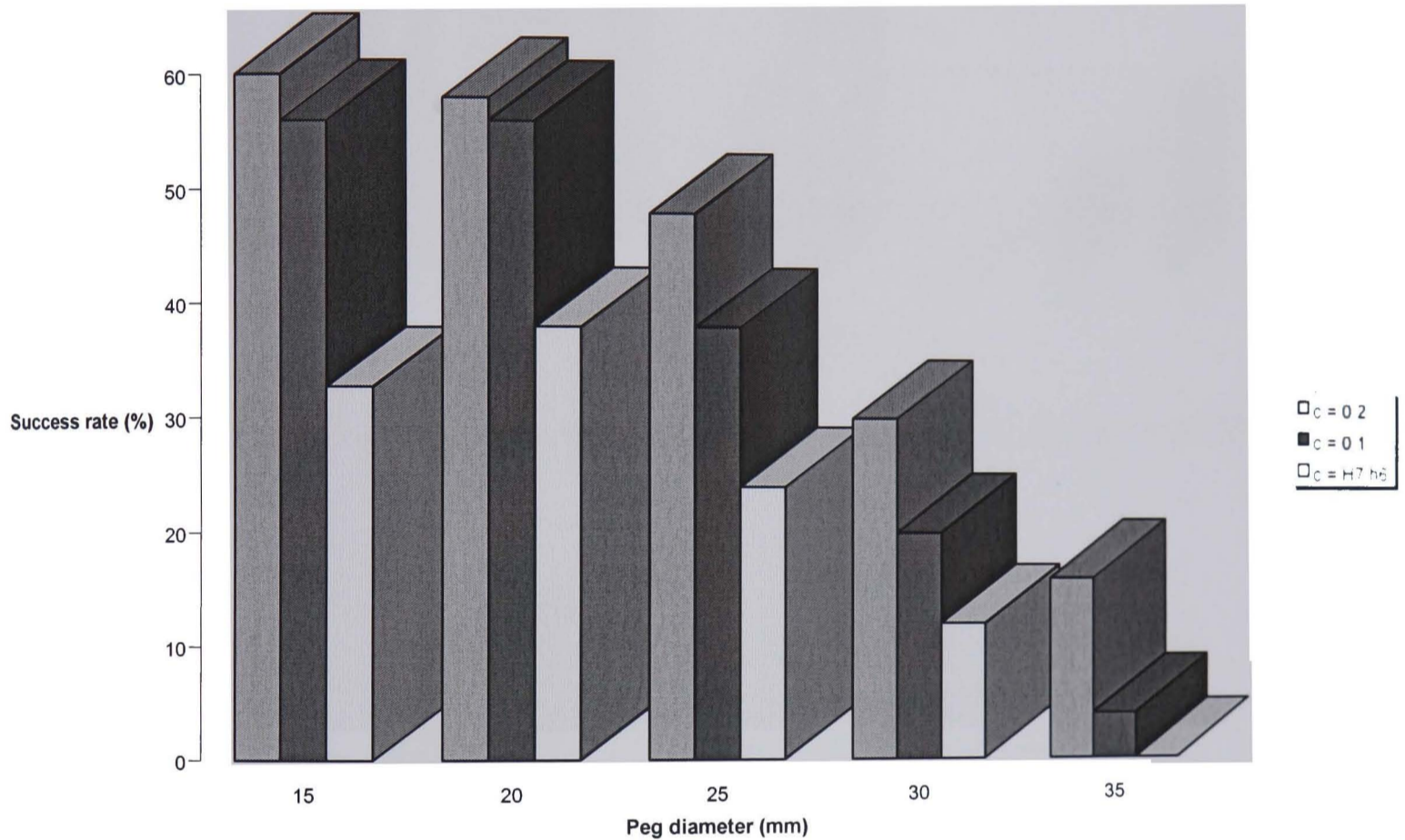


Figure 8.7 The success rate of range of pegs of different diameter

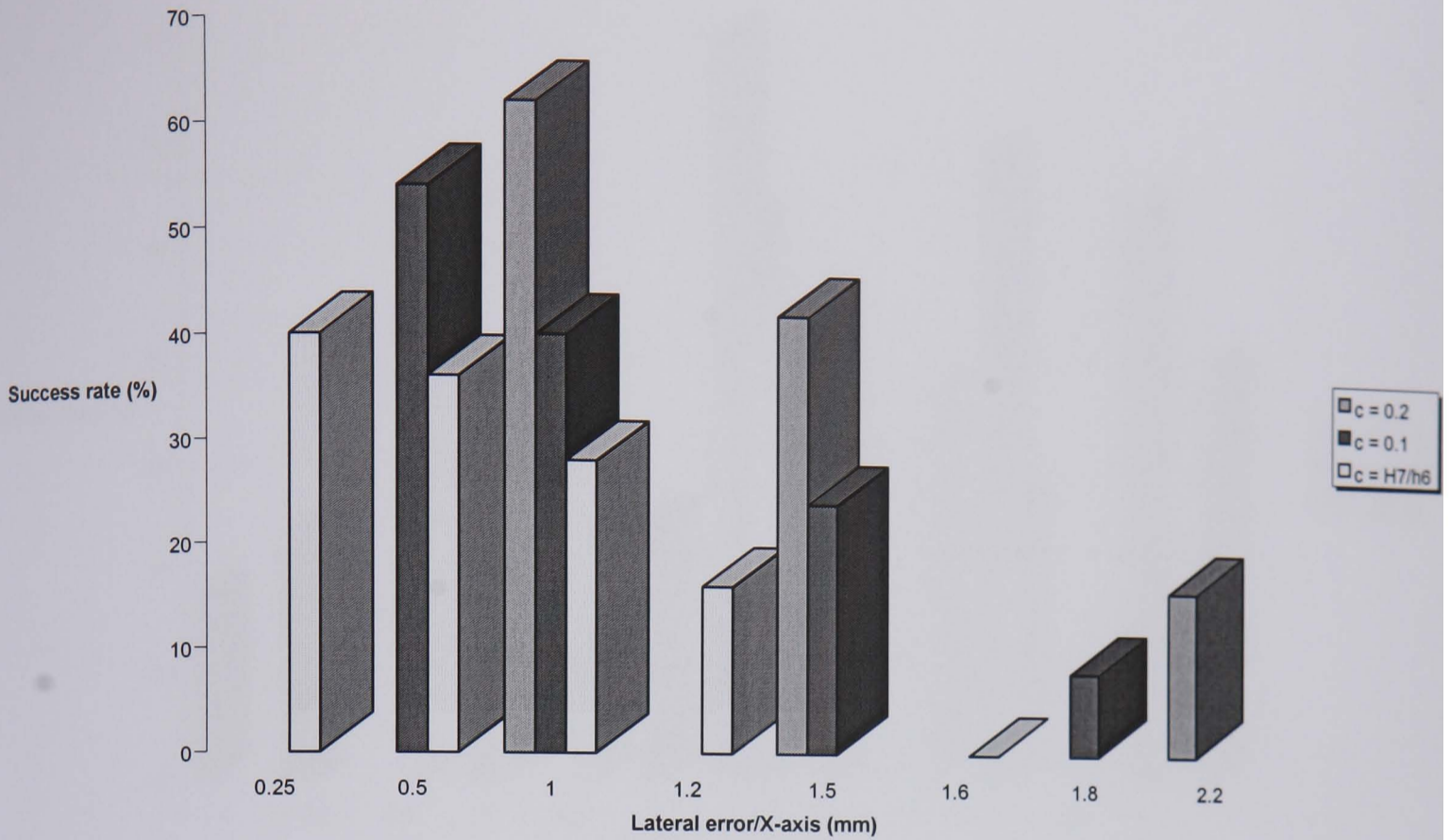


Figure 8.8 The success rate against range of lateral misalignment on the X axis

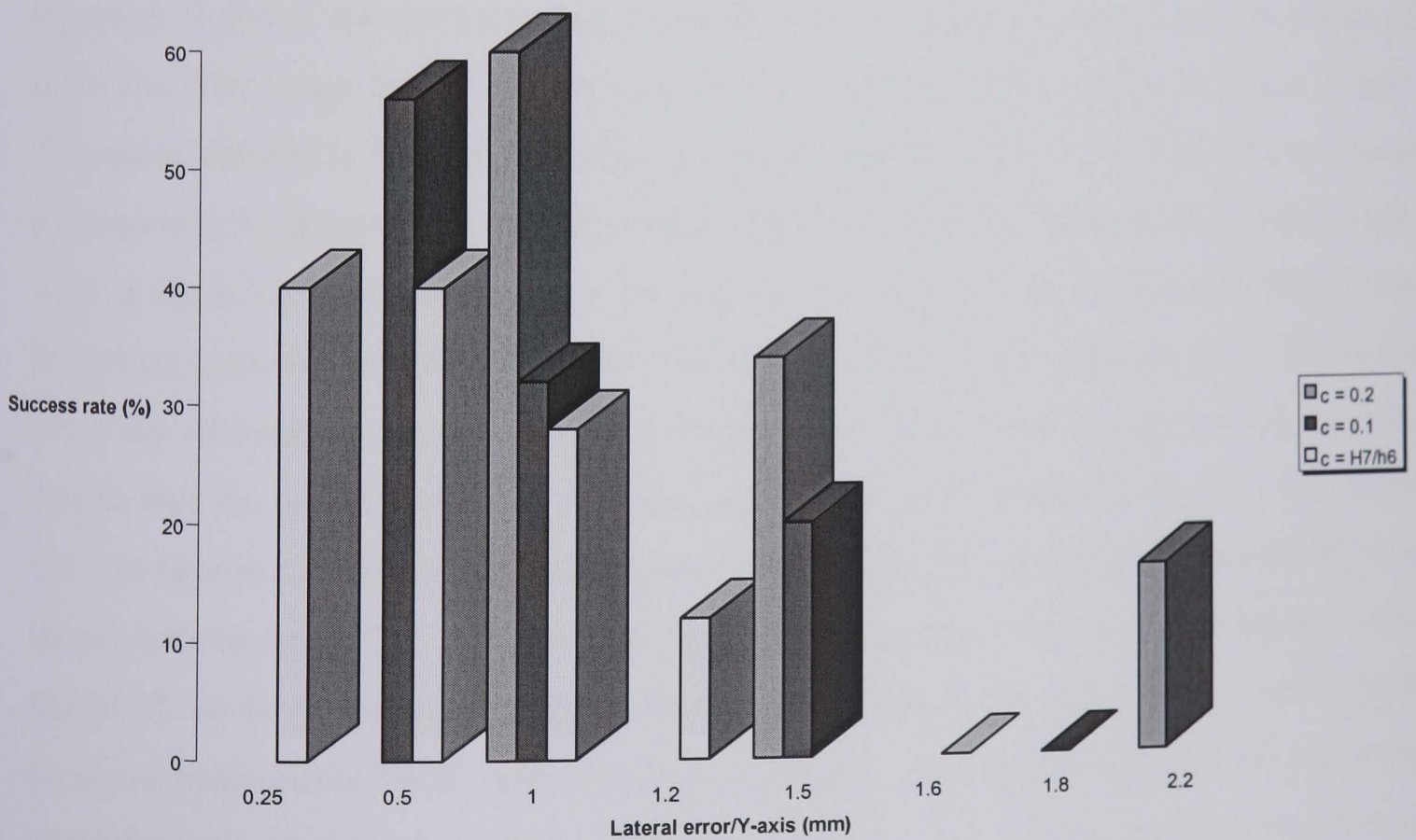


Figure 8.9 The success rate against range of lateral misalignment on the Y axis

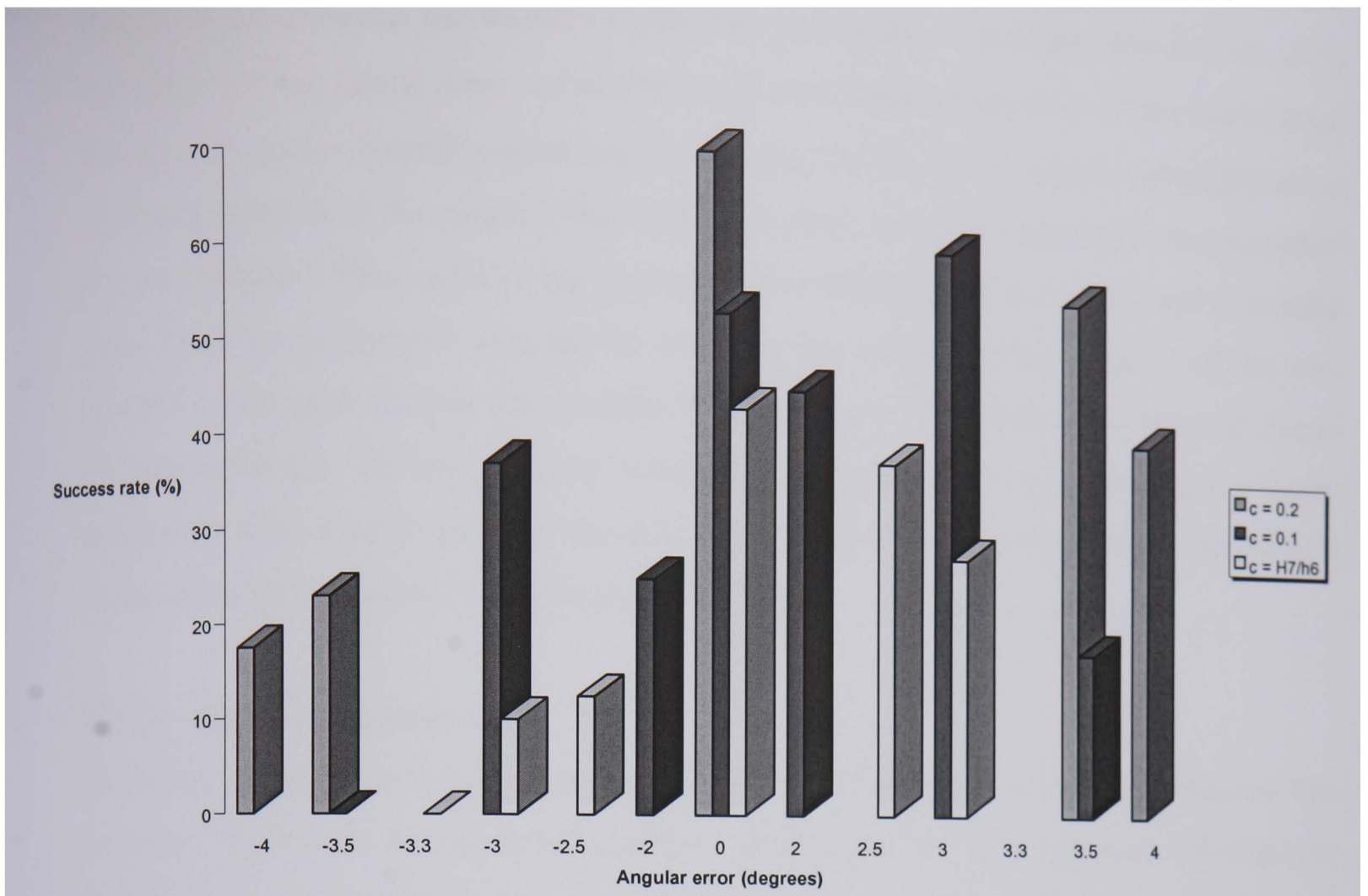


Figure 8.10 The success rate against a variable angular misalignment

Figure (8.7) shows the optimum peg diameter with the highest success rate is between 15 to 20 mm. The larger the size of the peg, the less chances for successful insertion actions. The reason for that is because the larger the peg diameter, the less flexible is the wrist and consequently it can not overcome the initial positional error during the initial contact stage. Also, in figure (8.7), the success rate for mating parts having large clearance is higher than for mating parts with smaller clearance; the reason for this is the clearance ratio. Where the larger the clearance ratio the easier the insertion and vice versa. In figures (8.8 and 8.9), despite that the success rate is not as high as with large clearances (over 0.3), they show that best results are achieved, for small clearance such as H7/h6, the maximum lateral error should be between 0.25 to 0.5 mm. For large clearance such as 0.2 mm the allowable error should be up-to 1 mm. Again, the reason for these results is the clearance ratio, small clearance ratio causes 3POC which leads to jamming. Note that in figure (8.10) where the angular misalignment is zero, it is assumed that there is other positional errors on either of the X or the Y-axis.

Also in the same figure, the reason why the success rate for -3° is higher than that for -2° is because at -3° the lateral error varied from 0.25 to 0.5 mm, however at -2° the lateral error is higher (1 mm). Generally speaking about figure (8.10), if the angular misalignment is positive (direction of the mouth of the hole), then there is higher chances for success rather if it was negative. This is due to the extra stage in which the peg has to pass and to transfer from negative to positive angular tilt (refer to the initial contact, stage 2 of the new assembly strategy in section 3.61 chapter 3) which cause inefficient rubber recovery due to the applied forces. To have a better understanding of the peg-hole experiments, a Scope and plotter were used to plot the traces of the insertion force against time, A selection of these charts are presented in figures (8.12 to 8.16).

8.3.2.1 Further experiments

As shown in figure (8.7) the larger the size of the peg becomes the lower the success rate becomes. The reason for that is because the rubber which holds the peg gets stiffer and the wrist loses its flexibility. To prove this, some experiments were repeated with peg diameters of 30 and 35 mm using the same clearances as before. However, this time the bore (rubber) which holds the peg (parts # 3 and 4 in assembly drawings, see appendix 3) was enlarged and thicker rubber is bonded by the same ratio for success which are shown in figure (8.7). From the same figure,

$$\frac{\text{Peg diameter}}{\text{Current rubber thickness}} = \frac{20}{6} = 3.33$$

This means that the new rubber thickness which is needed to hold the peg and provide the same success rate as for the 20 mm peg diameter,

$$\frac{30}{\text{New rubber thickness}} = 3.33$$

This should give a 9 mm thickness. So, after changing the rubber to the new thickness, the same diameters (30 and 35 mm) from figure (8.7) were tested (for experimental progress refer to table 2 in appendix 2) and the results are shown in figure (8.11).

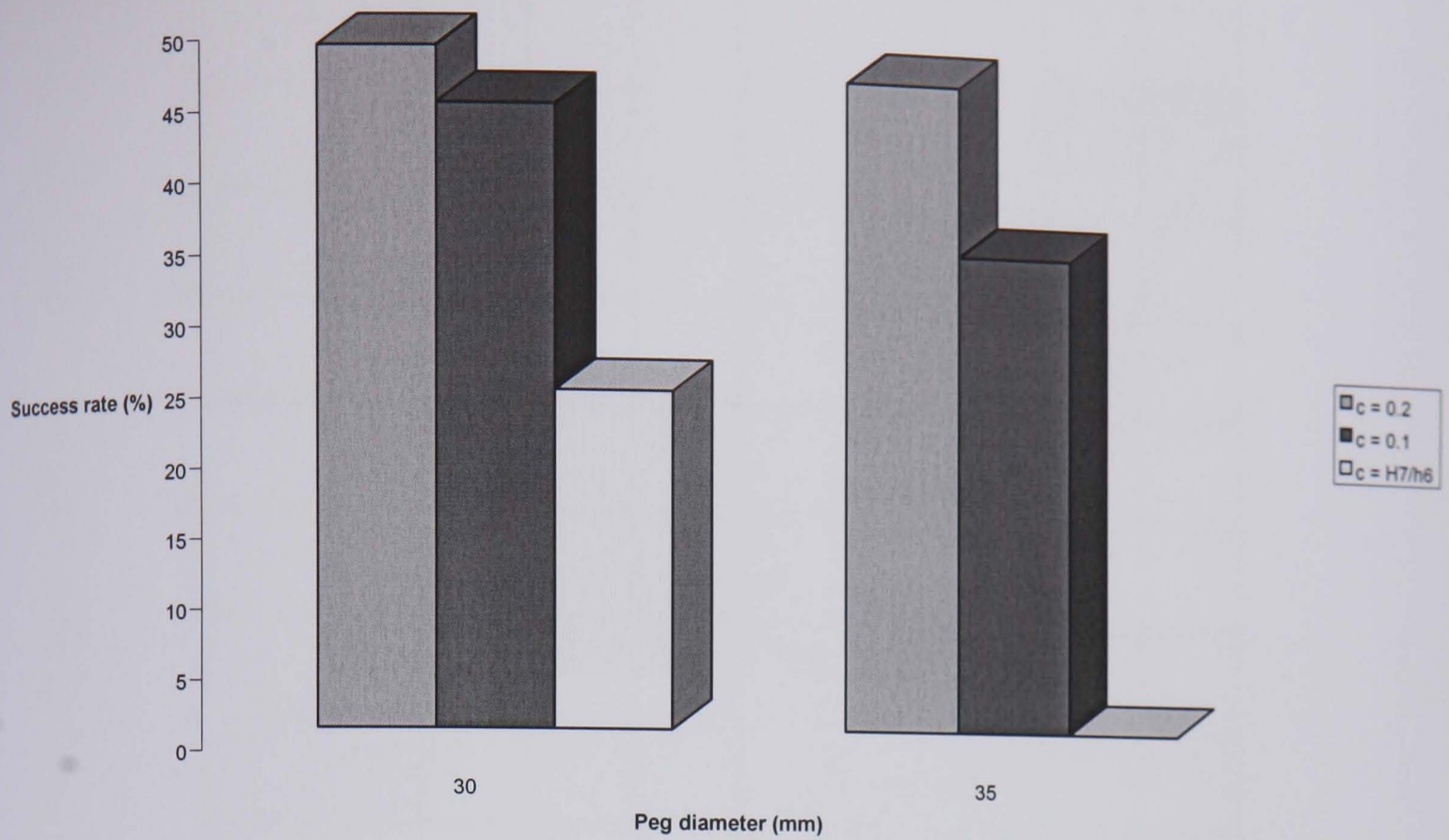


Figure 8.11 The success rate for 30 and 35 mm peg diameter

As shown in figure (8.11), the success rate has increased from that shown in figure (8.7), but it is still not the same as for peg diameter of 20 mm. The reason for that is that the 30 and 35 mm new pegs have become heavier which reduces the flexibility of the wrist.

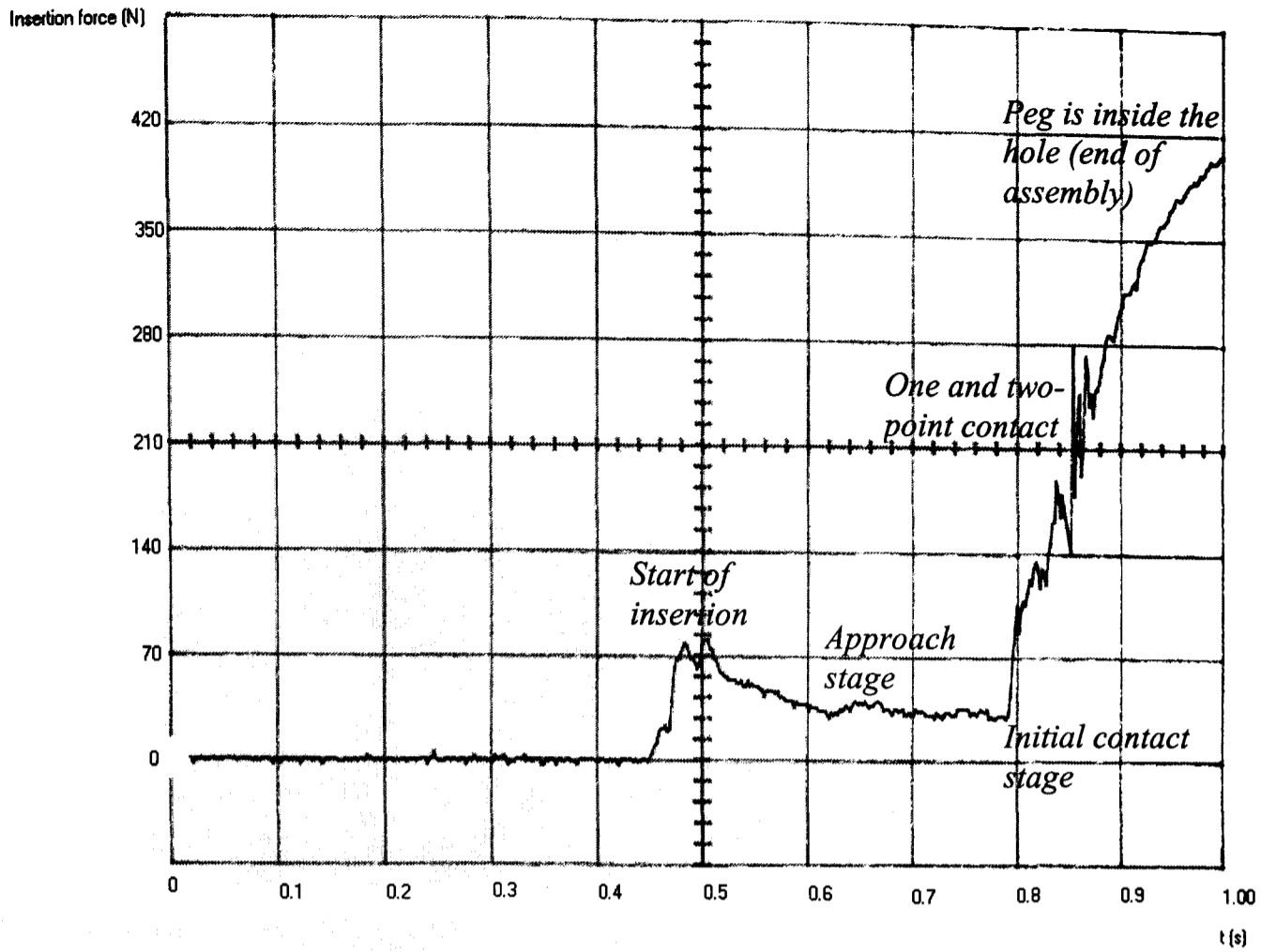


Figure 8.12 Peg diameter 15 mm and the clearance is 0.1 mm

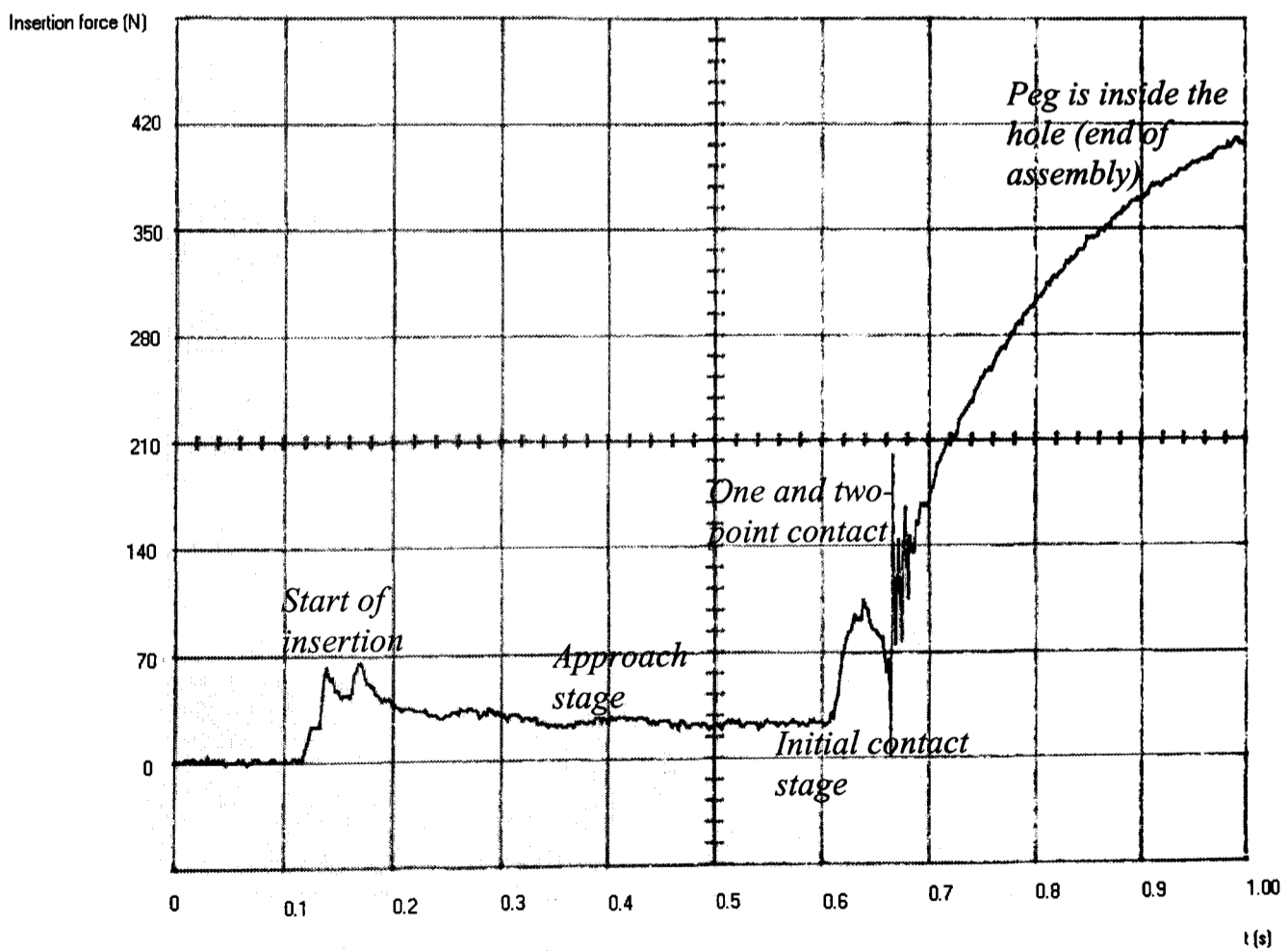


Figure 8.13 Peg diameter 20 mm and clearance 0.1 mm

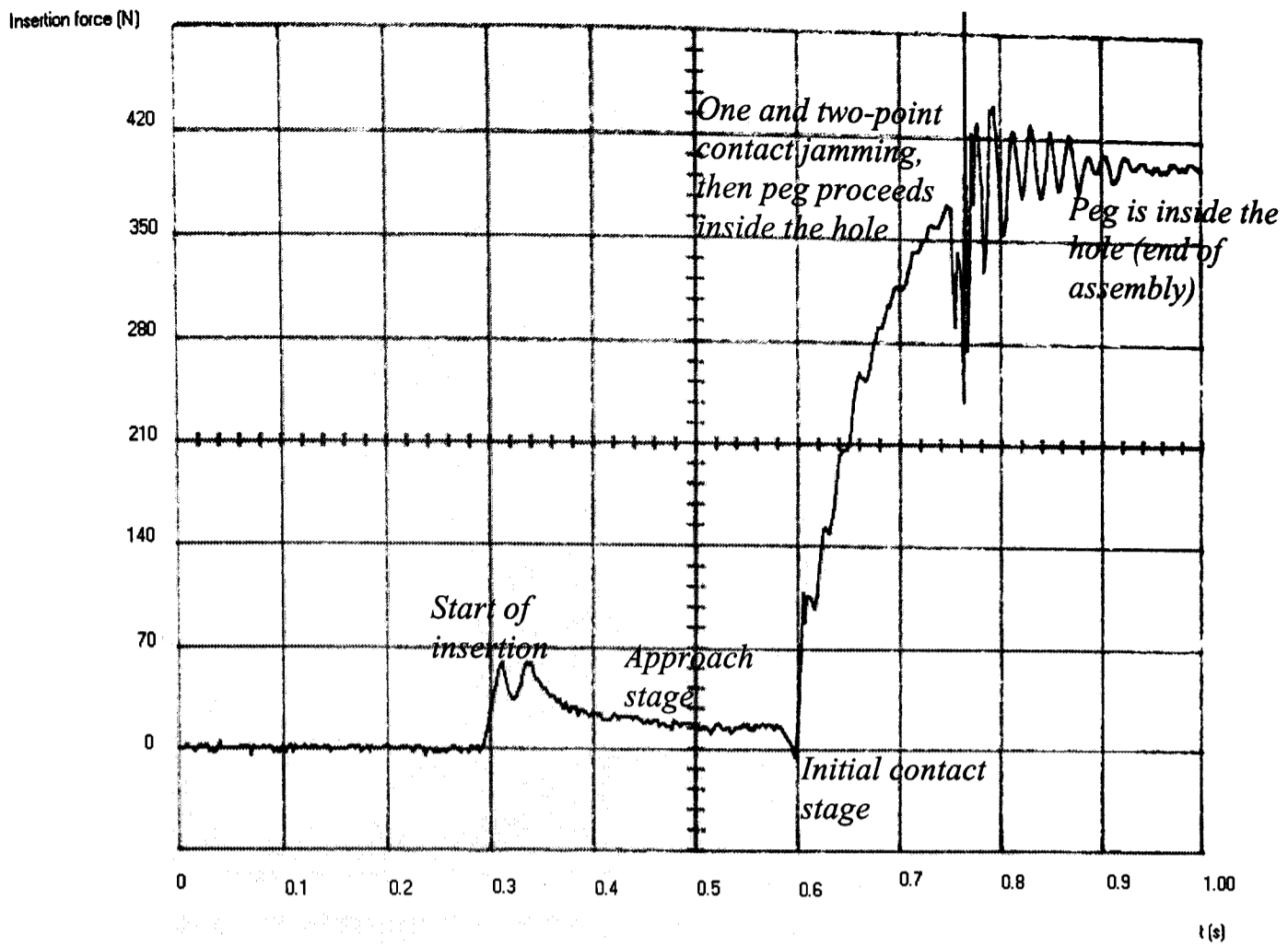


Figure 8.14 Peg diameter 25 mm and clearance 0.2 mm

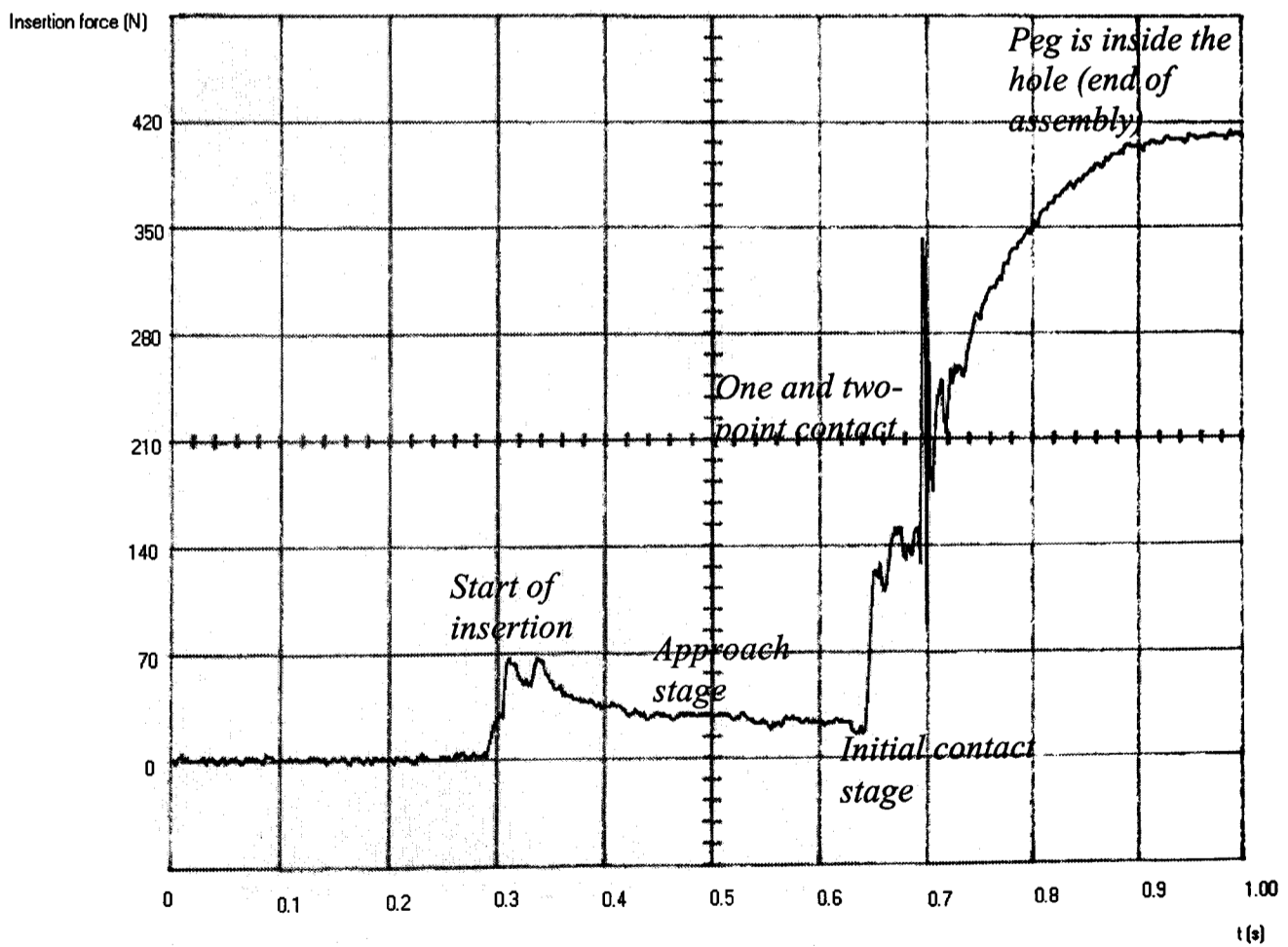


Figure 8.15 Peg diameter 30 mm and clearance 0.2 mm

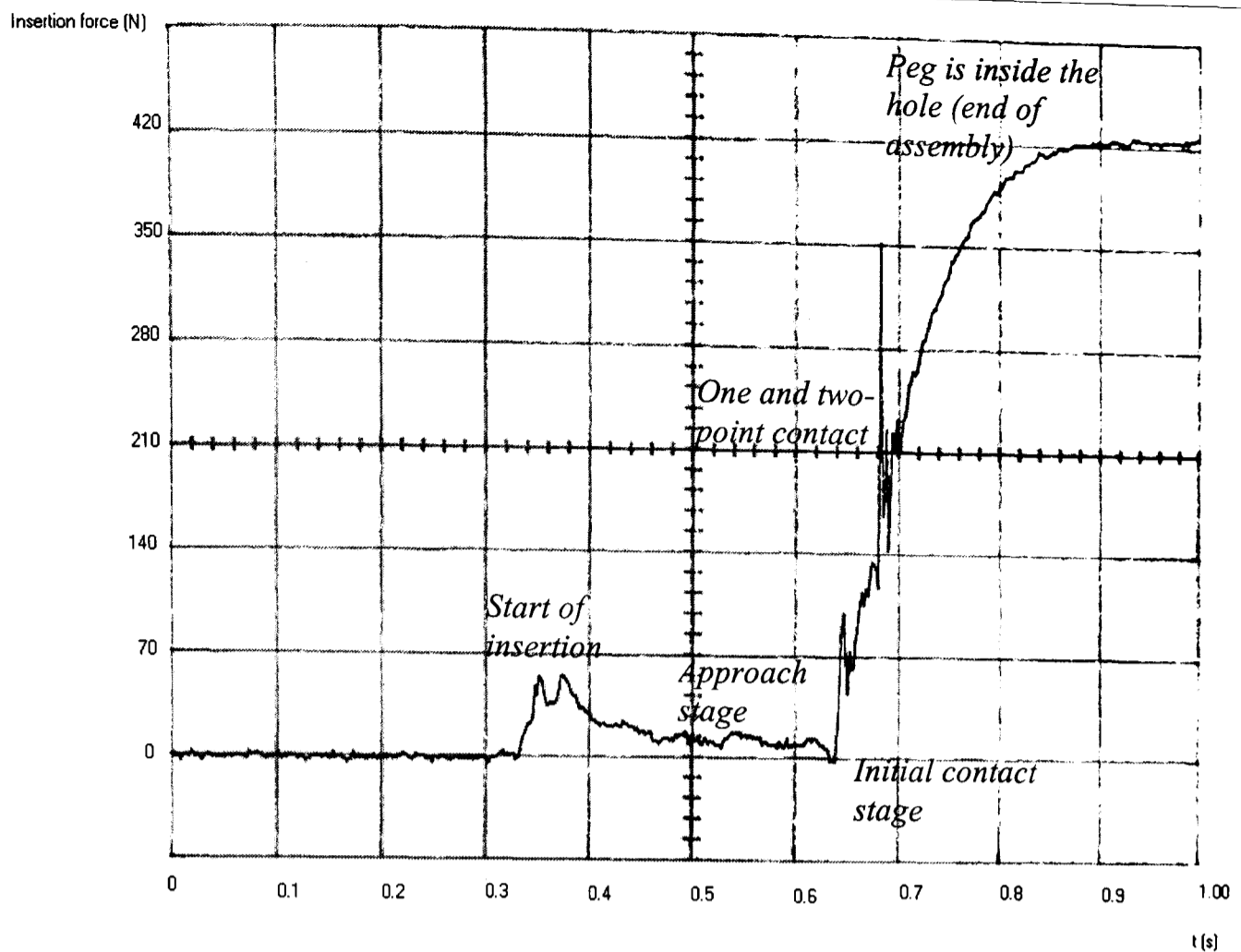


Figure 8.16 Peg diameter 35 mm clearance 0.2 mm

It can be noticed that the common element in figures (8.12 to 8.16) is the insertion time which is identical in all cases and it is about 0.075 seconds with the exception the one in figure (8.14) where initially the peg tends to jam inside the hole and suddenly it snaps inside the hole. Also, it can be noticed that the impulse force tends to increase dramatically with pegs having diameter over 20 mm. In normal assembly operations the impulse force has to be as small as possible. This fact indicates that the wrist functions better with pegs of diameter between 15 to 20 mm.

8.4 DISCUSSION

The preceding assembly experiments have demonstrated the capability of the CVHRCC in a real assembly operation environment. Though they highlighted the points where the CVHRCC works less effectively, whether because of an imperfect design of the wrist or the related environment. A full discussion of the experimental results compared to the theoretical ones is presented in chapter 9.

It can be seen in table (8.1), the relationship between the clearance, the positional error and the success rate is proportional. The smaller the clearance becomes the fewer chances are

for the peg to enter the hole. Although the success rate is over 96% for clearances over 0.3 *mm* in the first stage of experiments, in the second stage of the experiments the success rate has dropped, which is due to the increase in the peg diameter. In the second stage of the experiments, the instrumentation is attached to the wrist and the assembly machine to provide a direct reading of the insertion force without having to affect the insertion process. The illustrations of the insertion force shown in the scope charts (refer to figures 8.12-16) have demonstrated the sequence of the new assembly strategy and shown that best results are achieved with peg sizes between 15 to 20 *mm*. Also, best results are achieved when the clearance between the mating parts is over 0.2 *mm* (further discussion is presented in chapter 9).

Theoretically, it has been shown that horizontal assembly has similar conditions to the vertical one. However one of the lessons that can be learnt about the horizontal assembly, is that if possible to avoid it, then avoid it.

8.5 CONCLUSION

This chapter has led to the following conclusions:

1. The objective of the assembly operation experiments is to test the CVHRCC, and to learn more about the chamferless assembly from different directions.
2. The assembly rig used in the experiments is a basic assembly machine that has two functions:
 - a. to provide the CVHRCC with the motion and insertion force needed to achieve the peg-in the hole,
 - b. and to change the position of the hole as required (to displace).
3. The preceding experiments have shown that CVHRCC can accept a range of pegs from 15 to 35 *mm*, however it works more reliably with sizes between 15 to 20 *mm* in diameter. Also, it shows that the wrist can accommodate initial positional errors of up to 2 *mm* and 3° with clearances over 0.3 *mm* between the peg and the hole from the vertical direction. In addition, it was demonstrated that the larger the clearance is, the larger positional misalignment can be allowed.

CHAPTER 9

DISCUSSION

Considering the objective of the research in this thesis, a passive compliant wrist that can accommodate positional errors between chamferless cylindrical parts is described. The wrist was designed to function from the vertical as well as the horizontal directions. However, in practice the wrist did not operate correctly in the horizontal attitude due to the weight of the wrist, which causes the piston rod to bind at its end (at the CVHRCC).

The results of the peg-in hole insertion process which are presented in this thesis, can be discussed under two categories:

1. The peg-in hole simulation results: In chapter 6, the peg-in hole insertion process using a passive compliant wrist is modelled. The mathematical model was simulated using matlab-simulink software. The simulation results have suggested that for under 0.2 mm clearance, the CVHRCC can accommodate an initial misalignment between 1 mm to 1.5 mm, and for clearance of over 0.2 mm the wrist can accommodate an initial error between 0.5 mm to 1 mm. The reason, why for small clearance the allowable initial misalignment is larger than that for large clearance, is that the smaller the clearance, the larger the lateral distance (e) between the centre of the peg to the contact point becomes. Consequently, the reaction torque gets larger, which results in a greater angular tilt and lateral transition. Also, it was shown that in the presence of initial lateral misalignment, the initial angular misalignment has no effect on the outcome of the insertion process. Because the change in the magnitude of the insertion force is not significant ($F_Z = F_{in} \cos\theta_0$). Also, when there is only initial angular error, then the initial angular misalignment has to be smaller than the friction angle. Therefore, for clearance of less than 0.2 mm the allowable angular error is up-to 9°, and for clearance of over 0.2 mm the allowable angular error is between 9° to 12°.

In terms of stiffness, the simulation results showed that the wrist could have angular stiffness between 6800 Nmm/rad to 7500 Nmm/rad, and the lateral stiffness 82 N/mm to 86 N/mm. Also, the wrist can accept a peg of up-to 20 mm

diameter. During the simulation process it was noticed that whenever there is jamming occurring, then reducing the applied force facilitates the insertion process.

2. The peg-in hole experimental results: On the other hand, the experimental results of the chamferless peg-in hole insertion process have shown that the CVHRCC can accommodate reliably initial positional errors of up-to 1 mm and 3° for mating parts having clearance of over 0.3 mm (see figure 8.2). For clearance less than 0.2 mm, the success rate for pegs of 15 to 20 mm diameter is in the region of 60%, and the lower the clearance becomes, then the lower the success rate gets (see figure 8.9). Also, it was shown that for mating parts with diameter over 20 mm the success rate is low. However, when the wrist stiffness was decreased (section 8.5.2.1), then the success rate of mating parts of large diameter (≥ 30 mm) has increased (figure 8.13). In other words, providing the wrist with more flexibility has increased the assembly success rate of parts having small clearance. For instance, in the first stage of the experiments, the results obtained for a peg of over 16 mm diameter and clearance over 0.3 mm, the success rate is over 90%. Consequently, for 15 to 20 mm peg diameter and H7/h6 clearance the success rate is about 40% and the wrist has accommodated an initial misalignment of 0.5 mm and about 2.5°. However, for a large clearance ($c = 0.2$ mm) and the same peg diameters the success rate was about 60% and the initial misalignment is 1 mm and about 3.5°. It can be noticed that during the peg-hole experiments the larger the peg diameter is, the lower the success rate gets.

The experimental determination of the wrist stiffness has revealed two values for the angular and the lateral stiffness. Under small reaction forces on the peg while it is inside the hole in one or two point contact the wrist stiffness is 4800 Nmm/rad and 1.5 N/mm. However during the peg initial engagement with the hole the wrist stiffness found to be 6900 Nmm/rad and 30 N/mm.

Discussing the results, the empirical wrist stiffness lies within the boundary of the theoretical stiffness. Although the theoretical lateral stiffness is higher than the empirical one, during the simulation process there was not much difference in the simulation results

when using values of lateral stiffness of up-to 86 N/mm , the agreement between both theoretical and experimental results.

The wrist was designed to accept a peg of up-to 20 mm in diameter. In practice the wrist worked effectively with diameters between 15 mm to 20 mm , which lies within the boundary of the suggested theoretical diameter (refer to figure 6.33, chapter 6). Also, when working with peg of over 20 mm in diameter the wrist was struggling with this size and in particular when working with small clearance. Also, the reason why the wrist could not function properly with large pegs (over 20 mm diameter) is because the larger the peg, the more stressed gets the rubber/wrist and consequently the wrist less flexible to accommodate positional misalignments with the hole during the engagement stage. In addition, in theory the wrist is supposed to accommodate positional misalignment even in case of a small clearance between the peg and the hole. In practice when using mating parts with small clearance, during the engagement stage the wrist tilts the peg inside the hole creating 3 POC, which resulted in jamming. It can be said that there is an agreement between the theoretical and the experimental results for large clearances (over 0.2 mm) and below that the gap gets wide.

Now considering other assembly strategies and devices and comparing them to the CVHRCC; For instance, the RCC can accommodate positional errors with a clearance of 0.01 mm , but the allowable positioning error is 1 mm and 1° respectively (see table 2.1, chapter 2). Also, the RCC needs a chamfer on either of the mating parts. Other devices listed in table (2.1), when no chamfer on either of the peg or the hole, then the clearance has to be large (from 0.75 to 3 mm) to enable these devices to accommodate the required positional errors. Also, in some cases the mating speed is over the 1 second, while the mating speed of the CVHRCC is less than 0.1 second (Mating speed/time, is the time duration from the moment the peg contacts the upper surface of the hole until it breaks either one or two point contact and slides inside the hole). So, in terms of reliability and accuracy, when the clearance between the mating parts is over 0.3 mm and the initial misalignment is up-to 2 mm and 3° the CVHRCC is far more superior to these devices because of its simplicity and its low cost to use. On the other hand, if the assembly requires accommodating positional error with smaller clearances (<0.3 mm), then it is preferred to consider other alternatives.

In fact, a passive mechanism linkage developed by E. Caine [E. Caine et al, 1989] claims to be successfully used in a chamferless peg-in hole assembly operation. However, this mechanism requires manipulation from the operator during the assembly. Also this mechanism can not be used with assembly robot/machine due to the non-compatibility of its design.

Here is a summary of the advantages and disadvantages of the CVHRCC over other devices of the same category:

1. It is an inexpensive and simple wrist.
2. It can accommodate misalignment between chamferless mating parts.
3. It has low stiffness, which enables it to accommodate positional errors of up-to 1.5 *mm* and 3° with clearance over 0.2 *mm*.
4. The CVHRCC can accept peg of different diameters between 15 to 35 *mm*, however for reliable operation preferably have diameters in the range of 15 to 20 *mm*.
5. Unlike other devices, the technology used in this wrist can apply to other technologies, such as airborne fuelling and underwater assembly of oil pipes, etc.

Disadvantages:

1. It is heavier than other devices; weighing 3.10 *Kg* as opposed to ≤ 1 *Kg*.
2. It is limited to large clearances between the peg and the hole; over 0.3 *mm* it works very reliably, but with smaller clearances the CVHRCC becomes less efficient.
3. The soft housing (rubber) of the peg creates an undesirable initial positioning.
4. The projection of the centre of compliance is restricted to 150 *mm*, limiting the peg to a fixed length, or limited variations thereof.

The research went through stages to reach its final objective, starting from the new assembly strategy and the domino effect theory. The aim at that stage was to present the idea behind the strategy-so in the subsequent chapters the idea gets developed. As shown in chapters three through six, the aim was to establish the conditions for implementing the new assembly strategy by investigating the strategy dynamically and geometrically. Then a simulation model was built and used to establish an understanding of the behaviour of the passive compliant wrist during assembly operation. During the wrist structure stress analysis, the Algor finite element package was used. The problem with this software is that

it did not have the right processor to allow the user to perform an FEA of the wrist as a one unit. In the final stages of the FEA work, other packages were discovered that could do FEA for the whole mechanism.

Finally, as discussed in this chapter, the overall objective is to make a passive compliant wrist that can overcome positional errors between chamferless mating parts, this objective has been achieved. However, other points such as clearance between the mating parts or the horizontal assembly were not fully satisfied. Perhaps these features could be considered in other research and used as a reference for other researchers.

CHAPTER 10

CONCLUSIONS AND RECOMMENDATIONS

This chapter summarises the research documented in the thesis and provides recommendations for possible future research in this area or an area of a similar application.

10.1 CONCLUSIONS

In this thesis, a passive compliant wrist that can overcome positional errors between cylindrical mating parts is presented. The contribution of this wrist and research to the general knowledge is in that the wrist requires no chamfer on either of the peg or the hole, which is necessary to have when using other devices such as the RCC. Moreover, the theoretical model could be for future design of other devices that adapt the approach presented in this thesis. Also, different robotic assembly technologies to overcome the inaccuracy of the robot in positioning the peg into the hole were introduced. Considering the domino effect theory a new passive assembly strategy is proposed. An analysis of 2 and 3 dimensional space for the peg-hole problem (new assembly strategy) was detailed followed by a simulation programme for the proposed strategy. Following the wrist design, a passive compliant wrist was built. Wrist testing in a real assembly environment of chamferless peg-in hole is also described. General discussion of the achievements of this research and its shortcomings are also presented.

The major points of each chapter in the thesis are as follow:

- *Chapter 1:* This chapter has provided a brief background about the peg-in hole insertion process and its related problems. Also, it outlines the research objective and the methodology for achieving that objective.
- *Chapter 2:* In this chapter, robotic assembly methods to accommodate the angular/lateral misalignments between cylindrical mating parts during assembly operations were introduced. These methods are of different category from each other. Arguments for the use of any of those methods were put-up. However, it was noticed that the more complicated the assembly application become the more elaborated and expensive the assembly technique is required.

- *Chapter 3:* In this chapter, a new assembly strategy was presented. The strategy was inspired from the domino effect theory. A 2D-space analysis for this strategy is presented.
- *Chapter 4:* This chapter has dealt with the geometrical aspects of the 3D problem of the peg-hole strategy during the insertion process. Also it provided a better understanding for the geometrical conditions for successful or unsuccessful insertion process.
- *Chapter 5:* Unlike the previous chapter, this one describes the dynamics of the peg-hole process. It considers the friction between the mating parts and its related effects on the insertion process. Also, of the forces and moments that involved in the insertion process, the successful conditions were derived.
- *Chapter 6:* This chapter presents the modelling and simulation process for the chamferless peg-in hole assembly strategy. The simulation results have shown the theoretical behaviour and capabilities of the compliant wrist that needed to perform a real peg-in hole insertion process.
- *Chapter 7:* A passive compliant wrist (CVHRCC) is presented. The wrist description and the way it functions are described. Experiments for finding the wrist stiffness through practical and theoretical deflections of the wrist are detailed. Also, it shows the wrist design and stress analysis. A FEA to investigate the stresses inside the wrist structure have proved the wrist design.
- *Chapter 8:* In this chapter real assembly experiments along side the preparation for the assembly rig and its related tools is presented. It describes the process for calibrating the peg-wrist and its shortcomings. The assembly experiments have shown that the CVHRCC functions well in accommodating misalignments between the peg and the hole of over 0.2 mm clearance and within the 1.5 mm allowable lateral errors and 3° allowable angular error. In addition the experimental work have demonstrated the fact that the wrist can accept different pegs of different diameters and preferably 15 to 20 mm. Also, the wrist/assembly rig is incapable of achieving peg-in hole insertion process from the horizontal directions due to gravitational forces.
- *Chapter 9:* This is a general discussion of the research documented in the thesis. It discusses the differences in the theoretical and experimental results. In addition, a discussion and comparison between the compliant wrist of this research and other assembly methods and devices is presented. Also, arguments for the use of the

CVHRCC over other devices when and why are provided. Shortcomings of the research and the methodology used to achieve this research are also presented.

10.2 RECOMMENDATIONS

As already have been said in chapter (8), to solve the problem of the excessive forces that arise during the engagement between peg and the hole; an actuator could be integrated with the instrumented cross plate and the top floating unit of the CVHRCC. So, when reaction force arises and exceeds the prescribed value, a signal will be sent from the strain gauges to the actuators, then the actuator takes control over the wrist and it should rotate or slide the peg into the mouth of the hole where there is less reaction forces. One of the advantages of this method, is the ability to accommodate positional errors even in case of small clearance between the mating parts. On the other hand, the insertion time will get longer.

In regard to the horizontal assembly, a new design for the assembly rig could be made, for example, the wrist could be attached to a bracket from one side and the bracket attached to the top surface of the assembly machine through stiff rods. So in case of binding during horizontal assembly, the supporting rods should counteract the weight of the wrist, and this way side-assembly becomes possible.

Also, the CVHRCC could be used in applications other than assembly; such as tooling interface in machine tools or guiding pins in automated machines etc.

Also, this research could be used as a reference for other applications such as air-borne fuelling, where the problem is to align and to insert one fuel hose from the first aircraft into the fuel tank of the second aircraft. Another application is in the under-water pipe assembly. To engage the two pipes, they need to be aligned and then assembled. The common element in these examples is the alignment and insertion process, which is similar to the peg-in hole example.

REFERENCES

- Boothroyd G.**, "Design for assembly – the key to design for manufacture", *The Int. Jour of Advance Manufacturing Technology*, 2, pp. 3-11, 1987.
- Boothroyd G.**, "Design for assembly", *Jour. of Mechanical Engineering*, pp. 28-31, February 1988.
- Belforte G., Alfio N. D., and Romiti A.**, "A self-adaptive guided assembler (SAGA)", *Proc. Robot VI*, pp. 544-551, 1982.
- Bright G. and Moodley P.**, "Sound signatures assist assembly", *Assembly Automation*, V. 15, No. 3, pp. 21-23, 1995.
- Badger M. A.**, "The assembly robot: applications in flexible assembly systems", *Proc. of the 2nd European Conf. on Automated Manufacturing*, pp. 16-19, May 1983.
- Brussel V. and Simons J.**, "Automatic assembly by active force feedback accommodation", *Proc. The 8th Int. Symp. on Industrial Robots*, pp. 181-193, Stuttgart, West Germany 1978.
- Brussel V. and Simons J.**, "Robot assembly by active force feedback accommodation" *Annals CIRP* 28, pp. 397-401, 1979.
- Brussel V. and Simons J.**, "The adaptable or compliance concept and its use for automatic assembly by active force feedback accommodations", *Proc. 9th Int. Symp. on Industrial Robots*, pp. 167-181, Washington DC, 1979.
- Brussel V., Thielemans H. and Simons J.**, "Further development of the active adaptive compliant wrist (AACW) for robot assembly", *Proc. 11th Int. Symp. on Industrial Robots*, pp. 377-384, Tokyo, Japan 1981.
- Brussel V. and Simons J.**, "A self-learning robot for automatic assembly", *Proc. 1st Int. Conf. on Assembly Automation*, pp. 295-308, UK 1980.

- Brussel V. and Simons J.**, "Adaptive Assembly", Proc. 4th BRA Annual Conf., pp. 95-106, IFS, Kempston, UK 1983.
- Caine E.**, "Chamferless assembly of rectangular parts in two and three dimensions", MSc Thesis, Massachusetts Institute of Technology, 1982.
- Caine E., Lozano T., Seering W.**, "Assembly strategies for chamferless parts", IEEE Int. Conf. on Robotics and Automation, pp. 472-477, Scottsdale, AZ, May 1989.
- Cailot F. and Kerlidou M.**, "Air stream compliance", 5th Int. Conf. on Assembly Automation, France 1984.
- Cho H. S., Gho K. C.**, "The development of a flexible and sensible robot wrist for assembly processes", Korean Society of Mechanical Engineers 8, No. 5, pp. 488-497, 1984.
- Cho J. H., Warnecke and Gweon D. G.**, "Robotic assembly: a synthesizing overview", Robotica, V. 5, pp. 153-165, 1987.
- Chan S. P. and Liaw H. C.**, "Robust motion control for robotic assembly tasks using variable structure control scheme", Jour. of Intelligent and Robotic Systems, 18, pp. 67-86, 1997.
- Del Pobil A. P. and Cervera**, "Unsupervised learning for error detection in task planning", Computer Science Dept., Technical Report, Jaum I University, 1994.
- Dufay A. and Latombe J. C.**, "An approach to automatic robot programming based on inductive learning", Robotics Research, Brady and Paul, editors, pp. 97-115, 1984.
- Drazan J. and Hopkins S. H.**, "Semi autonomous systems for automatic assembly" Annal CIRP 33, pp. 291-294, 1984.

De Fazio L., “Displacement-state monitoring for the remote centre compliance (RCC) - Realizations and Application”, Proc. 10th Int. Symp. on Industrial Robots, pp. 559-560, Milia, Italy 1980.

Erdmann M., “On a representation of friction in configuration space”, The Int. Journal of Robotics Research, V. 13, No. 3, pp. 240-271, June 1994.

Erdmann M., Mason M. T., “An exploration of sensorless manipulation”, IEEE J. Automation 4, pp. 369-379, 1988.

Fakri A., Jutard A., Liegeois G., “Passive compliance wrist with two rotation centres for assembly robot (DCR-LAI device)”, Proc. of 5th Int. Conf. on Assembly Automation, Paris, pp. 235-241, May 1984.

Featherstone R., “The dynamics of rigid body systems with multiple concurrent contact”, The third Int. Symp., Cambridge, MA: MIT Press, 1986.

Gustavson E., “A theory for the three dimensional mating of chamfered cylindrical parts”, Trans. of ASME, 112 V. 107, , The Charles Stark Draper Laboratory, Cambridge, MA USA, March 1985.

Goto T., Onoyama T. and Takeyasu K., “Precise insert operation by tactile controlled robot HI-T-HAND Expert 2”, Proc. 4th Int. Symp. on Industrial Robots, pp. 154-160, Tokyo, Japan 1974.

Goto T., Inoyama T., and Takeyasu K., “Precise insert operation by tactile controlled robot”, The Industrial Robot, pp. 210-213, Sept. 1980.

Hoffman B. D., Pollack H., Weissman B., “Vibratory insertion process: A new approach to non-standard component insertion”, Robot 8, pp. 1-10, 1985.

Hakan Gurocak B., “Fuzzy rule base optimization of a compliant wrist sensor for robotic assembly”, Jour. of Robotic Systems, V. 13, PT. 7, pp. 475-487, 1996.

- Heiple A. R. and Carpenter S. H.**, "Acoustic emission from dislocated motion". Annals of the CIRP, V. 1, USA, 1993.
- Holcomb G. W.**, "Justifying flexible automation for PCB assembly", Assembly Automation, V. 15, No. 2, pp. 14-16, 1995.
- Hanafusa H. and Asada H.**, "An adaptive control of robot hand equipped with pneumatic proximity sensors", Proc. 6th Int. Symp. on Industrial Robots, D4, pp. 31-42, UK 1976.
- Hollingum J.**, "Robot system builds customised printed circuit boards", Assembly Automation, V. 11, No. 3, pp. 21-23, 1991.
- Havlik S.**, "A new elastic structure for a compliant robot wrist", Robotica, V. 1, Part 2, pp. 95-102, 1983.
- Hopkins S. H., Bland C. J., Byrne C. B.**, "A toolbox of assembly strategies", Proc. of the 18th Int. Symp. on Industrial Robots, Lausanne, Switzerland, pp. 145-156, April 1988.
- Haskiya W., Qiao H., Knight J., Pritchard F.**, "Peg-hole strategy and the domino effect theory", Proc. of The 13th National Conf. on Manufacturing Research, pp. 201-210, Glasgow, UK, Sept. 1997.
- Haskiya W., Maycock K., Knight J.**, "A passive compliant wrist for chamferless peg-in hole assembly operation from vertical & horizontal directions (cvhrcc)", Proc. of The Inst. of Mech. Eng., Part B, V. 212, pp. 473-478, 1998.
- Haskiya W., Qiao H., Knight J.**, "A new strategy for chamferless peg-hole assembly", IEEE Int. Symp. on Assembly and Task Planning, pp. 90-95, Marina del Rey, CA-USA, Aug. 1997.
- Haskiya W., Maycock K., Knight J.**, "Robotic assembly: chamferless peg-hole assembly", Robotica, V. 17, pp. 621-634, 1999.

Inoue H., "Force feedback in assembly tasks", Artificial Intelligence Laboratory, MIT, AI Memo-308, 1974, (Reprinted in Winston, P. H., and Brown, R. H., eds., Artificial Intelligence, pp. 222-241, An MIT Perspective, MIT Press 1979).

Jung M. and Gweon D. G., "An intelligent wrist mechanism for robot assembly of chamferless parts", IMACS, pp. 107-112, North-Holland 1993.

Kiss A., Lazar A. and Toth A. Z., "Dynamic analysis of the peg-hole insertion with stick-slip friction and impact", 7th Int. Daaam Symp., , Technical University of Vienna, 17-19th October 1996.

Kondoleon A. S., "Application of technology-economic model of assembly techniques to programmable assembly machine configuration", MSc Thesis, MIT Mechanical Eng. Dept. 1976.

Klaus K. W., "The infact compliance", Assembly Automation, V. 12, No. 3, pp. 11-14, 1992.

Kang S. and Chao H. S., "Vibratory assembly of prismatic parts using neural network-based positioning error estimation", Robotica, V. 13, pp. 185-193, 1995.

Kaczanowski St. and Aderek A., "Adaptive robot performed assembly", 4th CISM-IFTOMM Symp. on Theorie und Praxis der Roboter und Manipulatoren, Warsaw 1981

Lane J. D., "Evaluation of a remote centre compliance device for assembly applications", Proc. of the 1st Int. Conf. on Assembly Automation, pp. 443-472, March 1980.

Lynch P. M., "Economic-technological modelling and design criteria for programmable assembly machines", CSDL Report No. T-625, PhD Thesis, MIT Mechanical Eng. Dept. 1976.

Lozano-Pe`rez T., Matthew T. Mason and Russell Taylor H., "Automatic synthesis of fine-motion strategies for robots", *Robotic Research* - Brady and Paul, editors, pp. 65-96, 1984.

Motive A., "Automation for quality on Rover engine lines", *Assembly Automation*, pp. 10-15, Feb. 1990.

Mc Callion H., Johnson G. R. and Pham D. T., " A compliant device for inserting a peg in a hole", *The Industrial Robot*, pp. 81-87, 1979.

McWalter K., "Machine vision boosts PCB assembly processes", *Assembly Automation*, V. 13, No. 2, pp. 32-34, 1993.

Mashinostroeniya V., "Assembling joints by magnetic methods of orientation", *Russian Engineering* 56, No. 4, pp. 68-71, 1976.

Mashinostroeniya V., "Using a rotating magnetic field for the grippers of industrial robots", *Russian Engineering* 57, No. 6, pp. 43-45, 1977.

Nevins J. L. and Whitney D. E., "Assembly research", *Automatica*, V. 16, pp. 595-613, 1980.

Nevins J. L. and Whitney D. E., "Computer-controlled assembly", *Scientific American*, V. 238, No. 2, pp. 62-74, 1978.

Nilson N., "Principles of artificial intelligence", Tioga Publishing, California 1980.

Pham D. T., "On designing components for automatic assembly", *Proc. of the 3rd Int. Conf. on Automatic Assembly*, pp. 121-129, 1982.

Paulos E., Canny J., "Accurate insertion strategies using simple optical sensors", *IEEE Robotics and Automation*, pp. 1656-1662, 1994

- Park K. and Chao H. S.**, "A self-learning rule-based control algorithm for chamferless part mating", *Control Eng. Practice*, V. 2, No. 5, pp. 773-783, 1994.
- Penfold R.**, "Experimental noise cancelling unit", *Everyday Practical Electronics Publication*, USA, 1994.
- Qiao H.**, "Robotic peg-hole insertion operation analysis", PhD Thesis, De Montfort University, 1995.
- Qiao H., Parkin R., Dalay B.**, "Precise robotic chamferless peg-hole insertion operation without force feedback and remote centre compliance (RCC)", *Proc Inst. Mech. Engrs*, V. 208, pp. 89-104, Feb. 1994.
- Sanderson A. C., Perry G.**, "Sensor-based robotic assembly system: Research and applications in electronic manufacturing", *Proc. IEEE* 71, No. 7, pp. 856-871, 1983.
- Stepourjine R. and Rouget J. P.**, "Automatic insertion module for light robotics", *Proc. of The Development in Robotics*, pp. 197-204, 1983.
- Setchi R. and Bratanov D.**, "Three-dimensional simulation of accommodation", *Assembly Automation*, V. 18, N. 4, pp. 291-301, 1998.
- Simunovic S.**, "Force information in assembly process", 5th Int. Symp. on Industrial Robots, Chicago, September 1975.
- Simunovic S.**, "An information approach to part mating", PhD Thesis, MIT, Cambridge, Massachusetts, April 1979.
- Takeyasu K. and Kasai**, "Trainable assembly system with an active sensory table processing 6 axes", *Proc. 11th Int. Symp. on Industrial Robots*, pp. 210-212, Tokyo, Japan 1981.

- Takeyasu K., Goto T, Inoyama T.**, “Precision insertion control robot and it’s application”, ASME J. Engineering for Industry, pp. 1313-1318, Nov. 1976.
- Tsuruoka T., Fujioka H., Moriyama T. and Mayeda H.**, “3D analysis of contact in peg-hole insertion”, Proceeding of the 1997 IEEE Int. Symp. on Assembly and Task Planning, pp.84-89, Marina del-Rey, CA USA. August 1997.
- Volmer J., Jacobi P., Schwarz A. and Zachan H.**, “Positionierung von montagegreifern und werkzeugen durch industrierobotor”, Fertigungstechnik und Betrieb, pp. 742-747, Berlin 32, 1982.
- Whitney D. E.**, “Quasi-static assembly of compliantly supported rigid parts”, ASME Jour. of Dyn. Syst. Meas. Contr., V. 104, pp. 65-77, 1982.
- Whitney E. and Nevins J. L.**, “What is the RCC and what can it do?”, Proc. 9th Int. Symp. on Industrial Robots, Washington, D. C. USA, pp. 135-152, 1979.
- Whitney D. E.**, “Discrete parts assembly automation – an overview”, ASME Jour. of Dyn. Syst. Meas. Contr., 101, pp. 8-15, 1979.
- Whitney D. E.**, “Part mating in assembly”, Handbook of Industrial Robotics, Edited by Shimon Nof, pp. 1084-1116, 1986.
- Warnecke H. J., Walther M., Haaf D.**, “An adaptable programmable assembly system using compliance and visual feedback”, Proc. of the 10th Symp. on Industrial Robots, pp. 481-490, March 1980.
- Warnecke J., Frakenhauser B., Gweon D. G. and Cho H. S.**, “Fitting of crimp contacts to connectors using industrial robots supported by vibrating tools”, Robotica, V. 6, pp. 123-129, 1988.
- Won Jeong K. and Hyung Suck Cho**, “Development of a pneumatic vibratory wrist for robotic assembly”, Robotica, V. 7, pp. 9-16, 1989.

Watson P. C., (The Charles Stark Draper Laboratory), “Remote centre compliance device”, United States Patent 4098001, July 1978.

Watson P. C., “The remote centre compliance system and its application to high speed robot assembly”, SME paper, No. AD77-718, 1977.

Wang Y., Mason M., “Modelling impact dynamic for robotic operation”, Proc. of the 1987 IEEE Int. Conf. on Robotics and Automation, pp. 678-685, 1987.

Xu Y. and Paul R. P., “A robot compliant wrist system for automated assembly”, Proc. of the IEEE Int. Conf. on Robotics and Automation, pp. 1750-1755, Cincinnati, OH, 1990.

Yakimovich Y. A., “Automatic assembly of components by the jet method”, Russian Eng. 50, No. 6, pp.58-63, 1970.

APPENDIX 1

EXPERIMENTAL DETERMINATION OF THE MOMENT OF INERTIA FOR THE CVHRCC:

To determine the moment of inertia for the wrist, a Trifilar suspension was used. Firstly, the moment of inertia for the Trifilar, and then for both the trifilar and the wrist. Secondly, the moment of inertia for the wrist was the combined one minus the one for the trifilar. Figure (1) shows the trifilar, initially it was rotated about its centre for 30 seconds. The average cycles was 16 for that period.

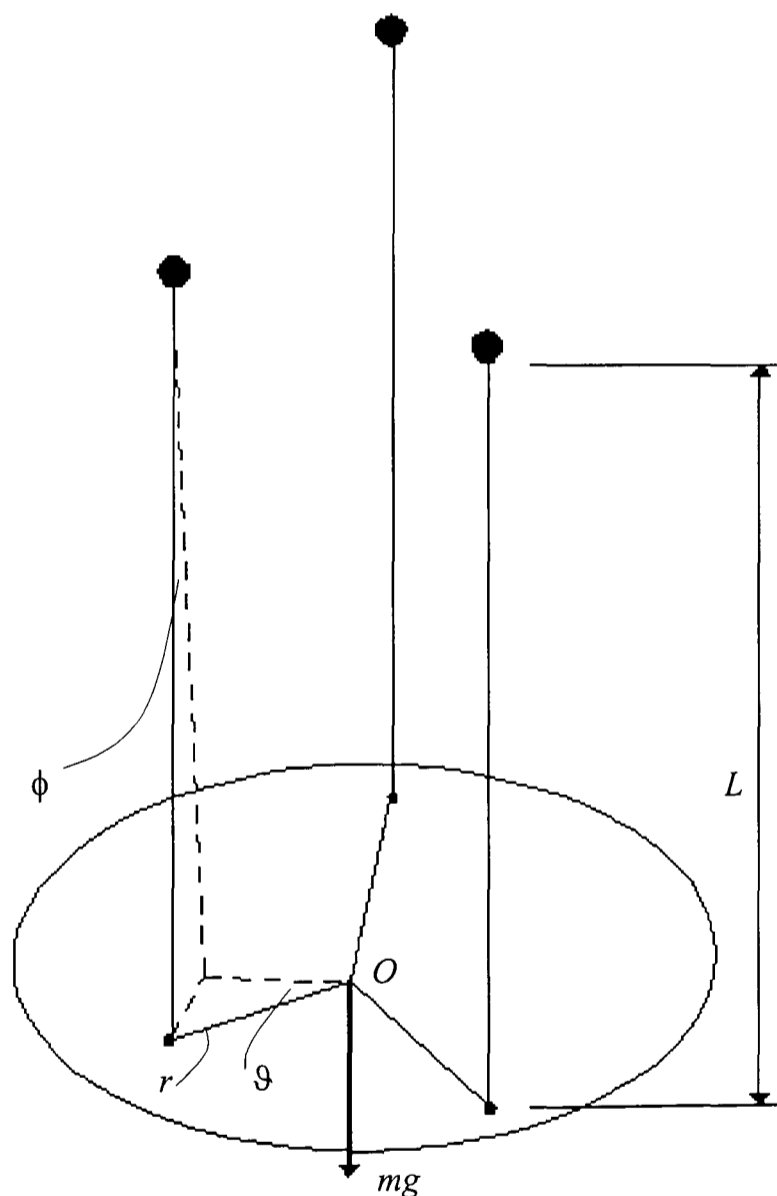


Figure 1 Schematic view of a Trifilar suspension

The periodic time for rotating the trifilar is given by

$$T = 2\pi \sqrt{\frac{IL}{mgr^2}} \quad (1)$$

Where:

T	periodic time = 30/16 (sec/rev)
I	moment of inertia
L	length of suspension wire = 1 m
m	mass of trifilar disc = 4.43 Kg
g	acceleration due to gravity = 9.81 m/s ²
r	radius of suspension = 0.15 m

Rearranging eq. (1) and substitute the above values,

$$I = \left(\frac{1.875}{2\pi} \right)^2 \left(\frac{4.43 \times 9.81 \times 0.15^2}{1} \right) = 0.087 \text{ Kg.m}^2$$

This is the moment of inertia for the trifilar. Now placing the wrist in the centre of the trifilar ($m = 4.43+3.1$) and rotating the system about its centre for 30 seconds gave 20 cycles or,

$$T = \frac{30}{20} = 1.5 \frac{\text{sec}}{\text{cycle}}$$

then the moment of inertia for both the trifilar and the wrist is

$$I = \left(\frac{1.5}{2\pi} \right)^2 \left(\frac{7.53 \times 9.81 \times 0.15^2}{1} \right) = 0.094 \text{ Kg.m}^2$$

So, the moment of inertia for the wrist is the difference between both wrist and trifilar,

$$I = 0.094 - 0.087 \cong 0.007 \text{ Kg.m}^2$$

Therefore the moment of inertia about the X or the Y axis is,

$$I_x = \frac{I_z}{2} = \frac{0.007}{2} = 0.0035 \text{ Kgm}^2$$

20	0.1	0.5	0	-3	2 of 5 in	40
20	0.1	0	0.5	3	3 of 5 in	60
20	0.1	0	0.5	-3	2 of 5 in	40
20	0.1	0.5	0.5	3	3 of 5 in	60
20	0.1	0.5	0.5	-3	2 of 5 in	40
20	H7/h6	0.5	0	0	3 of 5 in	60
20	H7/h6	0	0.5	0	3 of 5 in	60
20	H7/h6	0	0	2.5	2 of 5 in	40
20	H7/h6	0	0	-2.5	1 of 5 in	20
20	H7/h6	0.5	0	2.5	2 of 5 in	40
20	H7/h6	0.5	0	-2.5	1 of 5 in	20
20	H7/h6	0	0.5	2.5	2 of 5 in	40
20	H7/h6	0	0.5	-2.5	1 of 5 in	20
20	H7/h6	0.5	0.5	2.5	2 of 5 in	40
20	H7/h6	0.5	0.5	-2.5	1 of 5 in	20
25	0.2	1.5	0	0	4 of 5 in	80
25	0.2	0	1.5	0	3 of 5 in	60
25	0.2	0	0	3.5	3 of 5 in	60
25	0.2	0	0	-3.5	2 of 5 in	40
25	0.2	1.5	0	3.5	3 of 5 in	60
25	0.2	1.5	0	-3.5	1 of 5 in	20
25	0.2	0	1.5	3.5	3 of 5 in	60
25	0.2	0	1.5	-3.5	1 of 5 in	20
25	0.2	1.5	1.5	3.5	3 of 5 in	60
25	0.2	1.5	1.5	-3.5	1 of 5 in	20
25	0.1	1	0	0	3 of 5 in	60
25	0.1	0	1	0	2 of 5 in	40
25	0.1	0	0	2	4 of 5 in	80
25	0.1	0	0	-2	2 of 5 in	40
25	0.1	1	0	2	2 of 5 in	40
25	0.1	1	0	-2	1 of 5 in	20
25	0.1	0	1	2	2 of 5 in	40
25	0.1	0	1	-2	1 of 5 in	20
25	0.1	1	1	2	2 of 5 in	40
25	0.1	1	1	-2	1 of 5 in	20
25	H7/h6	1	0	0	2 of 5 in	40
25	H7/h6	0	1	0	3 of 5 in	60
25	H7/h6	0	0	2.5	1 of 5 in	20
25	H7/h6	0	0	-2.5	0 of 5 in	0
25	H7/h6	1	0	2.5	2 of 5 in	40
25	H7/h6	1	0	-2.5	1 of 5 in	20
25	H7/h6	0	1	2.5	2 of 5 in	40
25	H7/h6	0	1	-2.5	0 of 5 in	0
25	H7/h6	1	1	2.5	2 of 5 in	40
25	H7/h6	1	1	-2.5	0 of 5 in	0
30	0.2	1.5	0	0	3 of 5 in	60
30	0.2	0	1.5	0	2 of 5 in	40
30	0.2	0	0	3.5	2 of 5 in	40
30	0.2	0	0	-3.5	0 of 5 in	0
30	0.2	1.5	0	3.5	3 of 5 in	60
30	0.2	1.5	0	-3.5	1 of 5 in	20
30	0.2	0	1.5	3.5	2 of 5 in	40
30	0.2	0	1.5	-3.5	0 of 5 in	0
30	0.2	1.5	1.5	3.5	2 of 5 in	40
30	0.2	1.5	1.5	-3.5	0 of 5 in	0

30	0.1	1.5	0	0	2 of 5 in	40
30	0.1	0	1.5	0	2 of 5 in	40
30	0.1	0	0	3.5	1 of 5 in	20
30	0.1	0	0	-3.5	0 of 5 in	0
30	0.1	1.5	0	3.5	2 of 5 in	40
30	0.1	1.5	0	-3.5	0 of 5 in	0
30	0.1	0	1.5	3.5	1 of 5 in	20
30	0.1	0	1.5	-3.5	0 of 5 in	0
30	0.1	1.5	1.5	3.5	2 of 5 in	40
30	0.1	1.5	1.5	-3.5	0 of 5 in	0
30	H7/h6	1.2	0	0	2 of 5 in	40
30	H7/h6	0	1.2	0	1 of 5 in	20
30	H7/h6	0	0	3	0 of 5 in	0
30	H7/h6	0	0	-3	0 of 5 in	0
30	H7/h6	1.2	0	3	1 of 5 in	20
30	H7/h6	1.2	0	-3	0 of 5 in	0
30	H7/h6	0	1.2	3	1 of 5 in	20
30	H7/h6	0	1.2	-3	0 of 5 in	0
30	H7/h6	1.2	1.2	3	1 of 5 in	20
30	H7/h6	1.2	1.2	-3	0 of 5 in	0
35	0.2	2.2	0	0	2 of 5 in	40
35	0.2	0	2.2	0	2 of 5 in	40
35	0.2	0	0	4	1 of 5 in	20
35	0.2	0	0	-4	0 of 5 in	0
35	0.2	2.2	0	4	1 of 5 in	20
35	0.2	2.2	0	-4	0 of 5 in	0
35	0.2	0	2.2	4	1 of 5 in	20
35	0.2	0	2.2	-4	0 of 5 in	0
35	0.2	2.2	2.2	4	1 of 5 in	20
35	0.2	2.2	2.2	-4	0 of 5 in	0
35	0.1	1.8	0	0	1 of 5 in	20
35	0.1	0	1.8	0	0 of 5 in	0
35	0.1	0	0	3.5	0 of 5 in	0
35	0.1	0	0	-3.5	0 of 5 in	0
35	0.1	1.8	0	3.5	1 of 5 in	20
35	0.1	1.8	0	-3.5	0 of 5 in	0
35	0.1	0	1.8	3.5	0 of 5 in	0
35	0.1	0	1.8	-3.5	0 of 5 in	0
35	0.1	1.8	1.8	3.5	0 of 5 in	0
35	0.1	1.8	1.8	-3.5	0 of 5 in	0
35	H7/h6	1.6	0	0	0 of 5 in	0
35	H7/h6	0	1.6	0	0 of 5 in	0
35	H7/h6	0	0	3.3	0 of 5 in	0
35	H7/h6	0	0	-3.3	0 of 5 in	0
35	H7/h6	1.6	0	3.3	0 of 5 in	0
35	H7/h6	1.6	0	-3.3	0 of 5 in	0
35	H7/h6	0	1.6	3.3	0 of 5 in	0
35	H7/h6	0	1.6	-3.3	0 of 5 in	0
35	H7/h6	1.6	1.6	3.3	0 of 5 in	0
35	H7/h6	1.6	1.6	-3.3	0 of 5 in	0

Table 2 The additional peg-hole assembly experiments

Peg dia. (mm)	Clearance (mm)	$e_{x \max}$ (mm)	$e_{v \max}$ (mm)	θ_{\max}°	Assembly result (Total tries =5)	Success rate %
30	0.2	1.5	0	0	4 of 5 in	80
30	0.2	0	1.5	0	4 of 5 in	80
30	0.2	0	0	3.5	3 of 5 in	60
30	0.2	0	0	-3.5	2 of 5 in	40
30	0.2	1.5	0	3.5	3 of 5 in	60
30	0.2	1.5	0	-3.5	2 of 5 in	40
30	0.2	0	1.5	3.5	3 of 5 in	60
30	0.2	0	1.5	-3.5	2 of 5 in	20
30	0.2	1.5	1.5	3.5	2 of 5 in	40
30	0.2	1.5	1.5	-3.5	0 of 5 in	0
30	0.1	1.5	0	0	3 of 5 in	60
30	0.1	0	1.5	0	3 of 5 in	60
30	0.1	0	0	3.5	2 of 5 in	40
30	0.1	0	0	-3.5	1 of 5 in	20
30	0.1	1.5	0	3.5	3 of 5 in	60
30	0.1	1.5	0	-3.5	2 of 5 in	40
30	0.1	0	1.5	3.5	3 of 5 in	60
30	0.1	0	1.5	-3.5	1 of 5 in	20
30	0.1	1.5	1.5	3.5	3 of 5 in	60
30	0.1	1.5	1.5	-3.5	1 of 5 in	20
30	H7/h6	1.2	0	0	2 of 5 in	40
30	H7/h6	0	1.2	0	2 of 5 in	40
30	H7/h6	0	0	3	1 of 5 in	20
30	H7/h6	0	0	-3	0 of 5 in	0
30	H7/h6	1.2	0	3	2 of 5 in	40
30	H7/h6	1.2	0	-3	0 of 5 in	0
30	H7/h6	0	1.2	3	2 of 5 in	40
30	H7/h6	0	1.2	-3	0 of 5 in	0
30	H7/h6	1.2	1.2	3	2 of 5 in	40
30	H7/h6	1.2	1.2	-3	1 of 5 in	20
35	0.2	2.2	0	0	3 of 5 in	60
35	0.2	0	2.2	0	2 of 5 in	40
35	0.2	0	0	4	2 of 5 in	40
35	0.2	0	0	-4	1 of 5 in	20
35	0.2	2.2	0	4	3 of 5 in	60
35	0.2	2.2	0	-4	1 of 5 in	20
35	0.2	0	2.2	4	3 of 5 in	60
35	0.2	0	2.2	-4	1 of 5 in	20
35	0.2	2.2	2.2	4	2 of 5 in	40
35	0.2	2.2	2.2	-4	0 of 5 in	0
35	0.1	1.8	0	0	3 of 5 in	60
35	0.1	0	1.8	0	2 of 5 in	40
35	0.1	0	0	3.5	2 of 5 in	40
35	0.1	0	0	-3.5	1 of 5 in	20
35	0.1	1.8	0	3.5	2 of 5 in	40
35	0.1	1.8	0	-3.5	0 of 5 in	0
35	0.1	0	1.8	3.5	3 of 5 in	60
35	0.1	0	1.8	-3.5	0 of 5 in	0
35	0.1	1.8	1.8	3.5	3 of 5 in	60
35	0.1	1.8	1.8	-3.5	1 of 5 in	20
35	H7/h6	1.6	0	0	0 of 5 in	0

35	H7/h6	0	1.6	0	0 of 5 in	0
35	H7/h6	0	0	3.3	0 of 5 in	0
35	H7/h6	0	0	-3.3	0 of 5 in	0
35	H7/h6	1.6	0	3.3	0 of 5 in	0
35	H7/h6	1.6	0	-3.3	0 of 5 in	0
35	H7/h6	0	1.6	3.3	0 of 5 in	0
35	H7/h6	0	1.6	-3.3	0 of 5 in	0
35	H7/h6	1.6	1.6	3.3	0 of 5 in	0
35	H7/h6	1.6	1.6	-3.3	0 of 5 in	0

APPENDIX 3

SUMMARY OF FINITE ELEMENT RESULTS

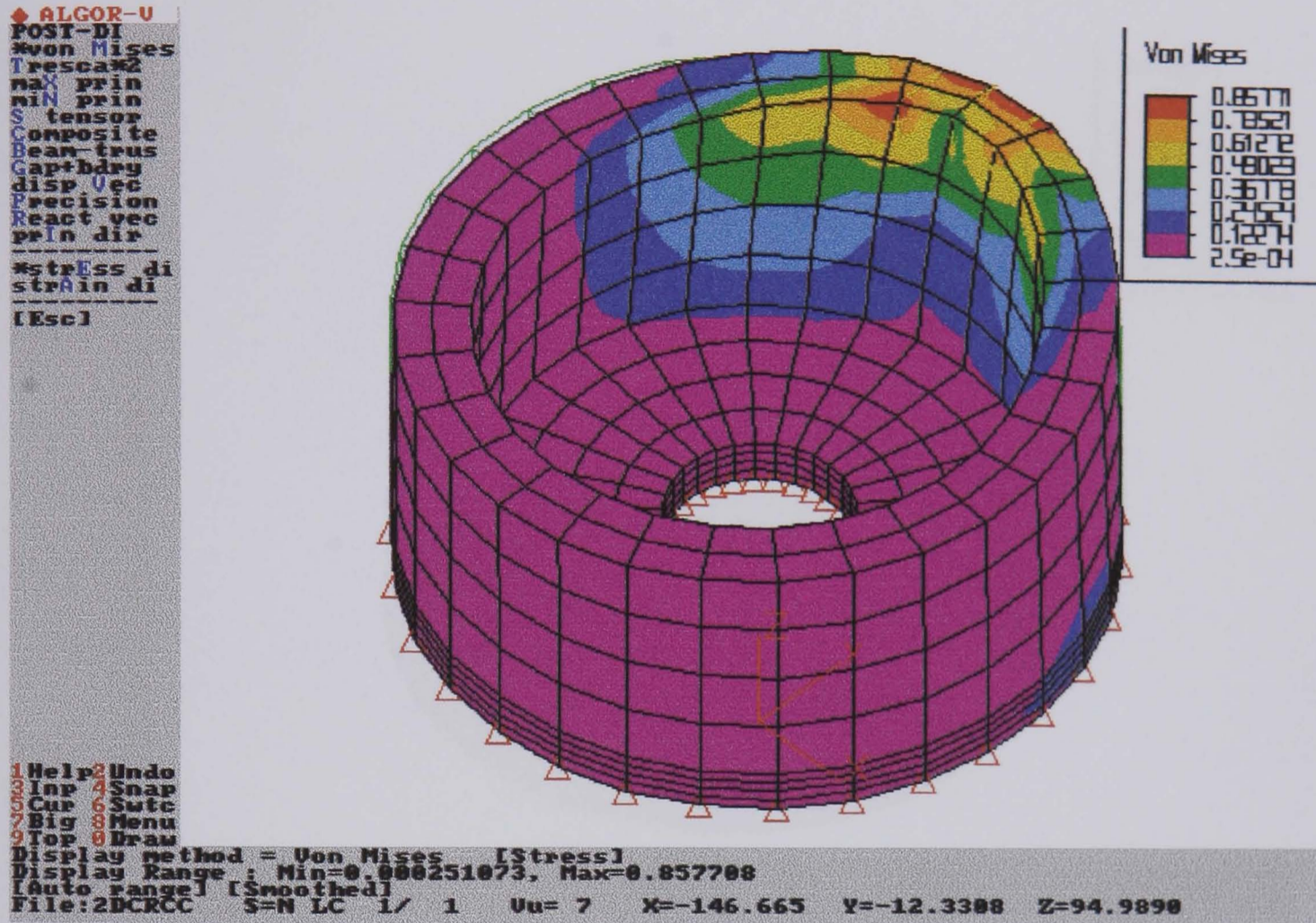
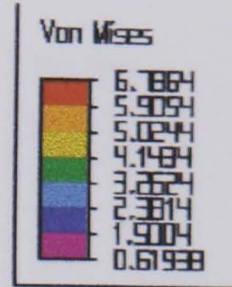
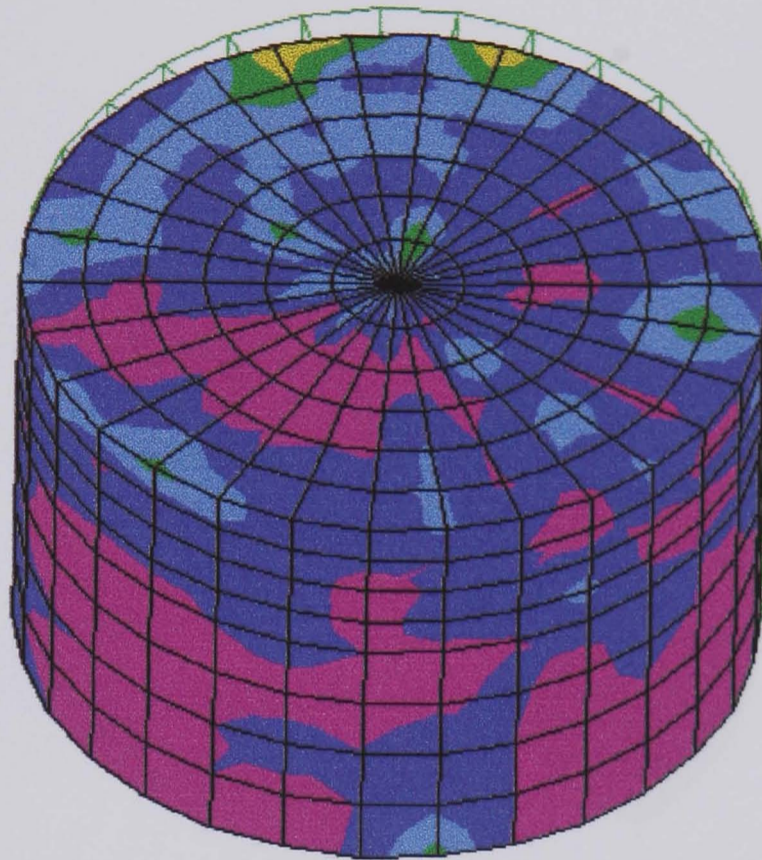


Figure 1 Results of FEA for the bottom plate

```

◆ ALGOR-U
POST-DI
*von Mises
Tresca*2
max prin
min prin
S tensor
Composite
Beam-trus
Gap+bdry
disp Vec
Precision
React vec
prin dir
-----
*stress di
strain di
-----
[Esc]

```



```

1 Help 2 Undo
3 Inp 4 Snap
5 Cur 6 Sutc
7 Big 8 Menu
9 Top 0 Draw

```

```

Display method = Von Mises [Stress]
Display Range : Min=0.619376, Max=6.78644
[Auto range] [Smoothed]
File:2dcrcc2 S=N LC 1/ 1 Uu= 7 X=-93.9482 Y=11.6854 Z=74.6943

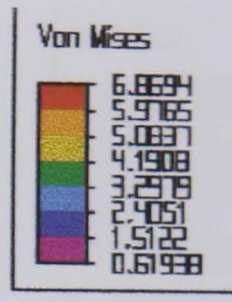
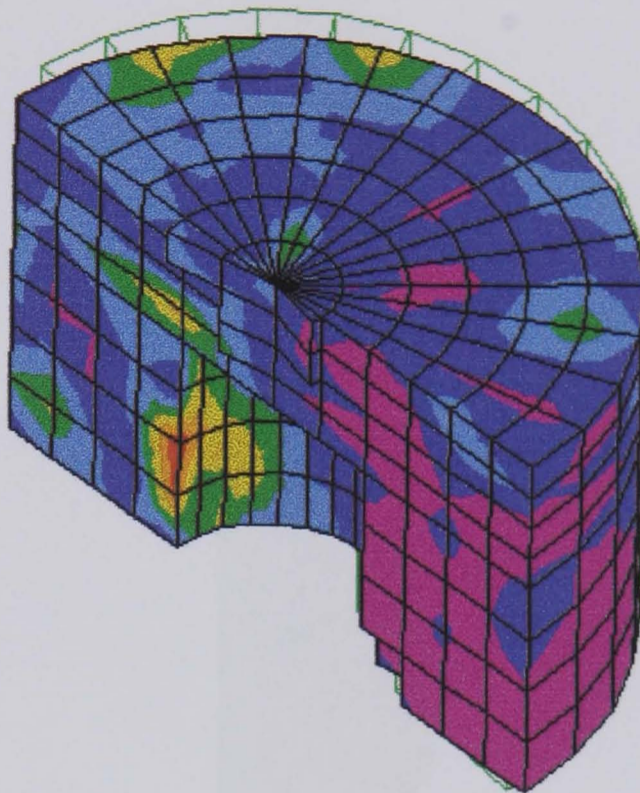
```

Figure 2 Results of FEA for the bottom plate of the floating unit

```

ALGOR-U
POST-DI
Von Mises
Tresca
max prin
min prin
S tensor
Composite
Beam-trus
Gap+bdry
disp Vec
Precision
React vec
prin dir
*stress di
*strain di
[Esc]

```



```

1 Help 2 Undo
3 Inp 4 Snap
5 Cur 6 Sutc
7 Big 8 Menu
9 Top 0 Draw

```

```

Display method = Von Mises [Stress]
Display Range : Min=0.619376, Max=6.86938
[Auto range] [Smoothed]
File:2dcrcc2 S=N LC 1/ 1 Vu= 7 X=-100.534 Y=16.4541 Z=82.7236

```

Figure 3 A slice into the bottom plate of figure (2)

```

◆ ALGOR-U
POST-DI
*Von Mises
TrescaK2
max prin
min prin
S tensor
Composite
Beam-trus
Gap+bdry
disp Vec
Precision
React vec
prin dir
-----
*stress di
*strain di
-----
[Esc]

```

```

1 Help 2 Undo
3 Inp 4 Snap
5 Cur 6 Sutc
7 Big 8 Menu
9 Top 0 Draw

```

```

Display method = Von Mises [Stress]
Display Range : Min=1.4593, Max=98.0287
[Auto range] [Smoothed]
File: CENROD S=N LC 1/ 1 Vu= 7 X=-94.6320 Y=41.9150 Z=96.5533

```

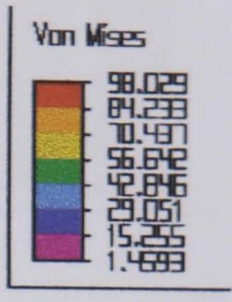
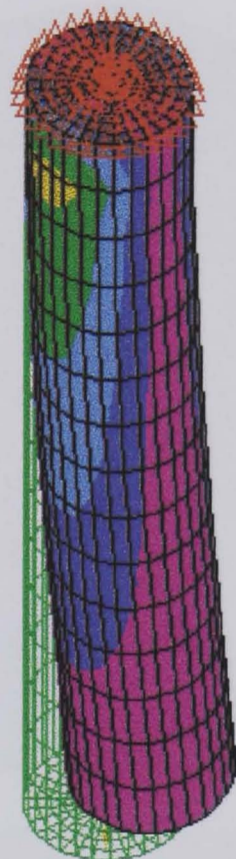


Figure 4 Results of FEA for the centre rod

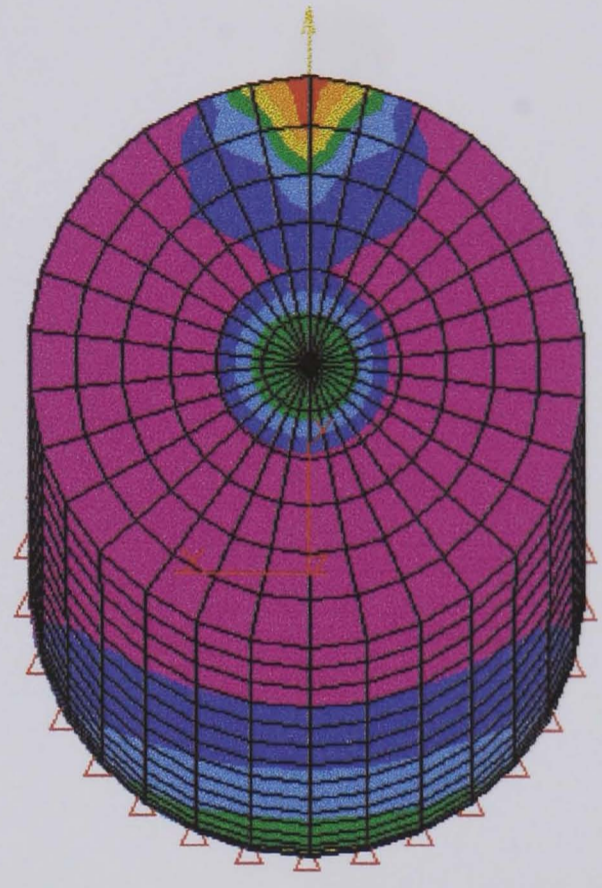
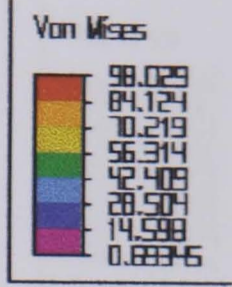
◆ ALGOR-U
 STRESS-DI
 disp Opt

 Hidden 1
 Light
 *Post
 Eq+other

 Aux post
 General
 *Smoothed
 *max abs
 *Mesh
 IgNd box

 Bitmap
 Display

 [Esc]



1 Help 2 Undo
 3 Inp 4 Snap
 5 Cur 6 Sute
 7 Big 8 Menu
 9 Top 0 Draw

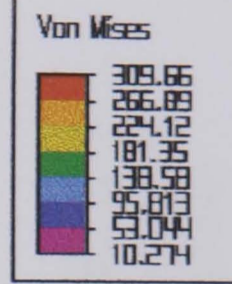
Display method = Von Mises [Stress]
 Full Range: Min=0.69345, Max=98.0287
 [Auto range] [Smoothed]
 File: CENROD S=N LC 1/ 1 Vu= 4 X=13.4898 Y=6.5448 Z=0.0000

Figure 5 A birds eye view of the centre rod

```

◆ ALGOR-U
STRESS-DI
disp Opt
Hidden 1
Light
*Post
Eq+other
Aux post
General
*Smoothed
*max abs
*Mesh
lgNd box
Bitmap
Display
[Esc]

```



```

1 Help 2 Undo
3 Inp 4 Snap
5 Cur 6 Sutc
7 Big 8 Menu
9 Top 0 Draw

```

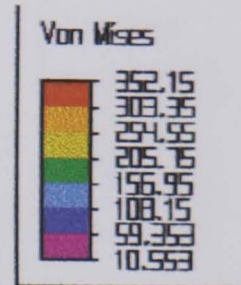
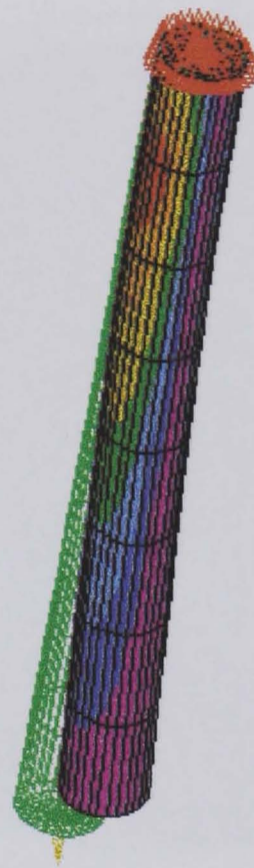
```

Display method = Von Mises [Stress]
Display Range : Min=10.2742, Max=309.661
[Auto range] [Smoothed]
File:2dcrcc7 S=N LC 1/ 1 Uu=H6 X=26.2695 Y=134.2774 Z=146.7570

```

Figure 6 Results of FEA for the vertical connection rod

◆ ALGOR-U
 STRESS-DI
 disp Opt
 Hidden 1
 Light
 *Post
 Eq+other
 Aux post
 General
 *Smoothed
 *max abs
 *Mesh
 IgNd box
 Bitmap
 Display
 [Esc]



1 Help 2 Undo
 3 Inp 4 Snap
 5 Cur 6 Sufe
 7 Big 8 Menu
 9 Top 0 Draw

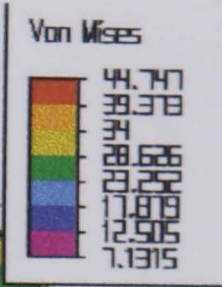
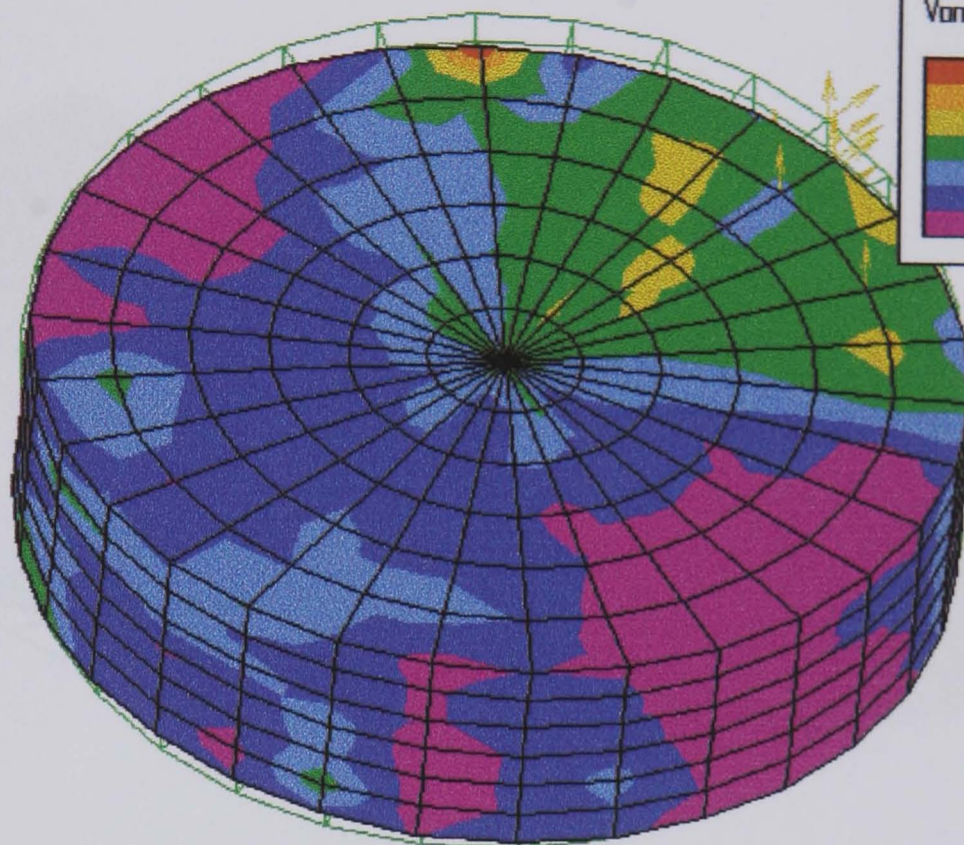
Display method = Von Mises [Stress]
 Display Range : Min=10.553, Max=352.152
 [Auto range] [Smoothed]
 File:2dcrcc4 S=N LC 1/ 1 Vu= 7 X=-92.0674 Y=59.7191 Z=107.3293

Figure 7 Results of FEA for the inclined rod

```

ALGOR-U
DRAW
Redraw
Pan
Zoom In
Zoom Out
Last zn
Enclose
Set u
View
User view
XX persp
Define vu
Jetview
last vu
[Esc]

```



```

1 Help 2 Undo
3 Inp 4 Snap
5 Cur 6 Swtc
7 Big 8 Menu
9 Top 0 Draw

```

```

Display method = Von Mises [Stress]
Display Range : Min=7.13151, Max=44.7471
[Auto range] [Smoothed]
File:2dcrcc5 S=N LC 1/ 1 Uu= 7 X=-128.121 Y=49.3276 Z=125.4755

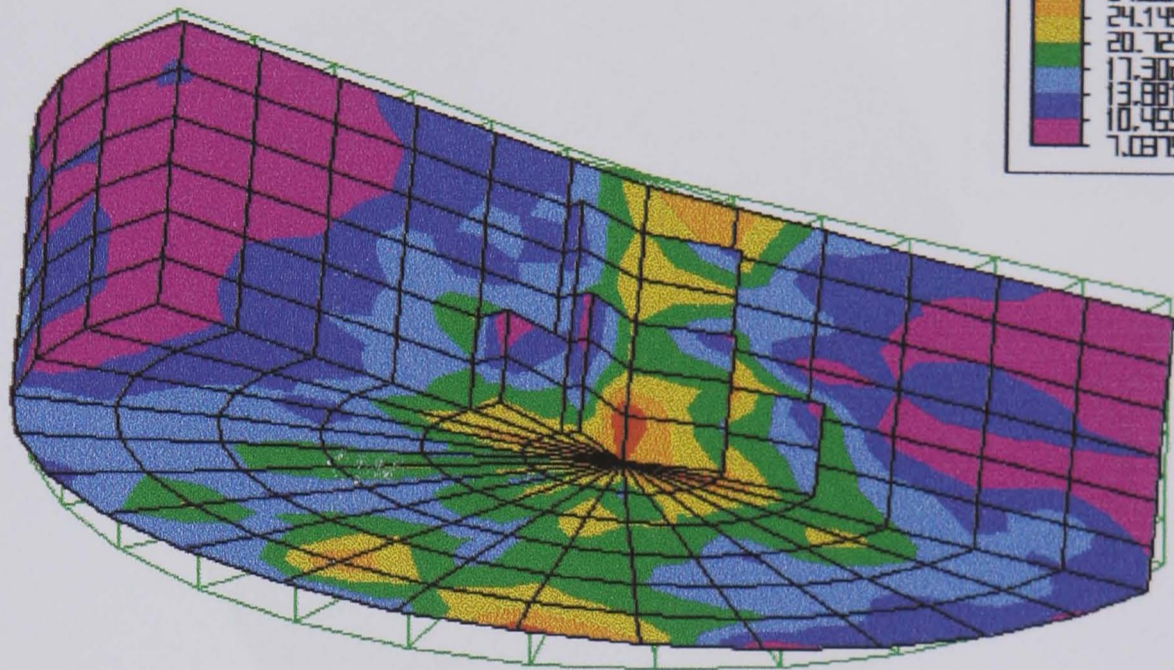
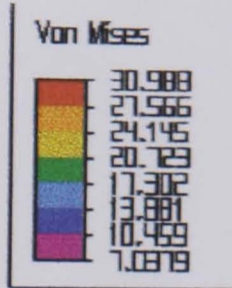
```

Figure 8 Results of FEA for the top plate of the floating unit

```

ALGOR-U
STRESS-DI
disp Opt
Hidden 1
Light
*Post
Eq+other
Aux post
General
*Snoothed
*max abs
*Mesh
lgNd box
Bitmap
Display
[Esc]

```



```

1 Help 2 Undo
2 Inp 3 Snap
3 Cur 4 Sutc
4 Big 5 Menu
5 Top 6 Draw

```

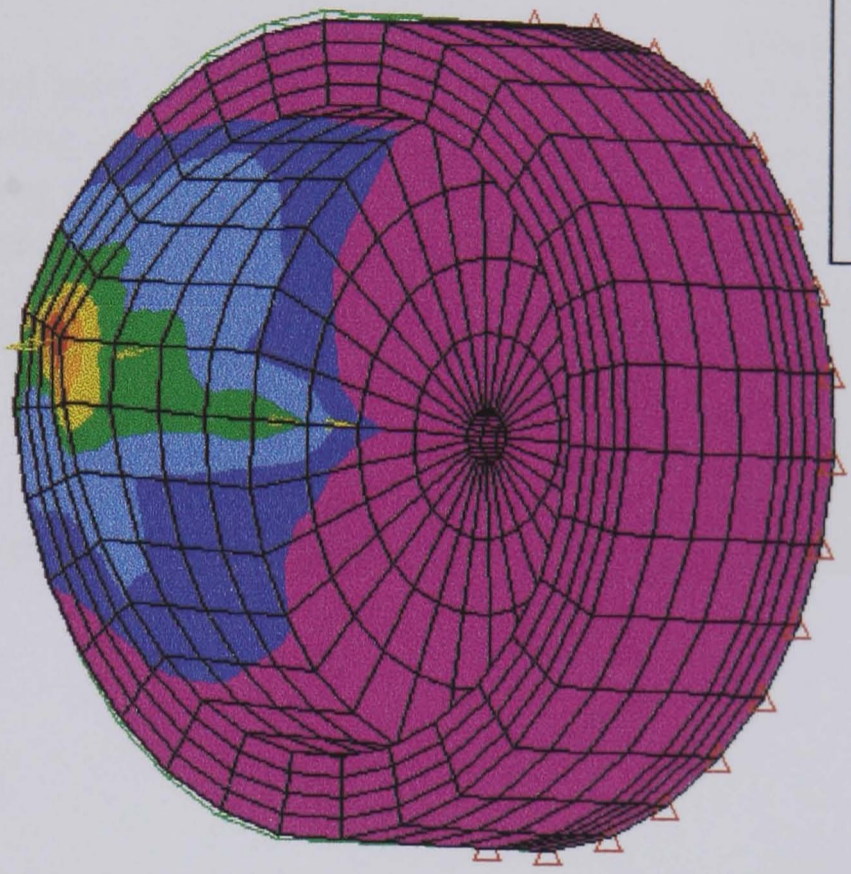
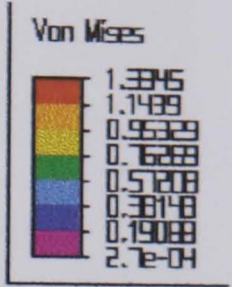
```

Display method = Von Mises [Stress]
Display Range: Min=7.03785, Max=30.9875
[Auto range] [Snoothed]
File:2dcrcc5 S=N LC 1/ 1 Vu=U5 X=82.1003 Y=36.4629 Z=188.3983

```

Figure 9 A slice into the top plate of figure (7.17)

◆ ALGOR-U
 STRESS-DI
 disp Opt
 Hidden I
 Light
 #Post
 Eq+other
 Aux post
 General
 #Smoothed
 #max abs
 #Mesh
 IgNd box
 Bitmap
 Display
 [Esc]



1 Help 2 Undo
 3 Inp 4 Snap
 5 Cur 6 Swtc
 7 Big 8 Menu
 9 Top 0 Draw

Display method = Von Mises [Stress]
 Display Range : Min=0.000274422, Max=1.3345
 [Auto range] [Smoothed]
 File:2dcrcc6 S=N LC 1/ 1 Uu=U7 X=-72.6152 Y=-36.3041 Z=20.8192

Figure 10 Results of FEA for the top plate of the fixed unit

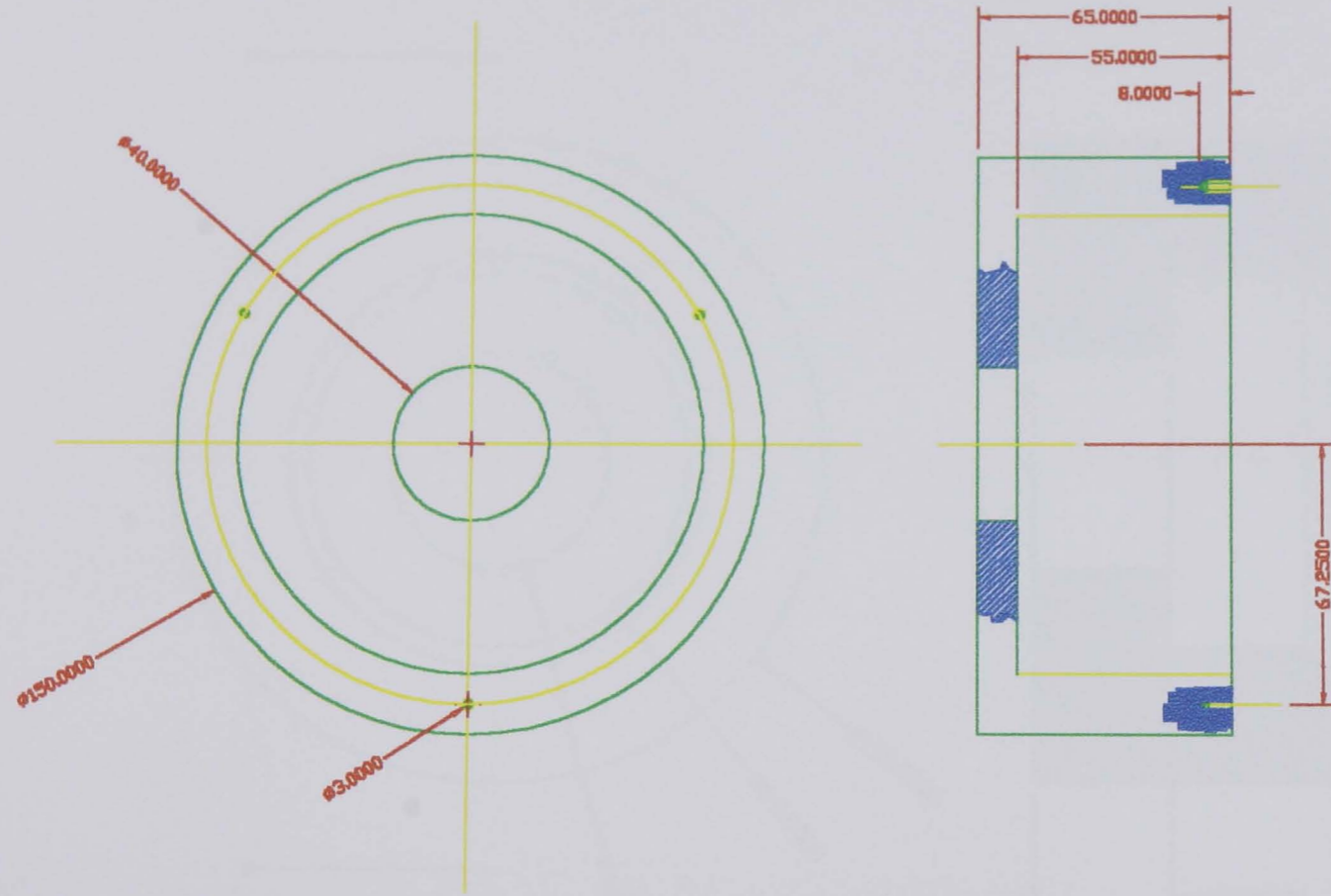
DRAWINGS & PUBLICATIONS

Table 1 Components References

Reference No.	Name	Material	Quantity	Manuf./ Assembly
1	External base	Aluminum	1	As in dwg.
2	Bottom sponge	Sponge F010111	1	2 Strips to glue then glue on 1, Bostik 1GA167
3	Internal sponge	Sponge F010104	1	2 Strips to glue then glue on 4, Bostik 1GA167
4	Internal base	Aluminum	1	As in dwg.
5	Supporting rod	Mild steel	3	As in dwg.
6	Angular rod	Mild steel	3	As in dwg.
7	Straight rod	Mild steel	1	As in dwg.
8	Upper base	Aluminum	1	As in dwg.
9	Upper sponge	Sponge F010109 & F010111	1 & 1	2 Strips to glue then glue on 10, Bostik 1GA167
10	Top plate	Aluminum	1	As in dwg.

ALL DIMENSIONS IN MM

PROJECTION



MATERIAL Aluminum

DRAWN WASIM

DeMontfort University
Department Of Mechanical Engineering

Date May/97

TITLE External Base

QUANTITY 1

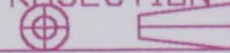
SCALE 0,5:1

CMU-RCC

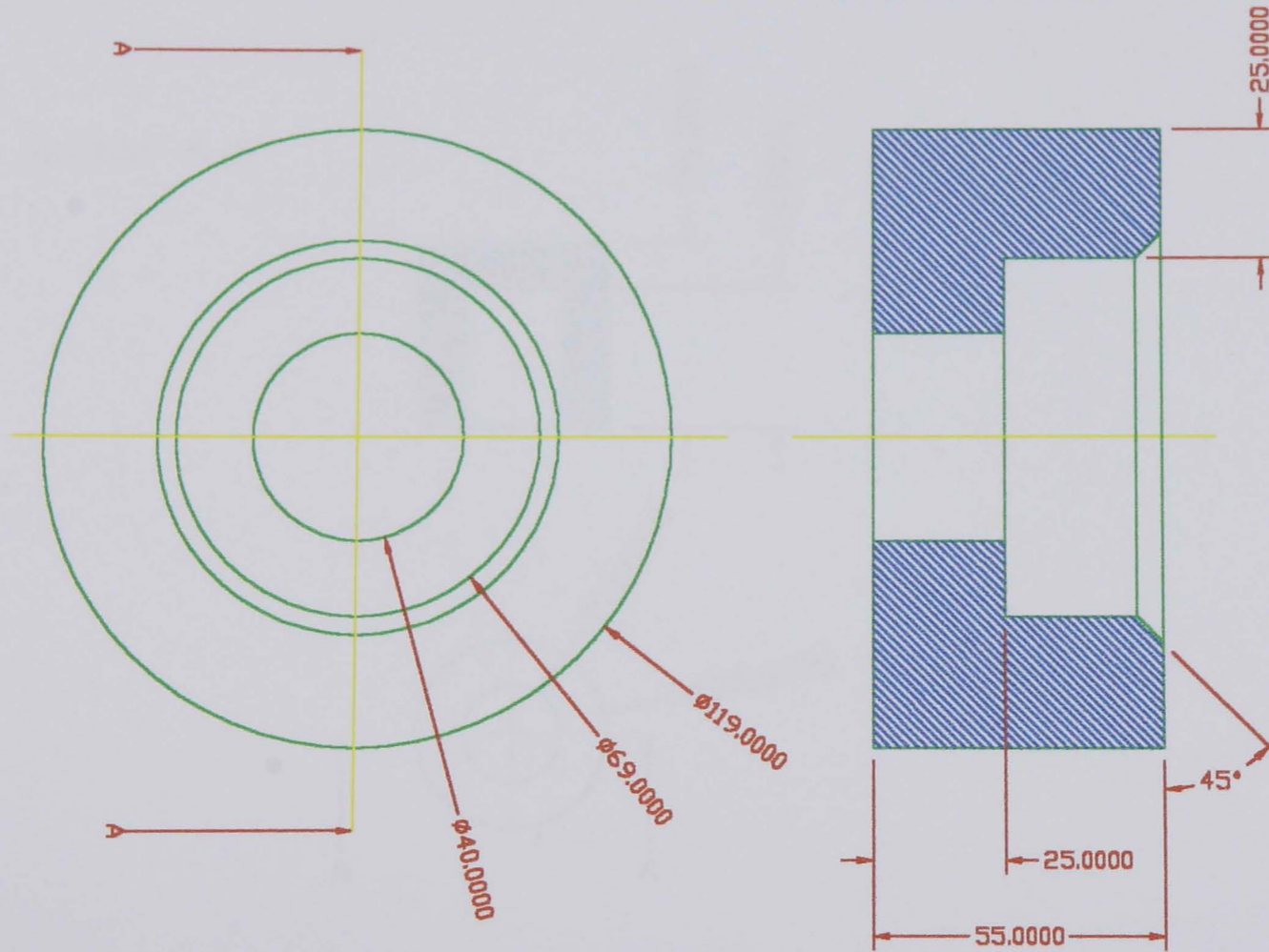
DRAWING No.1

ALL DIMENSIONS IN MM

PROJECTION



Section A-A



MATERIAL Spong F 010111

DRAWN WASIM

DeMontfort University
Department Of Mechanical Engineering

Date May/97

TITLE Bottom Spong

QUANTITY 1

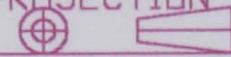
SCALE 0.5:1

CMH-RCC

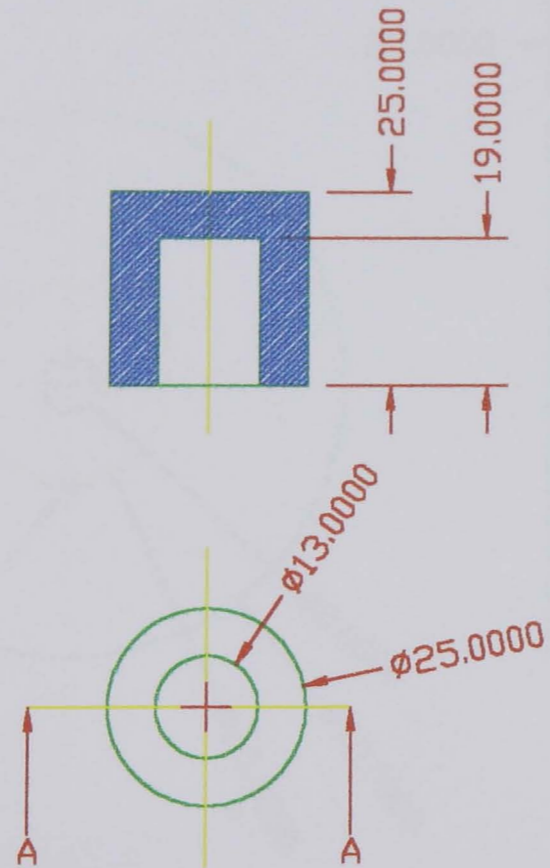
DRAWING No.2

ALL DIMENSIONS IN MM

PROJECTION



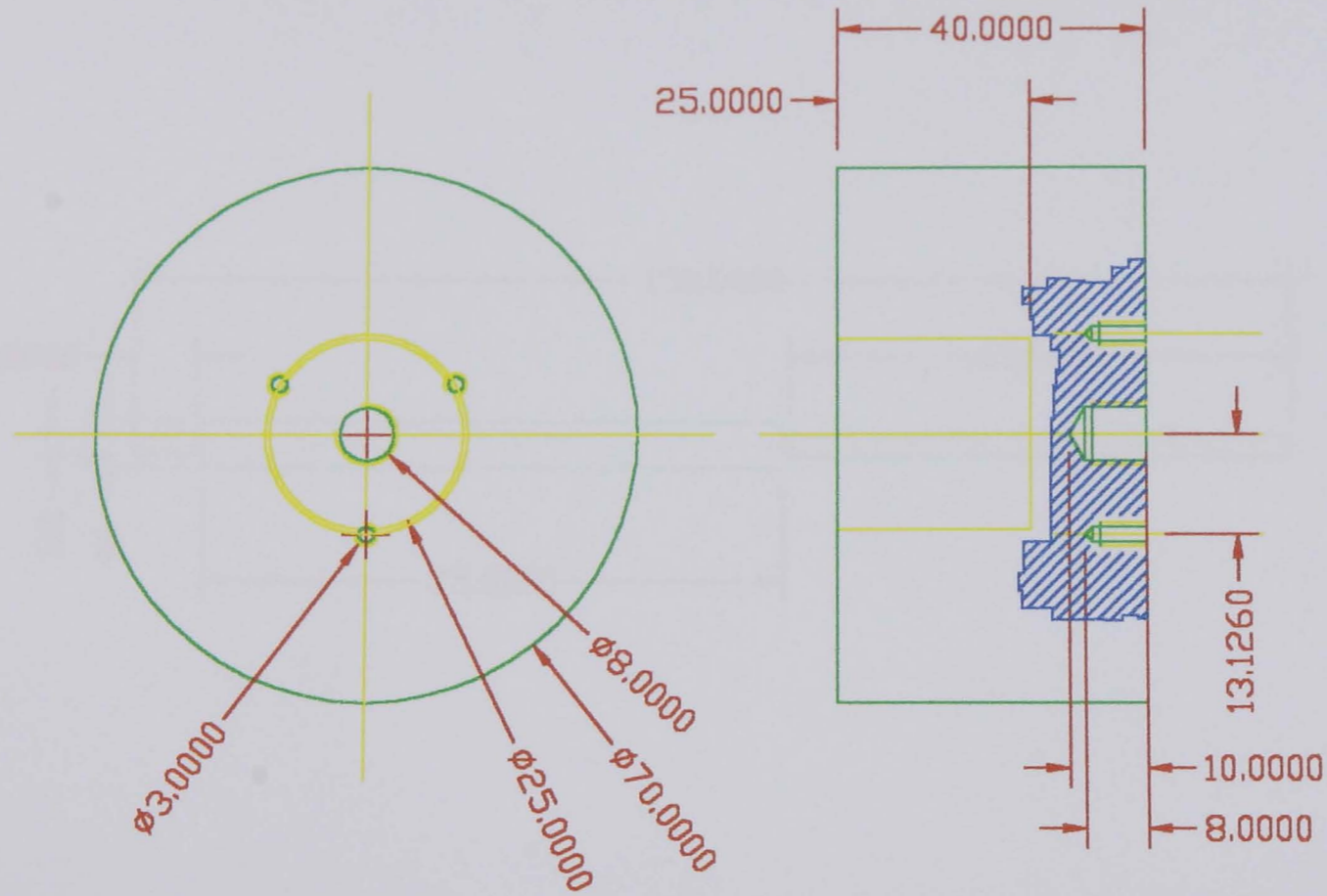
Section A-A



MATERIAL	Spong F 010104	DRAWN	WASIM	DeMontfort University	
		Date	May/97	Department Of Mechanical Engineering	
QUANTITY	1	TITLE		Internal Spong	
		SCALE	1:1	CMB-RCC	DRAWING No.3

ALL DIMENSIONS IN MM

PROJECTION



MATERIAL Aluminum

DRAWN WASIM

De Montfort University
Department Of Mechanical Engineering

Date May/97

TITLE Internal Base

QUANTITY 1

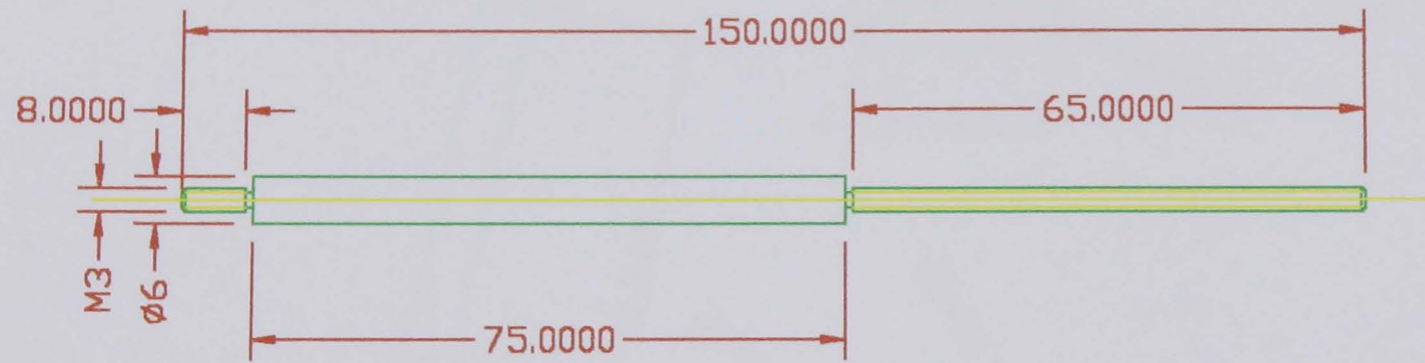
SCALE 1:1

WASIM-RCC

DRAWING No.4

ALL DIMENSIONS IN MM

PROJECTION



MATERIAL Mild Steel

DRAWN WASIM

DeMontfort University
Department Of Mechanical Engineering

Date May/97

TITLE Supporting Rod

QUANTITY 3

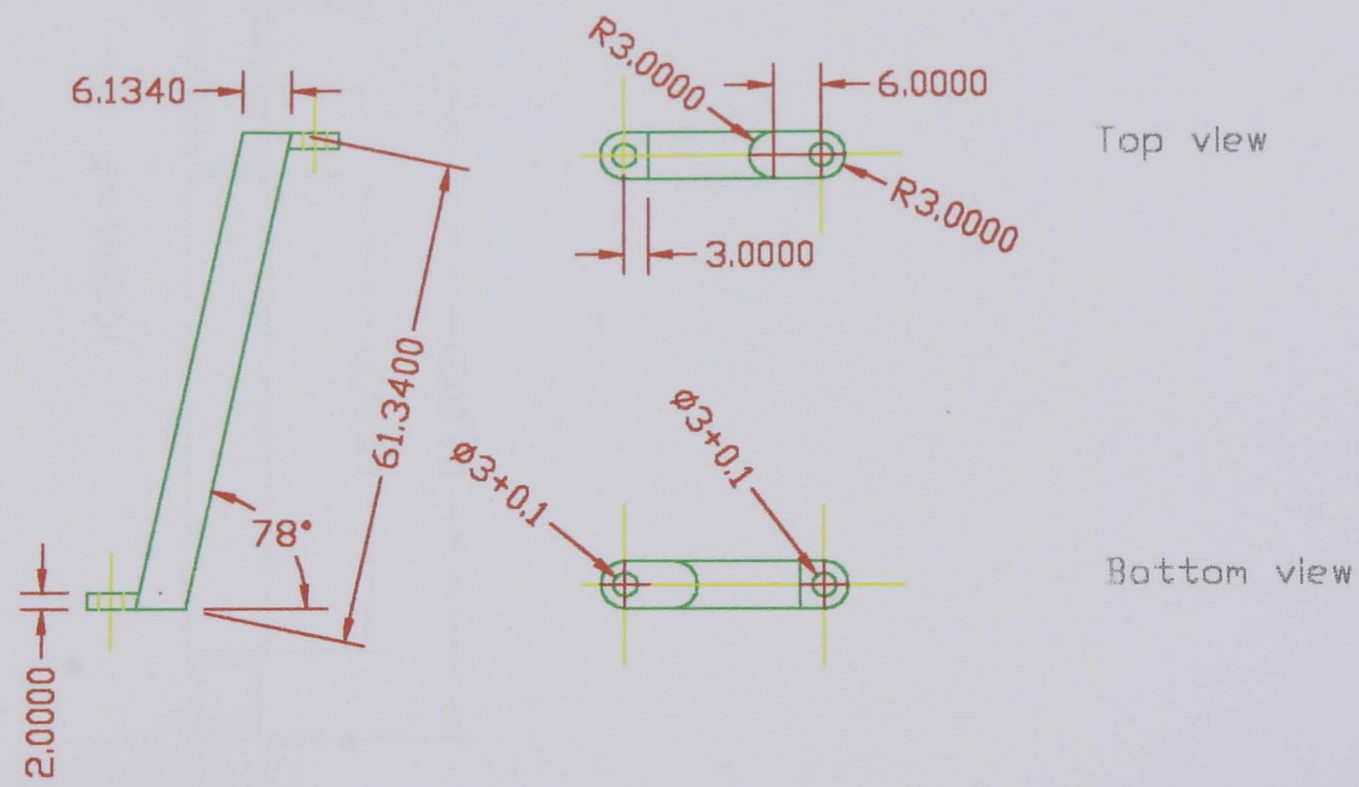
SCALE 1:1

CMB-RCC

DRAWING No.5

ALL DIMENSIONS IN MM

PROJECTION



MATERIAL

Mild Steel

DRAWN WASIM

DeMontfort University
Department Of Mechanical Engineering

Date May/97

TITLE Angular Rod

QUANTITY

3

SCALE 1:1

CVT-RCC

DRAWING No.6

ALL DIMENSIONS IN MM

PROJECTION



MATERIAL Mild Steel

DRAWN WASIM

DeMontfort University
Department Of Mechanical Engineering

Date May/97

TITLE Straight Rod

QUANTITY 1

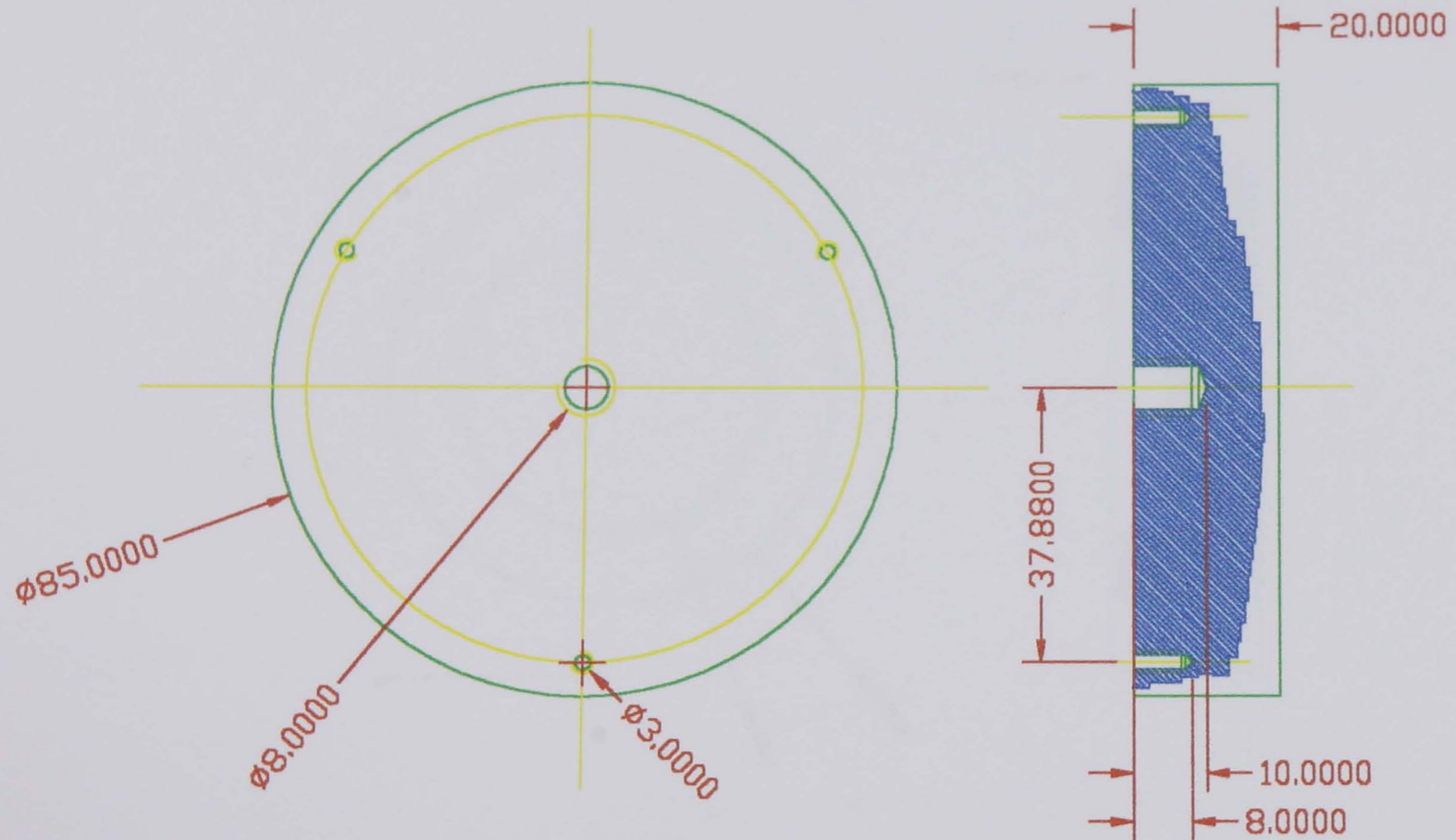
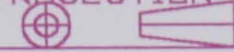
SCALE 1:1

CMH-RCC

DRAWING No. 7

ALL DIMENSIONS IN MM

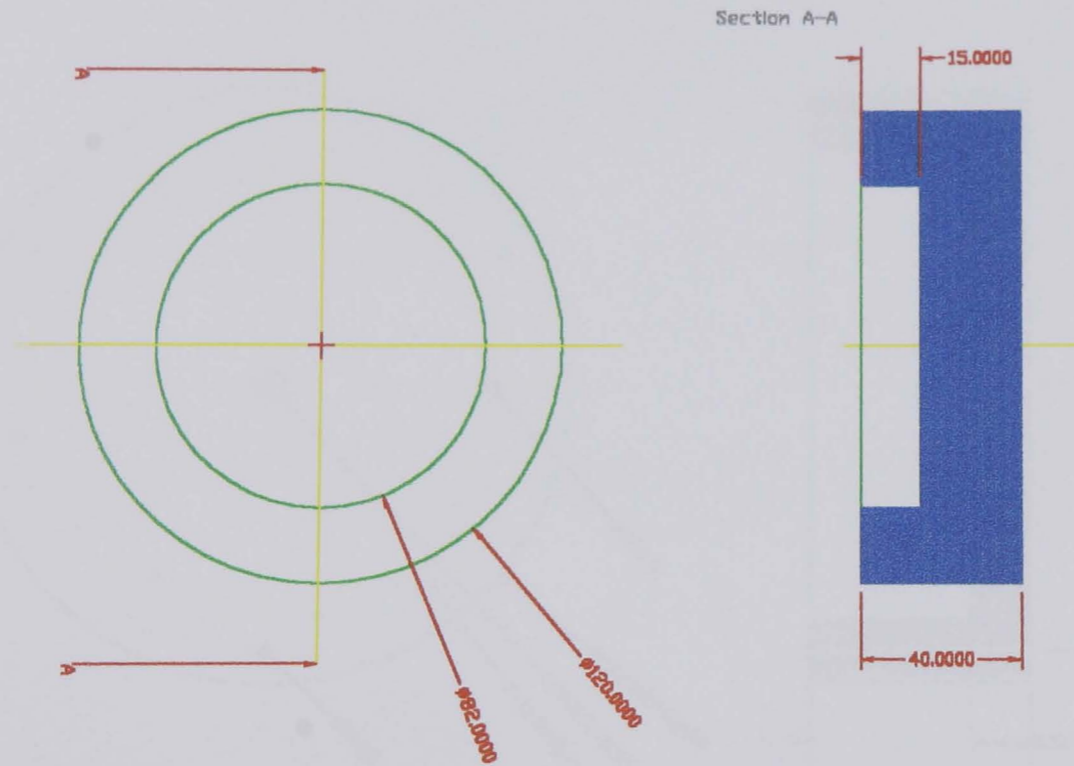
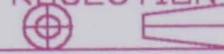
PROJECTION



MATERIAL	Aluminum	DRAWN	WASIM		
		Date	May/97		
QUANTITY	1	TITLE	Upper Base		
		SCALE	1:1	CMR-RCC	DRAWING No.8

ALL DIMENSIONS IN MM

PROJECTION



MATERIAL

Spong F010109 &

DRAWN WASIM
F010111

DeMontfort University
Department Of Mechanical Engineering

Date May/97

TITLE Upper Spong

QUANTITY

1 & 1

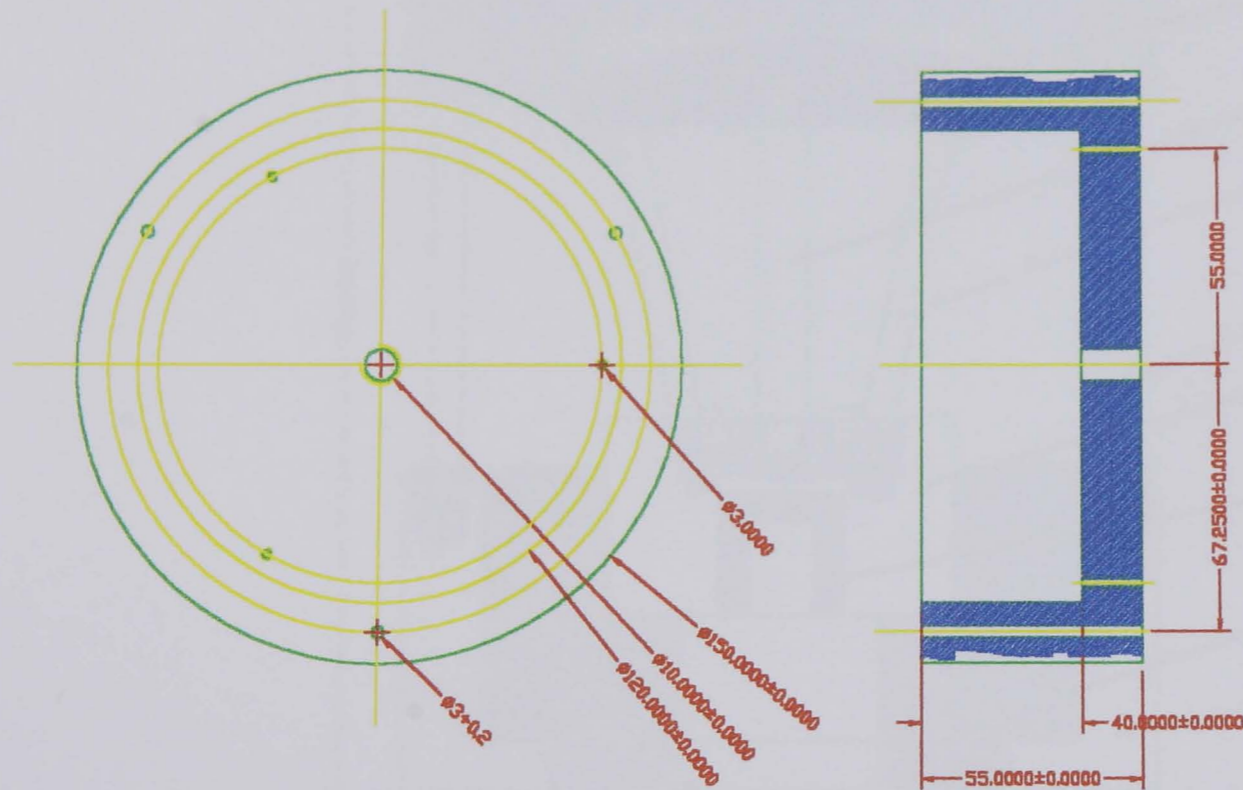
SCALE 0.5:1

CMH-RCC

DRAWING No.9

ALL DIMENSIONS IN MM

PROJECTION



MATERIAL Aluminum

DRAWN WASIM

DeMontfort University
Department Of Mechanical Engineering

Date May/97

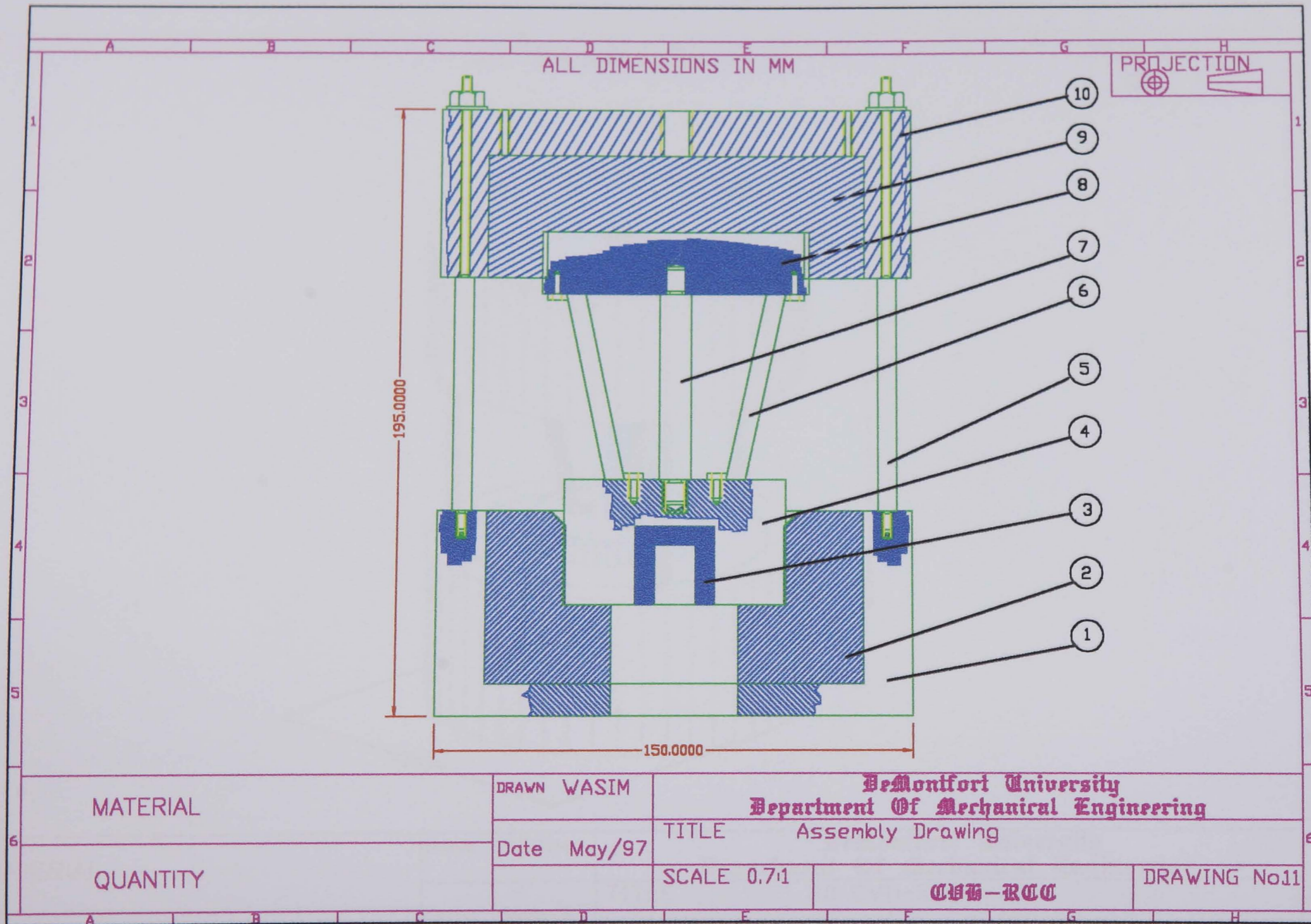
TITLE Top Plate

QUANTITY 1

SCALE 0.5:1

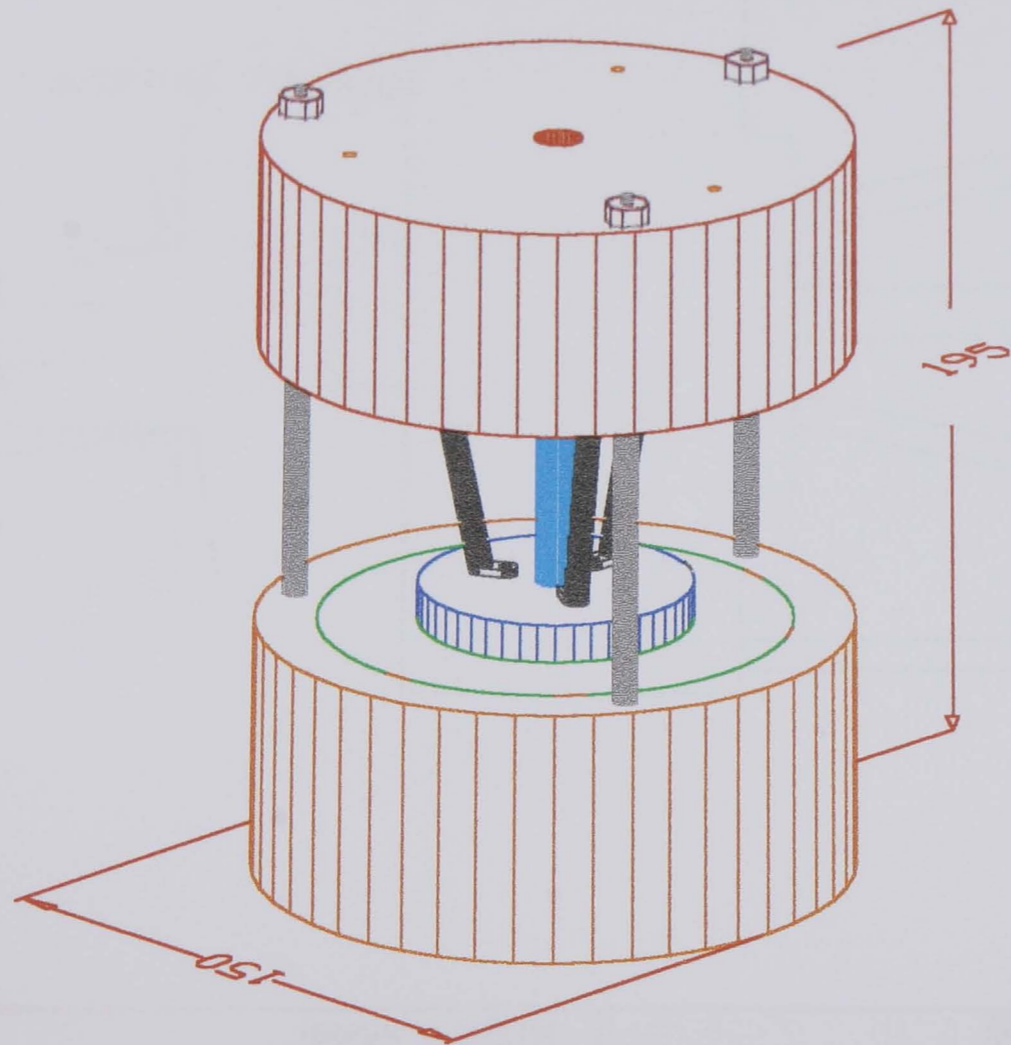
CMH-RCC

DRAWING No.10



ALL DIMENSIONS IN MM

PROJECTION



MATERIAL

DRAWN WASIM

DeMontfort University
Department Of Mechanical Engineering

Date May/97

TITLE 3D CVH-RCC

QUANTITY

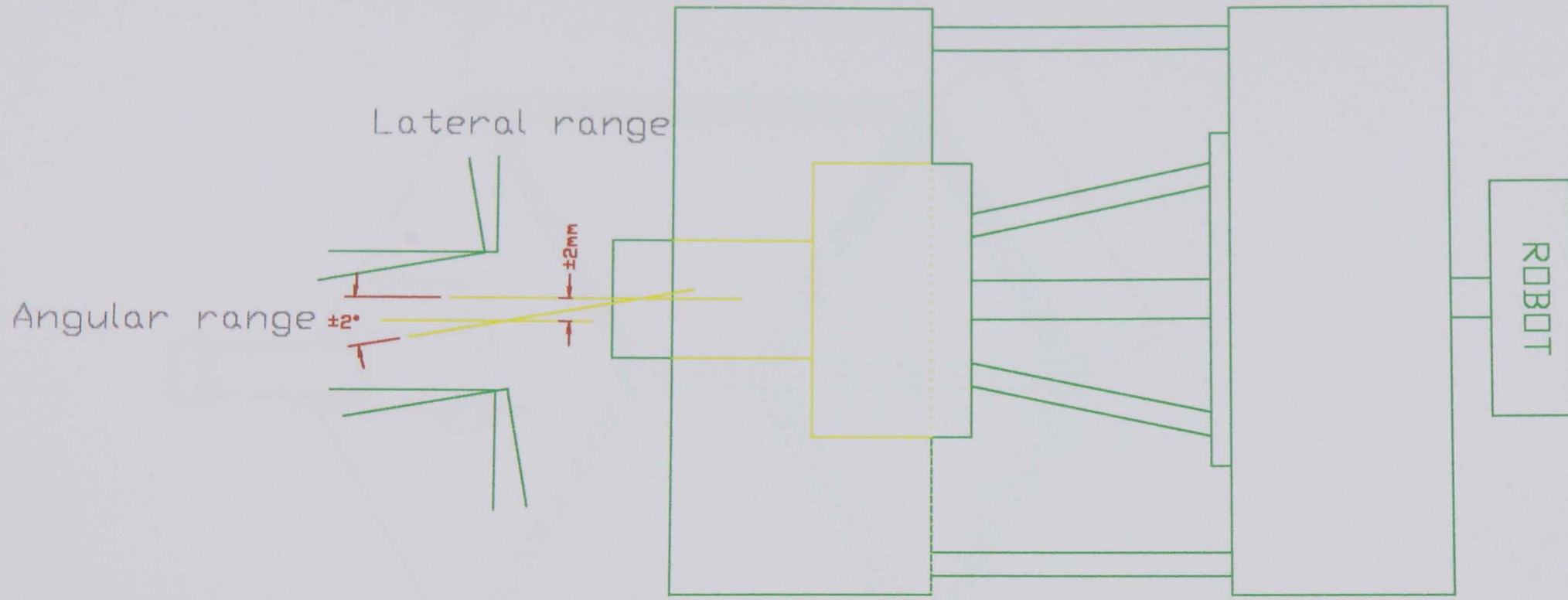
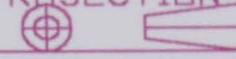
SCALE 1:2

CVH-RCC

DRAWING No12

ALL DIMENSIONS IN MM

PROJECTION



MATERIAL

DRAWN WASIM
DATE

DeMontfort University
Department Of Mechanical Engineering

CHECKED
DATE

TITLE Schematic drawing of range of motion
of CVH-RCC

QUANTITY

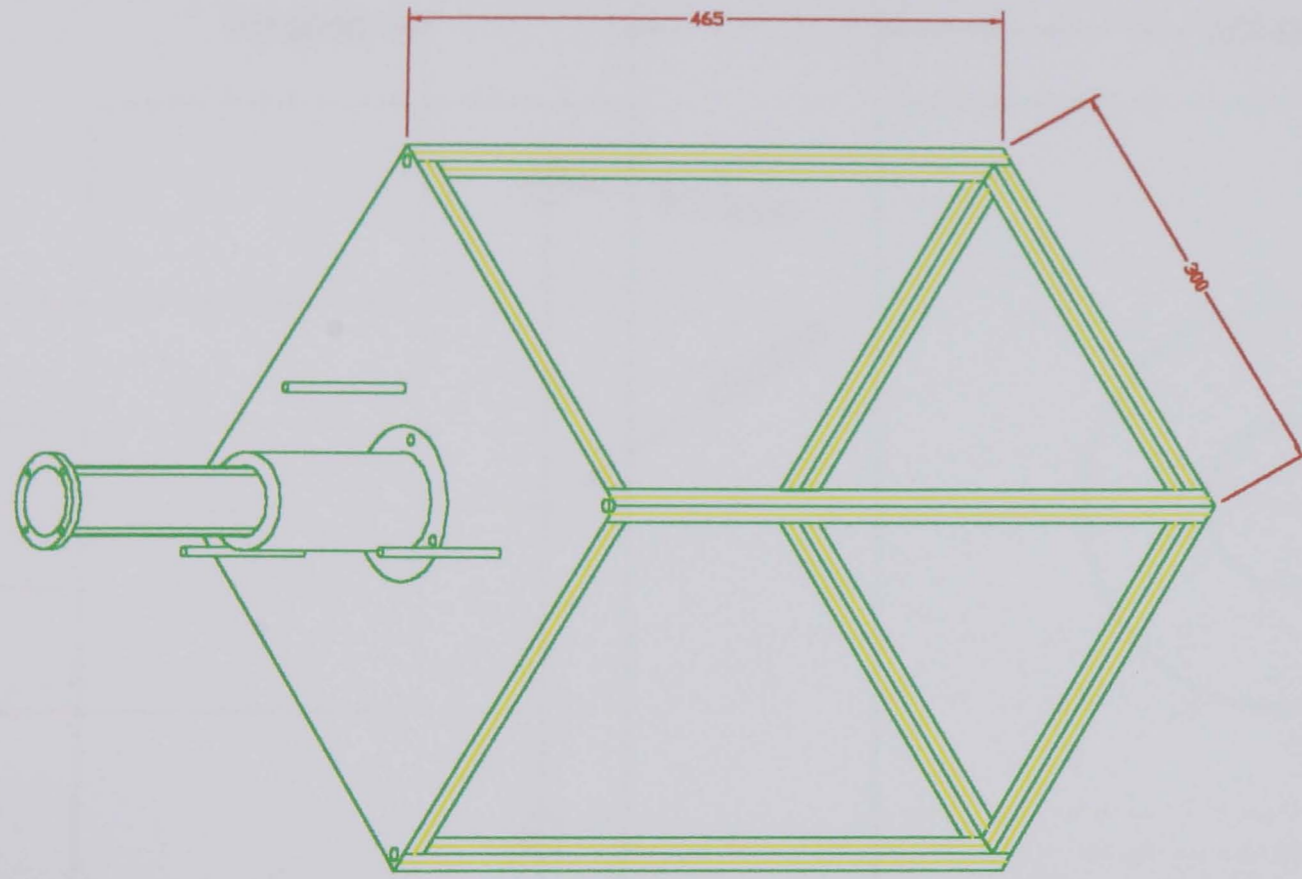
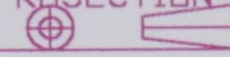
SCALE

CVH-RCC

DRAWING No13

ALL DIMENSIONS IN MM

PROJECTION



MATERIAL

DRAWN WASIM

DeMontfort University
Department Of Mechanical Engineering

QUANTITY

DATE May/97

TITLE
CVH-RCC Assembly rig, for peg-hole operations

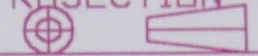
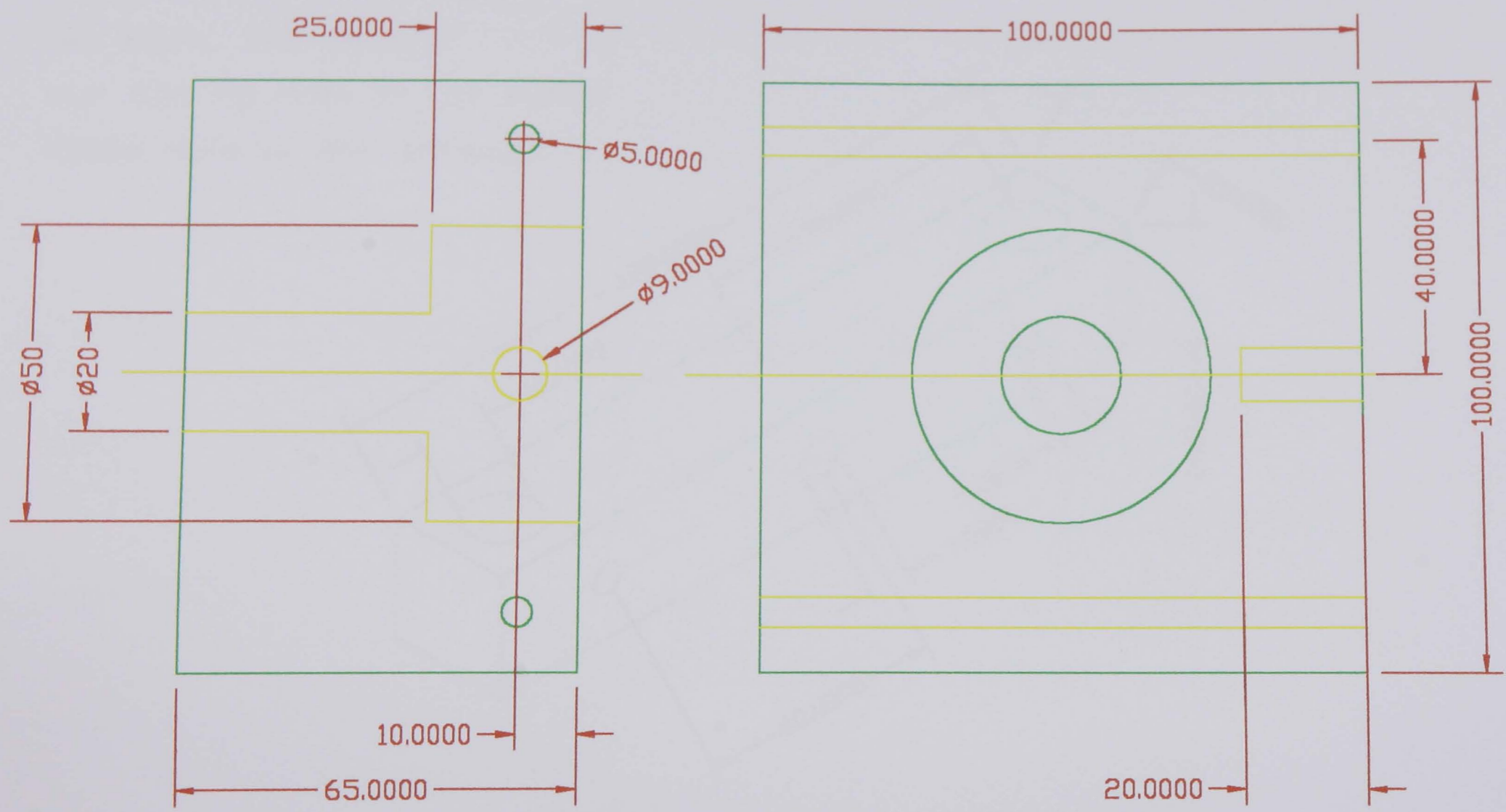
SCALE

CVH-RCC

DRAWING No.14

ALL DIMENSIONS IN MM

PROJECTION

MATERIAL Mild Steel

DRAWN WASIM
DATE

DeMontfort University
Department Of Mechanical Engineering

DATE May/97

TITLE Hole's plate

QUANTITY 1

SCALE 1:1

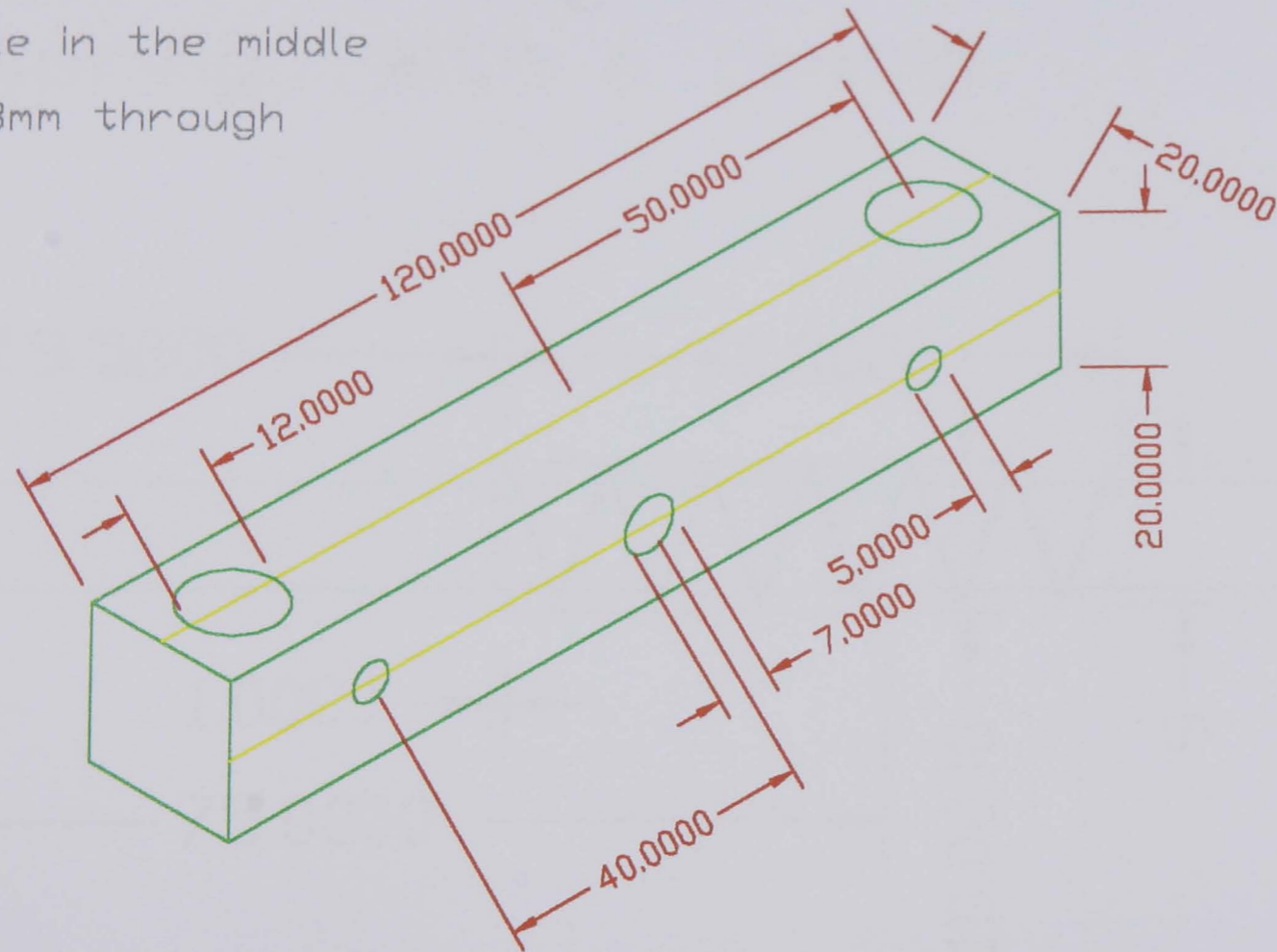
CMH-RCC

DRAWING No15

ALL DIMENSIONS IN MM

PROJECTION

Two bars, the second
bar has no hole in the middle
Middle hole is 3mm through



MATERIAL Aluminum

DRAWN WASIM

DeMontfort University
Department Of Mechanical Engineering

QUANTITY 2

DATE May/97

TITLE Bars for clamp mechanism

SCALE 1:1

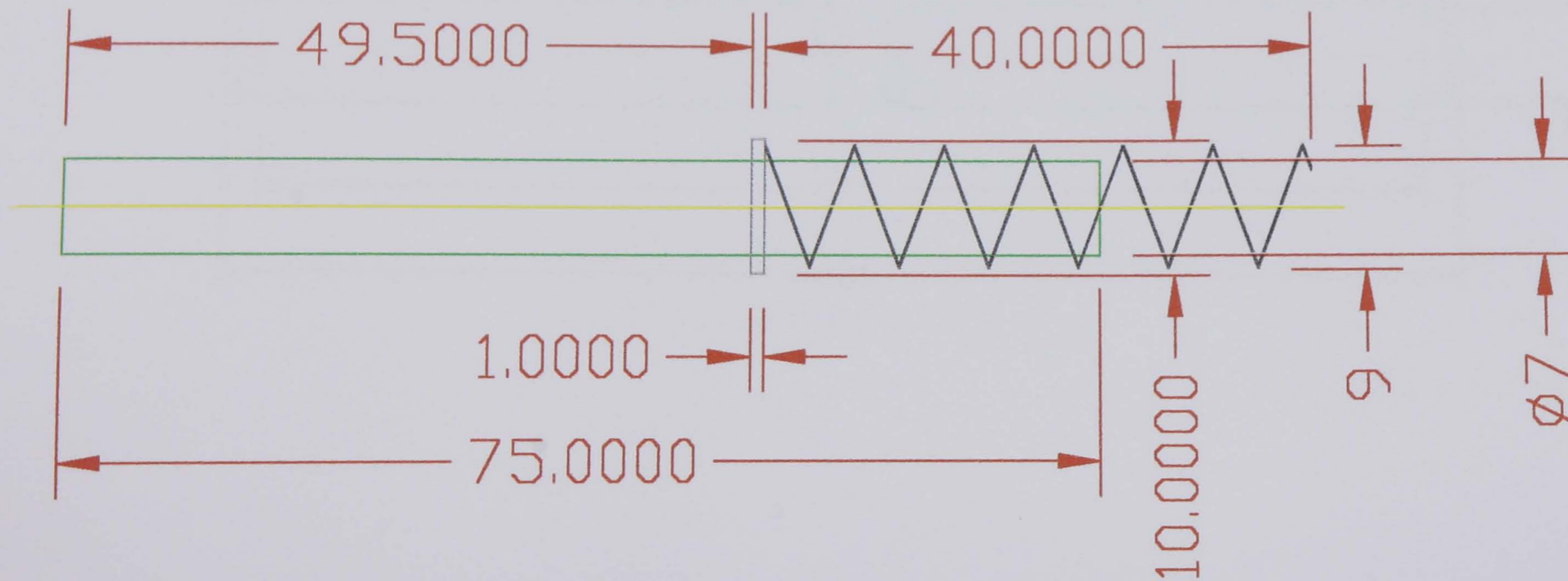
CMB-RCC

DRAWING No16

ALL DIMENSIONS IN MM

PROJECTION

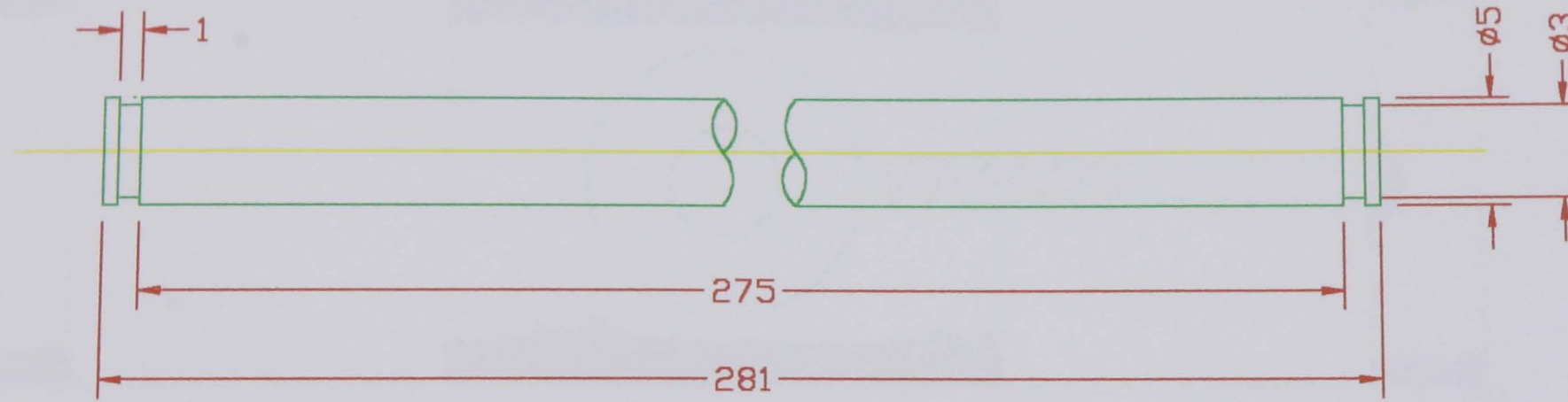
This is assembly dwg. of
bar & spring with a circlip



MATERIAL	Mild Steel	DRAWN	WASIM		
		De Montfort University Department Of Mechanical Engineering			
QUANTITY	1	DATE	May/97		
		TITLE	Ass. dwg. of a spring mounted on a bar		
		SCALE	1:1	CMH-RCC	DRAWING No.17

ALL DIMENSIONS IN MM

PROJECTION



MATERIAL Mild Steel

DRAWN WASIM

DeMontfort University
Department Of Mechanical Engineering

QUANTITY 2

DATE May/97

TITLE Slider

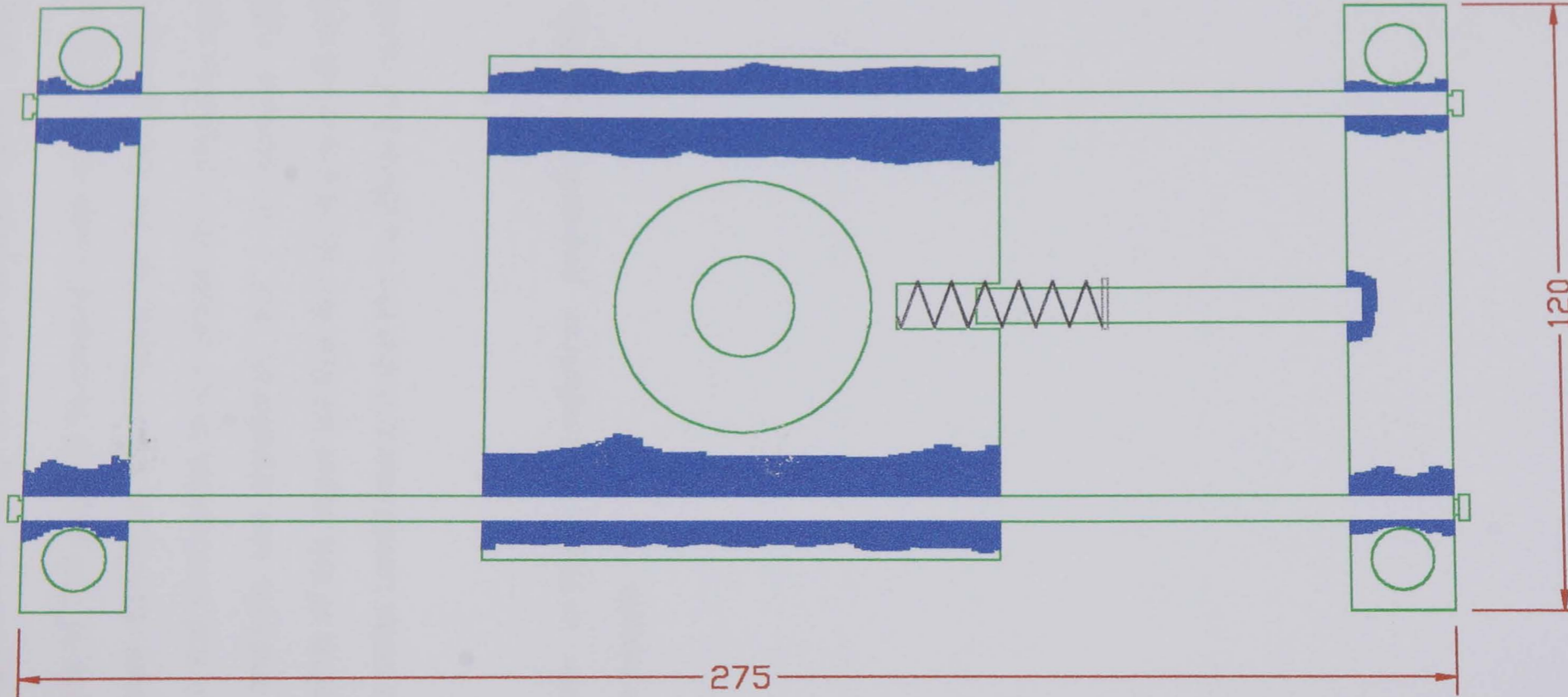
SCALE 1:3

CSH-RCC

DRAWING No.18

ALL DIMENSIONS IN MM

PROJECTION



MATERIAL

DRAWN WASIM

DeMontfort University
Department Of Mechanical Engineering

QUANTITY

DATE May/97

TITLE Hole's fixture

SCALE 1:1.333

CMR-RCC

DRAWING No.19

Peg-Hole Strategy And The Domino Effect Theory

Abstract: The purpose of this paper is to present a new strategy for chamferless peg-hole assembly from different directions that is based on the domino effect theory. This paper shows the differences and similarities in the chamferless peg-hole assembly from different directions, through analysis and simulation and a comparison with the domino effect theory. The major points of this paper are that the vertical and horizontal chamferless peg-hole assemblies have same conditions and that the coefficient of friction has to be as small as possible.

Indexing terms: new strategy, chamferless peg-hole assembly, vertical/horizontal assembly, simulation results

A New Strategy For Chamferless Peg-Hole Assembly

Abstract: One problem that arises during component assembly is that small errors in relative position or angular position can produce large forces. These forces can prevent successful completion of the assembly (jamming) and can cause damage to the parts or the assembly machine/robot.

To overcome these problems, its normal to use a Remote Centre Compliance (RCC) device. The limitation of the RCC is that it can only be used for top-down (vertical) assembly, and also the mating parts must have a chamfer to facilitate the assembly operation.

The approach presented here is a new strategy for chamferless peg-hole assembly from X/Y/Z directions. An investigation and a comparison between the vertical and horizontal assembly are presented followed by a simulation programme for testing the new strategy.

The major conclusion is that both assembly methods have same assembly conditions, and that the coefficient of friction has to be as small as possible.

Indexing terms: new strategy, chamferless peg-hole assembly, vertical/horizontal assembly, simulation results

A Passive Compliant Wrist For Chamferless Peg-In Hole Assembly Operation From Vertical & Horizontal Directions (CVHRCC)

Abstract: This paper presents a Chamferless-Vertical-Horizontal Remote Centre Compliance (CVHRCC) mechanism developed for robotic peg-in hole assembly operations. The wrist adopts the passive accommodation approach and differs from other devices in its category, in its ability to accommodate positional errors between the mating parts without a chamfer on either part. In addition, the wrist is designed to work from both the vertical and the horizontal directions.

A series of experiments have been carried out for testing the new wrist. The main conclusion of the assembly experiments is that the CVHRCC can work effectively from the vertical direction in accommodating positional errors between chamferless mating parts with large clearance (over 0.2mm) between the peg and hole.

Keywords: Robotic assembly; Assembly strategy; CVHRCC; Chamferless peg-in hole; Vertical/Horizontal direction.

Robotic Assembly: Chamferless Peg-Hole Assembly

SUMMARY:The peg-in hole insertion process is the most common task in the robotic/automated assembly industry. However, the inaccuracy of the assembly robot in positioning the inserted peg into the hole due to the uncertainty of the assembly environment, represent an obstacle in this area of automation. To overcome this problem, complex and expensive equipment has been designed. The objective of this paper is to provide an in depth understanding of the chamferless peg-hole assembly, by showing the geometrical, dynamical conditions for a successful assembly operation. Also, the results of this analysis have been simulated to demonstrate the chamferless peg-hole insertion process.

Keywords: Peg-in hole; Geometrical analysis; Dynamical analysis; Simulation.

A THEORETICAL AND EXPERIMENTAL STUDY FOR THE CHAMFERLESS PEG-IN HOLE INSERTION PROCESS, USING A PASSIVE COMPLIANT WRIST

Abstract: The paper presents a mathematical model for the chamferless peg-in hole insertion process. The insertion model is simulated using Matlab-Simulink software. The simulation results are correlated to the design of a passive compliant wrist that fits between the robot arm and the gripper. The wrist can overcome positional misalignment between cylindrical mating parts even in case of no chamfer on either the peg or the hole. The wrist has been tested in real assembly operations and proved to be successful.

Keywords: peg-in hole insertion process, simulation programme/results, compliant wrist, experimental results